Design of Linear Phase Sharp Transition FIR Filters to Detect Non-invasive Maternal and Fetal Heart Rate

Thesis submitted to Goa University

for the Award of the Degree of

DOCTOR OF PHILOSOPHY

in

Electronics

By

Niyan Joseph Savio Marchon

Under the Guidance of

Dr. Gourish M. Naik

Department of Electronics,

Goa University, Taleigao Goa

November 2018

CERTIFICATE

This is to certify that the thesis entitled, **"Design of Linear Phase Sharp Transition FIR Filters to Detect Non-invasive Maternal and Fetal Heart Rate"** submitted by **Mr. NIYAN JOSEPH SAVIO MARCHON** for the award of degree for Doctor of Philosophy in Electronics, is based on his original and independent research work carried out by him during the period of study, under my supervision. The thesis or any part thereof has not been previously submitted for any other degree or diploma of this or any other University or Institute.

(Prof. G. M. Naik)
Research Supervisor

(Ph.D. External Examiner)

Place: Goa University
Date: 5th March 2018

DECLARATION

I state that the present thesis entitled "**Design of Linear Phase Sharp Transition FIR Filters to Detect Non-invasive Maternal and Fetal Heart Rate"**, is my original contribution and the same has not been submitted on any occasion for any other degree or diploma of this or any other University or Institute to the best of my knowledge the present study is the 1st comprehensive work of its kind in the area mentioned. The literature related to the problem investigated has been cited. Due acknowledgements have been made whenever facilities and suggestions have been availed of.

Place: **Goa University**
Date: **5th March 2018**

(Niyan Joseph Savio Marchon)
Candidate

I dedicate the accomplishment of my thesis

In memory of my

Late parents, Aires and Angela Marchon.

'Commit your works to the Lord and your plans will be established.'

Proverbs 16:3

(Holy Bible)

Abstract

As reported in the WHO Media Centre, congenital anomalies affect approximately 1 in 33 infants and result in approximately 3.2 million birth defect related disabilities every year. The Infant Mortality Rate in India is 11 deaths per 1000 live births. Medical reports in the hospitals in the state of Goa also showed that the total infant deaths that occurred were due to congenital anomalies, birth asphyxia, etc giving rise to the need for monitoring fetal health early in pregnancy. Monitoring of fetal heart rate may help clinicians to recognize pathological conditions so as to enable doctors for proper intervention that could result in irreversible neurological damage or even fetal death.

Among various fetal monitoring techniques, the non-invasive fetal electrocardiogram (FECG) can be used to monitor fetal heart rates by placing the standard 12 lead surface ECG electrodes over the maternal abdomen. The maternal thoracic ECG can be taken as a reference signal along with the abdominal ECG. The non-invasive FECG contains potentially valuable information that assists clinicians to make appropriate and timely decisions, especially during the last weeks of the 3rd trimester of pregnancy or during labor. Due to the limitation of perfectly monitoring fetal heart rates, such as improving the signal to noise ratio of the abdominal ECG, researchers in the biomedical signal processing field have developed advanced FECG detection, extraction, and analysis methods. Among the number of detection and extraction techniques to separate the fetal ECG from the maternal ECG, this research work implemented and simulated techniques like independent component analysis, adaptive-network-based fuzzy inference system, template matching and correlation. Some of these mentioned methods for extracting non-invasive FECG have their own drawbacks.

In this thesis, we have proposed a linear phase sharp transition (LPST) FIR band pass filter (BPF) design of various filter orders with an arbitrary passband. Firstly, we apply the

single lead, non-invasive aECG signal to the LPST FIR BPF using the designated fiduciary edges with a sharp transition width. In the second stage, a QRS detector based on Pan Tomkins QRS detector algorithm is used to compute fetal or maternal heart rates. Our design allows the user to set the cut off frequencies for a narrow pass band width for any filter order. It also incorporates a very linear, sharp transition region while reducing the effects due to Gibb's phenomenon, thereby reducing the passband ripple of the filter. To study the merits of our filter design, the magnitude response of our proposed filter performance was compared to that of the Parks-McClellan (PM) filter for a range of filter orders.

In this research work, three LPST FIR BPF models were presented. The accuracy and failed detections were computed to evaluate the performance of the three LPST FIR BPF Models: I, II and III using the Physionet databases. LPST FIR BPF Model I employed a BPF containing a tandem of high pass and low pass FIR filters. LPST FIR BPF Model II described a technique of implementing an integrated BPF. The FIR BPF Model III used a novel technique to reduce Gibb's phenomenon at the fiduciary band edges of the band pass filter. In this method, equations are derived for slopes of the frequency response of the filters at the edges of the transition region and these slopes are matched. This reduces the effects due to Gibb's phenomenon, thereby reducing ripples at the edges of the transition region of the filter and hence reduces passband ripple and improves stopband attenuation of the filter. In an aECG signal, it is also observed that our designed LPST FIR BPFs were able to compute precise single fetus R-peaks and maternal R-peaks even when the FQRS and MQRS signals overlapped in the time domain or existed in very close proximity. Our filter designs are simple, versatile and analytical without extensive computations. Our method is helpful for implementing a mini health care unit, making it suitable for ambulatory and long-term monitoring for the maternal and fetal well-being.

Acknowledgments

I praise my Lord Jesus for His mercy and for His immense grace for allowing me to successfully complete this thesis.

I would like to acknowledge and thank my supervisor, Dr. Gourish Naik, Head of Department, Department of Electronics, Goa University, for his words of wisdom, constructive criticism, valued discussions, guidance and for his focused approach to this research. I appreciate his contribution towards my intellectual growth and development. I would like to thank Dr. K. R. Pai, my research co-guide, Professor and former Head of the Department of Electronics and Telecommunications at Padre Conceicao College of Engineering (PCCE) for his exceptional guidance in my research work and for his scientific and moral guidance without which this work would not be possible.

I wish to thank my Directors, Rev. Fr. Anthony Castello and Rev. Fr Seby Rodrigues, Dr. Mahesh Parappagoudar, Principal, PCCE and Dr. Stephen Baretto, Registrar, PCCE for their constant support and motivation. I would like to thank Dr. Luis Mesquita, Head of Department, Master of Engineering (IT) at PCCE, for his evaluation, valuable comments and insightful feedback of this work. I would like to thank Dr. Kevin Kreger and Mr. Gajanan Nagarsekar from Kallows Engineering India Pvt. Ltd, for the fruitful discussions that we have had in this research work.

A profuse thanks to Dr. Guruprasad Pednekar, Professor and Head of Department and Dr. Ajit Nagarsenkar, Associate Professor, Department of Obstetrics & Gynecology, Goa Medical College for all the valuable initial discussions we had regarding my research work. I sincerely acknowledge for all the medical knowledge and help rendered to me during my research work by Dr. Emmanuel Gracias, Joint Managing Director-Gracias Maternity Hospital and Dr. Shrutin Ulman, Senior Scientist (Leader Clinical Affairs and Outside Innovation) Philips Innovation Campus, Bangalore.

I gratefully acknowledge the significant contribution to this work by my colleagues from the Electronics and Telecommunication Department, PCCE, Dr. Jayalaxmi Devate and all the faculty members, especially Mr. Vaibhav Vernekar and Mr. Santosh Tari for their help and support. Similarly, I would like to thank the faculty at the Electronics Department, Goa University, i.e. Dr. Rajendra Gad, Dr. Jivan Parab and Dr. Ingrid Nazareth for all their guidance and support. I also thank my research colleagues at the Electronics department, Goa University: Mr. Narayan Vetrekar, Mr. Noel Tavares, Ms. Shaila Ghanti, Ms. Supriya Patil, Dr. UdaySingh Rane, Mr. Vasudev Mahale, Ms. Yogini Prabhu, Mr. Marlon Sequeira and the rest of the members for contributing immensely in managing my research work, for the unending tolerance and suggestions. A special thanks to Mr. William D'Souza, who has willingly helped me with all admin paper work during the FRC presentations. My thanks extends to Dr. V. Gopakumar, librarian, Goa University for all the help rendered during plagiarism studies.

Thanks goes out to Mr. Charlton Fernandes and Mr. Leroy Pereira for all the help and support given to me in Matlab simulations during the intial stages of my research work. I wish to thank my NASA colleagues, Ms. Alzira Xavier, Mr. Saish Vernekar and Ms. Aditi Silveira for their unrestrained enthusiasm, lively discussions and motivation throughout my years of research. I particularly thank Ms. Aditi, for cheerfully proof reading my journal articles, conference papers and my entire thesis. In addition, I would like to thank my other faculty colleagues, Mr. Joe Kurian, Ms. Anusha Pai, Ms. Razia Sardinha and Ms. Louella Mesquita who regularly inquired about my research work and encouraged me at all times.

Finally, I would like to thank my spiritual mentor, Br. Edmund Antao for his spiritual guidance in my life and all the core members from the Association of Crusaders for Jesus with Mary. I would like to thank my wife, Soraya Marchon and my three lovely daughters Keziah, Asriel and Zerah for their constant love and support at every stage of my research.

Thank you all!!

Contents

List of Figures

List of Tables

List of Abbreviations

AAMI	Association for the Advancement of Medical Instrumentation
ADC	analog to digital converter
adfecgdb	abdominal and direct fetal electrocardiogram database
aECG	abdominal electrocardiogram
AI	Artificial Intelligence
ANC	antenatal care
ANFIS	adaptive-network-based fuzzy inference system
ANN	artificial neural networks
ANSI	American National Standards Institute
AV	atrioventricular
BPF	band pass filter
BSS	Blind Source Separation
BW	bandwidth
CCWT	Complex Continuous Wavelet Transform
CTG	cardiotocography
DSP	Digital Signal Processing
DWT	Discrete Wavelet Transform
ECG	electrocardiogram
EFM	electronic fetal monitoring
EHG	electrohysterogram
EMG	electromyogram
F_1	accuracy
FD	failed detections
FECG	fetal electrocardiogram
FHR	fetal heart rate
FHRV	fetal heart rate variability
FIR	finite impulse response
FMCG	fetal magnetocardiogram
FN	False negative
FP	False positive

FPGA	field programmable gate array
FQRS	fetal QRS
FRM	frequency response masking
Fs	sampling frequency
FSM	Frequency sampling method
GA	Genetic Algorithm
GDP	gross domestic product
GND	ground
HPF	High pass filter
HR	heart rate
ICA	Independent Component Analysis
IEC	International Electrotechnical Commission
IIR	infinite impulse response
IMR	Infant Mortality Rate
IUP	intrauterine pressure
LA	left arm
LL	left leg
LMS	least mean square
LPF	Low pass filter
MAF	Moving Average Filter
MECG	maternal electrocardiogram
MHR	maternal heart rate
MQRS	maternal QRS
MRA	multiresolution analysis
MW	Mother Wavelet
NIFECG	non-invasive fetal electrocardiogram
nifecgdb	Non-Invasive Fetal Electrocardiogram Database
NIFHR	Non-invasive fetal heart rate
NLMS	normalized least mean square
PCA	Principle Component Analysis
PCG	fetal phonocardiography
Phy C	Physionet/Computing in Cardiology 2013 Challenge Database
PLI	power line interference
PM	Parks-McClellan

PPV	positive predictive value
PRB	Population Reference Bureau
PSO	particle swarm optimization
QRS	Central part of heart beat morphology
RA	right arm
RL	right leg
RLS	recursive least square
SA	sinoatrial
Se	sensitivity
SNR	signal to noise ratio
SQUID	superconductive quantum interference device
SVD	Singular Value Decomposition
TP	True Positive
WA-PM	Wavelet Analysis and Pattern Matching
WCT	Wilson's Central Terminal
WHO	World Health Organization
WT	wavelet transform

List of Symbols

a_k, b_k	filter coefficients
B	bandwidth
E (ω)	maximum weighted error
F_H	higher cut-off frequency
F_L	lower cut-off frequency
fs	sampling frequency
h (n)	impulse response coefficient
H (ω)	magnitude of the filter response
H_D (ω)	desired frequency response
Hz	Hertz
k_p	design parameter for pass band
k_{ph}	design parameter for pass band for high pass filter
k_{pl}	design parameter for pass band low pass filter
k_s	design parameter for stop band
k_{sh}	design parameter for stop band for high pass filter
k_{sl}	design parameter for stop band low pass filter
k_t	design parameter for transition band
k_{th}	design parameter for transition band for high pass filter
k_{tl}	design parameter for transition band low pass filter
N	filter order
n_i	time index corresponding to the i^{th} computed R fetal peak
P_f	fetal source dipole vector
P_m	maternal source dipole vector
Res	resolution
W (ω)	Weighting function
x (z)	input to the differentiator block
x_{maf} (i + j)	input to the moving average filter
x_{mi} (n)	input to the moving window integrator
y (z)	output of the differentiator block
y_{maf} (i)	output of the moving average filter
y_{mi} (n)	output of the moving window integrator

ΔF	narrow transition bandwidth
Δn	R-R peak interval
δ_p	passband ripple error
δ_s	stopband attenuation error
ω	frequency variable
ω_{ch}	passband edge frequency of the high pass filter
ω_{cl}	passband edge frequency of the low pass filter
ω_{p1}, ω_{p2}	fiduciary band edges for pass band of band pass filter
ω_{s1}, ω_{s2}	fiduciary band edges for stop band of band pass filter
ω_{sh}	stopband edge frequency of the high pass filter
ω_{sl}	stopband edge frequency of the low pass filter
$(\omega_{ch} - \omega_{sh})$	transition bandwidth

1

Introduction

1.1 Background and Motivation

Five years after Einthoven's first discovery of electrical activity in a human heart, Cremer identified the fetal electrocardiogram (FECG) from the abdominal and vaginal set of electrodes. Winkler discovered six years hence that a fetal heart rate (FHR) higher than 160 beats per minute (bpm) and less than 120 bpm indicated fetal distress [1]. Decelerations of the FHR predicts fetal hypoxia. It is reported in the World Health Organization (WHO) Media Centre 2012 that birth defects referred to as congenital anomalies affect approximately 1 in 33 infants and results in approximately 3.2 million birth defect related disabilities every year [2]. The infant Mortality Rate (IMR) of 2012 among the Indian states was 43.8 deaths per 1000 live births [3]. Madhya Pradesh, the central state in India scored the highest IMR of 62 while Goa scored the lowest IMR of 11 as shown in Figure 1.1. The Population Reference Bureau (PRB) which informs the world about health, population and the environment shows the region wise 2015 IMR as shown in Figure 1.2a [4] . The highest IMR in the world is in African countries. Among the South Asian countries, India displayed an IMR of 42 in 2015, slightly lower than recorded in 2012 as shown in Figure 1.2b. Reports in the local newspapers in the year 2012 showed that the total infant deaths at birth that occurred at the hospitals in the state of Goa, India were 249. The infant deaths were mainly due to congenital anomalies (35.7%), low birth weight (26.7%), sepsis (25.5%), birth asphyxia (5%) and others (8%) as shown in Figure 1.3 [5]. Also, all over the world, approximately 2.65 million stillbirths occur during pregnancy or labor, especially in developing countries [6].The occurrence of birth defects leading to death in infants is prevalent till today.

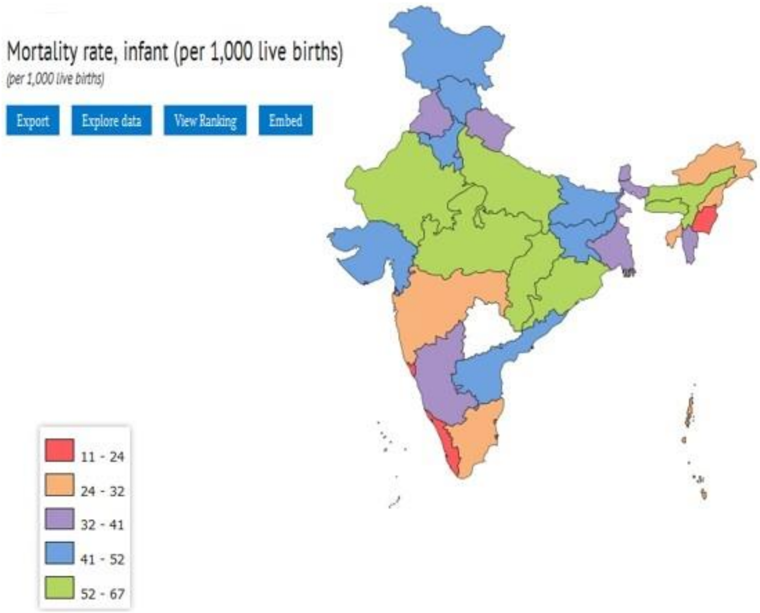

Figure 1.1: Infant Mortality Rate statistics of the Indian states in the year 2012 [3].

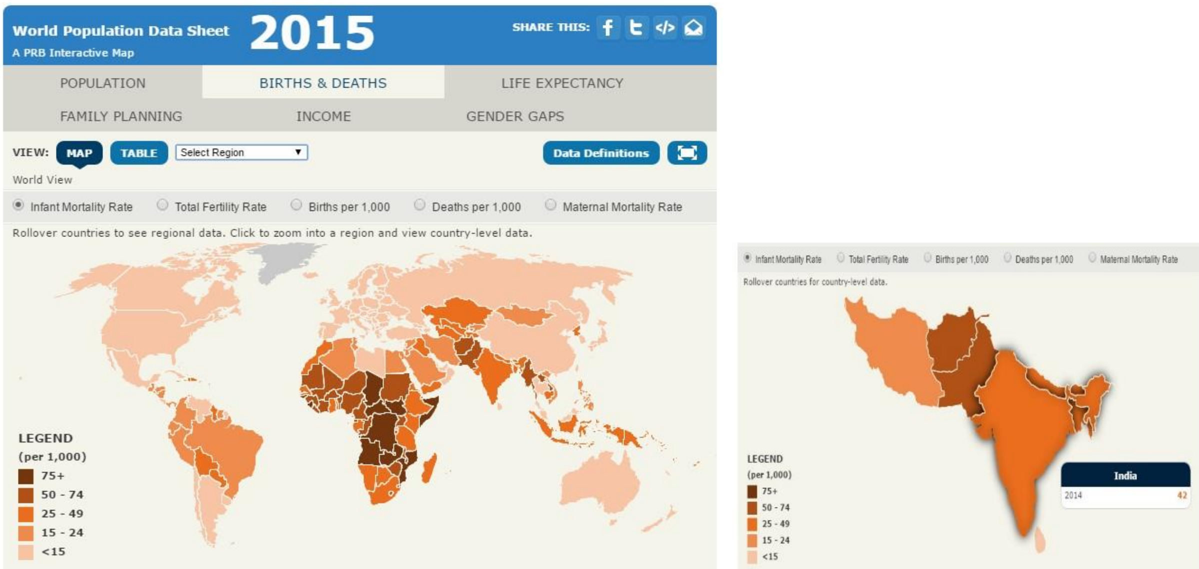

1.2 (a) 1.2 (b)

Figure 1.2: Population Reference Bureau 2015 data displaying (a) IMR of all countries (b) IMR of South Asia (India) [4].

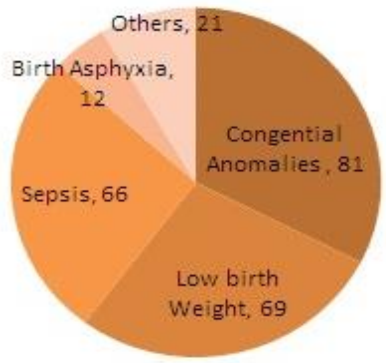

Figure 1.3: Cause of death in Infants at birth due to birth asphyxia at the hospitals in Goa, India (Newspaper report, Heraldo (Insight) Friday, May 17 2013) [5].

1.2 Need for fetal monitoring

The World Health Organisation released the antenatal care (ANC) model on 7th November 2016. This model envisions and promotes critical healthcare for diagnosis and prevention of all maternal and fetal diseases [7]. The model promises timely maternal and fetal assessment, health support by the clinicians which will further enhance the successful pregnancy outcomes. Ban Ki-Moon, the Ex-United Nations Secretary-General said in 2016**,** "To achieve the Every Woman Every Child vision and the Global Strategy for Women's, Children's and Adolescents' Health, we need innovative, evidence-based approaches to antenatal care. I welcome these guidelines, which aim to put women at the centre of care, enhancing their experience of pregnancy and ensuring that babies have the best possible start in life"

FHR monitoring is important to recognize pathologic conditions, typically asphyxia, with sufficient warning so as to enable intervention by the clinician [8]. It is a screening modulus of the fetus to detect problems in advance that could result in irreversible neurological damage or even fetal death [9]. More than 85 percent of all live births in the United States undergo electronic fetal monitoring (EFM) [10]. Indeed fetal health monitoring is of significant importance in obstetrical procedures and is now widely accepted as the need of the hour.With EFM came the following expectations – provision of accurate FECG information, information of value in diagnosing fetal distress, prevention of fetal death or morbidity and superiority over many methods. The fetus can be monitored electronically by two methods: direct (invasive) and indirect (non-invasive). In the direct invasive method, the FHR is measured by a scalp electrode which is attached to the fetal scalp by means of a coiled electrode [11]. In the indirect electronic monitoring method, such as using ultrasound Doppler principle with uterine contractions, FHR can be monitored, but not as precisely as the direct invasive FECG [8]. The ultrasound transducer with the coupling gel is applied to the mother's abdomen where the fetal heart response is best detected. During this measurement, the pulsations of the maternal aorta could be detected and erroneously considered as FHR [12]. The non-invasive FECG (NIFECG) by indirect method can therefore be used to overcome all these limitations by placing surface electrodes such as the 12 lead ECG electrodes over the maternal abdomen [13]. The maternal thoracic ECG can also be taken as a reference signal along with the abdominal ECG (aECG). A study was conducted during labour of about 75 pregnant mothers using non- invasive fetal monitor AN24 monitor and was compared with external methods, to check the accuracy and reliability of the FECG [14]. It was found that the direct scalp FECG gave the most accurate FHR than the conventional external methods, however this method could be used only during labor else it would cause risk and infection to the fetus. Therefore EFM using NIFECG recordings are most suitable for long term ambulatory use [15].

1.3 Economics to deal with fetal health care

The Indian government doesn't spend a lot low on antenatal care (ANC) as compared to other nations having similar poverty levels and per-capita income. WHO in its updates in the Global Health Expenditure database shows that the percentage of gross domestic product (GDP) is 1.407 % unlike countries like Sri Lanka, China and Brazil who spend 2 %, 3 % and 3.8 % on its GDP, respectively [16]. Detection of NIFECG signal and associated analysis as part of ANC is a very powerful and advanced method today in clinical diagnosis and biomedical applications. The NIFECG contains potentially valuable information that assists clinicians to make appropriate and timely decisions, especially during the last weeks of the 3rd trimester or at full term. There is a limitation to perfectly monitor fetal heart rates, improving the signal to noise ratio (SNR) of the NIFECG.

Researchers in the biomedical signal processing field have done extensive work in the last two decades towards advanced NIFECG detection, extraction, and analysis methods. A large number of detection and extraction techniques are used to separate the maternal ECG (MECG) from the FECG either by using single or multichannel signal sources. A single or multi- channel signal source can be used to extract the NIFECG from the aECG. The signals are processed by adaptive and non-adaptive methods that extract NIFECG. The drawback of non-adaptive techniques include it being time invariant. This is overcome by adaptive methods [17]. Researchers in this field have reinforced the extraction algorithms and improved the detection techniques, thereby leading to reduction in noise and acquisition of reliable NIFECG signals assuring fetal health during pregnancy and labor. Extensive work has been done to effectively and efficiently separate NIFECG from MECG using single and multichannel signal sources. Kalman filtering [18], combination of LMS (least mean square) algorithm and RLS (recursive least square) algorithm [19] are methods of linear adaptive processing while non-adaptive techniques include like artificial neural networks [20] and ANFIS (adaptive-network-based fuzzy inference system)[21]. Non-adaptive multi-channel techniques are BSS (blind source separation) and its variants such as ICA [22], PCA (principle component analysis) and SVD (singular value decomposition) [23]. Single channel signal sources processing uses non-adaptive methods such as correlation methods [24], subtraction [25], averaging techniques [26], finite impulse response (FIR) and infinite impulse response (IIR) filtering [27] and wavelet transform based techniques[28]. A literature review of the various techniques to extract FECG from the maternal abdominal ECG recordings are compiled well in [8, 11, 17] and most recently by Behar et al [6]. (For more details see section 2.8).

1.4 Physiology of the adult heart versus the fetal heart

The adult heart is a muscular organ that consists of two-chamber pumps, composed of an atrium and a ventricle. The atrium helps to move the blood into the ventricle. The ventricle, in turn, thrusts the blood either into the pulmonary or peripheral circulation. The Sinoatrial (SA) node which is the natural pacemaker in the heart is responsible for generating rhythmic impulses which cause rhythmical contractions of the heart muscle thereby conducting these impulses rapidly throughout the heart [29]. The SA node therefore controls the rate of contractions of the complete heart. The nodal fibres of the SA node propagate an action potential to both atria and from there through the atrioventricular (AV) bundle into the ventricles [30]. The bundle of His further delays the action potentials, allowing the atria to empty itself into the ventricles before the contraction of the ventricles. The Purkinje fibres which are relatively large fibres, transmit the action potential up to the apex of the heart to allow the ventricles to contract simultaneously.

The fetal heart has a few differences with respect to the adult heart as shown in Figure 1.4. For the fetus, the gas exchange takes place in the placenta which functions like fetal lungs and both the ventricles pump the blood throughout the body [31]. This is accomplished by the two shunts, namely, the foramen ovale (a gap in the septum dividing both sides of the heart) and the ductus arteriosus (a shunt between the pulmonary artery and the aorta) that link the outgoing vessels of both ventricles as shown in Figure 1.5. This allows the blood to enter the right atrium and to bypass the pulmonary circulation. Similarly, the ductus venosus which is a vessel that allows blood to bypass the liver. It carries blood with oxygen and nutrients from the umbilical cord straight to the right side of the fetal heart [32]. After birth, the foramen ovale closes with the first breaths and the ductus arteriosus partially closes in 10 to 15 hours after birth and takes up to three weeks for complete closure. The ductus venosus also closes shortly after birth, when the umbilical cord is cut and blood flow between the mother and fetus stops [32]. There are other minor changes that takes place in the baby’s heart within the first year after birth.

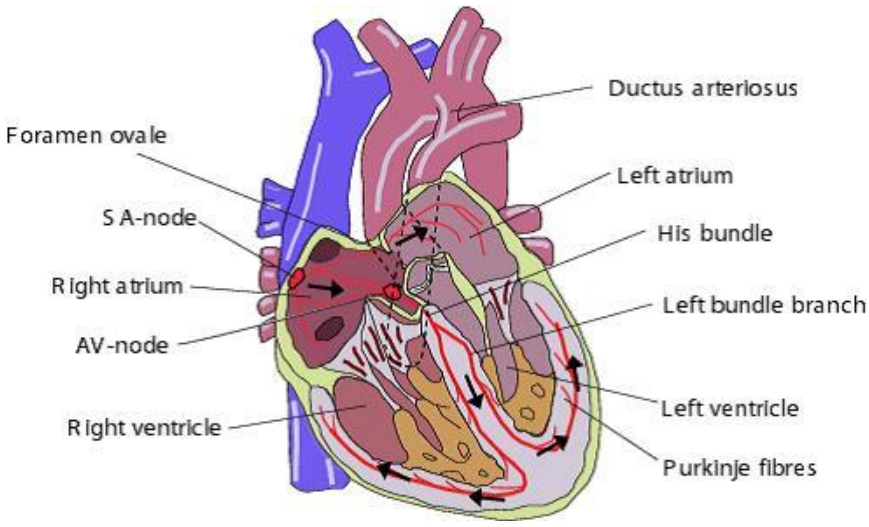

Figure 1.4: Anatomy of the fetal heart; adopted with permission from [11].

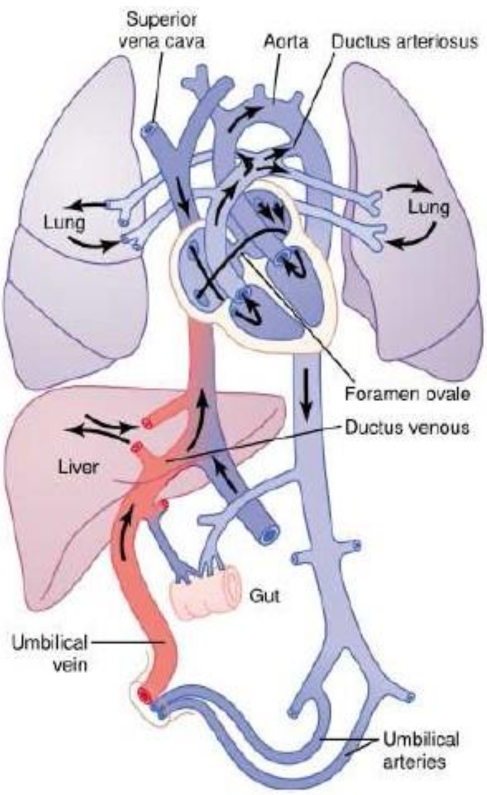

Figure 1.5: Organization of the fetal circulation involving the ductus venous, ductus arterious and foramen ovale [29].

1.5 Characteristics of the Fetal Electrocardiogram

The potential difference between two electrodes as a function of time (bipolar ECG recording) measured on the body surface results in the so called PQRST complex. Figure 1.6 shows a typical FECG waveform with its important features.

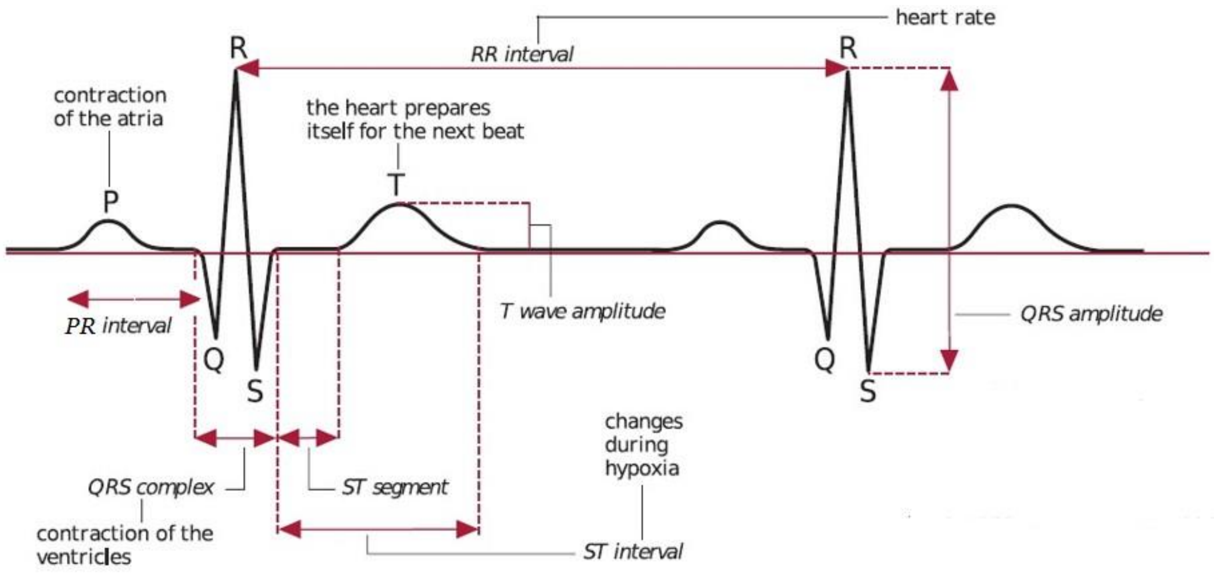

Figure 1.6: Representation of a fetal ECG waveform and its important features [58]

The depolarization of the atria is represented by the P-wave [29]. As the atria depolarizes completely, the ECG goes to zero amplitude. This period is represented by the PR interval. The ventricular depolarization is represented by the QRS (Central part of heart beat morphology) complex [29, 30]. The atrial repolarization coincides with the ventricular depolarization. The amplitude of the QRS complex is larger than the P wave because of the large muscle fibers in the ventricular walls which are responsible for the propagation of large amount of blood into the peripheral circulation. After the ventricles are depolarized completely the ECG again has a zero amplitude. The T wave is associated with the repolarization wave of the ventricles [30].

1.6 Differences between fetal and adult ECG

The direction of the electrical axis in the adult and fetal hearts are not the same. In the adult heart, the left ventricle has a larger muscular mass and hence the electrical axis points towards the left ventricle. In the fetal heart, the mass of the right ventricle is 60% larger than that of the left one (40%) [33]. Hence, the electrical axis of the fetal heart is expected to point towards the right ventricle [34]. Hence, each ECG representation for the fetus differs from the same ECG representation for the adult. The other differences in their RR-interval and morphology are: (i) The fetal heartbeat is almost twice as fast as an adult heartbeat with considerable changes in different stages of fetal cardiac development [35] as seen in figure 1.7.

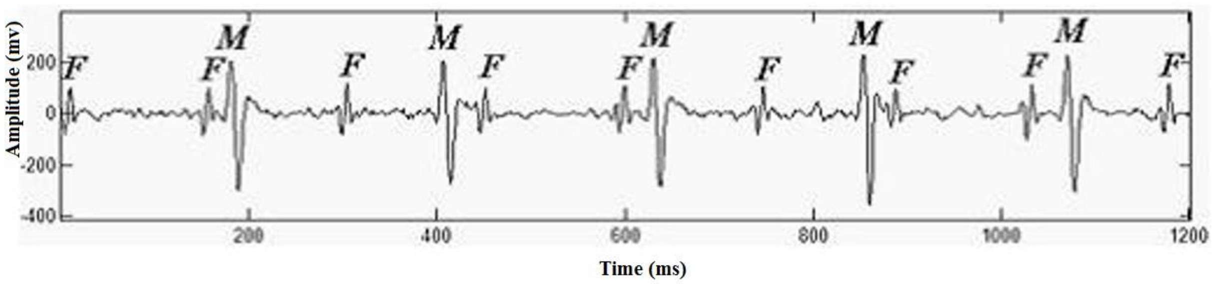

Figure 1.7: Representation of an FECG interleaved between MECG signals [35,39].
[F – fetal R-peak, M- maternal R-peak]

(ii) The heart-rate variability (HRV) of the fetus is also known to be simpler (less dynamic) than an adult. However, as the fetal autonomic nervous systems evolves, the HRV patterns also become more complex [36]. (iii) Morphologically, adult and fetal ECGs have rather similar patterns; but the relative amplitudes of the fetal complexes undergo considerable changes throughout gestation and even after birth. The most considerable change concerns the T-waves, which are rather weak for fetuses and newborns [37]. Table 1.1 lists the values of the various physiological parameters of MECG and FECG.

Table 1.1 Summary of the physiological parameters of MECG and FECG signals.

Physiological parameters	**MECG**	**FECG**
Heart rate range [38]	50 - 210 BPM	60 - 240 BPM
Expected heart rate (HR) [38]	80 BPM	140 BPM
QRS spectral energy [38]	10-30 Hz	20-60 Hz
Peak -to- peak amp. range [39]	100- 150 μ V	3 - 25 μ V
Bandwidth [39]	0.05 to 100Hz	0.1 to 100Hz

1.7 Clinical significance of the fetal ECG

Fetal development which lasts for 40 weeks begins with the heart beating at the 4^{th} week of pregnancy with the beat to beat frequency of 65 BPM and increases to about 140 BPM before delivery [15]. FECG allows for a deeper interpretation of the heart's electrical activity than merely assessing its rhythmic changes. This is achieved by performing a morphological analysis over the PQRST complex (see Figure 1.6). FECG analysis is rarely used in clinical practice, however many research studies have been done using the width and shape of the QRS complex, PR interval, QT interval and ST segment. A detailed overview can be read on available morphological features in [6]. Fetal distress and fetal asphyxia are too broad and vague to be applied with any precision to clinical situations (American College of Obstetricians and Gynecologists, 2005). Uncertainty regarding the diagnosis based on interpretation of FHR patterns has given rise to reassuring or non-reassuring patterns. Reassuring FHR patterns include the normal baseline FHR, moderate accelerations and variability with fetal movement, assuring the wellbeing of the fetus. Non-reassuring FHR patterns include tachycardia, bradycardia, absent variability, late decelerations, variable decelerations falling to less than 70 bpm for longer than 60 seconds, and prolonged decelerations. The baseline FHR decreases by 24 bpm between 16 weeks and term, or 1 beat/min per week. This slowing of the heart rate corresponds to maturation of parasympathetic heart control [40]. If the baseline fetal heart rate is less than 110 bpm, it is termed as bradycardia. The severe and prolonged hypoxia induces a prolonged fall in heart rate [41]. Bradycardia within the range of 80 to 120 bpm with good variability is reassuring while rates below 80 bpm is problematic and non-reassuring [42]. Causes of fetal bradycardia include congenital heart block [43].The baseline fetal heart rate greater than 160 bpm, is termed as tachycardia. Infections such as chorioamnionitis which causes maternal fever induces fetal tachycardia [44]. Beat-to-beat variability is affected by various pathological and physiological mechanisms. It is reported that the fetal body movements affect variability [45], while the baseline variability increases with advancing gestation [46]. The reduced beat-to-beat variability is a sign to indicate a seriously compromised fetus. It is also reported that reduced variability with decelerations is associated with fetal academia [47]. A consistently flat fetal heart rate baseline with absent variability and without decelerations within the normal baseline rate range may reflect a neurological damage in the fetus [42]. It is important that we understand the parameters of the fetal ECG signal which further aids the analysis of the fetal status and the EFM. As fetal hypoxia worsens, there are changes in the T wave and the ST segment of the fetal ECG. It is postulated that increasing T:QRS ratios reflect fetal cardiac ability to adapt to hypoxia and appears before neurological damage. Worsening hypoxia results in negative ST segment [48].

Many complications during antenatal and intrapartum periods may also lead to fetal hypoxia. Despite the various fetal compensatory mechanisms that take place, if hypoxia is prolonged, it can lead to acidosis (i.e. an increased acidity in the body fluids). Severe and acute acidosis are associated with significant morbidity and mortality [49, 50]. Hypoxia effectively reduces the energy storage available for repolarization of the myocardial cells, resulting in changes in the fetal heart rate variability (FHRV) and FECG waveforms [51]. Excessive uterine contractions are the leading cause of hypoxia, since they may decrease placental perfusion as well as compress the umbilical cord [52].

The fetus attempts to maintain the functioning of central organs as long as possible. The final stage of asphyxia is the collapse of the system with brain and heart failure. Asphyxia that lasts only for a few minutes might cause irrecoverable damage. In adults changes in the QT-interval are associated with myocardial ischemia [53], sudden cardiac death [54] amongst several other conditions. Thus, the fetal QT interval which can be recovered from the non-invasive FECG is of much interest in the monitoring of fetal hypoxia resulting in metabolic acidosis. The reliable assessment and diagnosis of changes in fetus condition is of major importance. Using diagnostic tools we can detect and evaluate these changes.

1.8 Organization of the thesis

The thesis is divided into five chapters. In Chapter One, An Overview of the need for monitoring and assessment of maternal and fetal Electrocardiogram for positive pregnancy is discussed. The chapter also includes the economics of the antenatal health care and a brief background to the physiology of the adult heart with comparison with the fetal heart. A clinical significance of the fetal ECG signal is also discussed in detail.

In Chapter Two, a comparison of the various fetal heart rate monitoring techniques are explained. It also includes a brief write up of the challenges in acquiring real time non-invasive fetal ECG using surface ECG electrodes from the maternal abdomen. The various electrode configurations are listed which includes our proposed optimum electrode placement schemes (an experimental case study is listed in Appendix A). A list of online public abdominal ECG databases available which have been used in this thesis is included in this chapter. Also, in this chapter a detailed literature survey is given of the various techniques used to extract the fetal ECG from the abdominal ECG signals. Some of the methods such as Independent Component Analysis (ICA), Adaptive neuro-fuzzy inference system (ANFIS), Correlations and our proposed synthesized template method were implemented to extract and compare the methods as listed in Appendix B. The chapter ends with the research objectives and the proposed linear phase FIR filter design.

Chapter Three in its introduction has the background on linear phase sharp transition FIR filters, their features, comparisons and problems encountered in implementation. The chapter then explains the proposed three design models of the linear phase sharp transition FIR filters namely, Model I: Composite band pass FIR filter using High pass – Low pass FIR filters in Tandem. Model II: an Integrated LPST FIR BPF and Model III, which deals with the novel technique of slope matching which is applied to the linear phase sharp transition FIR integrated band pass filter design. This chapter includes expressions for all the filter model parameters, impulse response coefficients and the magnitude responses of each of the filters. The results of the filter design are tabulated and compared. Similarly, the band pass FIR filter with and without slope matching are further compared with the Parks-McClellan algorithm (optimum FIR filter design).

Chapter Four describes the QRS detection algorithm for maternal and fetal R-peak detections and thereby the maternal and fetal heart rate variability.The performance parameters, sensitivity and positive predictive values including the accuracy and failed detections are computed to evaluate the performance of the three linear phase sharp transition (LPST) FIR filter Models I, II and III using the three Physionet databases.

Chapter Five gives the conclusions of the work done and future work proposed in this research. The thesis has appendices: Our proposed optimum electrode placement schemes with an experimental case study is listed in Appendix A. The implementation of FECG extraction techniques such as synthesized QRS template, ICA and ANFIS are explained in Appendix B. Displaying aECG signals and maternal and fetal heart rates using Matlab Mobile are given in Appendix C. The conventional three FIR design methods are reviewed, the filter design steps for the proposed LPST FIR filters, Model I and Model II are listed in Appendix D.

2

Literature survey of Extraction of Maternal and Fetal ECG

2.1 Techniques in monitoring fetal heart rate

Auscultation is one of the most primitive methods to monitor the fetus heart rate. The monitoring can be done either by using an ultrasound device or a fetoscope. However, a better option of using electronic monitoring was proposed when abnormal patterns were detected using auscultation technique [8]. This EFM system allowed the clinicians to record the fetal heart signals and later even analyse the readings to diagnose the fetal's health status. EFM can be categorized into two types namely, internal and external monitoring methods.

2.1.1 Invasive FECG monitoring

In the internal monitoring method, the invasive direct fetal scalp electrode is inserted just beneath the skin of the fetal's scalp as shown in Figure 2.1(c). The ECG readings of the electrode are recorded which are stored for future analysis. This is done to obtain accurate fetal ECG measurements during labour which may pose a slight risk of infection to the fetus [55].

The external electronic fetal monitoring can be done by various methods such as fetal phonocardiography (PCG), cardiotography (CTG), fetal magnetocardiogram (FMCG) and NIFECG as shown in Figure 2.1.

2.1.2 Phonocardiography (PCG)

Phonocardiography was first available as a clinically useful fetal monitor which is rarely used for clinical practice today. The microphone which is placed on the abdomen detects harmonic content of fetal heart sounds between 70 Hz and 110Hz as shown in the Figure 2.1(a). It also detects ambient noises. During contractions, the detection of fetal heart sounds are hampered by excessive abdominal wall movement. Fetal phonocardiography is also susceptible to movement artifacts effects [56]. The signal quality is also affected by the quantity of amniotic fluid, abdominal wall thickness and the maternal and fetal positions.

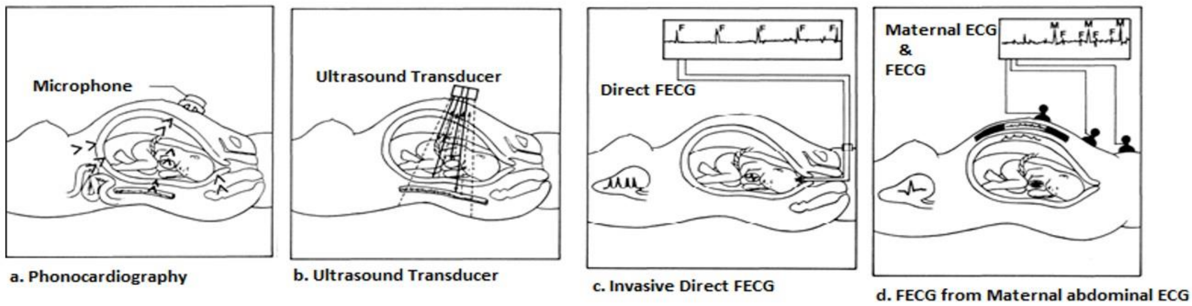

Figure 2.1: Various techniques of EFM [39] (a) Phonocardiography (b) Ultrasound transducer (c) Invasive Direct FECG (d) Non-invasive FECG.

2.1.3 Fetal magnetocardiogram (FMCG)

Magnetocardiograms are recordings of the magnetic fields generated by the currents flowing within the fetal heart. The only sensor that is sensitive enough to monitor such weak fields is a SQUID (superconductive quantum interference device) [57]. A major advantage of using fetal MCG for FHR derivation is that it is possible to obtain true beat-to beat data. FMCG can also be recorded reliably from the 20th week onward and can be used to classify arrhythmias such as heart blocks and atrial flutters [6]. While providing higher quality FHR, the major disadvantage of fetal MCG is the size and complexity of the instrumentation required (although smaller devices may become available). FMCG is very expensive to be widely used clinically [15].

2.1.3 Cardiotography (CTG)

We distinguish two types of CTG monitoring based on different stages of labour. Before the rupture of the membranes the external ultrasound probe and transducer are used to acquire FHR and uterine pressures, respectively [58]. After the rupture of membranes the electrode is attached to the fetus' scalp and the FHR is computed directly from the ECG's R-R intervals. The uterine pressures are obtained using an internal electrode placed in the vagina. The record is called intrauterine pressure (IUP). The external and internal monitoring is shown in Figure 2.2.

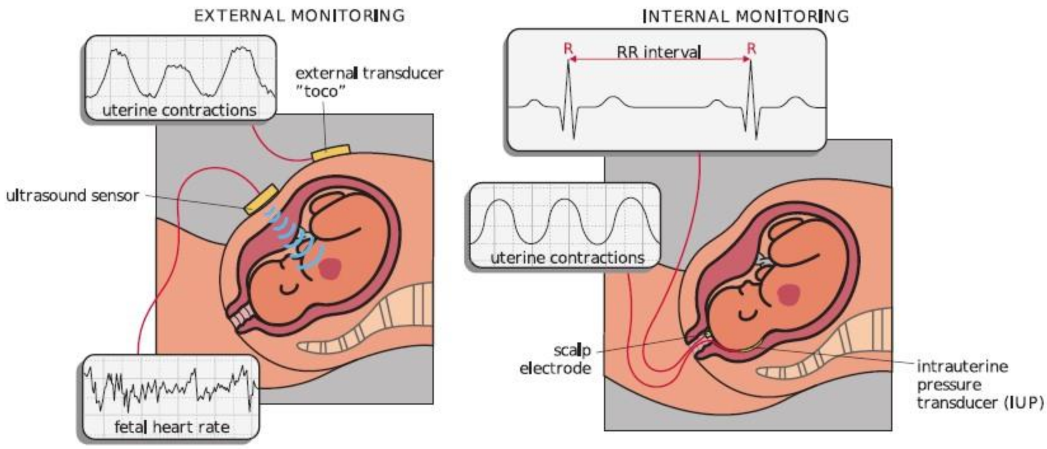

Figure 2.2: External and internal monitoring using Cardiotography [58].

The Doppler ultrasound principle uses a hand held device that is placed against the mother's abdomen that uses sound waves to indicate signals of fetal heartbeat as shown in Figure 2.1 (b). The Doppler ultrasound may help diagnose heart valve defects and congenital heart disease. Although the Doppler ultrasound technique displays a recording of FHR it requires an experienced midwife to skilfully place and reposition the transducer to insonate a 1.5 - 2 MHz signal towards the fetus [39]. Besides, it's not been proved that this high frequency signal is completely safe for the fetus. The Doppler procedure can be quite uncomfortable and problematic for the pregnant mother as it is not suitable for long periods of FHR recordings [59, 60]. Another major disadvantage of Ultrasound method is its sensitivity to movement. Due to the mother's movement during recordings and the misorientation of the transducer, the maternal heart rates can be misinterpreted as FHR [61]. As this method depends upon the movement of the heart valves which corresponds to the fetal heartbeat, it does not really give us accurate beat to beat analysis [8]. To add to the drawback, the Doppler uses an averaging system to calculate the FHR data which may not give us reliable data.

2.1.5 Non-invasive FECG (NIFECG)

By placing the surface ECG electrodes on the maternal abdomen, abdominal NIFECG is recorded as shown in Figure 2.1(d). This procedure is called non-invasive method which can be performed right from the 20th week of pregnancy. NIFECG extraction from the abdominal ECG can be carried out by suitable signal processing and appropriate filtering techniques. NIFECG carries vital information about the cardiac function of the fetus which is important in determining the fetal life, fetal development, fetal maturity, and existence of fetal distress or congenital heart disease. The morphology of the extracted NIFECG contains diagnostic information which can assist the clinician to take timely decisions during pregnancy or labour. The parameters from the NIFECG signal can be useful for most biomedical researchers and clinicians who are researching to make this technique a reliable method.

The other advantages of using NIFECG are that it provides FHR data with beat-to-beat accuracy, unobtrusive, risk-free ambulatory monitoring while now-a-days the mother herself can monitor the fetus status via the attached low power fetal monitor. One of the biggest challenges is the acquisition of the aECG signals in which the fetal ECG is buried among various noise signals, wherein the maternal ECG is the most significant noise among others. Due to this, NIFECG displays a low SNR. The amplitude of the NIFECG increases over the gestation periods but sees a dip in FECG during the 28th to 32nd week due to the layer called the vernix caseosa that surrounds the fetus [62]. Due to the uncertainty of the acquisition method and further to the beat to beat morphological analysis, the long term uninterrupted FHR monitoring for 24 hours a day is desirable. Additionally the maternal heart rate can also be recorded from the aECG along with the FHR.

Table 2.1: Internal and external FHR monitoring techniques [6,8,9,11,13].

Technique	Gestational age	Merits	Demerits	Accuracy
Direct scalp electrode (invasive)	At delivery only	▪ 100% accurate FHR. ▪ Morphological analysis possible ▪ High SNR ▪ Single channel	▪ Invasive. ▪ Risk to fetus. ▪ Can only be used at delivery and not daily monitoring.	100%
PCG	28 weeks delivery	▪ Cheapest method.	▪ Lowest SNR among all methods. ▪ Requires skilful clinician to locate fetus. ▪ Susceptible to movement artifacts effects. ▪ Not routinely employed for FHR monitoring by doctors.	60%
CTG	20 weeks delivery	▪ Cheap and easy to handle, useful during labour. ▪ Obtains smooth heart rate.	▪ Beat-to-beat analysis not possible. ▪ High frequency ultrasound radiation. ▪ Prone to maternal/fetal HR confusion. ▪ Fails during fetal or maternal movements. ▪ Used only for short term monitoring and depends on the quality images.	90%
FMCG	20 weeks delivery	▪ Gives accurate FHR. ▪ Beat to beat morphological analysis possible. ▪ Higher SNR.	▪ Costly. ▪ Requires skilled clinician. ▪ No long term monitoring possible to due to the apparatus size and cost. ▪ Observed as average signal.	100%
NIFECG	20 weeks delivery	▪ Easy to use and does not require skilled personnel. ▪ low cost ▪ Long term monitoring possible. ▪ Beat to beat morphological analysis possible.	▪ Low SNR, with potential drop in the FECG signal from 28th to 32nd week	90%

An overview of the merits and demerits for the internal and external techniques for fetal heart monitoring are discussed in Table 2.1. Although the CTG or Doppler method gives high success, it fails to give beat to beat accuracy due to its averaging procedure [63] and does not extend any help in monitoring fetal arrhythmia and also the future morphological research work. Phonocardiography is susceptible to movement artifacts and is hardly used today by clinicians. Therefore, the Doppler ultrasound and the abdominal FECG together are the most viable options for the monitoring of FHR.

2.2. Noise in abdominal ECG affecting FECG

The major drawback of using NIFECG is the low SNR because FECG is corrupted by the presence of noise elements such as MECG, power line interference (PLI), low frequency noise due to baseline wander, Electromyogram (EMG), Electrohysterogram (EHG) due to contractions, motion artifacts, noise due to surface electrode contact, noise due to the instrument etc [11, 64]. The morphology of the fetal signal can depend on certain parameters such as gestation age, presentation of the fetus and the configuration of the ECG electrodes applied to the maternal abdomen. To be familiar with the noise affecting the FECG, some of the prominent noise sources are listed below. Figure 2.3 shows the frequency spectrum versus amplitude of FECG with the associated noise sources.

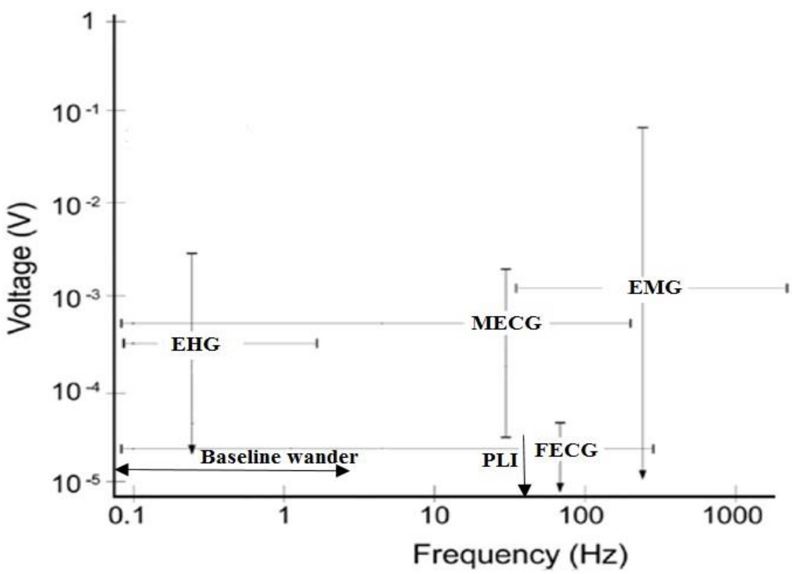

Figure 2.3: Frequency spectrum versus amplitude of various biosignals and some noise sources which interfere with FECG [11]. Note that, the amplitude of these signals depends on the site from which the data is recorded.

- MECG is the most predominant interfering signal with FECG in the aECG. The frequency spectrum of maternal ECG partially overlaps with the FECG as seen in Figure 2.3 [8]. It is evident that the amplitude of the MECG is almost 5-10 times that of FECG [6].
- PLI consists of the 50/60Hz noise signal and its harmonics which can alter the peak-to-peak ECG amplitude which can affect the fetal R-peak detection.
- Baseline wander is a low frequency noise which represents the maternal respiration. When this noise is added to aECG, the amplitude of the ECG varies by 15% [8].
- EMG is a maternal muscle noise due to the movement of the abdominal muscles and EHG is the noise associated with contractions of the maternal uterine muscle.
- Electrode contact noise is caused by loss of contact between the electrode and the maternal abdominal skin. These transitions may normally occur at the beginning of the recording and fades off over few seconds.
- Motion artifact which is due to the electrode interface /cable and inherent noise in monitoring instruments can be reduced or eliminated with proper design of the fetal monitors.

2.3 Challenges in extracting NIFECG using surface electrodes

With advanced signal processing techniques and biomedical engineering research, the SNR of the FECG can be enhanced by carefully acquiring the aECG from the maternal abdomen along with the maternal thoracic as reference MECG. After using appropriate filtering techniques to remove the above noise elements, the NIFECG can be obtained by efficient detection and extraction methods. The extracted FECG from the aECG is very small, about 5 times less in amplitude compared to the MECG and is sometimes embedded in the noise signals [25]. The maximum amplitude for FECG can record 60 μV while the MECG ranges from 100 to 150 μV [8]. Although the frequency bandwidth range of the FECG is 0.05–100 Hz it interestingly overlaps with the MECG [9].While FECG has been estimated to be ¼ of the total signal energy [8], the normal FHR ranges from 120 – 140 bpm and comparatively the maternal heart rate (MHR) ranges from 70 – 100bpm [17]. Figure 2.4 illustrates the invasive scalp FECG along with one of the aECG channels from the Physionet Abdominal and Direct Fetal Electrocardiogram Database (adfecgdb) [65,66] while Figure 2.5(a) shows the maternal thoracic channel of the Physionet Non-Invasive Fetal Electrocardiogram Database (nifecgdb) [67] along with one of the non-invasive aECG channel. The above signals clearly show the amplitude and frequency of the maternal and fetal signals.

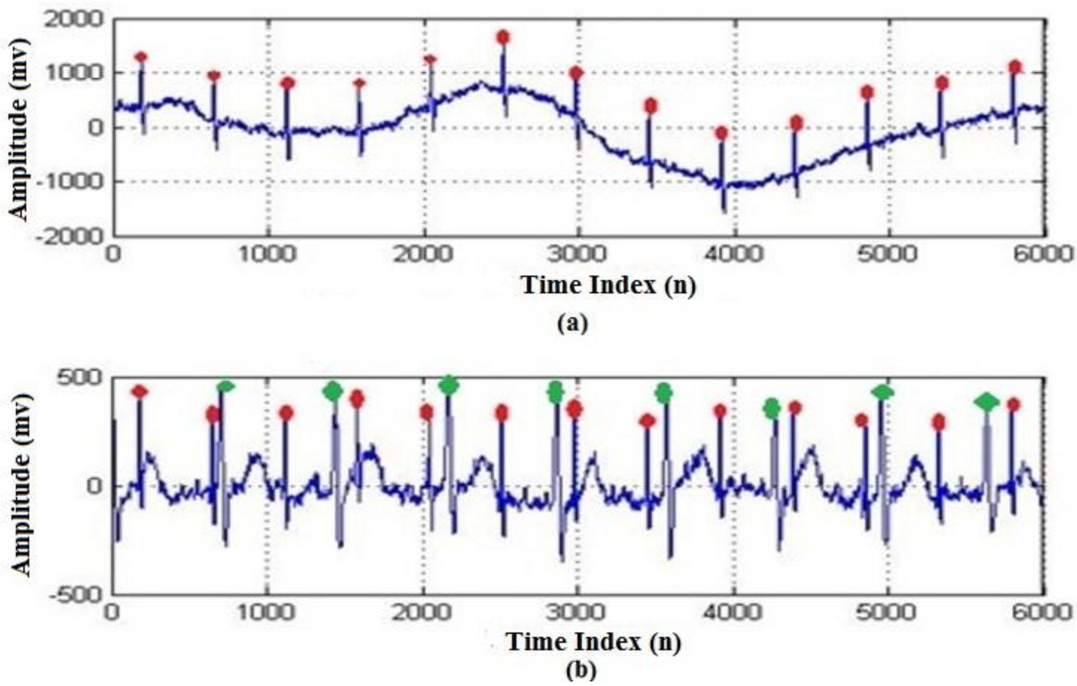

Figure 2.4: Physionet signals from adfecgdb database [66] a) Invasive fetal scalp ECG (the red dots indicate the fetal R peaks) b) One of the abdominal ECG channel (the green dots indicate the maternal R peaks). The FECG signal amplitude in this database is relatively good.

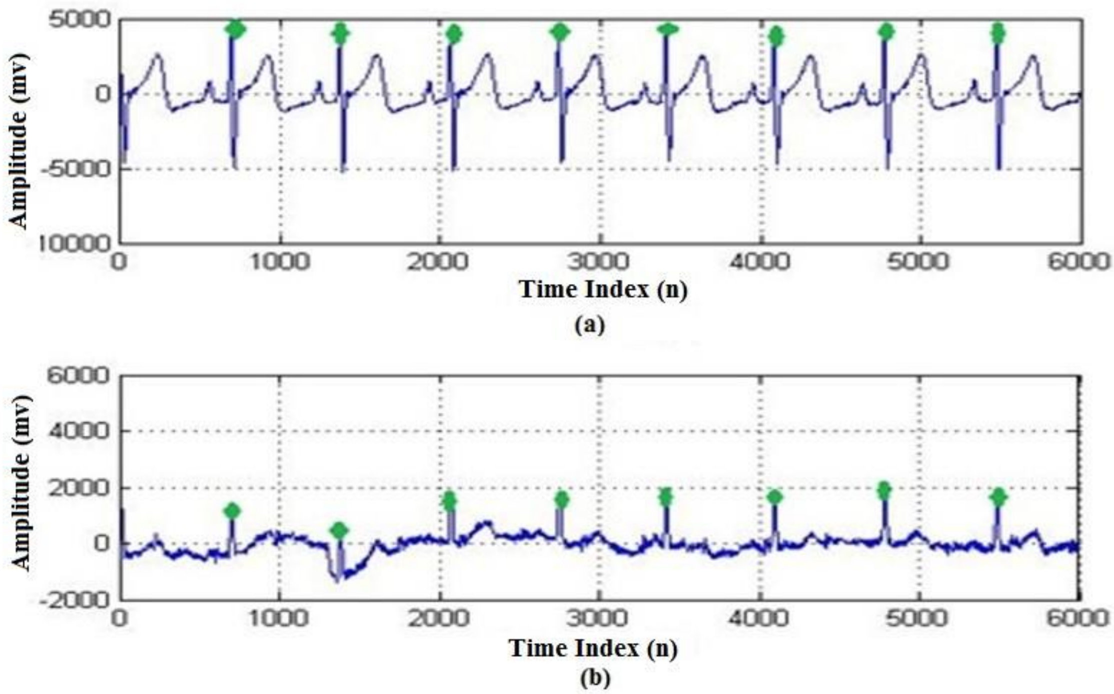

Figure 2.5: Physionet signals from nifecgdb database [67] a) Maternal thoracic ECG (the green dots indicate the maternal R-peaks). b) One of the abdominal ECG channel. The FECG and noise amplitude is very small compared to MECG signal.

Besides the noise sources stated in section 2.2 which corrupts the aECG and the required FECG, there are other reasons also that we need to take into consideration while acquiring FECG using surface electrodes. Changes in the volume conductor between the fetal heart and the abdominal electrodes change the FECG [62, 68, 69, 70]. In general, these changes are due to the (i) movement of the fetus (ii) development of the vernix caseosa [62, 71] or (iii) movement of the mother.

(i) In case of the fetal movement, it causes the distance between the heart and a particular electrode placed on the maternal abdomen to either decrease or amplify the corresponding FECG signal. During the first two trimesters of gestation (week 1 to week 27) the fetus moves a lot in the uterus and the orientation of the fetus is unknown. By the beginning of the third trimester of gestation (week 28), it commonly settles in a head-down position known as the vertex presentation

(96.8%), which is more appropriate for birth [6]. However the fetus may also settle in other presentations (see Figure 2.6).The orientation of the fetus influences the FECG recorded from the maternal abdomen using different ECG lead configurations [12].

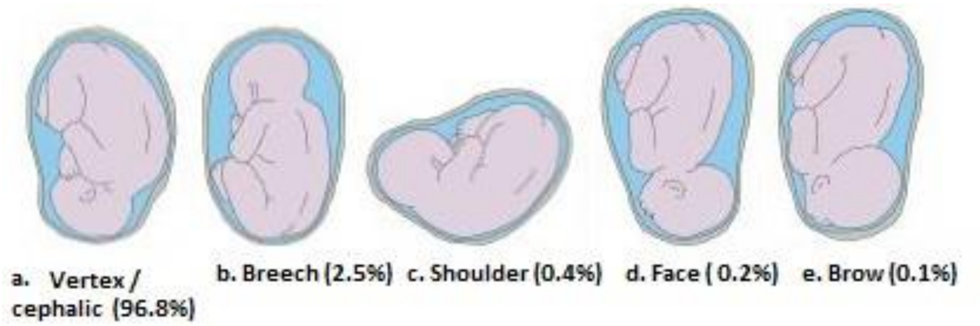

Figure 2.6: Different fetal presentations and their percentage of incidence at the end of third trimester [6].

(ii) At about the 28th week of gestation (see Figure 2.7), the fetus develops a protective non conducting layer called the vernix caseosa as shown in Figure 2.8 .The vernix caseosa insulates the fetus electrically from its surroundings, making it virtually impossible to record an FECG from the maternal abdomen. However, from about 32 weeks of gestation this protective layer starts to break down and from the 37th week of gestation the vernix caseosa dissolves in the amniotic fluid restoring the uniform conduction characteristics of the volume conductor [62].

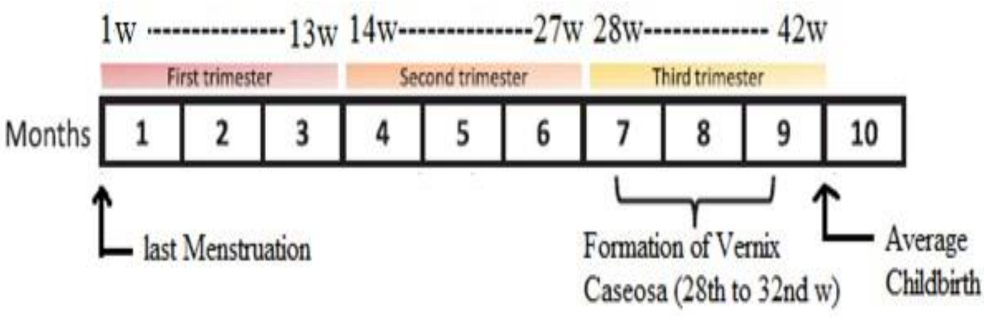

Figure 2.7: Prenatal development with respect to fetal monitoring (w = week) [13].

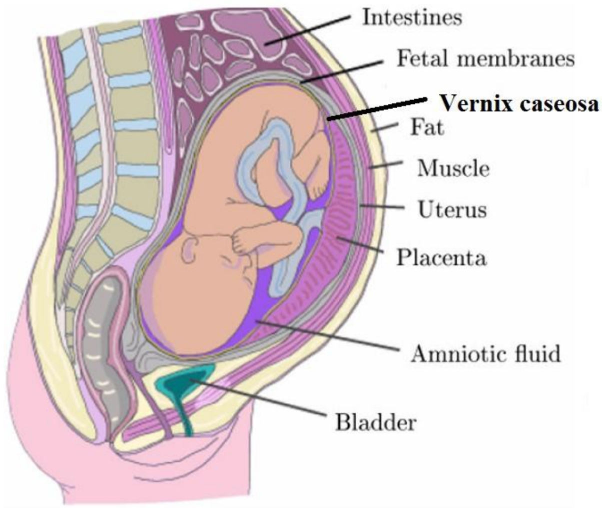

Figure 2.8: The vernix caseosa formed over the fetal skin that influences the FECG [6]

(iii) The third reason for the changes in the volume conductor is due to the movement of the mother who in turn causes a movement of the recording electrodes. The movement of the electrodes causes the conductive layer between the skin and the electrodes to change and hence causes a change in the properties of the volume conductor. This conductive layer is generated by the thermal excitation of metallic ions in the electrode [68]. These ions spread through the electrolyte, forming a layer balancing the electrode charge. Although the ions can move freely through the electrolyte, the speed of movement is limited and hence electrode movement is likely to disturb the balancing layer and hence the electrode-skin bias [68], resulting in artifacts in the recorded fetal ECG.

As seen in the Figures 2.4 and 2.5, the SNR of the NIFECG is quite low as compared to the MECG due to the size of the fetal heart and the conducting media between the fetal heart and the surface electrodes [9]. The maternal skin and muscle tissue acts as a volume conductor whose conductivity changes with the gestation age [6]. Another challenge for the biomedical signal processing engineers and researchers is to avoid confusion between FHR and MHR computation after extracting the aECG signal. Today the biggest boon is to derive significant fetal morphological parameters from the NIFECG signals to extract various fetal parameters such as fetal QRS (FQRS) morphology, shortening of QT, ST intervals [69] etc, that will enable fetal diagnosis at an early stage in pregnancy. In the market there are already various FHR monitors which detect FHR recordings such as, Monica AN24 monitor, Nottingham, United Kingdom, Meridian M100/M1000 monitors from MindChild Medical, Nemo Healthcare, Netherlands and PregSense, Israel [6]. The motivation to research and to build efficient FHR monitors to provide a complete set of fetal information to the clinician has not ended. This area of biomedical study is an ongoing process among many researchers today.

2.4 Placement of ECG electrodes over maternal abdomen

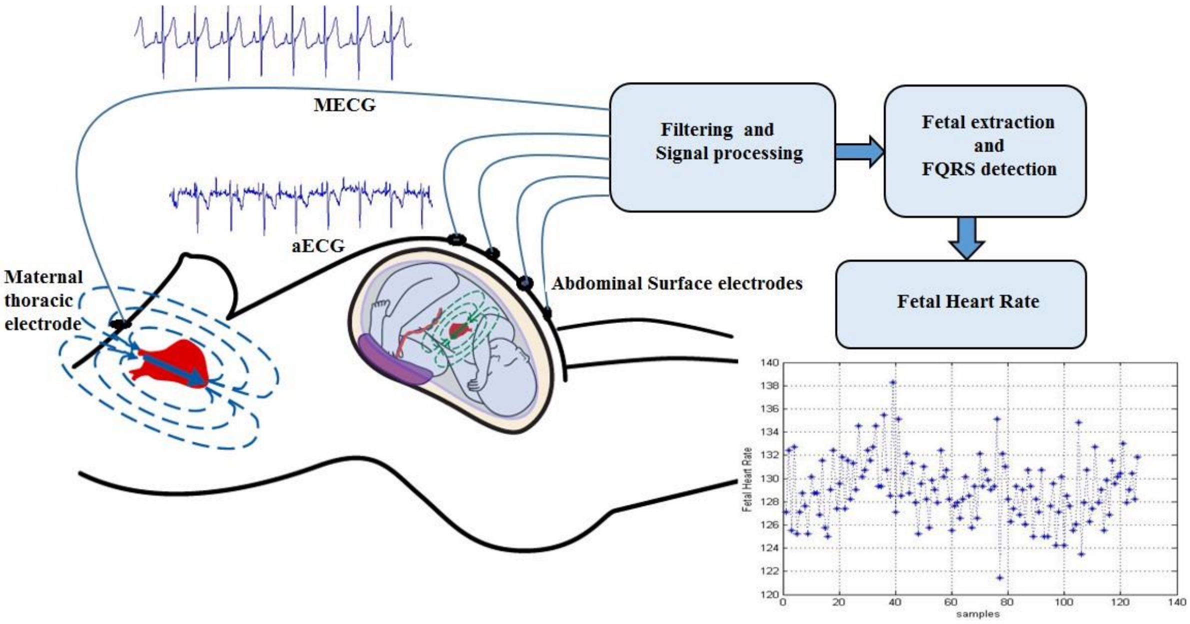

Figure 2.9: NIFECG acquisition process.

A few pointers were considered before setting up the configuration of the electrode placement over the surface of the maternal abdomen as seen in Figure 2.9. An ultrasound of the maternal abdomen can be done to investigate the presentation of the fetus in the womb as it varies with the gestation age right up to labor. Knowing the position of the fetus would enhance the chances of extracting better FECG waveforms. Care should be taken that at least one strong maternal thoracic signal can be recorded from the mother as a reference MECG signal to be used for certain extraction algorithms synced with other aECG channels. Abdominal ECG signals from one channel to multichannel can be used as per the requirement for the fetal detection techniques such as ANFIS [72, 73], ICA [74] etc. The aECG database can be sampled at 1 KHz with an ADC resolution of 16 bits and the recording time can range from 18 minutes (antepartum) to at least 30 minutes (at labor). These durations will be able to capture the various fetal conditions especially as the FECG is quasiperiodic in nature and the fetus is constantly moving in the uterus during labor. The aECG recordings can be taken from a group of subjects over a known gestation period starting at the 20^{th} week and follow up till labor. These measurements can be compared with the patient's clinical information using other methods such as CTG and ultrasound. Proper electrode placement on the maternal abdomen determines the measured signal quality to a large extent, but much consensus has not been reached on standard electrode placement. For long monitoring periods, comfort in placing and wearing the sensors is important to the mother, thus imposing additional requirements on the electrode spacing and number of sensors used.

It is important to first observe the orientation of the fetus, size of the fetus and position of the placenta using the ultrasound. It is found that the largest fetal R wave can be accomplished when the active electrodes are perpendicular to the trunk of the fetus on the mother's abdominal wall. So in this position the electrodes are located according to the electric axis of the fetal heart. After the ultrasound is done, an optimum electrode placement configuration or grid can be used to extract FHR from the aECG till the end of the third gestation.

The procedure used here is to locate bipolar ECG electrodes on the surface of the pregnant mother's abdomen. The concept used here is based on the single dipole vector described in [75]. The combination of all cardiac vectors emitting from the maternal or fetal heart is considered to be a single source dipole vector represented by P_m and P_f, respectively. The vector r is the distance between the two source vectors P_m and P_f as shown in the Figure 2.10. A good quality FECG signal largely depends upon the configuration and placement of the electrodes on the mother's abdomen. Although a set standard of the electrode configuration is not yet derived [6], few authors in this biomedical field proposed various procedures and measurements to derive good quality aECG signals.

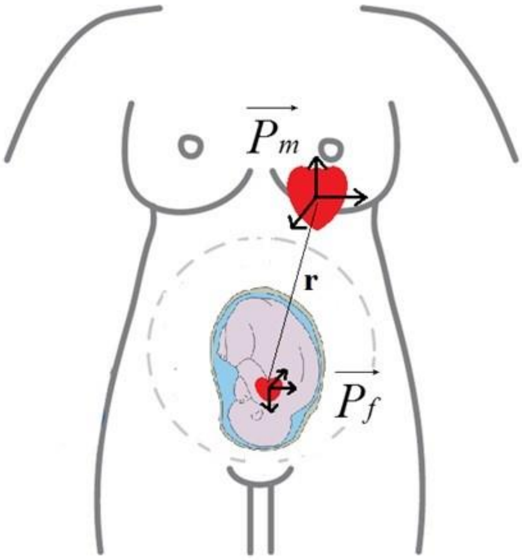

Figure 2.10: Maternal and fetal dipole vector represented by P_m and P_f respectively. The vector r is the distance between the two source vectors P_m and P_f [75].

2.5 ECG Electrode configurations

Some researchers would depend on prior knowledge of the position of the fetus using ultrasound, some would go by the normal position of the fetus as vertex (head down) which is at the end of the third trimester. Some authors would cover the entire abdomen area with electrodes so as to pick the maximum fetal cardiac signals or some would use a proper strategy to locate and place the ECG electrodes. Configurations by different authors are listed and reviewed in [6, 76] in Figure 2.11, where GND is considered as the inactive electrode representing common ground.

Scheme 1: [5 electrodes] The four active bipolar ECG electrodes are placed in a circular fashion keeping the reference electrode at the pubic area as shown in Figure 2.11a. This configuration is used by the fetal monitor device, Monica Healthcare Ltd AN24 (Nottingham, United Kingdom) [77].

Scheme 2: [8-10 electrodes] There are two configurations using 8 electrodes, in Figure 2.11b a triangular shape structure covers the lower area of the abdomen [75] while in Figure 2.11c, two smaller circles are used above and below the navel and at the lower part of the abdomen for better FECG and uterine measurements [78].The aECG recordings were taken from 8 women at labor.

Scheme 3: [11 -12 electrodes] The authors used three placement schemes in this configuration to record each measure for a duration of 24 seconds using the standard 12-lead ECG machine, made by Nihon Kohden Corporation [79]. In all the three configurations, six active electrodes were placed in a hexagonal structure keeping the navel at the centre with a radius of 10 cm as shown in Figure 2.11d. Two of the limb electrodes F and R were placed at the uterus fundus and pubic respectively for all the three configurations. The remaining two limb electrodes L and N (reference) were changed for the three configurations, namely (i) configuration 1: L = right flank; N = below the navel (ii) configuration 2: L = left flank; N = below the navel (iii) configuration 3: N = right flank; L = below the navel.

Scheme 4: [14 electrodes] The authors used AD Instruments, New Zealand to collect 20 minute data from 10 different subjects aged between 21 to 33 with gestational periods ranging from 20 to 28 weeks [80].Channel 1 was set for the thoracic reference MECG while from the active electrodes 2 to 8 which are placed on the circumference, only 6 to 8 abdominal leads were used for fetal signal processing as seen in Figure 2.11e.

Scheme 5: [32 electrodes] The authors used MindChild Meridian fetal monitoring System, USA [81] which uses a configuration using 32 electrodes as shown in Figure 2.11f. The electrodes cover the entire abdomen, sides and back. Electrodes marked in blue show the corresponding good signal quality while active electrodes in red have low signal quality [82]. Although the coverage of the fetal cardiac signal is maximum the subjects may find it uncomfortable to use the electrode belt array for daily monitoring. In the case when a belt array of 72 electrodes is used for monitoring, the extracted information can be redundant and time consuming [83]. A smaller set of electrodes of 8 to 10 sensor electrodes is sufficient to obtain the required fetal information. We proposed three placement configurations based on the standard 12-lead ECG machine. An experiment was performed on a single pregnant woman with single fetus to obtain the maternal and fetal heart rate. The details of the measurement in given in Appendix A.

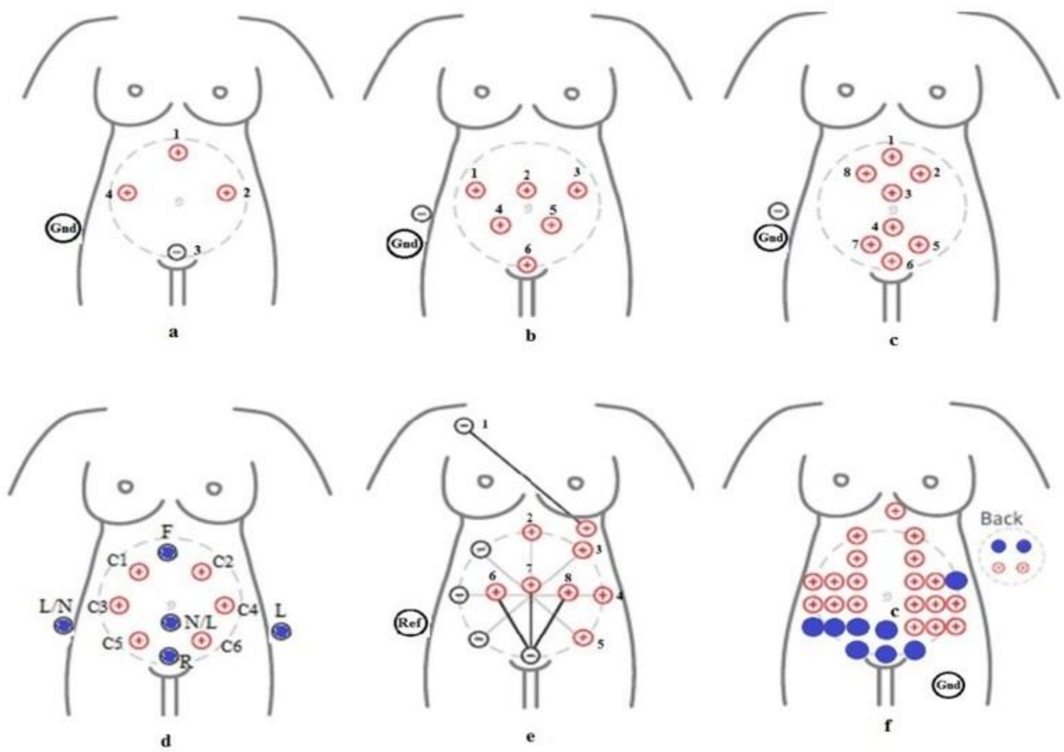

Figure 2.11: Various electrode configurations used by authors [6, 77] (a) Scheme 1: [5 electrodes] Monica Healthcare Ltd AN24 [78] (b) and (c) Scheme 2: [8 -10 electrodes] [75, 78] (d) Scheme 3: [11-12 electrodes] [79, 84] (e) Scheme 4: [14 electrodes] [80] (f) Scheme 5: [32 electrodes] [82].

2.6 Review of ECG electrode placement configurations for fetal monitoring.

The Table 2.2 shows the comparison of some of the electrode placement configurations or grid set up over the maternal abdomen to monitor the FECG non-invasively. Comparisons have been made on the basis of the number of electrodes placed on the maternal abdomen, the filter design parameters used for pre-processing such as Bandwidth (B), Sampling Frequency (fs), Resolution (Res) of the ADC and the Gain. Some of the authors did specify the number of pregnant women as subjects with its recordings and gestation periods in weeks. The method used by various authors to extract FECG is also listed.

Table 2.2: Comparison of various electrode placement configurations for FECG monitoring [76].

Author	Number of Electrodes	Electrode Placement	B , fs, Res and Gain	Subjects & Records	Gestation Period	Method used for FECG Extraction
Bergveld et al., 1986 [65]	4 electrodes	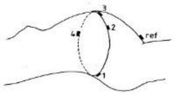 side view	B = 0.2 to 120 Hz	37 subjects	20 – 37 weeks	Measurement Principle method
Oostendorp et al.,1989 [70]	32 electrodes	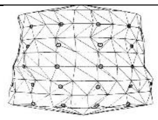	fs = 500Hz	6 subjects with 37 recordings	20 – 40 weeks	Homogeneous volume conduction model
Callaerts et al., 1994 [87]	32 electrodes	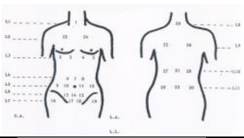	*Filters :* F_H (1st Order) = 20Hz to 50Hz F_L (2nd Order) 70Hz fs =500Hz , Res = 12 bits	14 records: 7/8 signals per subject : 3 thoracic , 4/5 abdomen for 12 subjects.	-	Singular Value Decomposition (SVD)
Taylor et al., 2003 [88]	12 to 16 electrodes	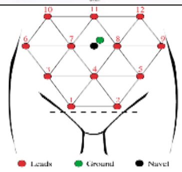	fs = 512Hz res = 12 bits multichannel	241 subjects with 250 recordings	241 singleton (15–41 weeks), 58 twin (16–35 weeks) and 5 triplet (20 – 33 weeks)	Linear regression to analyse QRS intervals and construct time specific reference ranges
Peddaneni et al., 2004 [89]	8 channels and 2 reference (central & ground)	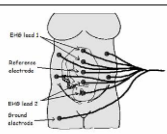	*Filter:* B = 0.1Hz – 100Hz (60 Hz Notch) fs = 400Hz ; Res = 16 bits, Gain = 6500	11 subjects	-	Blind Source Separation (BSS)
Ungureanu et al.,2005 [60]	12 electrodes (Portis-32/ASD)	Unipolar leads 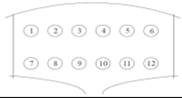	fs = 400 Hz Res = 22 bits (LSB res. = 7.52 mv)	-	-	Correlation functions
Chia et al., 2005 [90]	3 electrodes 3M Red Dot 2237	Three electrodes placed in an equilateral triangle formation on the maternal abdomen.	-	Recording of 100 subjects for 10 minutes each.	18 weeks to full term	Cancellation of maternal template in 1st and 2nd derivative of abdominal signals.

Vullings et al.,2006 [91]	12 abdominal leads and 2 shoulder leads (Portis-6/ASD)	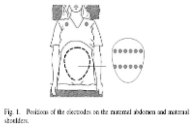	fs = 400 Hz ; Res = 22 bits	-	-	Extension of linear prediction method
Karvounis et al.,2007 [39]	4 electrodes	1[st] –Symphysis pubis and 3 other bipolar leads 	*Filter :* F_H = 100Hz F_L = 4 Hz fs = 300 Hz ; Res = 12 bits Gain = 7800	i) 8 records of 60s for 8 subjects. ii) 10 records of 15 minutes for 5 subjects	20 – 41 weeks	3 stage method: time frequency analysis, complex wavelet and Heuristic algorithm
Martens et al., 2007 [92]	13 electrodes (Porti5-24/ASD)	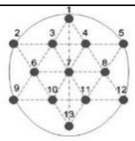	Gain =20	20 subjects 20 records (30 min/s)	19 weeks to early labour	Sequential estimation method
Graatsma et al., 2008 [93]	5 electrodes AN24 fetal ECG monitor	Two electrodes along the midline (at the side of the uterine fundus and above the symphysis), one at each side of the uterus, and the ground electrode on the left flank.	B = 1-70 Hz fs = 300 Hz	15 hour recordings of 150 subjects	20-40 weeks	Improved fetal monitoring using external FECG
Vullings et al., 2009 [94]	8 electrodes (HP8040)	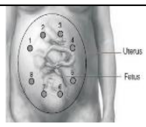	F_H = 1.5Hz (FIR) FIR notch filter (50Hz) fs = 1KHz Gain = 500	7 records of 10 minutes each	37 - 41 weeks	Weighted Averaging of mECG segements (WAMES)
Ravindrakumar et al.,2010 [95]	Electrodes less than 71	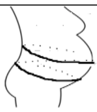 Electrodes as a Spiral belt	-	-	-	Modified Independent Component Analysis (ICA) Algorithm.
Clifford et al ., 2011 [82]	32 electrodes (E-Trolz) / Red = High Black = low (signal Quality)	Arbitrarily chosen for max. coverage. 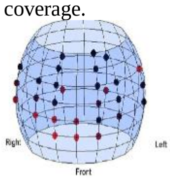	fs = 1KHz	-	35-41 weeks	Comparison of FHR variation and ST levels with Fetal Scalp Electrode (FSE) data.
Algunaidi et al., 2011 [96]	4 electrodes (BIOPAC -MP-100A)	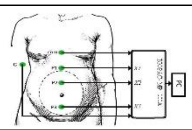	fs = 256 Hz Res = 12 bits	30 records of 60 seconds each	36 – 38 weeks	Peak detection Algorithm
Rooijakkers et al.,2012 [78]	8 electrodes	4 bipolar leads 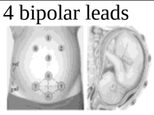	fs = 1KHz	20 records : 8 subject: (9.5 hours total time)	40 week During labour (full term)	ECG R peak detection algorithm.
Rooijakkers et al.,2014 [38]	6 electrodes	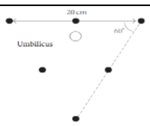	-	5 abdominal measurement of 20 minutes each	39 week (cephalic Presentation)	Electrode grid used for various test measurements.
Zhang et al., 2014 [79], 2015[84]	1350P-ECG- a 12-lead 10 electrodes ECG	3 schemes 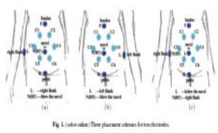	F_H = 75Hz 500 Hz	78 subjects (24 seconds)	3[rd] trimester	Adaptive R wave detection Algorithm
Andreotti et al., 2014 [80]	8 electrodes ADI ML138 Octal Bio Amp &Power Lab 16/30	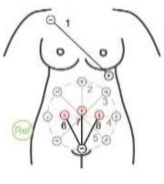	F_H = 1KHz	10 subjects 20 minutes	20 to 28 weeks	MECG estimation techniques & principles of evolutionary computing to detect fetal peaks.

2.7 Public abdominal ECG databases

The increasing interest in the NIFECG extraction and research work created a need for database where biomedical researchers could compare their extraction/detection results. Few freely available online databases emerged over the last one decade, are summarized below:

2.7.1 Abdominal and Direct Fetal Electrocardiogram Database (adfecgdb)

The adfecgdb database [66] provides four abdominal ECG recordings (channel 2 to 5) for 5 minutes each from five different subjects during the 38-41 week gestation period. In addition, for each subject, a simultaneously recorded scalp or direct fetal ECG record (channel 1) is a golden reference in the evaluations to be made on the respective records.

2.7.2 Non-Invasive Fetal Electrocardiogram Database (nifecgdb)

The nifecgdb database [67] provides 55 records of different lengths from a single subject taken from the 20th week of pregnancy. Channels 1 and 2 represent maternal thoracic ECG signals while channels 3 to 6 are abdominal ECG recordings with only maternal QRS reference annotations.

2.7.3 Physionet/Computing in Cardiology Challenge (Phy C) 2013 Database

The Physionet /Computing in Cardiology Challenge database [97] includes 447 minutes of data, with up to 4 channels, resampled at 1 KHz. We used for our simulation a database with 75 records (set a) with 3 to 4 channels each with FQRS annotations for reference. This is the largest publicly available FECG dataset to date, available on Physionet.

A summary of the above three databases are given in Table 2.3. However, the present databases are still very limited in i) Number and duration of the recordings ii) Variety of weeks of gestation iii) Information on the subject's pathophysiological background iv) Expert's annotations of the FQRS locations v) Events such as fetal movement and presence of ectopic beats and vi) Standard database for future FECG morphology. Hence, there is a demand for a more complete database, which may allow FHRV and morphological analysis of the FECG.

Table 2.3: Comparison of the three online Physionet databases [66, 67, 97] .

Database parameter	nifecgdb	adfecgdb	Phy C 2013 (set a)
Number of Electrodes	6 (2 : maternal thoracic 4 : abdominal channels)	4-5 (1 : Direct fetal scalp 3-4 : abdominal channels)	4 (4: abdominal channels)
Bandwidth	0.01- 100Hz	1 to 150Hz	*
Sampling frequency	1 KHz	1 KHz	1 KHz
ADC resolution	16 bits	16 bits	16 bits
Gestation age (weeks)	21- 40	38-41	*
Number of records	55	5	75
FQRS annotation Available	No	Yes	Yes

*Data not Known

2.8 Techniques for NIFECG Extraction

This section briefly explains the taxonomy of the various techniques of extraction of the non-invasive FECG as shown in Figure 2.12. Three of the techniques are implemented and simulated in Appendix B using Matlab.

2.8.1 Adaptive Processing Technique

Adaptive filters are self-adjusting filters whose transfer function acts according to an optimization algorithm driven by an error signal. The adaptive noise canceller requires a reference input that should be uncorrelated with the signal of interest and closely correlated with the interference. The adaptive filter learns and adapts the characteristics of the reference signal and modifies it so that it is similar to the influencing interference. Various adaptive filters have been used in the past for MECG noise cancellation and to extract FECG. These methods train an adaptive or matched filter to remove the MECG using one or more maternal thoracic signals as reference channels to extract the FECG. The adaptive filtering methods more importantly require a reference MECG channel. These methodologies include least mean square (LMS) algorithms, recursive least square (RLS) algorithms, artificial intelligence techniques, fuzzy inference systems, genetic algorithms and Kalman filters [17].

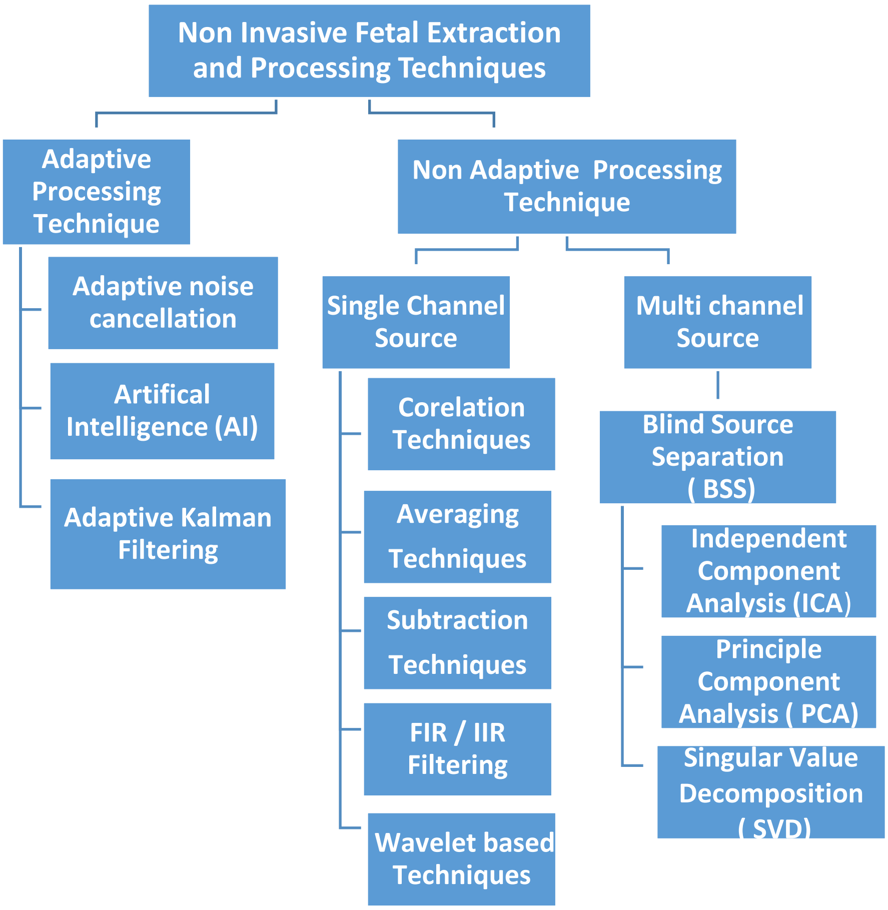

Figure 2.12: Taxonomy of Techniques for NIFECG Extraction.

2.8.1.1 Adaptive noise cancellation

R. Swarnalatha et al. [98], used multistage adaptive filtering for FECG extraction in which the maternal thoracic ECG was used as a reference signal for MECG cancellation and different filter combinations were tested with LMS, normalized least mean square (NLMS) and RLS algorithms. Similarly, in Widrow et al. [99] a linear adaptive filter was used. These methods were not the best for clinical practice as they failed to extract FECG when the maternal and fetal signals overlapped each other. Widrow et al. [100] used the adaptive noise cancellation system to cancel periodic interferences in aECG to produce a clear FECG signal. Later Widrow et al. [101] again used adaptive noise cancellation to reduce periodic or stationary random interference in periodic and random signals using LMS adaptive filter. Martens et al. in his research works in 2004 [102] and 2006 [103] proposed an improved adaptive canceller for decreasing the fundamental PLI. M. Ungureanu et al. [104] proposed an adaptive subtraction technique to subtract MECG after detecting and removing aECG signal segments with high amplitude variations due to uterine contractions. M. Z. U. Rahman et al. [105] also developed adaptive filtering techniques for noise elimination with various algorithms for the removal of noise from ECG signals

2.8.1.2 Artificial Intelligence (AI)

Some AI techniques mainly based on neural networks have been very useful for real-time applications like FECG signal recording and analysis. Marques et al., 1994 [106] used artificial neural networks (ANN) for FHR baseline determination. Selvan et al., 2000 [107] proposed that the two popular techniques, namely adaptive noise cancellation and adaptive signal enhancement were efficient techniques for processing of aECG by using neural networks. Reaz et al., 2004 [108] and Amin et al., 2011[109] described FECG extraction through an adaptive linear (adaline) neural network filter. The adaline neural network was trained to eliminate the MECG component in the aECG signal. In 1999, Giovanni Magenes et al. [110] proposed neural and fuzzy classifiers to distinguish between normal and pathological fetal states. Azad 2000 [111] developed a fuzzy-based approach to extract the FHR by detecting the QRS complex in the FECG signal. Kezi S.V. et al., 2005 [21] proposed an adaptive neuro fuzzy logic technique for the elicitation of FECG signal by eliminating the MECG signal from the aECG signal. According to G. Camps et al. [112] in 2001, FECG can be extracted using FIR neural network in order to provide highly nonlinear dynamic capabilities. Warrick et al. [113] described the signal processing tools and neural networks which were used to develop an automated technique to detect the FHR pattern of baseline, acceleration and decelerations.

Amalgamation of different adaptive techniques and training algorithms are replaced to overcome limitations of individual techniques giving rise to a large number of new intelligent systems. Assaleh et al [114] used ANFIS to nonlinearly align the maternal ECG signal with the components of maternal ECG in the aECG signal. Identified maternal components were cancelled from the aECG signal and finally FECG signal was extracted. In Nasiri et al. [115], Genetic Algorithm (GA) acts as a tool for training the ANFIS structure, which identifies the non-linear transformation. M. Ahmed et al. [116] proposed a technique for FECG extraction based on GA working with an adaptive filter. T. M. Nazmy et al. [117] classified ECG signals using adaptive neuro-fuzzy inference system. A. Sargolzaei et al. [118] developed ANFIS trained with particle swarm optimization (PSO) methodology using four different techniques for the extraction of FECG signal.

2.8.1.3 Adaptive Kalman Filtering

R. Vullings et al. [119] proposed an adaptive Kalman Filter for enhancing the SNR of ECG signal. The Kalman filter, a general class of adaptive filter uses only an arbitrary MECG as reference for MECG cancellation and FECG extraction. The Bayesian filter framework was used by Sameni [120] to extract FECG from single channel aECG. However, as mentioned in [120], the filter fails to discriminate between the maternal and fetal components when the MECG and FECG overlap in time. V. P. Oikonomou et al. [121] developed a Bayesian method for FECG signal extraction integrated with PCA technique. Y. Yin et al. [122] Extracted FECG signal by using Bayesian inference with Neural Networks. The drawbacks of Bayesian modelling and Kalman filtering are that it involves mathematical complexity and computation is time consuming.

2.8.2 Non adaptive processing technique

2.8.2.1 Single channel non adaptive processing technique

2.8.2.1.1 Correlation Technique

In this technique a correlation function is subtracted from the aECG to yield the desired FECG. However, correlation techniques are not very efficient and effective in the detection of non-stationary signals like ECG. Van Bemmel [24] proposed a method using auto correlation and cross correlation techniques for detecting the presence of a fetal heart signal in an aECG signal corrupted by noise. Z. Shi and C. Zhang [123] combined non-Gaussianity and time-correlation of the source signals for FECG extraction. The correlation coefficients of the estimated FECG that were higher than 0.9 were considered to be a good extraction.

2.8.2.1.2 Averaging Technique

It is one of the commonly used methods to extract the waveform of the MECG using only the abdominal lead. Due to the large amplitude in the aECG signal, the R-waves of the MECG signal are easily detected by threshold detectors. Hon et al. [26] proposed the averaging methodology for FECG signal enhancement. The negative aspect of signal averaging is that it removed short term changes in the ECG waveform and moreover, the presence of significant low frequency noise components reduced the effectiveness of averaging [17].

2.8.2.1.3 Subtraction Technique

The method of subtraction of the MECG signal from the aECG signal is one of the most primitive methods. The resulting FECG signal with noise is obtained, while the noise is filtered out. Bergveld et al. [25] proposed a subtraction method but the major challenge was that the amplitude of the thoracic MECG rarely matched the scale of the MECG present in the aECG signal. As a result correct FECG is hardly ever obtained. C. Levkov et al. [124] used this subtraction methodology for power line interference elimination from ECG signals without degrading the signal spectrum.

2.8.2.1.4 Filtering Techniques

Since FECG is our signal of interest, all other noise including MECG is considered as artifact. The FECG signals are filtered by using various filtering methodologies like linear time domain filters, frequency domain filters, FIR filters, IIR filters and Wiener filters. Frequency domain filters can also be used such as, low pass, high pass, band pass and notch filtering features [125]. Kam. A and Cohen. A [27] proposed two different techniques. One method used IIR filter with genetic algorithm adaptation. The other method used IIR filters with genetic algorithm without adaptation. The extracted FECG was good compared to the one obtained using methods that employ genetic algorithm alone. Alcaraz et al. [126] implemented different filters for filtering baseline wandering, high frequency noise and the power line interference was eliminated by notch filtering. L. Chmelka and J. Kozumpl [127] used Wiener filtering for ECG denoising. The limitations of the Wiener filter [128] are the requirements of autocorrelation matrix, cross-correlation vector and matrix inversion, which also lead to a time consuming process [17].

2.8.2.1.5 Wavelet transform based method.

The Wavelet transform (WT) is a time scale representation and efficient mathematical tool for analyzing non-stationary and fast transient signals. One of the main properties of WT is that it can be implemented by means of a discrete time filter bank [17]. Wavelet transform based approach proposed in Papadimitriou et al. [129] efficiently eliminates transient spikes and reduces both Gaussian and coloured noise without affecting or destroying the information content of the signal. The method developed by Echeverria et al. in [130] used multi-resolution wavelet decomposition for FECG acquisition. The wavelet analysis and pattern matching were used in the pre-processing stage to suppress noise and then maternal QRS complexes were cancelled by means of pattern matching and template subtraction. Again in 1998, Echeverria et al., [131] developed a reliable procedure for off-line processing of aECG called Wavelet Analysis and Pattern Matching (WA-PM). Mochimaru et al. [132] used wavelet based methods to detect the FECG. To remove the large baseline fluctuations in the signal as well as to remove the noise, multiresolution analysis (MRA) was used. Complex Continuous Wavelet Transform (CCWT) based technique was implemented by Karvounis et al. [133] along with modulus maxima theory to detect fetal QRS complexes from multichannel MECG recordings. Also Karvounis et al. [134] described a three stage method which was used to extract FHR based on time frequency analysis and complex wavelets and pattern matching techniques. A combination of Wavelet and ICA was proposed by [135]. Using this method, FHR was detected and the Q, R, and S waves were visible without any signal amplification. An algorithm was proposed by Almagro et al. [136] to design a new Mother Wavelet (MW) called abdominal ECG Mother Wavelet (aECG MW) for effective extraction of FECG. A way for detecting QRS complex based on dyadic wavelet transform was represented by Kadambe et al. in [137]. They have designed a Spline wavelet for detecting QRS complex which was the transient part in the ECG signal. Real time FECG feature extraction system was developed by Desai et al., 2012 in [138] based on multi-scale Discrete Wavelet Transform (DWT). Wavelet based peak detection detects QRS complex more accurately for identifying peaks and valleys of noisy FECG signal [139]. Ye Datian et al. [28] implemented a wavelet analysis method to effectively detect FECG. Khamene et al. [140] also efficiently developed a wavelet transform based method to extract the FECG from the composite abdominal signal.

2.8.2.2 Multichannel non adaptive processing technique

BSS and ICA have become promising tools for developing work in recent biomedical signal processing research works. There are different techniques of BSS methodologies, ICA, PCA and signal decomposition techniques. In 2004, Chareonsak et al. [141] proposed a real time

BSS method that can be used to separate the FECG from the aECG effectively. Jafari et al. [142] have addressed the problem of FECG extraction using BSS in the wavelet domain. Blind source separation methods can also be combined with wavelet decomposition methods [143] for denoising and extracting FECG from composite abdominal ECG signal. Karvounis et al. [144] proposed a three stage methodology adopting BSS technique. The extracted FECG was compared with real FECG signal and was found to be correlated with the true FECG.

2.8.2.2.1 Independent Component Analysis

In 2000, de Lathauwer et al. [145] proposed the technique of ICA, to extract FECG from multilead potential recordings on the mother's abdomen. ICA aims at the direct reconstruction of the different statistically independent bioelectric source signals, as well as the characteristics of their propagation to the electrodes. D. E. Marossero et al. [146] proposed an efficient method using the mermaid algorithm for ICA method, where the performance of the Mermaid algorithm, based on minimizing Renyi's mutual information, was evaluated. ICA, using higher order statistics to decompose the signal into statistically independent components, has already been used in single pregnancies to distinguish between MECG and FECG signals [147]. Najafabadi et al. [148] also applied the ICA for the separation of FECG and MECG signal from the aECG. It is concluded that ICA works magnificently in order to extract FECG. Y. Ye et al., 2008 [74] proposed a neural network based ICA algorithm, called Fast Adaptive orthogonal group algorithm to separate mixtures of sub Gaussian and super Gaussian source signals. D. Luo [149] discussed the nonlinear blind mixed ECG signals separation technology and introduced the model of the ICA algorithm and the implementation methods. Martın-Clemente [150] described a fast and simple algorithm that was developed based on ICA but computationally demanding calculations were substituted to make it simpler in FECG extraction. Camargo-Olivares et al. [151] described multidimension ICA based approach extraction method was presented which was more appropriate than ICA in FECG extraction.

Estimated maternal signals were subtracted from the aECG, however this approach fails when the FECG is weaker than the residual noise. A method presented in [152] was based on non-stationary ICA and wavelet de-noising. Due to low amplitude and poor SNR of the FECG recorded at the abdominal region of a pregnant woman, the proposed algorithm removed the maternal ECG, reduced motion artifact and enhanced the FECG signal. Here due to the non-stationary nature of the FECG signal, non-stationary ICA method was used to eliminate maternal complex. In [153], ICA based BSS methods were used for extracting FECG, which showed that reconstruction of FECG could be possible by means of higher order statistical tools. Hyvarinen [154] proposed the fast and robust fixed point algorithms for ICA, which can be used efficiently to extract FECG. I. Romero [155] investigated the performance of principle component analysis in denoising ECG signals recorded in ambulatory conditions.

2.8.2.2.2 Singular Value Decomposition

Spatial filtering techniques such as singular value decomposition (SVD), blind and semi-blind source separation, can be considered as decomposition methods that are driven by data, which creates the required basis functions from the data itself, by maximizing several statistical quantities of signal segregation. Gao et al. [156], described a method which was employed with the combination of SVD and ICA for FECG signal separation from aECG. This method uses SVD of the spectrogram followed by an iterative application of ICA. Barros et al. [157] proposed a semi blind source separation algorithm which has been developed and requires prior information about the auto correlation function of the primary sources to extract the FECG signal.

De Lathauwer et al. [158] have discussed the pros and cons of techniques relying on the ordinary SVD, quotient SVD and multilinear SVD for the elicitation of the FECG from multilead cutaneous potential recordings. The multilinear SVD approach has the advantage that the mixing matrix can be estimated in an unsupervised way. In addition, the separation of the measurements into statistically independent source signals is easier to interpret than decomposition in time-orthogonal principal components. On the other hand, the algorithm is computationally more complex. Table 2.4 presents several methods proposed in the literature for the extraction of FECG. Due to the fact that there is no benchmark database for this area, therefore, each approach is evaluated and performed using different approaches by authors. The FECG extraction techniques such as synthesized template method, ICA and ANFIS are implemented and compared using Matlab in Appendix B.

2.9 Discussion and summary

The experimental recordings were conducted to collect an aECG signal from a single pregnant woman to access the best electrode position configuration (see Appendix A). It was noted in our experiment that the fetus was too small and the small heart was extremely weak and thus the FECG signals were very small compared to the maternal signals picked through the aECG. This maternal-fetal amplitude ratio is almost the same in the case of the nifecgdb records wherein the MECG amplitude is very large compared to the fetal amplitude. Moreover the noise overrides the aECG signals, making it even more difficult for the separation of fetal signals from the aECG. The best recordings would be of a near full time mother with a normal size baby. It was observed that the scheme 2 gave the best results whose average FHR value was closer to the average FHR taken using CTG, while the schemes 1 and 3 gave MHR values. This could have been because the leads may have been placed very close to each other. In our next experiment, the distance of leads (inter electrode distance) from WCT can be varied and also around the abdominal circumference. More positions can be researched so that we get equivalent height to the baby’s ECG peak in our database before processing the raw measurements so as to isolate FECG from the MECG. In the future, a larger database for various subjects having different gestation ages can be planned with recordings of more clinical reports for each subject.

Table 2.4: Summary of existing FECG extraction techniques.

Author	Technique	Database	Accuracy (%)
Mooney et al.,1995 [159]	Adaptive algorithm	5 abdominal leads (several records)	85
Azad et al., 2000 [111]	Fuzzy approach	3 abdominal leads (5 records)	89
Khamene et al.,2000 [140]	Quadratic spline wavelet	5 abdominal & 3 thoracic	100
Pieri et al., 2001 [160]	Matched Filter	3 abdominal leads	65
Camps et al.,2001 [112]	FIR neutral network	Synthetic & real Registers	91
Ibrahimy et al.,2003 [161]	Statistical Analysis	One abdominal lead 5 records, 20 minute	89
Karvounis et al., 2004 [133]	Complex wavelets	3 abdominal leads 15 records,1 minute	99.5
Karvounis et al., 2006 [134]	Time Frequency methods	4 long records 15 minutes	96
Karvounis et al., 2007 [39]	Time frequency Analysis	3 abdominal leads 8 short records	99.19
Karvounis et al., 2007 [39]	Time frequency Analysis	3 abdominal leads 10 short records	97.35
Swarnalatha et al.,2009 [162]	Wavelet adaptive filter	SISTA/DAISY & Physionet data	90
Swarnalatha et al.,2010 [98]	Multistage Adaptive Filter	SISTA/DAISY & Physionet data	89
Swarnalatha et al.,2010 [163]	ANFIS & Wavelet method	5 different subjects	100

The three proposed FECG extraction algorithms namely, Synthesized QRS template method, ICA and ANFIS have been evaluated to extract FHR and the results are compared using the records of Physionet abdominal and direct fetal ECG database (see Appendix B).

In the proposed synthesized QRS template algorithm, the filtered aECG was multiplied with the respective synthesized pulse trains having QRS (tau) = 100ms for maternal and QRS (tau) = 45ms for fetal. Further the FHR was computed giving us accurate heart rates except for some sections of the record r04 and r07 of the adfecgdb as the original signal was corrupted with noise. However since both the MECG and FECG are quasi periodic and non-stationary signals, a large QRS peak can be missed if the beat per minute (k) is altered. Also since we need to know the rate (beat per minute) in advance of both the MECG and FECG signals, this method cannot be used in the unsupervised mode and hence may not be efficient to extract accurate maternal and fetal heart rates.

The proposed ICA method is a statistical technique and its accuracy is based on using a large number of noise free maternal abdominal input channels. The following conditions must be met for ICA to function correctly: i) the number of measured signals should be equal to or greater than the number of input sources ii) it should possess an instantaneous linear time invariant mixing matrix iii) the input sources should be statistically independent and iv) the sources should be non-gaussian and/or auto correlated sources [164]. In our application of maternal and fetal QRS separations, the first two do not fully satisfy because the artifacts increase the number of sources and fetal movement leads to a non-invariant mixing matrix. The maternal ECG is the strongest independent source of the four measured abdominal signals. Hence, it would result in at least one independent component. For records, where clean ECG signals and an invariant mixing matrix exist, ICA would also be able to separate the fetal ECG. This method is also based on the supervised selection of channels to be given to stage 2 and hence is not efficient. Our objective was to obtain fetal R-peaks from single channels.

ANFIS is an adaptive noise cancellation system which may have advantages over some methods. It is suitable for nonlinear applications, and has less mathematical analysis and requires less inputs to extract FECG due to the neutral network. ANFIS requires an additional maternal thoracic ECG signal as reference signal for adaptive cancellation of the maternal ECG. This method depends on how well one trains the ANFIS structure to compute the estimated output FECG signal. However this technique may not be very useful to be implemented in real time applications in embedded systems and DSP cores. The ANFIS module estimated the FECG output which was given to the modified QRS detector for fetal heart rate calculations. The failed detections for the records r04 and r07 were large and the adaptive threshold could not detect some of its fetal R-peaks (see Appendix B). We connected our Android smartphone to Matlab via the Matlab Mobile [165] as shown in Appendix C. The Matlab simulation plots and FHR values were viewed on the smartphones using MATLAB Mobile [72].

Correlation techniques are not very efficient and effective in the detection of non-stationary signals like ECG. Subtraction method is a simple technique, but the major challenge is that the amplitude of the thoracic MECG rarely matches the scale of the MECG present in the aECG signal. As a result correct FECG is hardly ever obtained. Wavelet transform method can be used for the pre-processing stage to suppress noise and maternal cancellation can be done by template subtraction. As IIR filtering being a nonlinear method, our technique of using linear phase sharp transition FIR filter is less complex and does not involve many iterations as the filter response is specified precisely over the entire band. With the knowledge of the fiduciary edges and the fair estimate of the spectral overlap of maternal and fetal ECG, accurate FHR and maternal heart rate can be obtained.

The Fourier transform is a simple technique which can play a very important role to detect FECG signals, however if the aECG is contaminated with noise then it may be difficult to locate the fetal peaks. Our main objective is to separate the MECG and FECG particularly, the QRS complex of each and detect the FHR and missing beats, if any, which will indicate the fetal health status. The aim is also to improve the signal processing aspects of FECG by developing a new and simple technique by filtering FECG signals extracted from the aECG Physionet database. The basic idea behind the method is to use such quasi-periodic cardiac signals, to design filtering technique and evaluate the output QRS complexes which obtain the fetal heart rate variability. The two main concerns in the separation of the mother-fetal QRS are (i) The aECG has a low SNR due to the interferences from MECG and other noise signals such as electromyogram (EMG) and motion artifacts [9]. (ii) The MECG and FECG almost share the same frequency band [6] and overlap in time and partly in frequency domain [24]. Due to these inherent problems, it is challenging to successfully extract FQRS from aECG, which contains MECG which is the major noise signal. Moreover, the FECG has an amplitude less than 20% of the MECG [8] and each of the two ECG signals have distinct cardiac beat to beat ranges. The fetal's cardiac beats/minute is faster than that of the mother's which ranges from 120 – 160 bpm compared to the MHR which is approximately 70 – 100 bpm [166].

2.10 Goal of this study

2.10.1 Research Objectives

The objective of the research is to design and synthesize linear phase sharp transition FIR band pass filters with designated fiduciary edges in the light of the literature cited above. Further, the synthesized filters were required to possess the following desirable features:

a. Sharp transition with low passband ripple and large stopband attenuation.
b. Well behaved function to model filter frequency response.
c. Impulse response coefficients related to designated fiduciary edges.
d. Finite transition width with well-defined stopband, transition band and passband regions unlike the classical designs.
e. FIR filter design for lower filter orders (N) with arbitrary passband and not necessary an equiripple filter.
f. Simple design with less complex computations.

2.10.2 Proposed Methodology : Linear phase sharp transition FIR filter design

In pursuant to the stated objective, the method of the filter synthesis proposed by us is as follows.

The salient points of our synthesis are given below:

i. The entire range [0,π] of the frequency variable ω is split into three main regions, namely stopband, transition and passband for either of the low pass, high pass or band pass filters.

ii. Each region of the magnitude response is defined in terms of a cosine/sine function of ω, conforming to the filter specifications.

iii. The magnitude response function is assumed to be in the form given by Eq. (2.1) for N odd and Eq. (2.2) for N even respectively.

$$H_r(\omega) = 2\sum_{n=0}^{\frac{N-3}{2}} h(n)\ \sin\omega\left(\frac{N-1}{2}-n\right) \qquad \text{N odd} \qquad (2.1)$$

$$H_r(\omega) = 2\sum_{n=0}^{\left(\frac{N}{2}\right)-1} h(n)\ \sin\ \omega\left(\frac{N-1}{2}-n\right) \qquad \text{N even} \qquad (2.2)$$

where, n = time index ; N = order of the filter.

iv. Applying cosine transformation to the magnitude response H(ω) in Eq. (2.1) and (2.2), we obtain the impulse response sequence as given in Eq. (2.3)

$$h(n) = \frac{1}{\pi}\left[\int_0^{\pi} H(\omega)\ \sin(k\omega)\ \ d\omega\right] \qquad (2.3)$$

Where, $n = 0,1,2,\ldots\ldots\ldots..,\left(\frac{N-3}{2}\right)$ $\quad for\ \ N\ Odd$

$n = 0,1,2,\ldots\ldots\ldots..,\left(\frac{N}{2}-1\right)$ $\quad for\ N\ Even$ and $k = \left[\left(\frac{N-1}{2}\right)-\ n\right]$ for all N.

v. The integral in (2.3) is similar to the inverse Fourier transform integral. The impulse response is extracted from Eq. (2.1) and Eq. (2.2) using the orthogonal property of the cosine /sine functions.

vi. The design parameters k_s, k_t and k_p are used in the sine/cosine functions defining the stopband, transition and passband, respectively. These parameters control the shape of the magnitude response function H (ω) in the three referred regions.

vii. The discontinuity present at the fiduciary band edges of the passband-transition and transition – stopband regions due to Gibb's phenomenon are minimal in the magnitude response.

viii. To further reduce the ripples on either side of the discontinuities in the magnitude response, a technique known as slope matching is used.

ix. A sharp transition width is realized using the user based fiduciary band edges ω_{s1}, ω_{p1}, ω_{p2} and ω_{s2} such that we get a variable, almost flat passband with minimum passband loss and appreciable stopband attenuation with least ripples.

In summary, the filters proposed by us:

- Have minimum passband loss and large stopband attenuation.
- Have minimum discontinuities at band edges, with slope matching technique.
- Have a finite width in the transition region.
- Have reduced ripples in the passband and stop band regions due to Gibb's phenomenon.
- Do not involve optimization steps but use simple computations involving trigonometric functions with low filter order to closely match the desired response.
- Have derived closed form expression for the impulse response sequence by formulating a magnitude response that is practically realizable as in Equations (2.1) and (2.2).

3

Design of Linear Phase Sharp Transition FIR Filters

3.1 Background theory of FIR filters

A filter is a system or a network that is designed to selectively alter the spectral content of the input wave shape, amplitude or the phase in a specified manner. The most common filtering objectives include improving the signal to noise ratio, separate frequency components or extract certain information from signals for applications in biomedical, speech or image signal processing and other areas.

Digital filter design is a process of deriving the filter transfer function H(z) which satisfies the set of given specifications. The linear time invariant frequency selective filters can be classified in two categories, namely infinite impulse response and finite impulse response filters [167] and are represented by Eq. 3.1 and 3.2 respectively.

$$y(n) = \sum_{k=0}^{\infty} h(k)\, x(n-k) \tag{3.1}$$

$$y(n) = \sum_{k=0}^{N-1} h(k)\, x(n-k) \tag{3.2}$$

The distinct difference between the two is that the impulse response of IIR has infinite length, whereas FIR has fixed duration of length N. Additionally the Eq. 3.1 for IIR filters can be expanded as,

$$y(n) = \sum_{k=0}^{N} b_k\, x(n-k) - \sum_{k=1}^{M} a_k\, y(n-k) \tag{3.3}$$

where, a_k and b_k are the filter coefficients of IIR filters and from Eq. 3.3 we can conclude that y(n) is a function of past outputs as well as present and past inputs. However an FIR system only depends upon the present and past input values. If we set $a_k = 0$ in Eq. 3.3, we obtain the original FIR Eq. 3.2.

We chose to use FIR filters for our application having the following advantages:

i. FIR filters have linear phase response with no phase distortion and are suitable for our application unlike the IIR filters that display the non-linearity at band edges.

ii. Non recursive FIR filters are stable while the stability of IIR is not assured.

iii. In our application of designing linear phase filter with sharp transition width more coefficients may be required as compared to IIR filters. However, this limitation of more processing time with memory storage, longer delays and more computations can be overcome today by using fast computers and DSP processors for real time implementations.

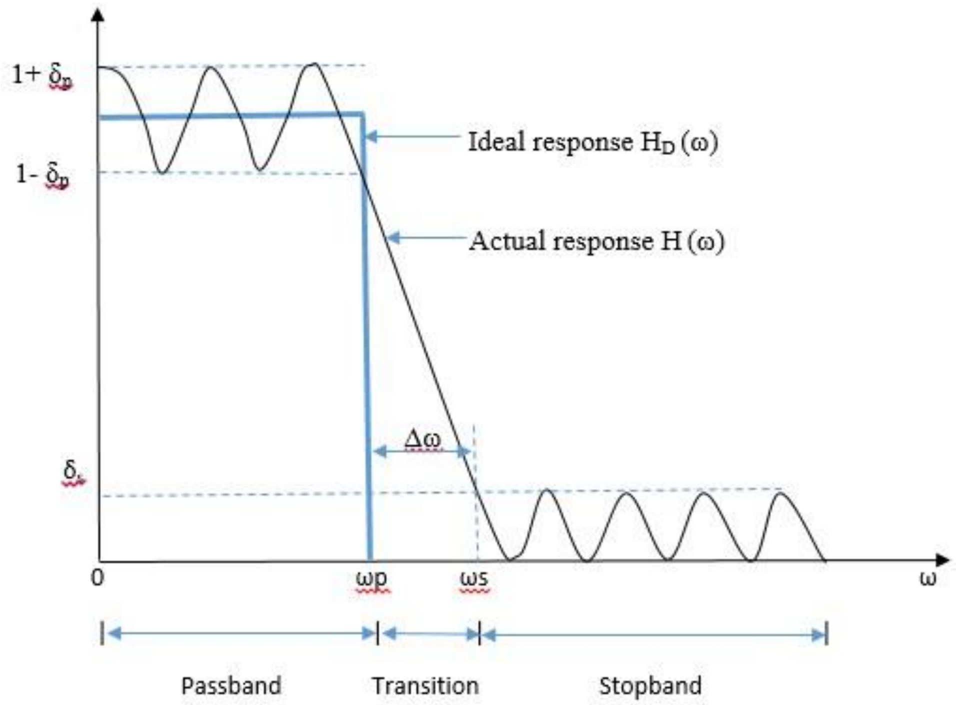

Figure 3.1: Frequency response of a low pass filter.

Filters, in practice, may not exhibit a flat passband, and a deviation of H (ω) from 0 dB is called magnitude distortion while, changes in the linear phase is called phase distortion [167]. With reference to the magnitude response of a low pass filter in Figure 3.1, the magnitude is unity with a passband ripple error of ± δp such that,

$$1-\delta_p \le |H(\omega)| \le 1+\delta_p \qquad 0\le \omega \le \omega_p \tag{3.4}$$

The magnitude approximates 0 with a stopband attenuation error δs such that,

$$|H(\omega)| \le \delta_s \qquad \omega_s \le \omega \le \pi \tag{3.5}$$

Eq. 3.5, describes the stopband ripple to have maximum gain or minimum attenuation in the stopband region. A_p is the passband ripple given by, $20\log_{10}\left(\frac{1+\delta p}{1-\delta p}\right)\ dB$

While the stopband attenuation is given by $-20\log_{10}\delta_s\ dB$, the deviations are expressed in decibels and the magnitude response is normalized to 1 (0 dB) [168].

To summarize causality aspects while designing the FIR digital filter, we need to see that the filter is causal wherein the output of the filter at time n_0 depends on the input applied at and before n_o and not after n_o.

a. As per Paley - Weiner theorem [169], the magnitude response H (ω) can be zero at some frequencies but cannot be zero over finite band of frequencies since the integral in [169] then will become infinite as per Eq. 3.6.
b. The desired frequency response is given by ,

$$H_d(e^{j\omega}) = \sum_{n=-\infty}^{\infty} h_d(n)\, e^{-j\omega n}. \tag{3.6}$$

To achieve FIR filter, we can truncate the impulse response for a finite duration sequence of length N.

$$h(n) = \begin{cases} h_d(n) & 0 \le n \le N-1, \\ 0 & otherwise. \end{cases} \tag{3.7}$$

The frequency response for this finite duration will be,

$$H(e^{j\omega}) = \sum_{n=-\infty}^{\infty} h(n)\, e^{-j\omega n},$$
$$= \sum_{n=0}^{N-1} h_d(n)\, e^{-j\omega n}. \tag{4.8}$$

A causal FIR filter obtained by simply truncating the impulse response of the ideal filter exhibits an oscillatory behavior in its magnitude response which is more commonly referred to as Gibb's phenomenon [170]. The oscillatory behavior of the magnitude response is on both sides of the cutoff frequency at which the ideal response is discontinuous and the peak ripple moves closer to the discontinuity. As the order of the filter is increased, the number of ripples in both passband and stopband increases and the ripples are squeezed into a narrower interval about the discontinuity. However the overshoots which occur on both sides of the transition region remain the same independent of the filter order and are approximately 18% of the difference between the passband and stopband magnitudes of the ideal filter [171].

3.2 Types of linear phase FIR filters

Due to their simplicity, linear phase FIR filters have many applications in the speech and biomedical signal processing research area as well due to their guaranteed stability, negligible phase distortion and low coefficient sensitivity. Depending upon the number of coefficients (N) being odd or even and the impulse response h (n) being symmetrical or anti-symmetrical, linear phase FIR filters can be of four types and have the property of having a linear phase [167,168]. However the signal passing through a filter having nonlinear characteristics will have phase distortion. The frequency components in the output signal will each be delayed by an amount not proportional to the frequency thereby alternating their harmonic relationships.

Table 3.1: Linear phase FIR filters types [167,168].

Filter type (unit sample response)	Impulse response h(n) and number of filter coefficients	Frequency response $H_r(\omega)$	Remark
Type 1 : Symmetric $H(\omega) = H_r(\omega)\, e^{-j\omega(N-1)/2}$ N = odd	$h(n) = h(N-1-n)$; *(N-1)/2*	$H_r(\omega) = h\left(\frac{N-1}{2}\right) + 2\sum_{n=0}^{\frac{N-3}{2}} h(n)\cos\omega\left(\frac{N-1}{2} - n\right)$	-
Type 2 : Symmetric $H(\omega) = H_r(\omega)\, e^{-j\omega(N-1)/2}$ N = even	$h(n) = h(N-1-n)$; *N/2*	$H_r(\omega) = 2\sum_{n=0}^{\left(\frac{N}{2}\right)-1} h(n)\cos\omega\left(\frac{N-1}{2} - n\right)$	$H_r(0)$ gives maximum value, while $H_r(\pi) = 0$
Type 3 : Anti Symmetric $H(\omega) = H_r(\omega)\, e^{j[-\omega(N-1)/2 + \pi/2]}$ N = odd	$h(n) = -h(N-1-n)$; *(N-1)/2*	$H_r(\omega) = 2\sum_{n=0}^{\frac{N-3}{2}} h(n)\sin\omega\left(\frac{N-1}{2} - n\right)$	$H_r(0) = 0$ and $H_r(\pi) = 0$
Type 4 : Anti Symmetric $H(\omega) = H_r(\omega)\, e^{j[-\omega(N-1)/2 + \pi/2]}$ N = even	$h(n) = -h(N-1-n)$; N/2	$H_r(\omega) = 2\sum_{n=0}^{\left(\frac{N}{2}\right)-1} h(n)\sin\omega\left(\frac{N-1}{2} - n\right)$	$H_r(0) = 0$ and $H_r(\pi)$ gives out a maximum value

With reference to the listed four types as seen in Table 3.1, it can be analyzed that for filter Type 2, $H_r(0)$ gives a maximum value while $H_r(\pi) = 0$ makes it suitable for low pass filter. In Type 3, since Hr (0) = 0 and Hr (π) = 0, this is not suitable for either low pass nor high pass, but is most suitable for band pass filter. For Type 4 filter, Hr (0) and Hr (π) gives maximum value, thus is suitable for a high pass filter. Type 1 is the most preferred of the four when symmetric h (n) is concerned and the center of symmetry for all types is given as (N-1)/2. The main objective of the FIR coefficient's calculation is to obtain values of h (n) so that the resultant filter meets the designed specifications. Several methods are available for obtaining h (n) such as window method, frequency sampling and optimal methods and all three lead to linear phase FIR filters.

3.3 Linear phase filters using window method

Let us take $H_d(\omega)$ and $h_d(n)$ as the desired frequency and desired impulse response respectively, of an FIR filter where, $H_d(\omega)$ is the Fourier transform of $h_d(n)$, both given by the Eq. 3.9 and Eq. 3.10, respectively.

$$H_d(\omega) = \sum_{n=0}^{\infty} h_d(n)\, e^{-j\omega n}, \tag{3.9}$$

where, $$h_d(n) = \frac{1}{2\pi}\int_{-\pi}^{\pi} H_d(\omega)\, e^{j\omega n} d\omega\ . \tag{3.10}$$

Note that, h_d (n) is infinite in duration and must be truncated say, at n = N-1 to yield a filter of length N. Truncation of H_d (n) of length N-1 is the same as multiplying h_d (n) by a rectangular window as defined in Eq. 3.11.

$$w(n) = \begin{cases} 1\ , & n = 0,1.....N-1, \\ 0 & \mathit{otherwise.} \end{cases} \tag{3.11}$$

Therefore, the impulse response for the FIR filter turns out to be,

$$h\ (n) = h_d\ (n)\ \omega(n) \tag{3.12}$$

$$h(n) = \begin{cases} h_d(n) & n = 0,1.....N-1, \\ 0\ , & \mathit{otherwise.} \end{cases} \tag{3.13}$$

Also, convolution of H_d (ω) with W(ω), the Fourier transform of ω (n) gives us the frequency response of the FIR filter , H (ω).

Thus , $$H(\omega) = \frac{1}{2\pi}\int_{-\pi}^{\pi} H_d(v)\ W(\mathrm{w}-v)\ dv. \quad (v \text{ being the dummy frequency variable}) \tag{3.14}$$

And where, Fourier transform of the window function is given by,

$$W(\omega) = \sum_{n=0}^{N-1} w(n)\ e^{-j\omega n}. \tag{3.15}$$

For rectangular function replace ω (n) = 1 in Eq. 3.15 we get Eq. 3.16,

$$\begin{aligned} W(\omega) = \sum_{n=0}^{N-1} e^{-j\omega n} &= \frac{1-e^{-j\omega N}}{1-e^{-j\omega}} \\ &= e^{-j\omega(N-1)/2}\ \frac{\sin(\omega \mathrm{N}/2)}{\sin(\omega/2)} \end{aligned} \tag{3.16}$$

This window function has a magnitude response,

$$|W(\omega)| = \frac{|\sin(\omega \mathrm{N}/2)|}{|\sin(\omega/2)|} \qquad -\pi \leq \omega \leq \pi \tag{3.17}$$

The width of the transition region between the passband and stopband in H (ω) reduces with the width of the main lobe of W (ω), with increase in the length of the filter order (N) [168]. However the area under the side lobes remains constant. The rectangular window has large side lobes in W (ω) and causes large passband ripple related to Gibb's phenomenon. These side lobes are caused by the abrupt discontinuity at the edge of the window [167]. The demerits of the rectangular window is overcome by the use of various other window functions such as Hamming, Hanning, Blackmann, Barlett,Kaiser,Tukey and others. All of these have lower side lobes than of rectangular and hence less passband ripple. Figure 3.2 compares the time and frequency domain of various window types for N = 1001 simulated in Matlab. Table 3.2 lists the window types with its main lobe width and stopband attenuation [167,168].

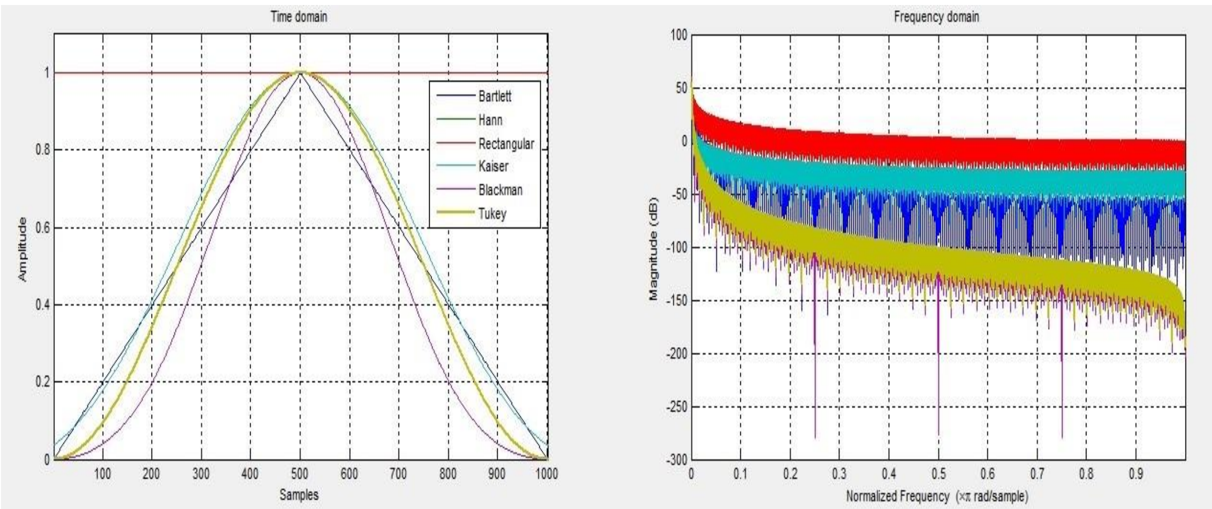

3.2 (a) 3.2 (b)

Figure 3.2: Comparisons of various window types for filter order (N) = 1001 (a) time and (b) frequency domain.

Table 3.2: Various Window types with its main lobe width and stopband attenuation [167,168].

Window type	Main lobe width	Stop band attenuation peak (20 $\log_{10} \delta_s$)
Rectangular	$4\pi/N$	-21 dB
Hanning	$8\pi/N$	-44 dB
Hamming	$8\pi/N$	-53 dB
Blackman	$12\pi/N$	-74 dB
Barlett	$8\pi/N$	-25 dB
Kaiser	variable	variable

There are lesser ripples for the Hanning window as compared to the rectangular window but the transition width increases which can be compensated by increase of N. There is a fundamental tradeoff between the main lobe width and the side lobe amplitude.

3.4 Linear phase filters using frequency sampling method (FSM)

This method allows recursive implementation of FIR filters leading to computationally efficient filters [167]. The method is accomplished in a two stage process. In the first stage, the magnitude response from the user $H_d(e^{jw})$ is frequency sampled by at $\omega = (2\pi k)/N$ samples, where N is the order of the filter to obtain the desired frequency response $H_d(k)$. By applying inverse discrete Fourier transform to $H_d(k)$ in the 2nd stage, we obtain impulse response h (n) which will have a total number of N samples of FIR filter impulse response. The impulse response h (n) is given by,

$$h(n) = \frac{1}{N}\sum_{k=0}^{N-1} H_d(k)\, W_N^{-nk} \qquad n = 0,1.....N-1 \text{, where } W_N = e^{-j\frac{2\pi}{N}} \tag{3.18}$$

It has two methods, depending on when $\omega = 0$ (Method I of FSM) or $\omega \neq 0$ (Method II of FSM). In Method I of FSM which is preferred, we sample at $\omega = (2\pi k)/N$ for k =0,1….N-1 to obtain $H_d(k) = H_d(e^{jw})|_{\omega = (2\pi k)/N}$. If we want h (n) to be real coefficients (real values), then we have to put a condition on the $H_d(k)$ to ensure h (n) is real.

For real value h (n), the filter coefficients can then be written as, `

$$h(n) = \frac{1}{N}\left\{H_d(0) + 2\sum_{k=1}^{(N-1)/2} \mathrm{Re}\left[H_d(\mathrm{k})\, e^{j2\pi kn/\mathrm{N}}\right]\right\} \qquad \text{N is odd} \tag{3.19}$$

All the complex terms shall appear in complex conjugate pairs. The terms can be matched by comparing the exponentials in Eq. 3.18. The term H_d (k) $e^{j2\pi kn/\mathrm{N}}$ should be matched by the term that has the exponential $e^{-j2\pi k/\mathrm{N}}$ as a factor. This requires that H_d (0) is real and H_d (N-k) = H_d*(k) , k = 1,2 …(N-1)/2 , N is Odd and if H_d (N-k) = H_d*(k) , k = 1,2 …(N-1)/2 and Hd (N/2) = 0, N is even [5].

$$h(n) = \frac{1}{N}\left\{H_d(0) + 2\sum_{k=1}^{(N/2)-1} \mathrm{Re}\left[H_d(\mathrm{k})\, e^{j2\pi kn/\mathrm{N}}\right]\right\} \qquad \text{N is even} \tag{3.20}$$

3.5 Optimal linear phase FIR filters

As seen in Eq. 3.4, the actual frequency response oscillates between 1-δp and 1- δp in the passband while it oscillates between 0 and δs in the stopband. This filter design is based on a Chebyshev approximation problem, wherein the weighted approximation error between the desired response, H_d (ω) and actual frequency response, H (ω) is equally spread across the stopband and passband of the filter minimizing the maximum error. The resultant filter may have similar amplitude ripples in both the bands which are called equiripple [167,168]. The error function can be expressed as,

$$E(\omega) = W(\omega)\ [H_d(\omega) - H(\omega)] \tag{3.21}$$

where, W(ω) is the weighing function.

The main objective is to find the h (n), such that the value of the maximum weighted error |E (ω)| is minimum in the stop and pass bands expressed as min [max |E (ω)|] [170]. The ripples will alternate in sign between the two equal amplitude levels. These minima and maxima points are known as extremal frequencies which are not known in advance like those of the band edges. An iterative process known as Remez algorithm is used which locates the extremal frequencies. This process step relies on the alternation theorem which specifies the number of extremal frequencies that can exist for a given filter order. After locating the optimal set of extremal frequencies the actual h (ω) and h (n) of the filter are easily obtained. Parks McClellan (PM) routines can be used for designing the LP FIR filters based on Chebyshev approximation criterion and implemented with the Remez exchange algorithm [168]. FIRPM() routine in the Signal toolbox of Matlab implements the Parks-McClellan (PM) algorithm which uses the Remez exchange algorithm and Chebyshev approximation theory to design linear phase FIR filters with an optimal fit between the desired and actual frequency responses.

The most advantageous aspect of using the window method is its simplicity, it involves the least amount of computations for almost all the window types. The only demerit of this type is its lack of flexibility. Due to the effect of convolution of the frequency spectrum of the desired response and the window function, the passband and stopband edge frequencies cannot be precisely specified. The frequency sampling method can be chosen when the arbitrary amplitude response is required. However this method lacks control of the passband ripples and the band edge frequencies. The optimal method scores over the other two as it is efficient and yields good magnitude responses and is based on the concept of equiripple passband and stopband.

3.6 Background of linear phase FIR filter designs

For many digital signal processing applications, FIR filters are preferred over their infinite impulse response counterparts as the former can be designed with exact linear phase, guaranteed stability, free of phase distortion, absence of limit cycles and low coefficient sensitivity. However, FIR filters used in applications demanding narrow transition bandwidth require considerably more arithmetic operations than their IIR equivalents. Since the FIR filter length is inversely proportional to transition bandwidth, its complexity becomes prohibitively high for sharp filters, which causes serious implementation problems [167]. First, a very large number of multipliers render real time high speed implementation impractical. Second, the round off noise power generated by a filter with a large number of nontrivial coefficients will be unacceptable unless the word length of the registers and arithmetic units are sufficiently high. Finally, filters with a large number of nontrivial coefficients have a high coefficient sensitivity. As a consequence, very sharp filters will have high hardware complexity, high coefficient sensitivity and high round off noise unless the filter coefficient vector is sparse. Several methods have been proposed for reducing the arithmetic complexity of sharp transition FIR digital filters, some of the methods and techniques are listed below:

Charalambous et al., [172] presented a program for over 400 design examples for FIR linear phase symmetric and symmetric fan 2D digital filter design. The technique is convergent and did not suffer from degeneracy. Pei et al., [173] proposed a method of designing equiripple linear phase FIR phase with linear constraint by carrying out the Remez exchange technique and the design is optimal in the minimax sense. Yim Yong [174] says that if the frequency response of the original band filter and its complementary filter are masked and recombined, a narrow transition band filter can be achieved. Jing Z. et al., [175] say that a low pass filter with narrow transition band can be realized by a structure mainly composed by few FIR filters used for implementation of a fast convolution algorithm. Principe et al., [176] presented the design and implementation of linear phase FIR filter mainly for low frequency EEG signals which uses loose frequency response characteristics and good time resolution. Rabiner et al., [177] in his paper, discusses a novel implementation for narrow band FIR filter using the technique of decimation and interpolation. The filter can be realized with a large reduction of number of multiplication per sec over standard direct form implementation. Also the design has less round off noise and less severe coefficient sensitivity problems. In another paper, Rabiner et al., [178] describes in detail the designing of linear phase FIR filters based on the Chebyshev approximation. The paper uses special techniques to obtain optimal low pass or bandpass filters.

Lim Y.C et al., [179], using frequency response masking (FRM) approach presented an algorithm for the h (n) up sampling ratio techniques to select the optimal k value for a K stage design and algorithm for H (ω) ripple compensation. The design was compared with Remez exchange algorithm. Saramaki et al., [180,181] described how FRM can be used to reduce the number of arithmetic hardware to implement low pass FIR filters and further in addition of using the Matlab Remez routine which will simplify the designing of sub filters rather than using linear programming. Zhang et al., [182] uses a modified FRM approach to design sharp FIR filters using a new technique called Interpolated FIR. This method is designed for one of the sub filters which saves 24% of the number of multipliers as compared to the FRM approach. Neuvo et al., [183] designed a narrow band symmetrical FIR BPF. This method is applicable to linear and nonlinear cases with the multipliers and adders in this case to be $1/\sqrt{\Delta F}$, where ΔF is the required narrow transition bandwidth, the designed structure allows simple tuning of the centre frequency. Rodrigues et al., [184] describes a modified FRM method using low pass and bandpass sub filters which are designed as linear phase equiripple FIR filters. It further uses trigonometric functions to obtain h (n) to reduce Gibb's phenomenon. The filter model is formulated using sinusoidal functions of frequency to evaluate the impulse response coefficients in closed form. The band pass filter (BPF) uses a centre frequency for fixed passband widths. The BPF eliminates one masking filter thereby reducing the complexity of FRM technique.

Rodrigues et al., in [185] proposes a low pass sharp FIR filter with low complexity with less filter order. The design transition parameter k_t can be varied for narrow to wideband filters. The obtained filter length and delays are less than the FRM technique. Mintzer et al., [186] describes a computer program by Park McClellan to design an optimal FIR band pass filter. Here the order of the filter is the input to the program. The task was to find the lowest order filter which satisfies certain maximum ripple requirement. Rajan et al., [187] designed a sharp cut off wide band FIR filter where the interpolating factors L (optimal value) are derived. This reduces the multiplier and adders in the overall realization. The authors claim that the two branch realization is more efficient than the direct form technique with a slight increase in delays and in the noise performance. Saramaki at el., [188] present two methods - the first one uses Remez multiple exchange and optimizes the shaping filter and the interpolator of the IFIR filter. This method being efficient reduces the arithmetic hardware and delays. In the second method the interpolator was derived based on the recursive running sums which further reduced the number of multiplier and adders in the implementation.

Vaidyanathan et al., [189] presented an optimal design of linear phase FIR filter for flat passband and equiripple stopbands using Remez algorithm for the design of weighted Chebyshev FIR filters. The flatness of the passbands is to a prescribed degree. The overall filter is designed for order N even. Sheikh et al., [190] describes the technique for designing narrow band and wideband linear phase FIR filter band on FRM method. It uses sparse FIR design and masking filter using fixed integer linear programming optimization. Alam et al., [191] presents a low power narrow transition FIR method using FRM implemented using a field programmable gate array (FPGA). This hardware was used for narrow band filters and could be extended for wideband filters. Yang et al., [192] presents a new structural design of sharp transition FIR filter using FRM method using several simple sub filters achieving a significant saving of 20% in arithmetic hardware. Henzel et al., [193] describes an FIR filter design based on the desired H (ω) and the iteratively reweighted Chebyshev error minimization. It is suitable for a high filter order. Alkhairy et al., [194] presents in detail the design of an optimal FIR filters based on the Chebyshev approximation. The algorithm converges and requires 0 (M^2) computations per iteration, where M is the filter length.

3.7 Proposed Methodology: Linear phase sharp transition FIR filters

In this section, we have proposed a simple design of linear phase sharp transition FIR filters for lower orders with arbitrary passband and not necessarily an equiripple filter. The designs are categorized into three models namely - Model I, a composite band pass filter comprised of individual high pass and low pass filter designs, Model II is an integrated band pass filter and Model III consisting of the improvised version of the band pass filter with a proposed slope matching technique.

To evaluate each of the filter designs we first apply the single lead non-invasive aECG signal to the LPST FIR band pass filter using the designated fiduciary edges with a sharp transition width. Later in chapter 4, an FQRS detector based on Pan Tomkins QRS detector algorithm [195] detects the R-peaks to compute FHR for a single fetus. This method is also extended to obtain simultaneously the MHR of the adult mother [196]. In all processing we are not unduly concerned with any distortion that can occur at the output of the filter (not being optimum). It is sufficient to identify the QRS complex precisely. The detection of the FQRS is evaluated using each of the filter designs in chapter 4. Our proposed technique eliminates the need for a centre frequency nor the fixed passband width as it is used in [184]. Our design allows the user to set the cut off frequencies for a narrow pass band width for any filter order. It also incorporates a very linear sharp transition width while reducing the effects due to Gibb's phenomenon thereby reducing the passband ripple of the filter [171]. To study the merits of our filter design, the magnitude response of our proposed filter design was compared with the PM algorithm for a range of filter orders. These filters have many applications in the speech and biomedical signal processing research. Our technique being single channel lead makes it very convenient and comfortable for a maternal home care for long term monitoring.

3.7.1 Maternal and fetal frequency spectrum

Depending on the gestation age the FHR changes. After four weeks of pregnancy the FHR is around 70 bpm [197]. It rises to 175 bpm by the end of the first trimester. The FHR thereafter decreases to around 110 – 160 bpm at the average childbirth (around 42 weeks) [198].

To obtain the maternal QRS (MQRS) and FQRS frequency spectrum, a literature survey was compiled. The recorded values for the following parameters, namely, maternal QRS amplitude ($MQRS_A$), fetal QRS amplitude ($FQRS_A$), maternal QRS width ($MQRS_W$), fetal QRS width ($FQRS_W$), MQRS frequency bandwidth ($MQRS_{BW}$) and FQRS frequency bandwidth ($FQRS_{BW}$) are as shown in Figure 3.3. However just knowing the QRS width does not tell us the frequency spectrum of that ECG signal.

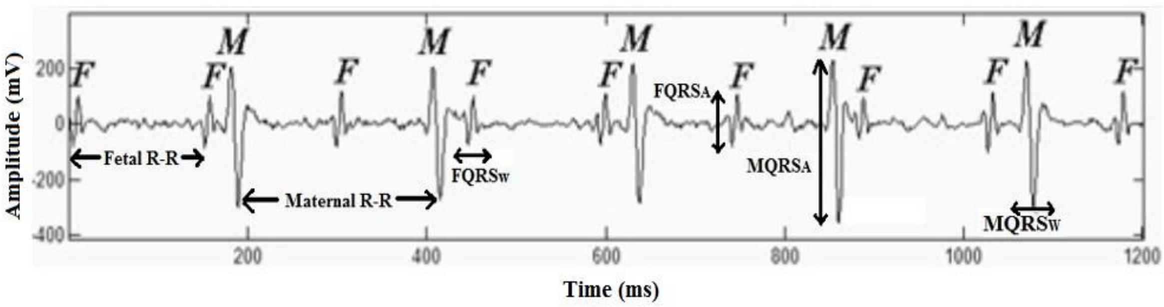

Figure 3.3: Bandwidth and amplitude of maternal- fetal ECG signals [35].

Table 3.3 and Table 3.4 summarize the maternal and fetal parameters in time and frequency domain, respectively. Maternal beats per minute (bpm) normally ranges from 50 to 210 bpm with an average of 80 or 89 bpm [75, 166]. While the FECG bandwidth ranges from 0.05 – 100 Hz [8] , the fetal beats per minute are recorded by various authors such as 60-240 bpm [75] , 120 – 160 bpm [166] and 110 – 160 bpm [199] where mostly all have taken the average value as 140 bpm.

Table 3.3: Maternal and Fetal parameters: QRS amplitude, QRS width and QRS frequency bandwidth.

Time domain			
$MQRS_A$	**$FQRS_A$**	**$MQRS_W$**	**$FQRS_W$**
100 - 150 μv [8]	60 μv [8]	120 ms [166]	80 ms [166]
150 μv [17]	30 μv [17]	100 ms [17]	50 ms [17], 53 ms [200]
300 μv [201]	10-20 μv [201]	100 ms [75]	3- 25ms [75]

Table 3.4: Maternal and Fetal parameters: QRS frequency bandwidth.

Frequency domain	
MQRS bandwidth ($MQRS_{BW}$)	**FQRS bandwidth ($FQRS_{BW}$)**
18 – 35 Hz [166]	27-53 Hz [166]
10 - 40 Hz [201], 10 - 25Hz [202], 10 – 30 Hz [75]	Starts at 20 Hz [201]
5 – 15 Hz [195] , 2 - 20 Hz [203] 1-30 Hz [205]	15 – 40 Hz [204] 20 – 60 Hz [75]

To compare the MQRS and FQRS band pass frequencies for the maternal thoracic and fetal scalp ECG signals, we marked the Q-R-S fiducial edges for MECG and FECG of the Physionet databases. The Fast Fourier Transform (FFT) was obtained for the above records and average frequency range for the records is shown below:

a) Maternal and fetal QRS band pass frequency spectrum from the two Physionet databases [65] is: $MQRS_{BW}$ ~ (10 – 34 Hz) and $FQRS_{BW}$ ~ (20 – 56 Hz). We estimated the frequency range for the $MQRS_{BW}$ to be 18 – 32 Hz.

b) Our proposal for the maternal and fetal QRS band pass frequencies: From the above literature, we estimated the maternal beats per minute range to be 70 – 100 BPM (1.166_{min} – 1.666_{max} bps) and the fetal beats per minute range to be 110 – 140 BPM (1.833_{min} – 2.333_{max} bps).

$$\text{Minimum frequency ratio}=\left(\frac{\text{fetal}_{\text{bps}}}{\text{maternal}_{\text{bps}}}\right)_{\min}=\frac{1.833}{1.166}=1.572$$

$$\text{Maximum frequency ratio}=\left(\frac{\text{fetal}_{\text{bps}}}{\text{maternal}_{\text{bps}}}\right)_{\max}=\frac{2.333}{1.666}=1.400$$

$$\text{Average frequency ratio} = \left(\frac{1.572 + 1.4}{2}\right) = 1.486$$

We can obtain fetal QRS lower fiduciary ($FQRS_{\text{Lower fiduciary edge}}$) and Upper fiduciary ($FQRS_{\text{Upper fiduciary edge}}$) frequencies from the average frequency ratio and the maternal frequency range.

$FQRS_{\text{Lower fiduciary edge}} = MQRS_{\text{Lower fiduciary edge}}$ x Average frequency ratio = 18 x 1.486 ~ 27 Hz

$FQRS_{\text{Upper fiduciary edge}} = MQRS_{\text{Upper fiduciary edge}}$ x Average frequency ratio = 32 x 1.486 ~ 48 Hz

We can conclude that, we can design an LPST high pass FIR filter with a cut-off of 27Hz which is the lower fiduciary edge of the fetal spectrum that will remove all the artifacts, low frequency noise including baseline wander frequencies. This is followed by a low pass FIR filter with a cut-off of 48Hz which is the upper fiduciary edge of the spectrum of FECG. This cut off frequency will remove the PLI frequency at 50Hz and the PLI harmonics and other high frequency noise. To effectively extract the required fetal information from the aECG following, LPST FIR filters were designed.

3.8 Design of composite LPST FIR BPF Model I

3.8.1 Design and model for LPST FIR high pass filter

In this section, the design of the high pass with a sharp transition and a linear phase FIR filter is presented. For the proposed high pass filter model, the three regions of the filter response H (ω) are modelled using trigonometric functions of frequency as shown in Figure 3.4. (See Annexure D1 for more details).

$$\left.\begin{array}{ll}\text{Region 1 (stopband)}: H(\omega) = \delta_s\left[1 - \cos(k_{sh}\,\omega)\right] & 0 \le \omega \le \omega_{sh} \\ \text{Region 2 (transition)}: H(\omega) = \delta_s + (1-\delta_p-\delta_s)\sin\left[k_{th}(\omega-\omega_{sh})\right] & \omega_{sh} \le \omega \le \omega_{ch} \\ \text{Region 3 (passband)}: H(\omega) = (1-\delta_p) + \delta_p\sin\left[k_{ph}(\omega-\omega_{ch})\right] & \omega_{ch} \le \omega \le \pi\end{array}\right\} . \quad (3.22)$$

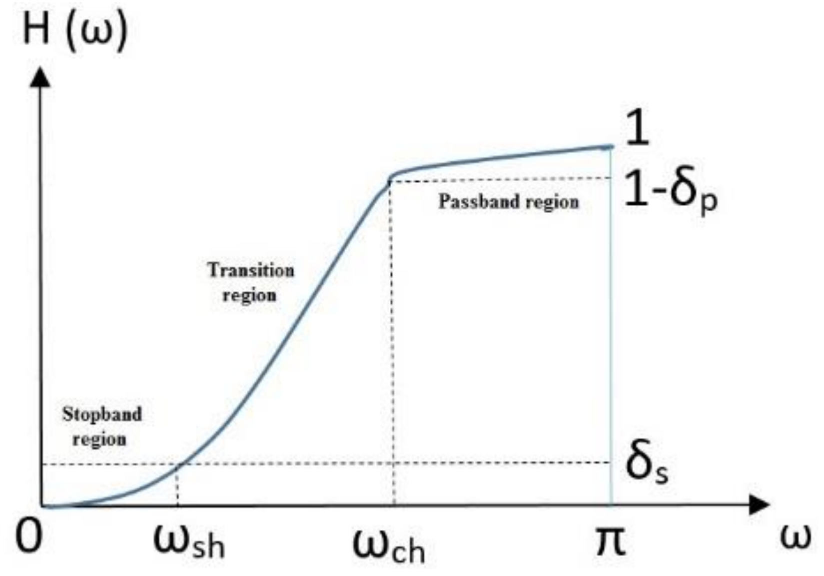

Figure 3.4: LPST FIR HPF Model I magnitude response H (ω) showing the three regions

Using the Eq. (3.22), the filter design parameters k_{sh} , k_{th} and k_{ph} for the three regions of the high pass filter are evaluated and listed in Eq. (3.23).

$$\left.\begin{aligned} k_{sh} &= \frac{\pi}{2\omega_{sh}} \\ k_{th} &= \frac{\pi}{2\,(\omega_{ch} - \omega_{sh})} \\ k_{ph} &= \frac{\pi}{2(\pi - \omega_{ch})} \end{aligned}\right\} \tag{3.23}$$

where, ω_{sh} is the stopband edge frequency while ω_{ch} is the cut off frequency in the passband. δ_s and δ_p are the stopband attenuation and passband ripple, respectively.

3.8.2 Expressions for the impulse response coefficients for a LPST FIR HPF

The impulse response coefficients h(n) for the high pass FIR filter are obtained by computing the weighted integrals of the magnitude response over the three regions shown in the filter model magnitude response in Figure 3.4. (See Annexure D1.1 for more details).

$$h(n) = \frac{1}{\pi}\left[\int_0^{\pi} H(\omega)\ \sin(k\omega)\ \ d\omega\right] \tag{3.24}$$

$$h(n) = \frac{1}{\pi}\left\{\int_0^{\omega_{sh}} H(\omega)\ \sin(k\omega)\ \partial\omega\ + \int_{\omega_{sh}}^{\omega_{ch}} H(\omega)\ \sin(k\omega)\ \partial\omega\ + \int_{\omega_{ch}}^{\pi} H(\omega)\ \sin(k\omega)\ \partial\omega\right\} \tag{3.25}$$

The Eq. (3.25) is evaluated to obtain the expression for the high pass filter model impulse response h (n) given by Eq. (3.26).

$$\begin{aligned}
h(n) = &\left\{ \left(\frac{\delta_s}{k\pi}\right)(1 - \cos(k\omega_{sh})) + \left(\frac{\delta_s}{2\pi}\right)\left[\frac{\cos((k + k_{sh})\,\omega_{sh}) - 1}{(k + k_{sh})} + \frac{\cos((k - k_{sh})\,\omega_{sh}) - 1}{(k - k_{sh})}\right]\right\} \\
&+ \left\{ \left(\frac{\delta_s}{k\pi}\right)(\cos(k\omega_{sh}) - \cos(k\omega_{ch}))\ + \left(\frac{1 - \delta_p - \delta_s}{2\pi}\right)\right. \\
&\left.\left[\frac{\sin((k_{th} - k)\,\omega_{ch} - k_{th}\,\omega_{sh}) + \sin(k\omega_{sh})}{(k_{th} - k_{sh})} + \frac{\sin(k\omega_{sh}) - \sin((k_{th} + k)\,\omega_{ch} - k_{th}\,\omega_{sh})}{(k_{th} + k_{sh})}\right]\right\} \\
&+ \left\{ \left(\frac{1 - \delta_s}{k\pi}\right)(\cos(k\omega_{ch}) - \cos(k\pi)) + \left(\frac{\delta_p}{2\pi}\right)\right. \\
&\left.\left[\frac{\sin((k_{ph} - k)\,\pi - k_{ph}\,\omega_{ch}) + \sin(k\omega_{ch})}{(k_{ph} - k)} + \frac{\sin(k\omega_{ch}) - \sin((k_{ph} + k)\,\pi - k_{ph}\,\omega_{ch})}{(k_{ph} + k)}\right]\right\}
\end{aligned} \tag{3.26}$$

3.8.3 Design and model for LPST FIR low pass filter

As before, the design of the LPST low pass FIR filter starts with the three regions of the filter response modelled using trigonometric functions of frequency shown in Figure 3.5. (See Annexure D2 for more details).

$$\left.\begin{array}{lll}
\text{Region 1 (passband)}: & H(\omega) = (1 - \delta_p) + \delta_p \cos(k_{pl}\ \omega) & 0 \le \omega \le \omega_{cl} \\
\text{Region 2 (transition)}: & H(\omega) = \delta_s + (1 - \delta_p - \delta_s)\ \cos\left[k_{tl}\ (\omega - \omega_{cl})\right] & \omega_{cl} \le \omega \le \omega_{sl} \\
\text{Region 3 (stopband)}: & H(\omega) = \delta_s - \delta_s \sin\left[k_{sl}\ (\omega - \omega_{sl})\right] & \omega_{sl} \le \omega \le \pi
\end{array}\right\}. \tag{3.27}$$

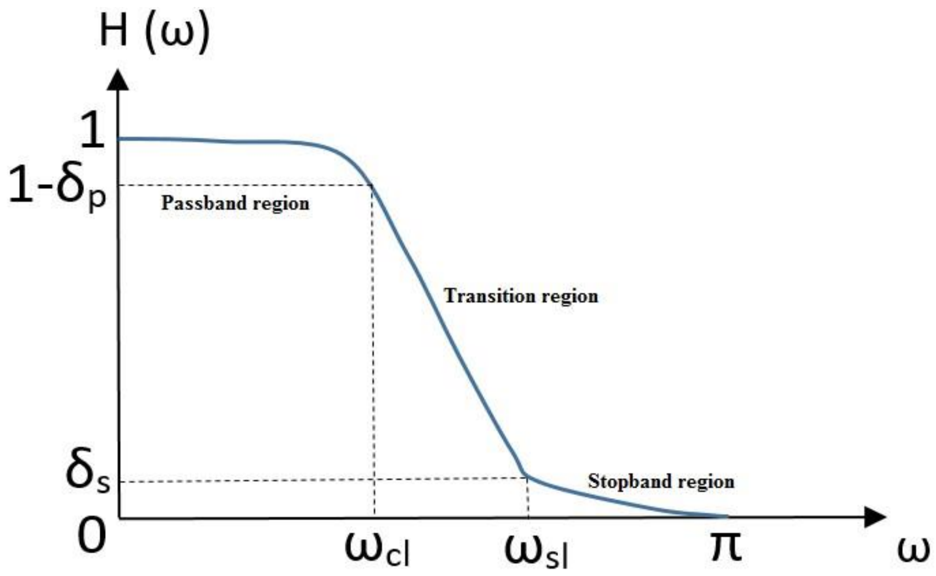

Figure 3.5: LPST FIR LPF Model I magnitude response H (ω) showing the three regions

Using the Eq. (3.27), the filter design parameters k_{pl}, k_{tl} and k_{sl} for the three regions of the low pass filter are evaluated and listed in Eq. (3.28), where, ω_{sl} is the stopband edge frequency while ω_{cl} is the cut off frequency in the passband.

$$\left.\begin{aligned} k_{pl} &= \frac{\pi}{2\omega_{cl}} \\ k_{tl} &= \frac{\pi}{2\,(\omega_{sl} - \omega_{cl})} \\ k_{sl} &= \frac{\pi}{2(\pi - \omega_{sl})} \end{aligned}\right\} \qquad (3.28)$$

3.8.4 Expressions for impulse response coefficients for the LPST FIR LPF

Proceeding as in the development of Eq. (3.26), the impulse response coefficients h (n) for the low pass FIR filter is obtained in Eq. (3.29). (See Annexure D2.1 for more details).

$$h(n) = \left\{\left(\frac{1}{k\pi}\right)\left[(1-\delta_p-\delta_s)\ \sin(\mathrm{k}\,\omega_{cl})+\delta_s\ \sin(\mathrm{k}\,\pi)\right]\right\}$$
$$+\left\{\left(\frac{\delta_p}{\pi(k_{pl}{}^2-k^2)}\right)\left[k_{pl}\sin(k_{pl}\omega_{cl})\cos(k\omega_{cl})-k\cos(k_{pl}\omega_{cl})\sin(k\omega_{cl})\right]\right\}$$
$$+\left\{\left(\frac{(1-\delta_p-\delta_s)}{\pi(k_{tl}{}^2-k^2)}\right)\left[k\sin(k\omega_{cl})+k_{tl}\sin(k_{tl}(\omega_{sl}-\omega_{cl}))\cos(k\omega_{sl})-k\cos(k_{tl}(\omega_{sl}-\omega_{cl}))\sin(k\omega_{sl})\right]\right\}$$
$$+\left\{\left(\frac{\delta_s}{\pi(k_{sl}{}^2-k^2)}\right)\left[k_{sl}\cos(k_{sl}(\pi-\omega_{sl}))\cos(k\pi)+k\sin(k_{sl}(\pi-\omega_{sl}))\sin(k\pi)-k_{sl}\cos(k\omega_{sl})\right]\right\}, \quad (3.29)$$

where $k \neq (k_{tl}, k_{pl}$ *and* $k_{sl})$.

3.8.5 Expression for the frequency response of the composite LPST FIR filter Model I

Let h (n) be the impulse response coefficients of an N point LPST filter where, $0 \leq n \leq N-1$ and where,

$$\mathrm{k} = \left[\left(\frac{\mathrm{N-1}}{2}\right)-\mathrm{n}\right] \text{ and } \mathrm{n} = 0,1,2,..,\left(\frac{\mathrm{N-3}}{2}\right) \text{ for N Odd} \quad (3.30)$$

and

$$\mathrm{k} = \left[\left(\frac{\mathrm{N-1}}{2}\right)-\mathrm{n}\right] \text{ and } \mathrm{n} = 0,1,2,..,\left(\frac{\mathrm{N}}{2}-1\right) \text{ for N Even} \quad (3.31)$$

From Table 3.1, we selected the appropriate type of impulse response for the high pass and low pass linear FIR filters listed below.

Type 2: Symmetric Even: Symmetric Impulse response, h *(n) = h (N-1-n)* for N Even.

$$H_r(\omega) = 2\sum_{n=0}^{\left(\frac{N}{2}\right)-1} h(n)\ \cos\ \left(\omega\left(\frac{N-1}{2}-n\right)\right) \quad (3.32)$$

This filter design is not suitable for high pass filters as the H (0) gives a maximum value, while H (π) = 0. Hence the filter design is most suitable for low pass filters.

Type 4: Anti Symmetric Even: Anti Symmetric Impulse response, *h (n) = - h (N-1-n)* for N Even.

$$H_r(\omega) = 2 \sum_{n=0}^{\left(\frac{N}{2}\right)-1} h(n) \sin\left(\omega\left(\frac{N-1}{2} - n\right)\right) \tag{3.33}$$

This filter design has H (0) = 0 while H (π) gives out a maximum value. The condition is most appropriate for high pass filters only and not for low pass filters. The LPST FIR filters used in tandem were high pass filters using Type 4 from Eq. 3.33 while the low pass filters used Type 2 from Eq. 3.32. As per the literature review and the assumptions made for FQRS band frequencies the following fiduciary frequencies for the FIR filters were substituted. For HP filter: ω_{sh} = 27 Hz and ω_{ch} = 28Hz, while LP FIR filter: ω_{cl} = 48Hz and ω_{sl} = 49Hz.

3.8.6 Synthesis results of composite LPST FIR BPF Model I

The LPST high pass and low pass filters are designed for the desired filter specifications as shown in Table 3.5 and 3.6 respectively. The measurement of the magnitude response of these filters are also compared in Table 3.5 and 3.6 with the filter design specifications.

Table 3.5: LPST HPF specifications along with measured magnitude response values.

LPST filter (filter order (N) = 1000)	**Passband edge (ω_{ch}) rad/s**	**Stopband edge (ω_{sh}) rad/s**	**Transition bandwidth (ω_{ch} - ω_{sh}) rad/s**	**Max. passband loss (dB)**	**Min. stopband attenuation (dB)**
Design specifications	56 π	54π	2π	±0.873	40
Measured specifications	57.3π	52π	5.3π	+0.284 , -0.183	38

Table 3.6: LPST LPF specifications along with measured magnitude response values.

LPST filter (filter order (N) = 1000)	**Pass band edge (ω_{cl}) rad/s**	**Stop band edge (ω_{sl}) rad/s**	**Transition bandwidth (ω_{sl} - ω_{cl}) rad/s**	**Max. passband loss (dB)**	**Min. stopband attenuation (dB)**
Design specifications	96 π	98 π	2 π	± 0.873	40
Measured specifications	95.5π	99.86 π	4.36π	-0.132	37.16

Table 3.7: Variations of passband loss and stopband attenuation for HPF with various filter orders (N).

Filter order (N)	**200**	**500**	**1000**	**1500**	**2000**
Passband loss (dB)	0.534	0.164	0.284	0.044	0.076
Stopband attenuation (dB)	21.04	30.56	38	39.44	39.67

Table 3.8: Variations of passband loss and stopband attenuation for LPF with various filter orders (N).

Filter order (N)	**200**	**500**	**1000**	**1500**	**2000**
Passband loss (dB)	0.569	0.442	0.132	0.1277	0.1264
Stopband attenuation (dB)	25.59	32.46	37.16	38.6	39.5

3.8.7 Discussions for composite LPST FIR BPF Model I

Tables 3.7 and 3.8 depict the performance of the filter for various filter orders (N). There is a reduction of Gibb's phenomenon with these filter designs. For conventional FIR sharp transition filters, the peak passband ripple due to Gibb's phenomenon is about 18%. Using our proposed LPST high pass and low pass FIR filters, we observed from Tables 3.7 and 3.8 the following : i) The passband losses are quite low and ii) The ripple decreases for higher filter order. The sampling rate, N = 1000 is much higher than the Nyquist rate (approximately 200Hz) and is chosen to improve the quality of the extracted FECG.

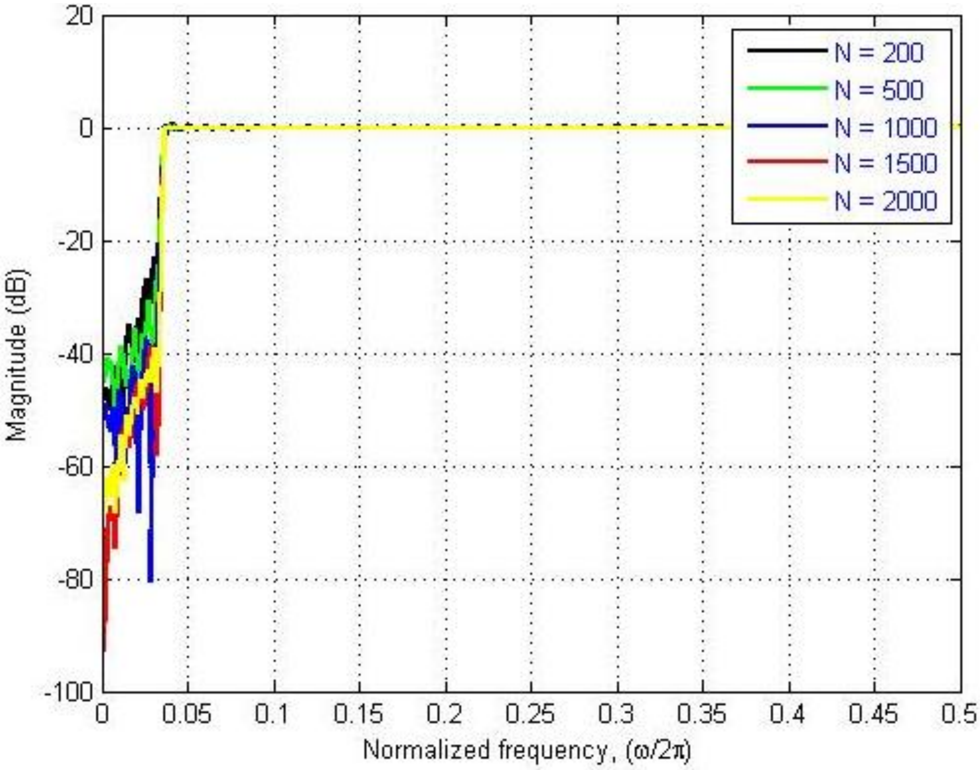

3.6 (a)

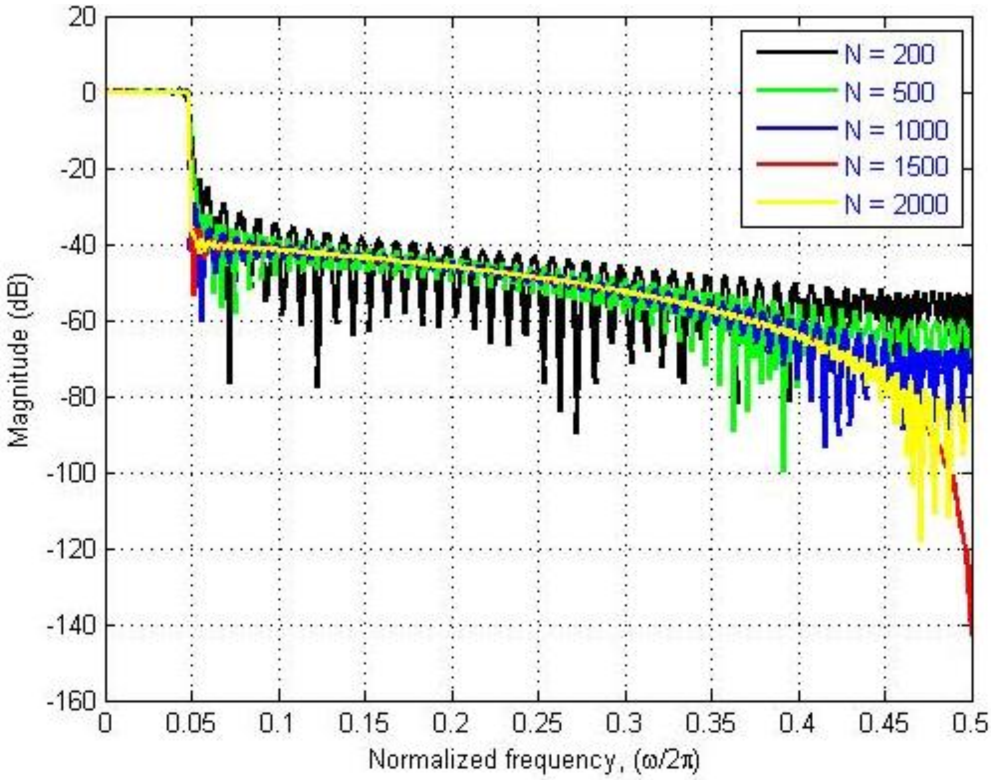

3.6 (b)

Figure 3.6: Magnitude response of LPST FIR filters for various filter orders (a) HPF (b) LPF.

Various filter orders (N = 200, 500, 1000, 1500, 2000) were also implemented to check the performance of the filters as shown in Figure 3.6a and 3.6b. These filters are unlike the classical filters in that they possess a narrow stopband and/or passband and also sharp transition regions. We designed both the FIR filters such that the magnitude H (ω) in the passband and stopband are not constant but inserted a small amount of ripple of 0.01 in the stopband as well as passband so that, Paley-Wiener criterion is not violated. Both the FIR filters were designed for sharp transition width (ω_s - ω_c) of 1Hz or 2π rad/s.The magnitude response, the linear plot and the magnified view of the pass band for both HPF and LPF are shown in Figures 3.7a to 3.7f respectively with the filter order N equal to 1000.

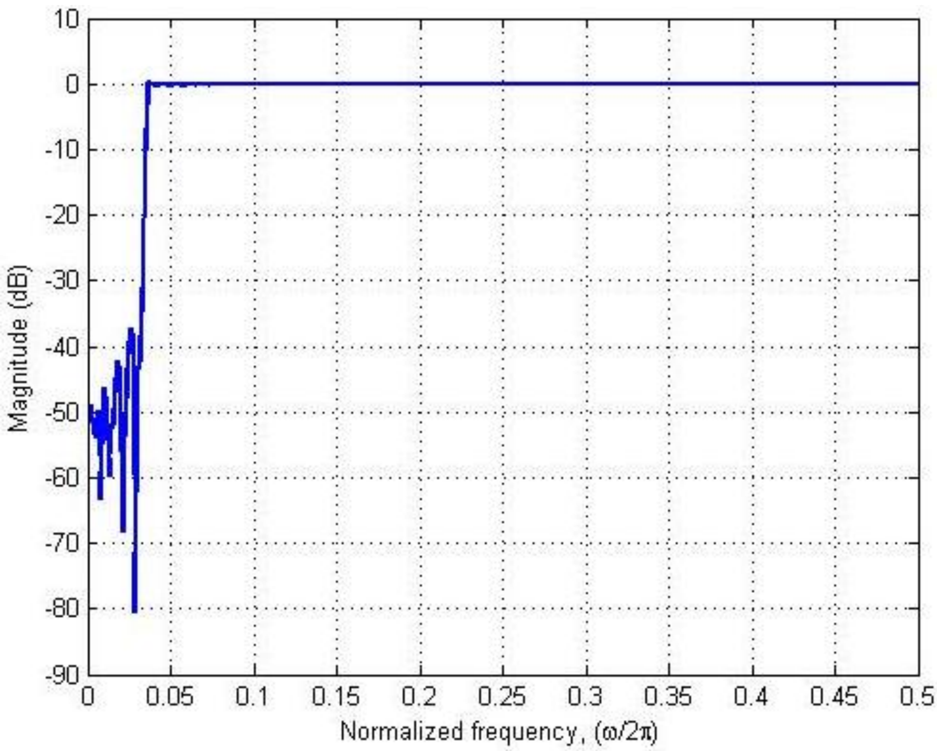

3.7 (a)

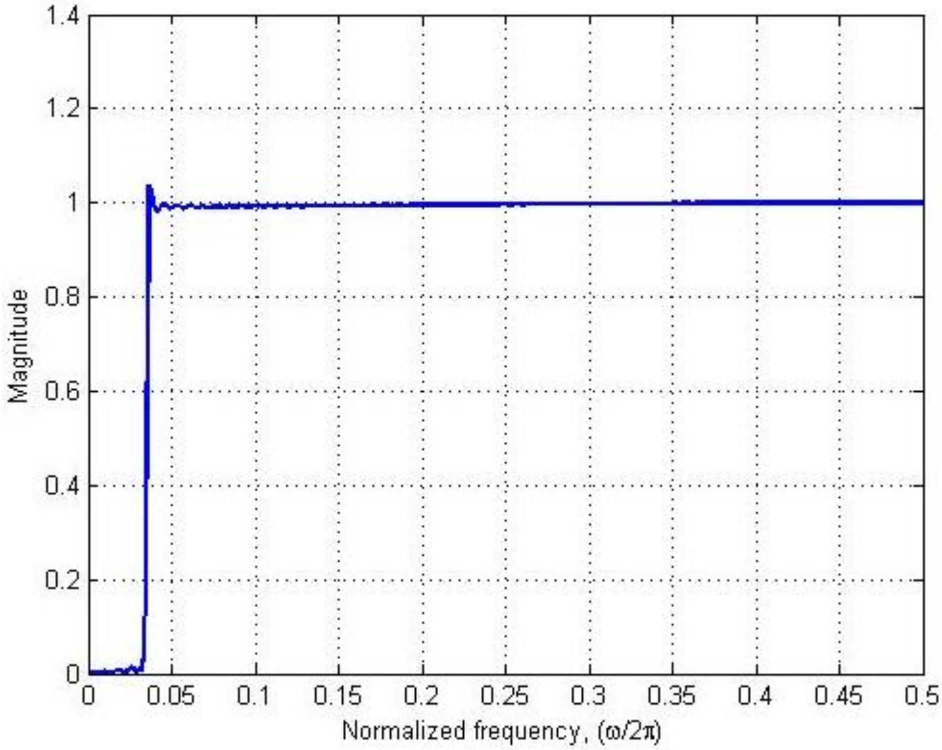
1.4
1.2
1
0.8
0.6
0.4
0.2
0
Magnitude
0
0.05
0.1
0.15
0.2
0.25
0.3
0.35
0.4
0.45
0.5
Normalized frequency, (ω/2π)

3.7 (b)

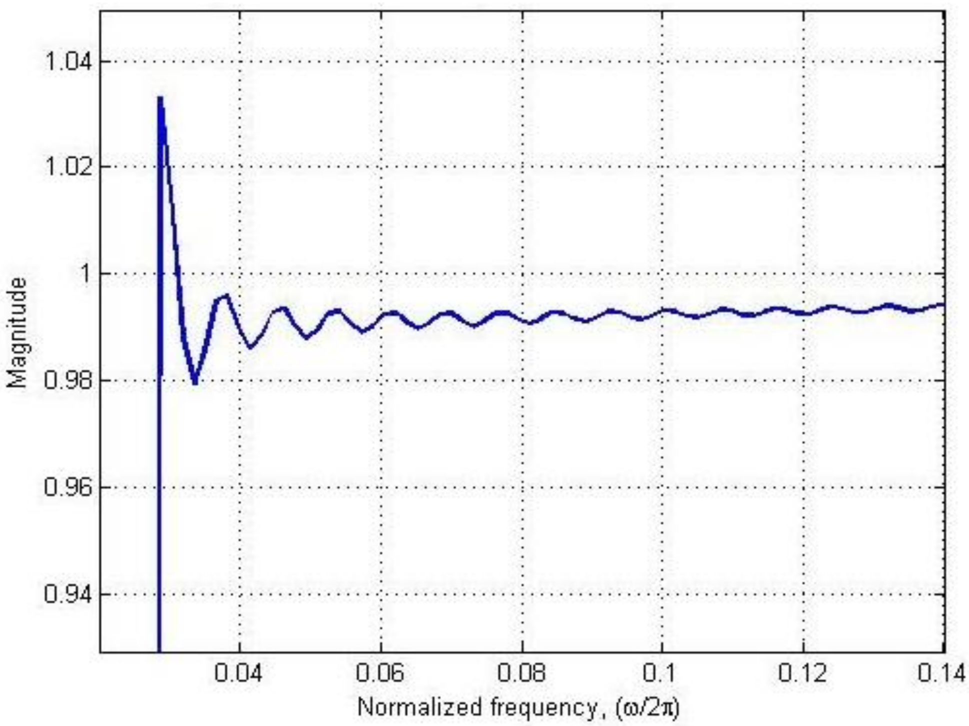
1.04
1.02
1
0.98
0.96
0.94
Magnitude
0.04
0.06
0.08
0.1
0.12
0.14
Normalized frequency, (ω/2π)

3.7 (c)

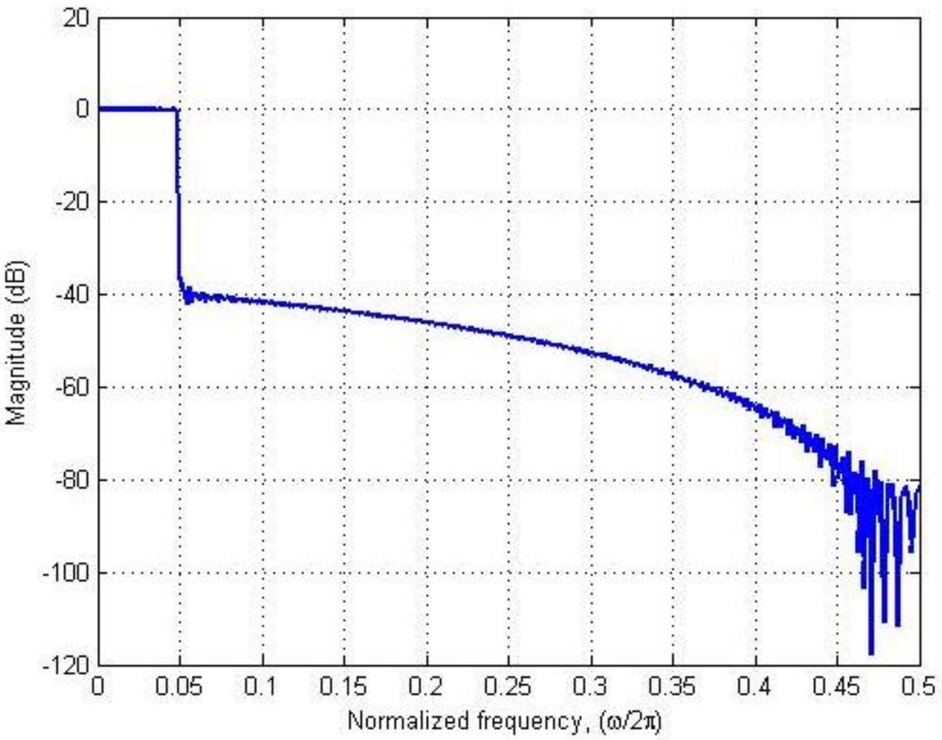
20
0
-20
-40
-60
-80
-100
-120
Magnitude (dB)
0
0.05
0.1
0.15
0.2
0.25
0.3
0.35
0.4
0.45
0.5
Normalized frequency, (ω/2π)

3.7 (d)

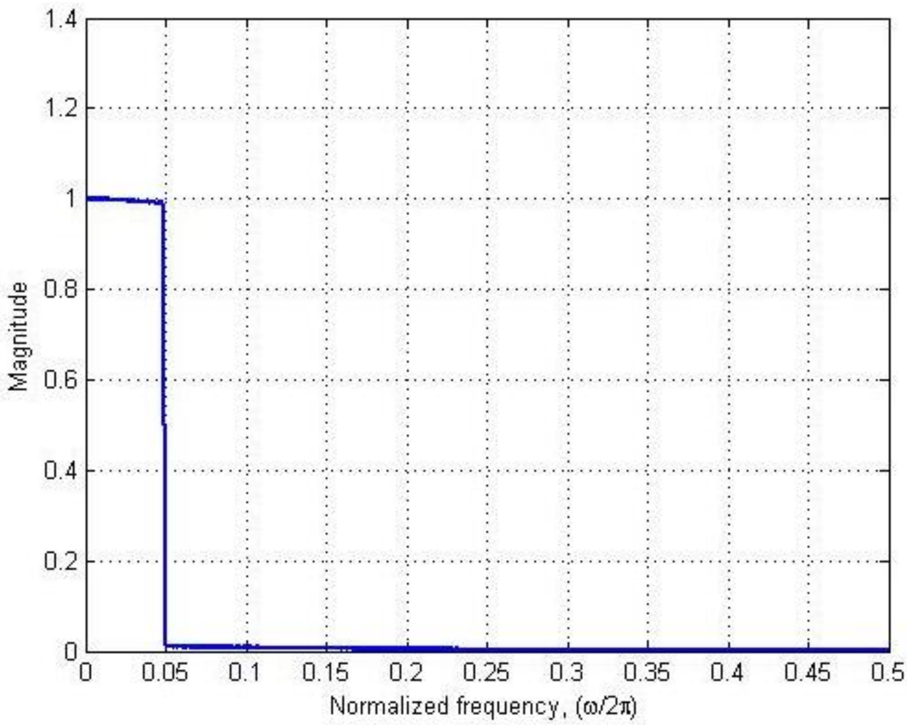
1.4
1.2
1
0.8
0.6
0.4
0.2
0
Magnitude
0
0.05
0.1
0.15
0.2
0.25
0.3
0.35
0.4
0.45
0.5
Normalized frequency, (ω/2π)

3.7 (e)

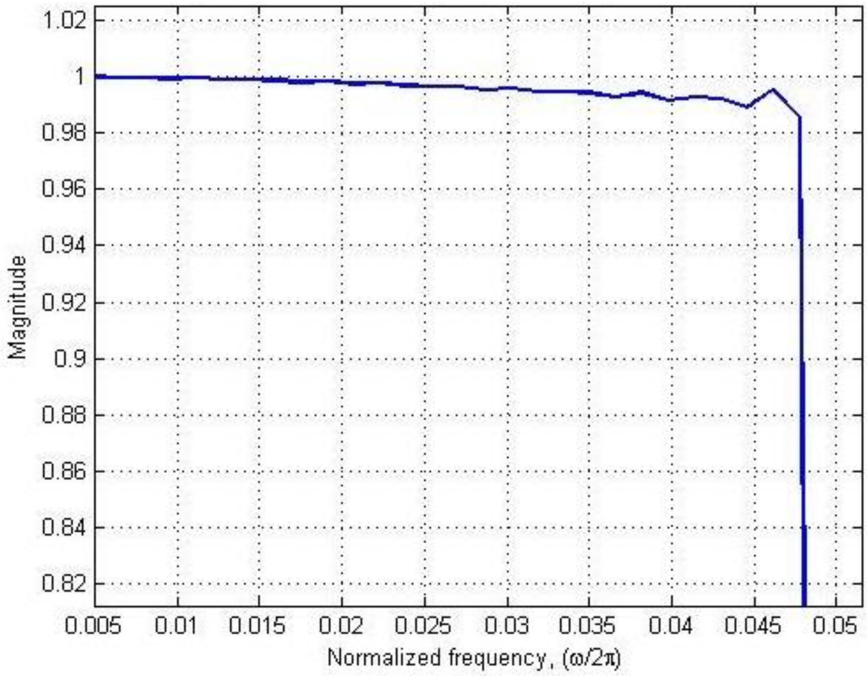

3.7 (f)

Figure 3.7: (a) Magnitude response of the proposed LPST FIR HPF with filter order N = 1000 (b) Linear plot (c) Magnified view of the passband (d) Magnitude response of the proposed LPST FIR LPF with filter order N = 1000 (e) Linear plot (f) Magnified view of the passband.

3.9 Design of LPST FIR BPF Model II

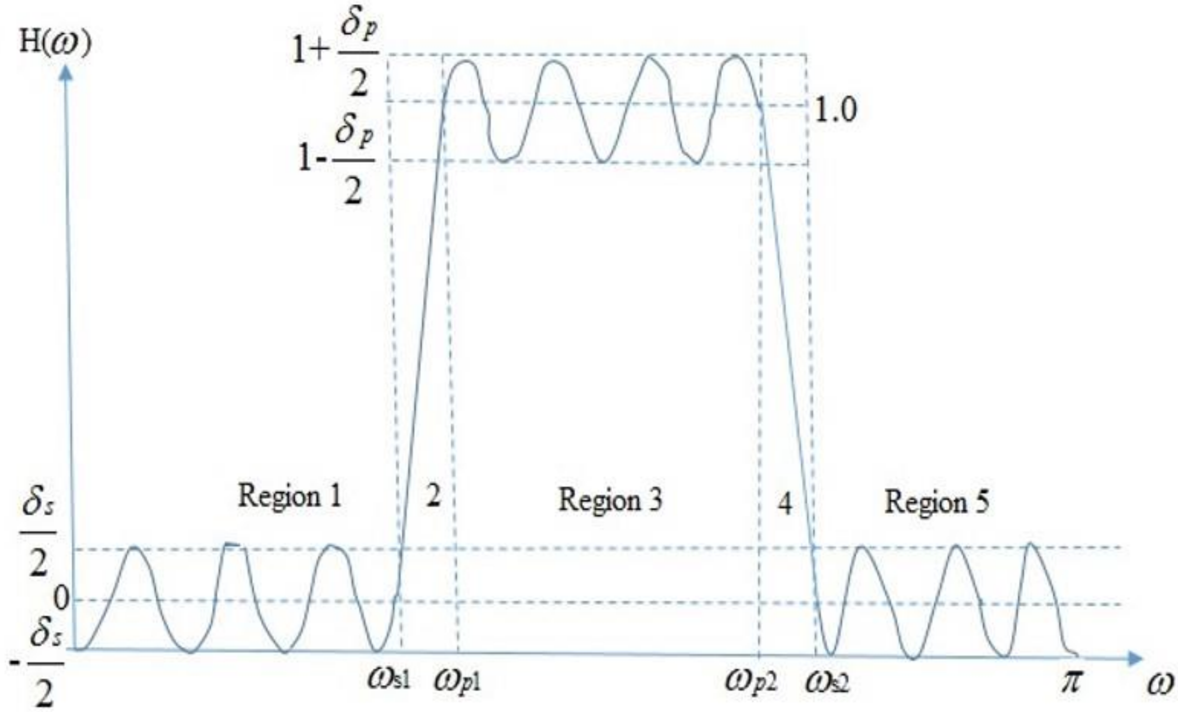

Figure 3.8: LPST FIR BPF Model II magnitude response H (ω) showing the five regions.

3.9.1 Design and model of LPST FIR BPF Model II

For the proposed LPST FIR BPF model II, the five regions of the filter response are modelled using trigonometric functions of frequency. The filter model magnitude response H (ω) is shown in Figure 3.8 (See Annexure D3 for more details).

The frequency response for the five regions are listed in Eq. (3.34).

$$\left.\begin{array}{ll}
\text{Region 1: } H(\omega) = -\dfrac{\delta_s}{2}\cos(k_1\,\omega) & 0 \le \omega \le \omega_{s1} \\
\text{Region 2: } H(\omega) = k_2\,(\omega-\omega_{s1}) & \omega_{s1} \le \omega \le \omega_{p1} \\
\text{Region 3: } H(\omega) = 1 + \dfrac{\delta_p}{2}\sin(k_3\,(\omega-\omega_{p1})) & \omega_{p1} \le \omega \le \omega_{p2} \\
\text{Region 4: } H(\omega) = 1 - k_4\,(\omega-\omega_{p2}) & \omega_{p2} \le \omega \le \omega_{s_2} \\
\text{Region 5: } H(\omega) = -\dfrac{\delta_s}{2}\sin(k_5\,(\omega-\omega_{s2})) & \omega_{s2} \le \omega \le \pi
\end{array}\right\} . \qquad (3.34)$$

Using Eq. (3.34), the filter design parameters k_1, k_2, k_3, k_4 and k_5 for the five regions of the band pass filter are evaluated and listed in Eq. (3.35).

$$\left.\begin{array}{l}
k_1 = \dfrac{2\pi m_1 + \dfrac{\pi}{2}}{\omega_{s1}} \\
k_2 = \dfrac{1}{(\omega_{p1} - \omega_{s1})} \\
k_3 = \dfrac{(2\,m_3 + 1)\pi}{(\omega_{p2} - \omega_{p1})} \\
k_4 = \dfrac{1}{(\omega_{s2} - \omega_{p2})} \\
k_5 = \dfrac{2\pi m_5 + \dfrac{\pi}{2}}{(\pi - \omega_{s2})}
\end{array}\right\} \qquad (3.35)$$

where, ω_{s1} and ω_{s2} are the stopband edge frequencies while ω_{p1} and ω_{p2} are the passband edge frequencies. δ_s and δ_p are the stopband and passband ripple respectively, while m_1, m_3 and m_5 are integers.

3.9.2 Expression for impulse response coefficients for the LPST FIR BPF Model II

The impulse response coefficients h (n) for the band pass FIR filter is obtained in Eq. 3.36, based on the procedure outlined in section 3.7 (See Annexure D3.1 for more details).

$$
\begin{aligned}
h(n) = & \left\{ \left(\frac{\delta_s}{4\pi}\right) \left[\frac{\cos((k+k_1)\,\omega_{s1}) - 1}{(k+k_1)} + \frac{\cos((k-k_1)\,\omega_{s1}) - 1}{(k-k_1)} \right] \right\} \\
& + \left\{ \begin{array}{l} \left(\frac{k_2}{k\pi}\right) \left[(-\omega_{p1}) \cos(k\omega_{p1}) + (\omega_{s1}) \cos(k\omega_{s1}) \right] - \\ \left(\frac{k_2}{k^2\pi}\right) \left[\sin(k\omega_{p1}) - \sin(k\omega_{s1}) \right] + \left(\frac{k_2\omega_{s1}}{k\pi}\right) \left[\cos(k\omega_{p1}) - \cos(k\omega_{s1}) \right] \end{array} \right\} \\
& + \left\{ \begin{array}{l} \left(-\frac{1}{\pi}\right) \left[\frac{\cos(k\omega_{p2}) - \cos(k\omega_{p1})}{k} \right] + \left(\frac{\delta_p}{4\pi\,(k-k_3)}\right) \left[\sin\left[(k-k_3)\,\omega_{p2} + k_3\,\omega_{p1}\right] - \sin(k\omega_{p1}) \right] \\ + \left(\frac{-\delta_p}{4\pi\,(k+k_3)}\right) \left[\sin\left[(k+k_3)\,\omega_{p2} - k_3\,\omega_{p1}\right] - \sin(k\omega_{p1}) \right] \end{array} \right\} \\
& + \left\{ \begin{array}{l} \left(\frac{1}{k\pi}\right) \left[-\cos(k\omega_{s2}) + \cos(k\omega_{p2}) \right] + \left(\frac{k_4}{k\pi}\right) \left[(\omega_{s2}) \cos(k\omega_{s2}) - (\omega_{p2}) \cos(k\omega_{p2}) \right] \\ + \left(\frac{k_4}{k^2\pi}\right) \left[\sin(k\omega_{s2}) - \sin(k\omega_{p2}) \right] + \left(\frac{k_4\omega_{p2}}{k\pi}\right) \left[-\cos(k\omega_{s2}) + \cos(k\omega_{p2}) \right] \end{array} \right\} \\
& + \left\{ \left(\frac{-\delta_s}{4\pi}\right) \left[\left(\frac{\sin((k_5-k)\,\pi - k_5\omega_{s2}) + \sin(k\omega_{s2})}{(k_5-k)} \right) - \left(\frac{\sin((k_5+k)\,\pi - k_5\omega_{s2}) - \sin(k\omega_{s2})}{(k_5+k)} \right) \right] \right\}
\end{aligned}
\tag{3.36}
$$

where , $k = \left[\left(\frac{N-1}{2}\right) - n \right]$.

We can choose the effective pass band width ($\omega_{p2} \sim \omega_{p1}$) such that ($\omega_{s1} \sim \omega_{p1}$) = ($\omega_{s2} \sim \omega_{p2}$), is as small as possible for sharp transition of passband edge. Once ω_{p1}, ω_{p2}, ω_{s1} and ω_{s2} are chosen k_1, k_2, k_3, k_4 and k_5 are determined.

3.9.3 Expression for the frequency response of the LPST FIR BPF Model II

Let h (n) given by Eq. (3.36) be the impulse response coefficients of an N point linear phase FIR filter where, $0 \le n \le N\text{-}1$ and

$$k = \left[\left(\frac{N-1}{2}\right) - n \right] \; and \; n = 0,1,2,..........,\left(\frac{N-3}{2}\right) \quad for \;\; N \;\; Odd \tag{3.37}$$

and $$k = \left[\left(\frac{N-1}{2}\right) - n \right] \; and \; n = 0,1,2,..........,\left(\frac{N}{2} - 1\right) \quad for \; N \; Even. \tag{3.38}$$

In the case of anti-symmetric response with N Odd (Type 3) from Table 3.1, the frequency response of the band pass FIR filter is given by Eq. 3.39,

$$H_r(\omega) = 2\sum_{n=0}^{\frac{N-3}{2}} h(n)\ \sin\left(\omega\left(\frac{N-1}{2} - n\right)\right). \tag{3.39}$$

This response is most suitable for the proposed band pass filter as H (0) = 0 and H (π) = 0. If we refer to Eq. 3.37, k is an integer for N odd. Other constraints are as follows: (i) In Eq. 3.35, $k \neq k_1$, $k \neq k_3$ and $k \neq k_5$ and (ii) k_1, k_3 and k_5 should not be integers. However k_2 and k_4 do not have any constraints.

3.9.4 Synthesis results of LPST FIR BPF Model II

The LPST FIR BPF was implemented using Eq. 3.36. The following FQRS band pass fiduciary edge cut off frequencies (rad/s) were substituted as per Figure 3.8: $\omega_{s1} = 70\pi$, $\omega_{p1} = 72\pi$, $\omega_{p2} = 96\pi$ and $\omega_{s2} = 98\pi$. Also stop band and passband ripples are $\delta_s = \delta_p = 0.01$. Equal transition width at both ends were chosen for the pass band to be 2π rad/s or 1 Hz. The measurement of the magnitude response of the band pass filters are compared in Tables 3.9 and 3.10 along with the filter design specifications.

Table 3.9: LPST FIR BPF Model II specifications of passband and stopband edges along with measured magnitude response values (filter order N =1001).

Band pass LPST filter	**Stopband edge (ω_{s1}) rad/s**	**Passband edge (ω_{p1}) rad/s**	**Passband edge (ω_{p2}) rad/s**	**Stopband edge (ω_{s2}) rad/s**
Design specifications	70π	72π	96π	98π
Measured specifications	64.68π	73.22π	92.3π	100.08π

Table 3.10: LPST FIR BPF Model II specifications of transition bandwidth, passband ripple and stopband attenuation along with measured magnitude response values.

LPST filter (filter order (N) = 1001)	Transition bandwidth ($\omega_{p1} - \omega_{s1}$) rad/s	Transition bandwidth ($\omega_{s2} - \omega_{p2}$) rad/s	Max. passband loss (dB)	Min. stopband attenuation (dB)
Design specifications	2π	2π	±0.873	40
Measured specifications	8.54π	7.78π	+ 0.47, - 0.13	40

Table 3.11: Variations of passband loss and stopband attenuation for LPST BPF Model II with various filter orders (N).

Filter order (N)	201	501	1001	1501	2001	5001
Passband loss (dB)	1.5	±0.5	±0.13	±0.1	±0.04	±0.03
Stopband attenuation (dB)	23.5	35.8	40	43	46	46

3.9.5 Discussions of LPST FIR BPF Model II

We designed a LPST FIR BPF such that the magnitude H (ω) in the passband and stopband are not constant but inserted a small amount of ripple of 0.01 in the stopband as well as passband so that, Paley- Wiener criterion is not violated. The FIR filter was designed for sharp transition width (ω_s - ω_c) of 1Hz or 2π rad/s. Table 3.11 depicts the performance of the filter for various filter orders (N). There is a reduction of Gibb's phenomenon with these filter designs. In our proposed band pass LPST FIR filters, the passband losses are quite low as can be seen from Table 3.10. It can also be seen that the stopband attenuation surpasses the design specification at higher orders and the passband ripple decreases for higher filter order as seen from Table 3.11. The sampling rate, N = 1001 is much higher than the Nyquist rate (approximately 200Hz) and is chosen to improve the quality of the extracted FECG. Various filter orders (N = 201, 501, 1001, 1501, 2001 and 5001) were implemented to check the performance of the filters as shown in Figure 3.9d. These filters are unlike the classical filters in that they possess a narrow stopband and/or passband and also sharp transition regions. The magnitude response, the linear plot and the magnified view of the BPF are shown in Figures 3.9a to 3.9c, respectively with the filter order N equal to 1001. As seen from Figure 3.10, the average transition width approaches the design specifications at higher orders.

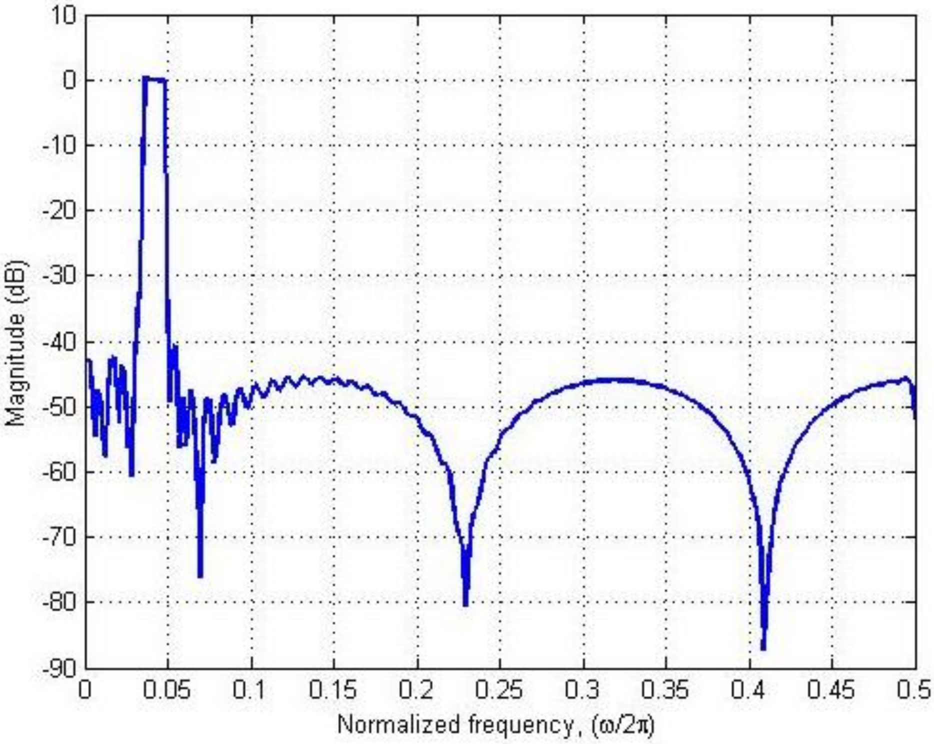

3.9 (a)

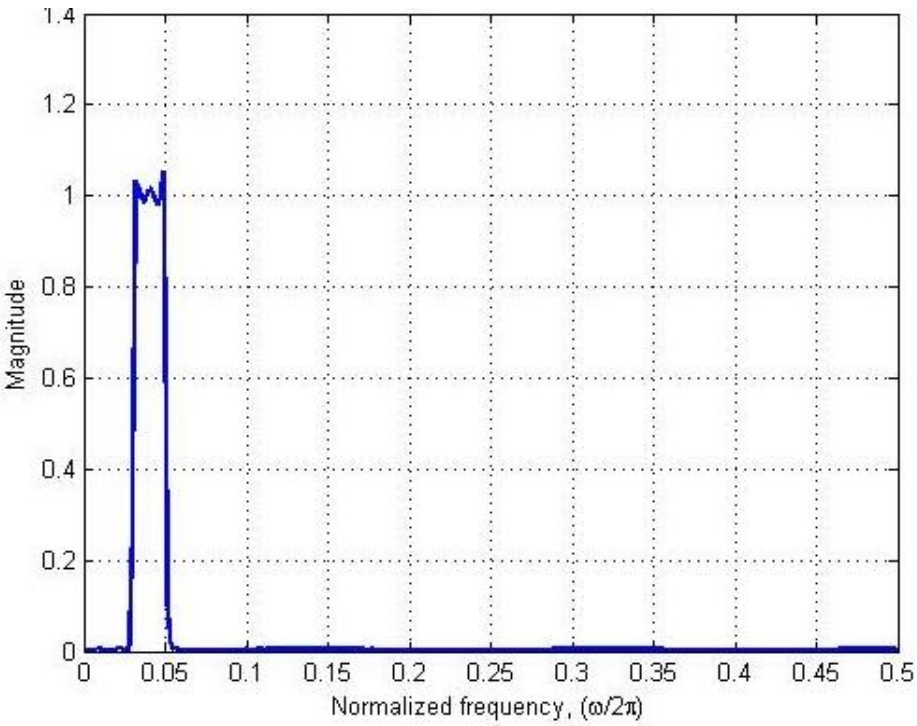

3.9 (b)

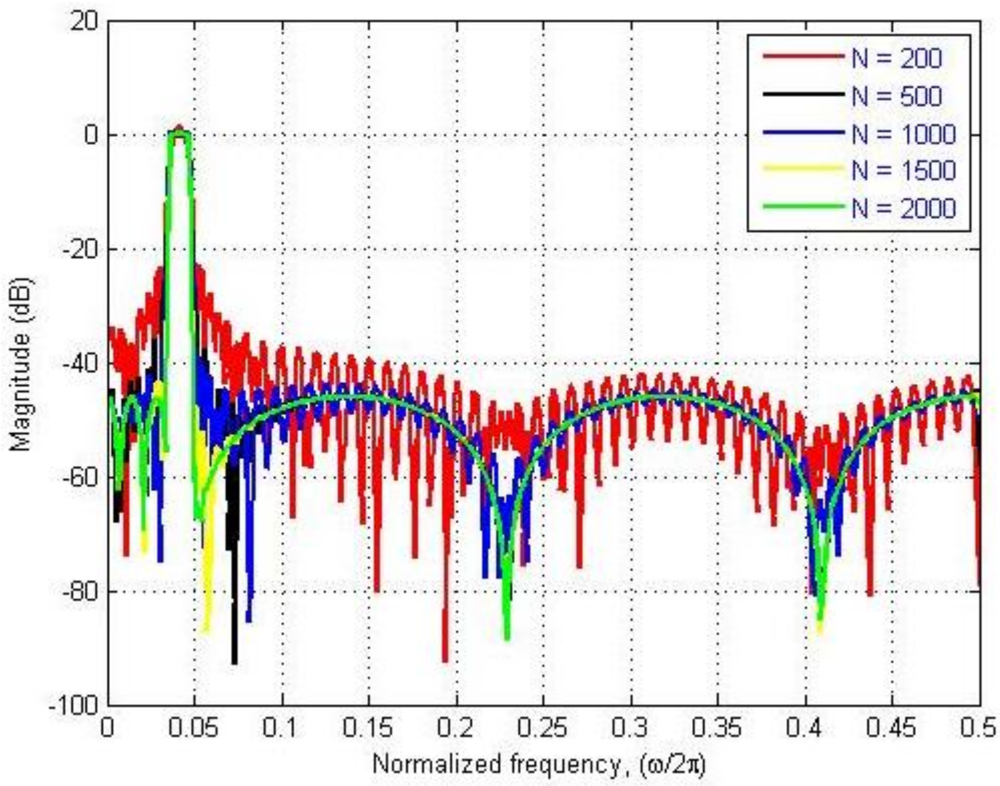

3.9 (c)

Figure 3.9: (a) Magnitude response of the proposed LPST FIR BPF Model II with filter order N = 1001 (b) Linear plot (c) Magnitude response of the LPST FIR BPF Model II for various filter order (N).

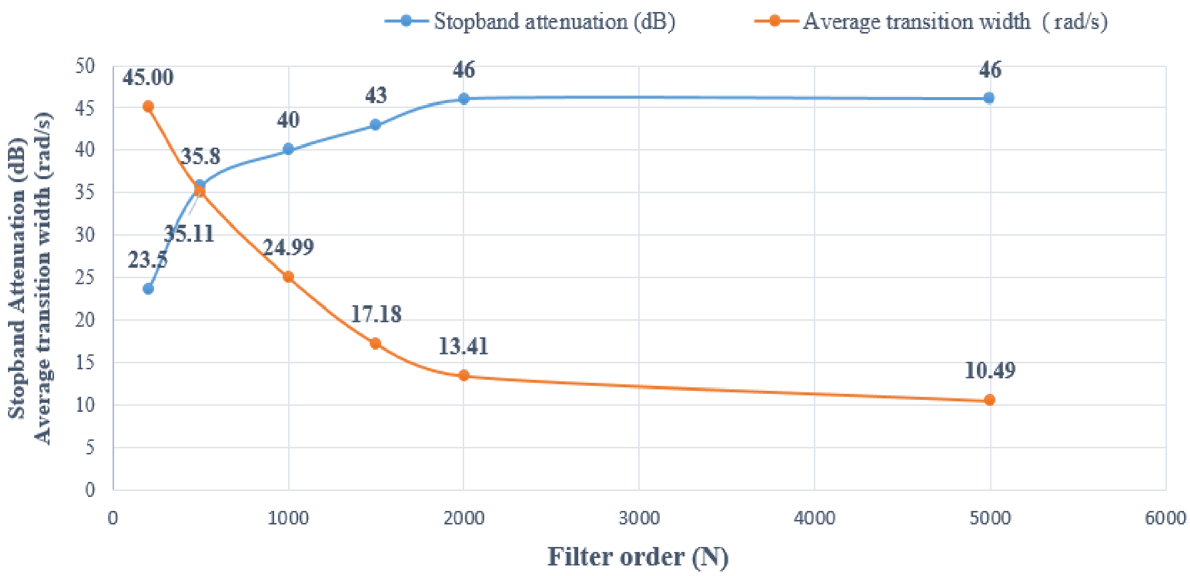

Figure 3.10: Average LPST FIR BPF Model II transition width (ω_s - ω_c) and stopband attenuation for various filter order.

3.10 Design of LPST FIR BPF Model II with Slope Matching Technique (Model III)

3.10.1 Introduction to Slope Matching Technique

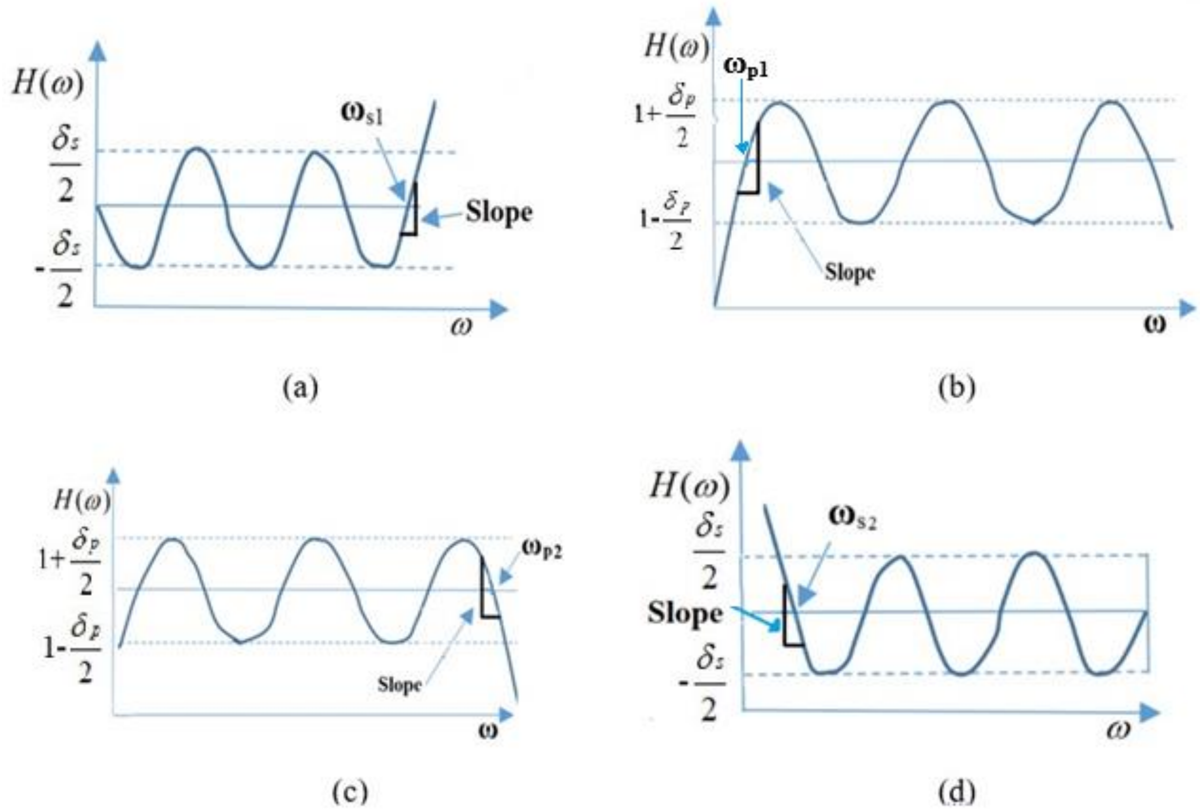

Figure 3.11: Illustrates the novel slope matching technique with the aid of the expanded views (*from Figure 3.8*) of the passband and stopbands for all four points of discontinuity with the slopes at their fiduciary edges. (a) Fiduciary edge at ω_{s1} (b) Fiduciary edge at ω_{p1} (c) Fiduciary edge at ω_{p2} (d) Fiduciary edge at ω_{s2}.

The filter response functions of a filter design are discontinuous at the passband edge which leads to ripples at the points of discontinuity. Normally the points of discontinuity for the band pass filter will be at four points, they are (a) at the end of the stopband region and start of the transition region (ω_{s1}) (b) at the end of transition region and start of the passband region (ω_{p1}) (c) at the end of the passband region and start of the transition region (ω_{p2}) (d) at the end of the transition region and start of the stopband region (ω_{s2}). In this model III, a slope matching technique is proposed wherein, the slopes of the magnitude response are equalized at these points of discontinuity or fiduciary edges of fetal frequency spectrum. Figure 3.11 illustrates the novel slope matching technique for all four points of discontinuity. The slopes are equalized at the following fiduciary edges: ω_{s1}, ω_{p1}, ω_{p2}, and ω_{s2} (slopes are the derivatives of H (ω) with reference to ω at each fiduciary edge). The slopes are equalized at these fiduciary edges with reference to Eq. (3.34) and (3.35) as shown in Figure 3.11. The proposed technique makes the function continuous at these points reducing the overshoots due to Gibb's phenomenon. The slope matching will have an impact on the peak ripple by reducing it at the points of discontinuity. Additionally, there is an improvement in the filter response wherein the passband loss is reduced and the stopband attenuation is increased.

3.10.2 Slope matching technique at five regions of the LPST FIR BPF Model II

In this section the design of the LPST FIR BPF with slope matching technique is presented. The BPF is modelled over the same five regions for Type 3. The parameters of the model are evaluated by equalizing the slopes of the pseudo-magnitude response function at ω_{s1}, ω_{p1}, ω_{p2}, and ω_{s2}. This allows the proposed function to be continuous at the extremes of the transition region thus reducing the effects due to Gibb's phenomenon.

3.10.2 (a) Slope at stopband region 1, $\omega = \omega_{s1}$ (see Figure 3.11a).

From Eq. (3.34) we have, $H(\omega) = -\frac{\delta_s}{2}\cos k_1\ \omega.$

Differentiating Eq. (3.34), we obtain $\left.\frac{d(H(\omega))}{d\omega}\right|_{\omega=\omega_{s1}} = \frac{\delta_s}{2}k_1[\sin k_1\ \omega_{s1}].$

From Eq. (3.35) we have, $\omega_{s1}k_1 = 2\pi \mathrm{m}1 + \frac{\pi}{2}$. Using this relation in the above we

obtain , $$\left.\frac{d(H(\omega))}{d\omega}\right|_{\omega=\omega s1} = k_1\frac{\delta_s}{2} \quad . \tag{3.40}$$

3.10.2 (b) Slope at transition region 2, $\omega = \omega_{s1}$ (see Figure 3.11a).

From Eq. (3.34) we get, $H(\omega) = k_2 \ (\omega - \omega_{s1})$. Differentiating at $\omega = \omega_{s1}$ we obtain,

$$\left.\frac{d(H(\omega))}{d\omega}\right|_{\omega = \omega s1} = k_2 \ . \tag{3.41}$$

Equating Eqs. (3.40) and (3.41) to equalise the slopes at ω_{s1} for slope matching we get ,

$$k_2 = k_1 \frac{\delta_s}{2} \ . \tag{3.42}$$

3.10.2 (c) Slope at transition region 2, $\omega = \omega_{p1}$ (see Figure 3.11b)

From Eq. (3.34) we get, $H(\omega) = k_2 \ (\omega - \omega_{s1})$. Differentiating at $\omega = \omega_{p1}$ we obtain,

$$\left.\frac{d(H(\omega))}{d\omega}\right|_{\omega = \omega p1} = k_2 \ . \tag{3.43}$$

3.10.2 (d) Slope at passband region 3, $\omega = \omega_{p1}$ (see Figure 3.11b)

From Eq. (3.34) we get, $H(\omega) = 1 + \frac{\delta_p}{2} \sin(k_3 \ (\omega - \omega_{p1}))$ **.** Differentiating at $\omega = \omega_{p1}$ we

obtain,
$$\left.\frac{d(H(\omega))}{d\omega}\right|_{\omega = \omega p1} = k_3 \frac{\delta_p}{2} \ . \tag{3.44}$$

Equating Eqs. (3.43) and (3.44) to equalise the slopes at ω_{p1} we get,

$$k_2 = k_3 \frac{\delta_p}{2} \ . \tag{3.45}$$

3.10.2 (e) Slope at passband region 3, $\omega = \omega_{p2}$ (see Figure 3.11c)

From Eq. (3.34) we get, $H(\omega) = 1 + \frac{\delta_p}{2} \ \sin(k_3 \ (\omega - \omega_{p1}))$ **.** Differentiating at $\omega = \omega_{p2}$

we obtain, $H(\omega) = \frac{\delta_p}{2} \ k_3 \cos \ (k_3 \ (\omega_{p2} - \omega_{p1}))$ .From Eq. (3.35) we have, $k_3 \ (\omega_{p2} - \omega_{p1}) = 2\pi m3 + \pi$. Using this relation in the above we

obtain ,
$$\left.\frac{d(H(\omega))}{d\omega}\right|_{\omega = \omega p2} = - \ k_3 \frac{\delta_p}{2} \ . \tag{3.46}$$

3.10.2 (f) Slope at transition region 4, $\omega = \omega_{p2}$ (see Figure 3.11c)

From Eq. (3.34) we get, $H(\omega) = 1 - k_4 (\omega - \omega_{p2})$. Differentiating at $\omega = \omega_{p2}$ we obtain,

$$\left. \frac{d(H(\omega))}{d\omega} \right|_{\omega = \omega p2} = - k_4 . \tag{3.47}$$

Equating Eqs. (3.46) and (3.47) to equalise the slopes at ω_{p2} we get,

$$k_4 = k_3 \frac{\delta_p}{2} . \tag{3.48}$$

3.10.2 (h) Slope at transition region 4, $\omega = \omega_{s2}$ (see Figure 3.11d)

From Eq. (3.34) we get, $H(\omega) = 1 - k_4 (\omega - \omega_{p2})$. Differentiating at $\omega = \omega_{s2}$ we obtain,

$$\left. \frac{d(H(\omega))}{d\omega} \right|_{\omega = \omega s2} = - k_4 \quad . \tag{3.49}$$

3.10.2 (i) Slope at stopband region 5, $\omega = \omega_{s2}$ (see Figure 3.11d)

From Eq. (3.34) we get, $H(\omega) = - \frac{\delta_s}{2} \sin(k_5 (\omega - \omega_{s2}))$. Differentiating at $\omega = \omega_{s2}$ we obtain,

$$\left. \frac{d(H(\omega))}{d\omega} \right|_{\omega = \omega s2} = - k_5 \frac{\delta_s}{2} . \tag{3.50}$$

Equating Eqs. (3.49) and (3.50) to equalise the slopes at ω_{p2} for slope matching we get,

$$k_4 = k_5 \frac{\delta_s}{2}$$

(3.51)From Eqs. (3.42), (3.45), (3.48) and (3.51), a new relationship between the band pass filter design parameters for equalisation slope matching technique is finally obtained in Eq. (3.52) as,

$$k_2 = k_3 \frac{\delta_p}{2} = k_4 = k_5 \frac{\delta_s}{2} = k_1 \frac{\delta_s}{2} . \tag{3.52}$$

Expression for frequency response of an LPST FIR BPF Model III

As before, let h (n) be the impulse response coefficients of an N point linear phase FIR filter where, $0 \le n \le N\text{-}1$ and

$$k = \left[\left(\frac{N-1}{2}\right) - n\right] \text{ and } n = 0,1,2,\ldots\ldots\ldots.,\left(\frac{N-3}{2}\right) \quad \text{for N Odd} \tag{3.53}$$

and $$k = \left[\left(\frac{N-1}{2}\right) - n\right] \text{ and } n = 0,1,2,\ldots\ldots\ldots.,\left(\frac{N}{2}-1\right) \quad \text{for N Even.} \tag{3.54}$$

The expression for the frequency response is identical to the one given by Eq. (3.39). Thus,

$$H_r(\omega) = 2\sum_{n=0}^{\frac{N-3}{2}} h(n)\ \sin\left(\omega\left(\frac{N-1}{2} - n\right)\right). \tag{3.55}$$

In the case of anti-symmetric response with N Odd as given in Eq. (3.55), the response is most suitable for the proposed band pass filter as H (0) = 0 and H (π) = 0. If we refer to Eq. (3.53), k is an integer for N odd. Other constraints are as follows: (i) $k \neq k_1$, $k \neq k_3$ and $k \neq k_5$ and (ii) k_1, k_3 and k_5 should not be integers. However k_2 and k_4 do not have any constraints.

3.11 Synthesis of FIR BPF Model II (LPST BPF) versus FIR BPF Model III (LPST BPF$_{slope}$)

The two LPST BPF Models II and III, with and without slope matching respectively are subjected to the following FQRS band pass fiduciary edge cut off frequencies (rad/sec) : ω_{s1} = 70π, ω_{p1} = 72π, ω_{p2} = 96π and ω_{s2} = 98π and the stop band (δ_s) and passband ripple (δ_p) were each equal to 0.01. Equal transition width at both ends were chosen for the pass band to be 2π rad/sec or 1 Hz. It is found that the filter model LPST BPF$_{slope}$ reduces the amount of discontinuity at the pass band edges and reduces Gibb's phenomenon. The experimental results closely matched the design values and yielded stopband attenuation to be 80 dB which surpassed the expected design value. Table 3.12 and Table 3.13 list filter specifications obtained for various filter orders (N). The magnitude response of the BPF with their magnified views of the passband and stopband with and without slope matching techniques are shown in Figures 3.12.The filter specifications obtained with and without slope matching are summarized in Figures 3.13 and Figure 3.14. It is seen that, there is a marginal improvement in the transition region width at both the fiduciary edges using slope matching technique; however, there is a substantial improvement in the stopband attenuation. The filter model proposed in this paper achieved a trade-off between the transition region width and Gibb's phenomenon. In addition, emphasis is laid upon a good passband i.e low passband attenuation and good stopband i.e large stopband attenuation. Thus a threefold compromise is needed for the satisfactory performance of the filter in all the five bands in addition to a trade-off between Gibb's phenomenon and sharpness of the transition of the filter. All the five regions of the response are formulated in terms of sinusoidal function to achieve the twin objectives of reducing Gibb's phenomenon and ease of evaluating the closed form expression for the impulse response coefficients.

The band pass filter model with the proposed slope equalization is similar to the basic model of LPST BPF but is refined further by applying the slope matching technique. This proposed technique avoids a discontinuity at the edges of the passband and stopbands reducing the effects of Gibb's phenomenon and thus further improving the filter performance. Table 3.14 displays the percentage change in the peak passband for the filter Models II and III. It is seen that the percentage change in the peak passband for Model II of 4.35% is improved to 1.5% using Model III. The peak passband in conventional FIR designs is about 18% which is reduced to around 1.5 % with the use of trigonometric functions in the proposed filter model III combined with slope equalization technique.

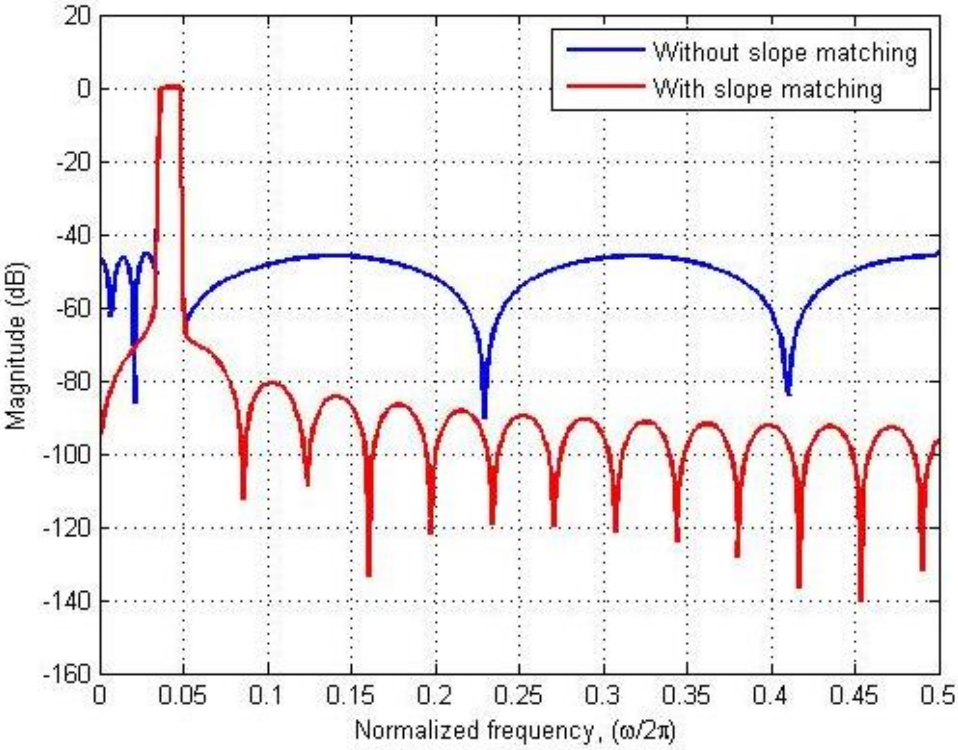
Without slope matching
With slope matching
Magnitude (dB)
Normalized frequency, (ω/2π)

3.12 (a)

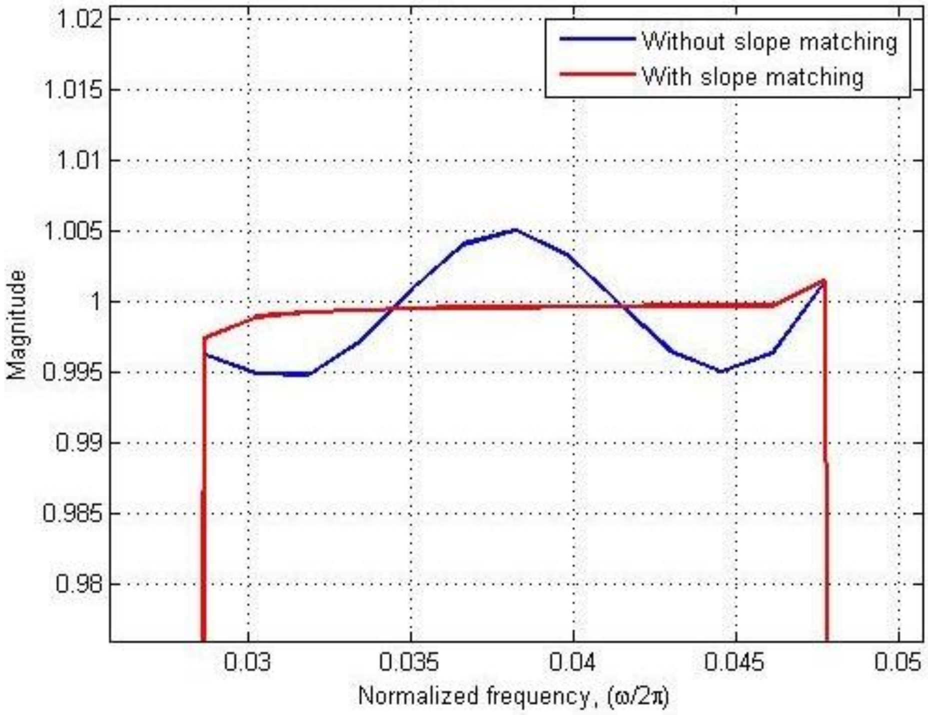
Without slope matching
With slope matching
Magnitude
Normalized frequency, (ω/2π)

3.12 (b)

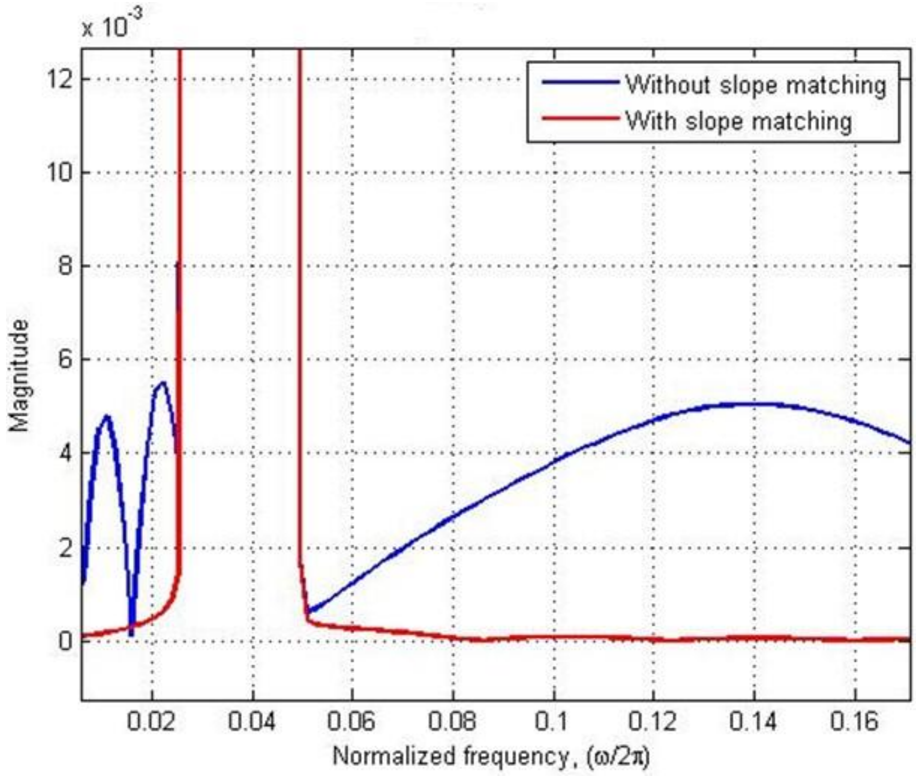

3.12 (c)

Figure 3.12: Magnitude responses of the LPST FIR band pass filters for with and without slope matching for N= 5001 (a) Magnitude response (b) Magnified view of the passband (c) Magnified view of the stopband.

Table 3.12: LPST FIR BPF Models specifications of passband and stopband edges along with measured magnitude response values. (N= 1001).

LPST BPFs	Stopband edge (ω_{s1}) rad/s	Passband edge (ω_{p1}) rad/s	Passband edge (ω_{p2}) rad/s	Stopband edge (ω_{s2}) rad/s
Design specifications	70π	72π	96π	98π
LPST BPF	66.84 π	73.22 π	95.5 π	100.44 π
LPST BPF_{slope}	67.28 π	73.22 π	95.5 π	99.48 π

Table 3.13: LPST FIR BPF Models specifications of transition bandwidth, passband ripple and stopband attenuation along with measured magnitude response values (N= 1001).

LPST BPFs	Transition bandwidth ($\omega_{p1} - \omega_{s1}$) rad/s	Transition bandwidth ($\omega_{s2} - \omega_{p2}$) rad/s	Max. passband loss (dB)	Min. stopband attenuation (dB)
Design specifications	2 π	2 π	±0.873	40
LPST BPF	6.38 π	4.94 π	+ 0.37, - 0.15	40.6
LPST BPF_{slope}	5.94 π	3.98 π	±0.13	42

Table 3.14: LPST FIR BPF Models peak passband change in percentage for with and without slope matching technique (N = 1000).

LPST BPFs	Max. passband loss (dB)	Peak passband Change (%)
LPST BPF	+ 0.37	4.35%
LPST BPF	- 0.15	1.715%
LPST BPF_{slope}	+ 0.13	1.5%
LPST BPF_{slope}	- 0.13	1.48%

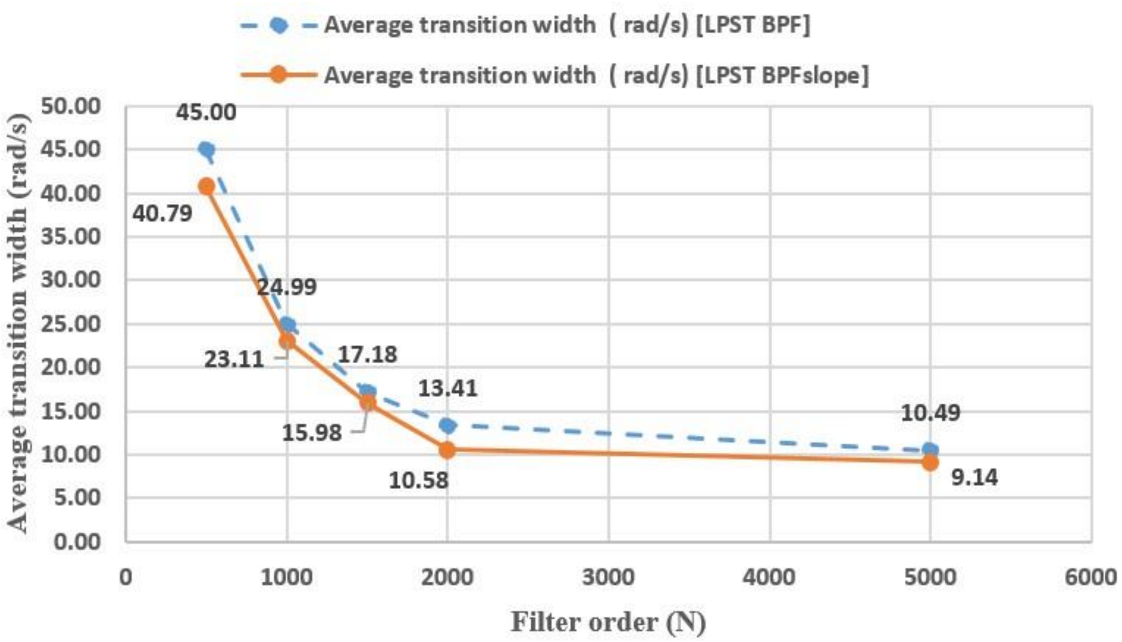

Figure 3.13: Average LPST FIR BPF transition width for various filter order (N).

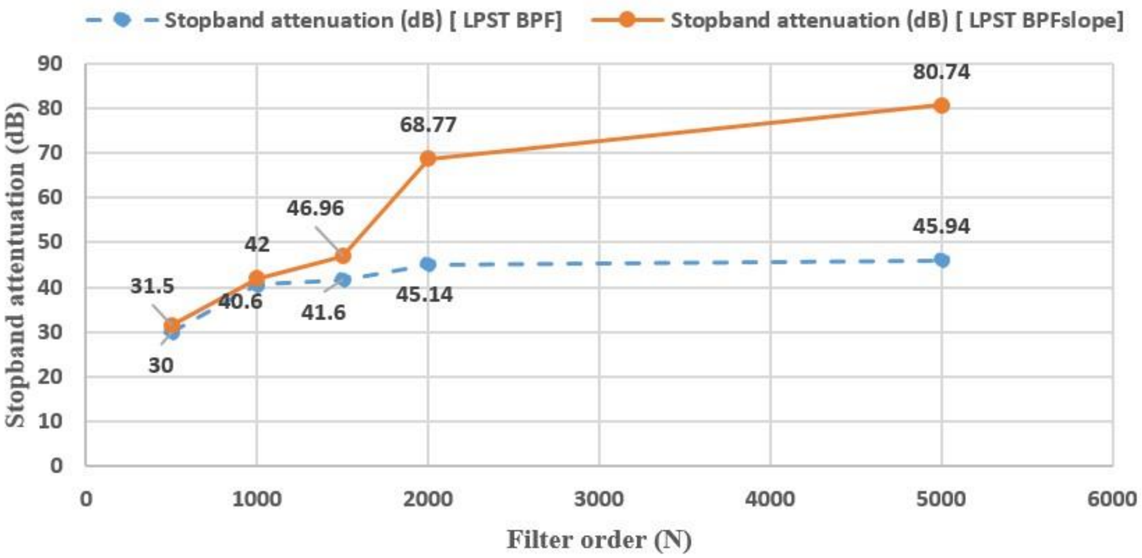

Figure 3.14: Stopband attenuation for various filter order (N).

3.12 Results and Synthesis of LPST FIR BPF Model III and Optimal FIR filter design (Parks McClellan algorithm)

Comparisons of the variations of passband loss and stopband attenuation of our method are compared with the PM algorithm in Figures 3.15 and 3.16, respectively. Using our method the passband loss gives minimum values as compared to the PM algorithm, especially at lower filter orders. At filter order 2001, the two algorithms have almost equal values. Similarly, PM algorithm stages a low stopband attenuation for all filter orders (N) from 101 to 2001. Comparison of the magnitude responses of PM algorithm versus our proposed LPST FIR Model III filter is seen in Figure 3.17. It is observed that Gibb's phenomenon is reduced completely at the transition edges of our proposed filter and is negligible at higher filter orders.

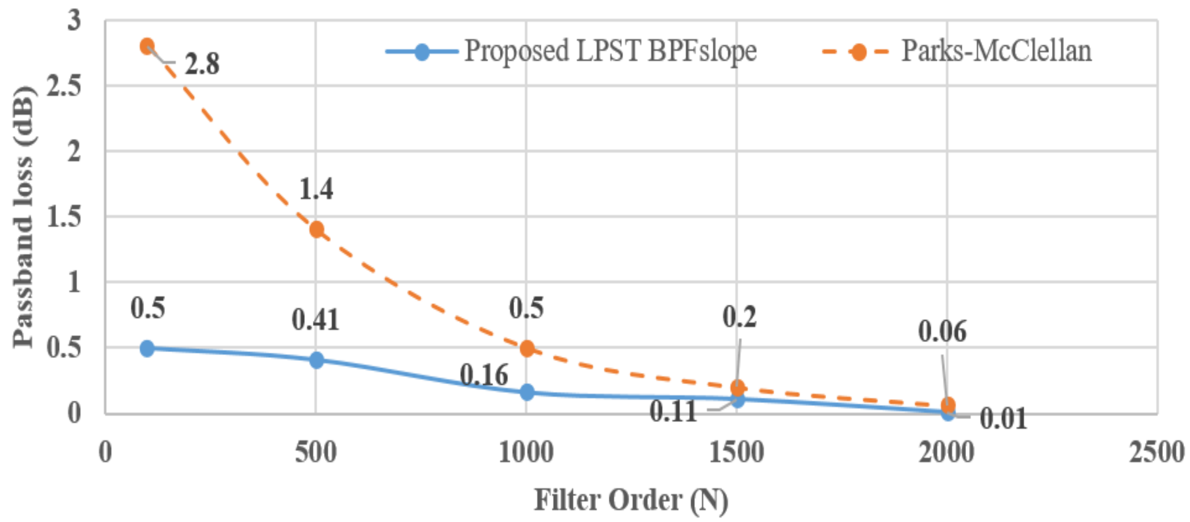

Figure 3.15: Comparisons of the variations of passband loss of our LPST FIR BPF Model III compared with the PM algorithm for various filter order (N).

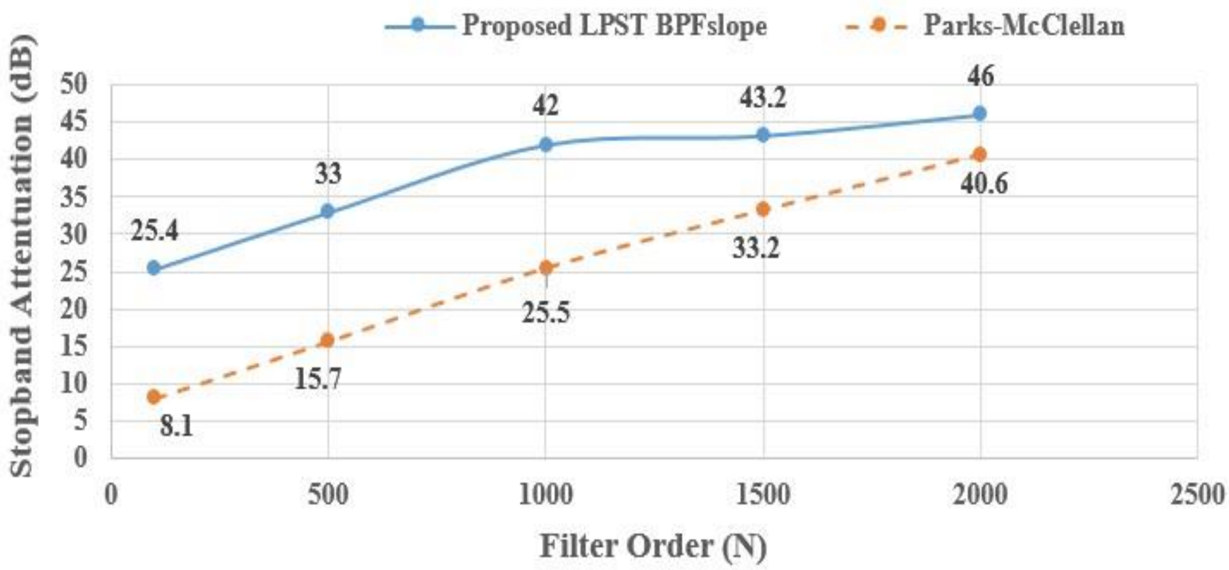

Figure 3.16: Comparisons of the variations of stopband attenuation of our LPST FIR BPF Model III compared with the Parks-McClellan algorithm for various filter order (N).

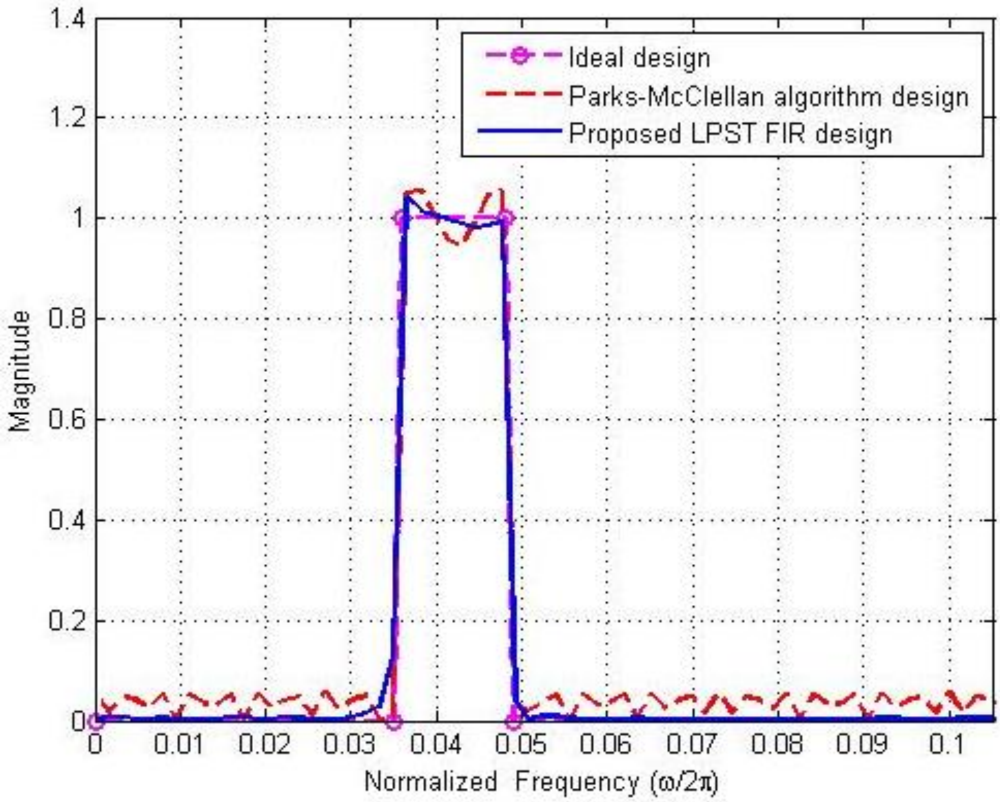

3.17 (a)

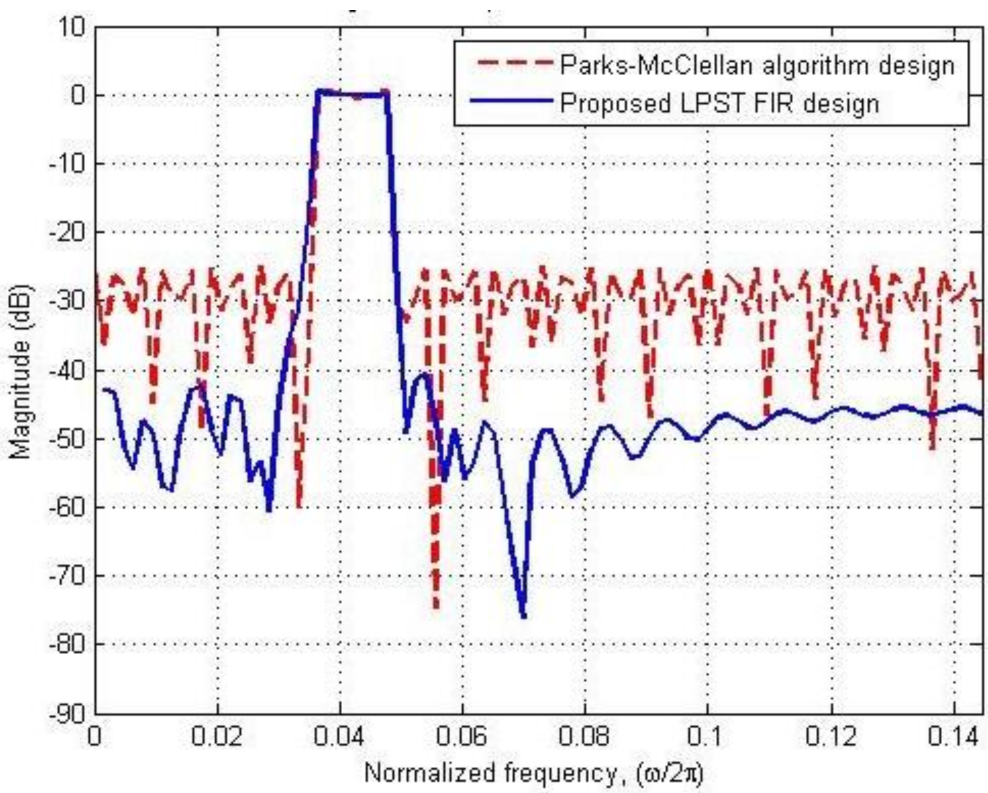

3.17 (b)

Figure 3.17: Comparisons of LPST FIR BPF Model III with PM algorithm. (a) Linear magnitude plot (b) Magnitude response.

3.13 Summary

This chapter presented the design of three models of linear phase sharp transition FIR filters with the required fiduciary band edges for maternal and fetal ECGs.

The LPST FIR BPF Model I employed a band pass filter containing a tandem of high pass and low pass FIR filters. We designed both the FIR filters such that the transition region width of each is 1 Hz. The passband losses are quite low and the ripple decreases for a higher filter order.

The LPST FIR BPF Model II described a technique of implementing an integrated LPST BPF. It is found that increasing the filter order (N) to 5001 has improved the filtering with respect to average transition bandwidth, passband ripple and stop band attenuation.

The third technique, LPST FIR BPF Model III, used a novel technique to reduce Gibb's phenomenon at the fiduciary band edges of the BP filter. The principle underlining this technique is to reduce the amount of discontinuity at the fiduciary edges of the magnitude response of the band pass FIR filter employed. This is achieved by matching the slopes of the magnitude response at the stopband/passband edges. It is observed that the stopband attenuation using this method is substantial compared to that obtained without slope matching. Additionally it is seen that, the proposed technique yields a marginal improvement in the transition region width at both the fiduciary edges. The LPST FIR BPF Model III with slope matching technique for lower orders obtained a fairly good magnitude response in all passband, stopband and transition regions with very little computation time and thus is suitable for real time processing of numerous records at a time compared to the bench marked Parks-McClellan algorithm. Almost all FIR filters have very low passband attenuation except those based on equiripple designs of lower order. All these equiripple designs are more focussed on reducing the transitions regions than improving the passband or stopbands. In our processing we are not unduly concerned with any distortion that can occur at the output of the filter (not being optimum). For lower orders, PM algorithm response is not optimum for both passband and stopband. It was found that the passband loss using our method gave minimum values as compared to the PM algorithm, especially at lower filter orders. However, at filter order 2001, the two algorithms had almost equal values. Similarly, the PM algorithm displayed low stop band attenuation for all filter orders from N= 101 to 2001. It is observed that Gibb’s phenomenon is reduced completely at the transition edges of the proposed filter and is negligible at higher filter orders. The transition width is reasonably sharp enough for our application to detect precise fetal R-peaks and thus the fetal health condition.

4

Maternal and fetal QRS detection

4.1 Introduction

The HRV has direct clinical significance and is, in fact, the most widely used fetal health parameter currently used in clinical practice. Moreover, when using Doppler ultrasound to determine the fetal heart rate non-invasively, the fetal HRV is basically the only source of information available. Since HRV is regulated by the autonomous nervous system, analysis of the HRV can provide information on the functioning and stage of development of this nervous system. This, in turn, can provide clinicians with information to assess fetal distress. To ensure accurate and reliable spectral analysis, however, the HRV information needs to be determined on a beat-to-beat basis and should essentially be artifact free. Doppler ultrasound devices generally provide a heart rate that is averaged over several beats and hence obscures HRV [206]. HRV determined with Doppler ultrasound typically also suffers from substantial artifacts (e.g. movement of the fetus often leads to the need of repositioning the ultrasound probe; in the time between repositioning, no heart rate data can be recorded) and hence provides inaccurate and unreliable spectral analysis results. Both the aforementioned problems (i.e. HRV not available on beat-to-beat basis and artifacts in the data) can be solved when determining the HRV from the FECG. The approach adopted in this chapter operates as an adaptive threshold and is chosen for its mathematical simplicity and low computational complexity.

This chapter is organized as follows. In Section 4.2 the detection of the QRS complexes is discussed based on Pan Tomkins algorithm [195] and in Sections 4.3 and 4.4, the performance of this detection method is briefly evaluated. Finally, Sections 4.5 to 4.7 provides the results of the FHRV using various Physionet database records.

4.2 QRS detection algorithm

The detection of QRS complexes is performed through a series of signal processing steps, illustrated in Figure 4.1. Each of the blocks in Figure 4.1 is discussed in more detail below.

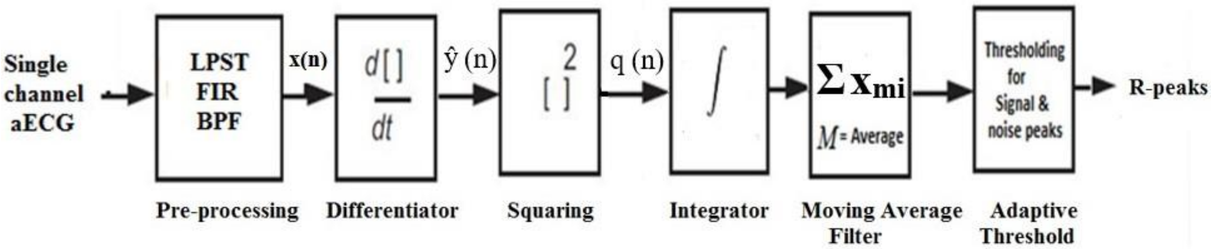

Figure 4.1: Block diagram of QRS detector to detect R-peaks [195].

4.2.1 LPST BPF pre-processing stage

In this stage, the aECG signal is filtered for noise and also the fiduciary band edges are set to filter the required signals for either maternal or fetal R waves. The design of the three Model LPST FIR filters are explained in detail in Chapter 3. The band pass filtered signal is given to the next stage, which is a differentiator.

4.2.2 Differentiator

In this stage, it provides information about the slope of the QRS complex. The slow varying P and T waves are attenuated while the peak-to-peak R wave signal corresponding to the QRS complex is further enhanced as seen in Figure 4.2. We used the 5 point derivative with the transfer function given in Eq. 4.1, which gives a linear range between 0 to 30Hz [195]. The difference Eq. of the differentiator is shown in Eq. (4.2).

The transfer function of the differentiator is,

$$H(z) = 0.1\left(2 + z^{-1} - z^{-3} - 2z^{-4}\right) = \frac{Y(z)}{X(z)}, \tag{4.1}$$

where, Y(z) and X(z) are the output and input of the differentiator, respectively.

$$y(z) = 0.1\left[\, 2x(z) + x(z)\, z^{-1} - x(z)\, z^{-3} - x(z)\, 2z^{-4} \right]$$

$$y(n) = \frac{\left[2.x(n) + x(n-1) - x(n-3) - 2x(n-4)\right]}{10} = h(n) * x(n) \quad (\text{* indicates convolution in time domain})$$

$$\hat{y}(nT) = \frac{\left[2.x(nT) + x(n-1)T - x(n-3)T - 2x(n-4)T\right]}{8} = \hat{h}(n) * x(n) \tag{4.2}$$

(where, $\hat{h}(n)$ is the appropriate expression for h(n))

The fraction 1/8 is the approximation of the original gain fraction of 1/10.

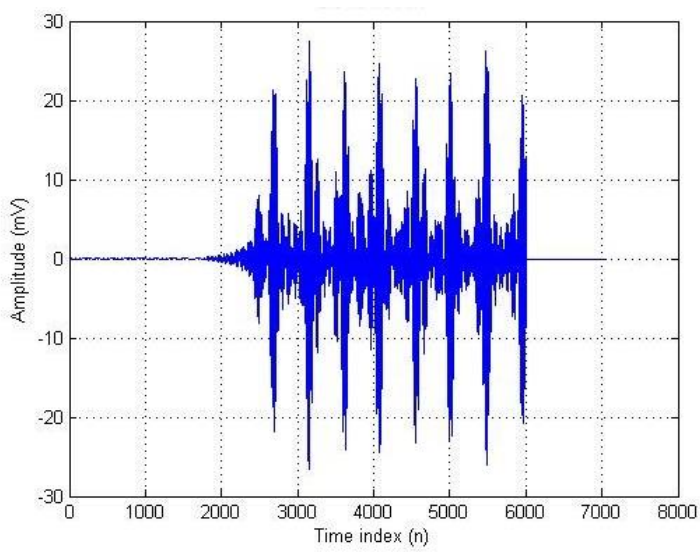

Figure 4.2: Differentiation of the band pass aECG signal.

4.2.3 Squaring

In this stage, the nonlinear processing of the signal obtains all positive values obtained by squaring the larger amplitudes and minimizing the smaller amplitudes as seen in Figure 4.3. Higher frequencies (R-peak) are normally characteristic of the QRS complex. After differentiation in the previous stage, point by point squaring the signal is done as given by Eq. 4.3.

$$q(nT) = \left[\ \hat{y}(nT)\ \right]^2 \tag{4.3}$$

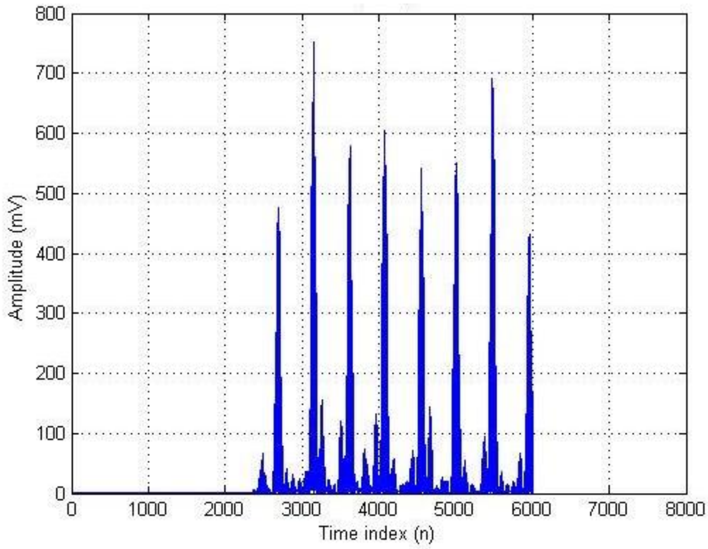

Figure 4.3: Squaring of the differentiated signal.

4.2.4 Moving Window Integration

The slope of the R wave alone is not the only way to detect a QRS event. This integrator sums the area under the squared waveform over a fixed interval, advances one sample interval, and integrates the new fixed window. The width of the moving window should be approximately the same as the widest possible QRS complex. For our sample rate of 1000 samples/s, the window is 152 samples wide (152ms). The width is long enough to include the time duration of extended abnormal QRS complexes. If the window is too large the integration waveform will merge the QRS and T complexes together, else if window is too small, a QRS complex could produce several peaks at the output of the stage.

$$y_{mi}(nT) = \frac{\left[\left(x_{mi}(\mathrm{nT} - (\mathrm{N}-1)T\right) + \left(x_{mi}\left(nT - (N-2)T\right)\right) + .. + x_{mi}(nT)\right]}{N}, \tag{4.4}$$

where, $y_{mi}(n)$ and $x_{mi}(n)$ are respectively, the output and input of the moving window block.

4.2.5 Moving Average Filter (MAF)

MAF is a simple low pass FIR filter commonly used for smoothing an array of sampled data or signal. It takes M samples of input at a time, takes the average of those M-samples and produces a single output point shown in Eq. 4.5

$$y_{maf}(i) = \frac{1}{M}\sum_{j=0}^{M-1} x_{maf}\left[i+j\right] , \tag{4.5}$$

Where, y_{maf} and x_{maf} are respectively , the output and input of the moving average filter block.

4.2.6 Adaptive threshold

The integrated signal is passed through a moving average filter and is subjected to an adpative threshold value to obtain signal and noise peaks. The signal peaks (maternal or fetal) are defined as those of R waves while the noise peaks are the T waves, muscles noise etc. The average value of the maxima index is taken as the R-peak. The threshold generated is automatically adjusted to float over the signal noise peaks. Low thresholds are possible because of the improvement of the signal-to-noise ratio by the band pass filter. The peak value and peak index are obtained from the integration output. The signal peak is adjusted as per the amplitude of each record. Below is the simple algorithm to detect the R-peak value (above the threshold value) based on the Pan Tomkins QRS detector algorithm [195].

noise_peak = 0.1 signal_peak ;

signal_peak = 0.6 peak_value + 0.4 signal_peak;

noise_peak = 0.4 peak_value + 0.6 noise_peak;

ATHD = noise_peak + 0.25 (signal_peak – noise_peak);

IF signal peak value ≥ ATHD;

“*Display R_peak_value, R_peak_ index and threshold value*”;

ELSE peak_value = noise_peak;

where, ATHD is the Adpative threshold, R_peak_value and R_peak_index are the detected R-peak and R-peak index values, respectively of the maternal or fetal QRS.

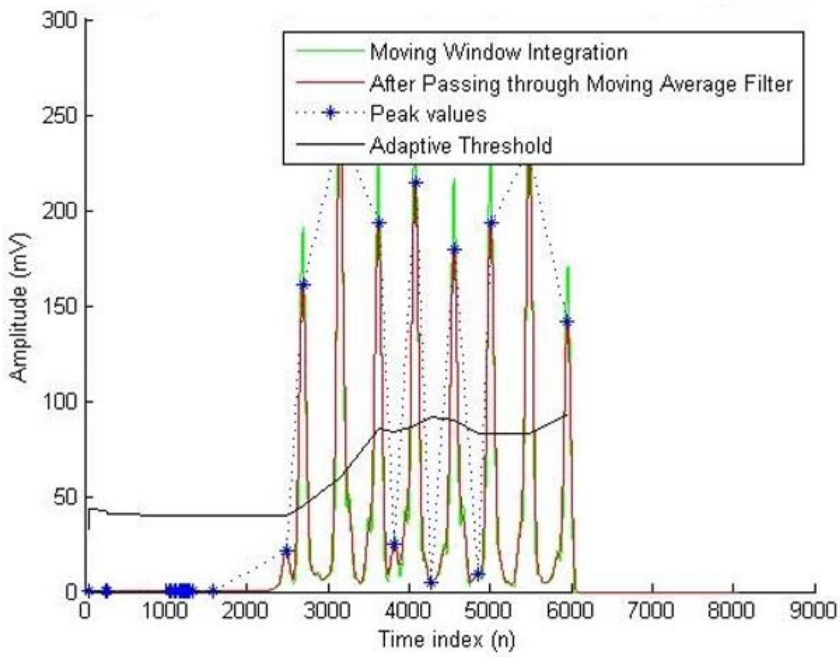

Figure 4.4: Moving window integrator and moving average filter with the adaptive threshold to detect R-peaks.

4.3 Performance evaluation of the QRS detector

The fetal and maternal R-peaks generated by our algorithms were compared with their true reference annotations, for example, for the Physionet database adfecgdb, the scalp fetal peak annotations from the website is the true reference. We used the distance based measure to assess the error for the fetal detection between the true R-peak location and the detected fetal R-peak using our algorithm (see Figure 4.5). As per ANSI/AAMI guidelines (ANSI/AAMI/ISO EC57 1998/(R) 2008) [6, 207], sensitivity (Se), positive predictive value (PPV), F_1 (accuracy) and failed detections (FD) are the classical statistics for evaluating QRS detectors as shown in Eq. 4.6, 4.7, 4.8 and 4.9 respectively.

- **Sensitivity (Se)** of the algorithm is the number of True Positive (TP) as a percentage of the total peaks that really exist.

$$Sensitivity(Se)\ \% = \frac{TP}{TP+FN} * 100\ \% \tag{4.6}$$

- **Positive Predictivity Value (PPV)** is the number of TPs as a percentage of the number of peaks detected by the algorithm.

$$Positive\ Predictive\ Value\ (PPV)\ \% = \frac{TP}{TP+FP} * 100\ \% \tag{4.7}$$

- **Accuracy (F_1)** is the measure of how accurately has the algorithm detected the R-peaks for that record. It is the average of Se and PPV.

$$Accuracy\ (F_1) = 2 \cdot \left(\frac{Se\ .\ PPV}{Se+PPV}\right) = \left(\frac{2.\mathrm{TP}}{2.\mathrm{TP} + \mathrm{FP} + \mathrm{FN}}\right) \tag{4.8}$$

- **Failed detections** is the total number of beats missed in FP and FN, considered to be failed detections given by,

$$Failed\ Detections\ (FD)\ \% = \frac{(FP+FN)}{TP} * 100\ \% \tag{4.9}$$

Where,

FP (False Positive) are beats identified by the algorithm when the clinician has not scored one.

FN (False negative) are beats missed by the algorithm when the clinician has scored one. (for example, missed the R index peak value more than +/- 20ms).

TP (True Positive), where both annotations agree on the time of the event.

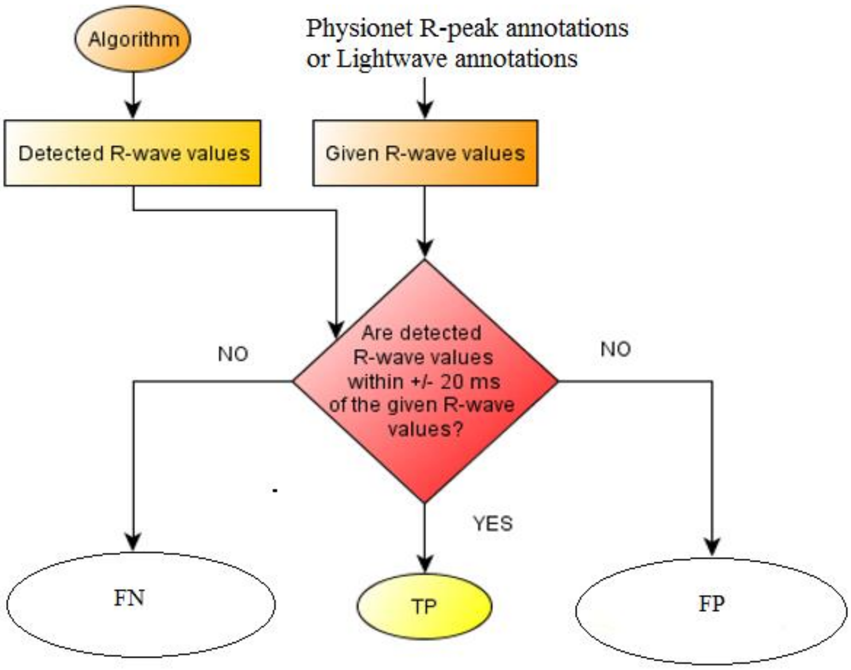

Figure 4.5: Performance of the aECG QRS detector.

In this section, the fetal R-R interval (Δn) is calculated as ($n_{i+1} - n_i$) where, n_i is the time index corresponding to the i^{th} computed R fetal peak at the output of the FQRS detector (i = 1,2… i an integer) and fs = sampling frequency. The fetal or maternal heart rate is obtained for each record by computing using the Eq. (4.10).

$$Fetal\ /\ Maternal\ Heart\ Rate\ (bpm)\ =\ \frac{(\text{fs x } 60)}{\Delta n} \tag{4.10}$$

4.4 Fetal and maternal fiduciary band edges

To streamline and test an individual frequency band edge for fetal and maternal spectrum, we assigned various frequency ranges to verify the detection of heart rates for each of the ECG signals. As discussed in section 3.7.1 of Chapter 3, it is assumed that the beat frequency of the fetus is approximately 1.5 times that of the mother. A frequency overlap between the two ECG signals can be avoided if their individual band edges can be known in advance. It was computed that the fiduciary band edges for the fetal were: fs1/fp1 [27/28] Hz and fp2/fs2 [48/49] Hz keeping the frequency below the 50Hz to remove PLI. The average maternal fiduciary band edges were assumed to be fs1/fp1 [10/11 Hz] and fp2/fs2 [33/34] Hz. It is illustrated using LPST FIR filter that the fetal R-peaks are best detected between the range 35 Hz – 49 Hz as seen in Figure 4.6. The lower frequency range of 5 Hz – 49 Hz exhibits maximum false R-peaks. A similar trend is seen in Figure 4.7, where the maternal R-peaks were best detected between the frequency range of 5 - 21 Hz. At higher frequencies above 21 Hz, the QRS detector detected maximum false R-peaks. The filter Models can be compared for their accuracy (F_1) and failed detections using the following fiduciary band edges for fetal and maternal HR detection.

Fetal fiduciary band edges = fs1/fp1 [**35/36] Hz** and fp2/fs2 [**48/49**] Hz.

Maternal fiduciary band edges = fs1/fp1 [**5/6] Hz** and fp2/fs2 [**19/20**] Hz.

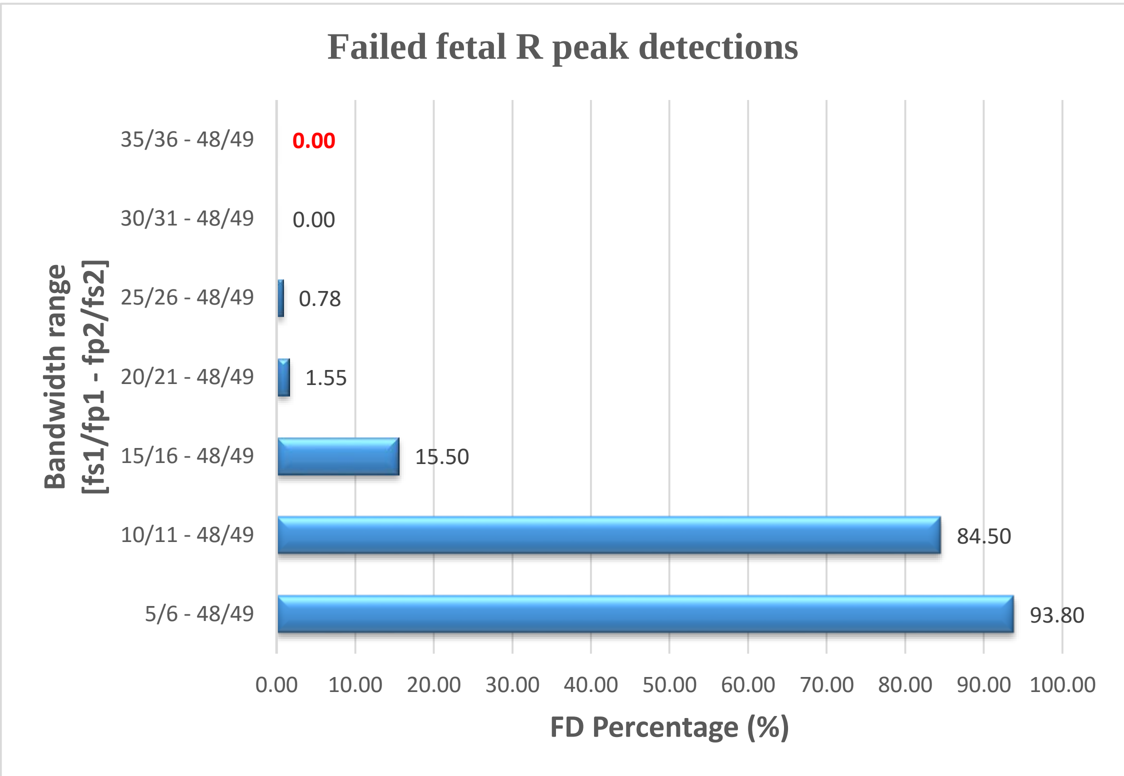

Figure 4.6: Failed fetal R-peak detections for various bandwidth ranges of adfecgdb database for record r01 (channel 4).

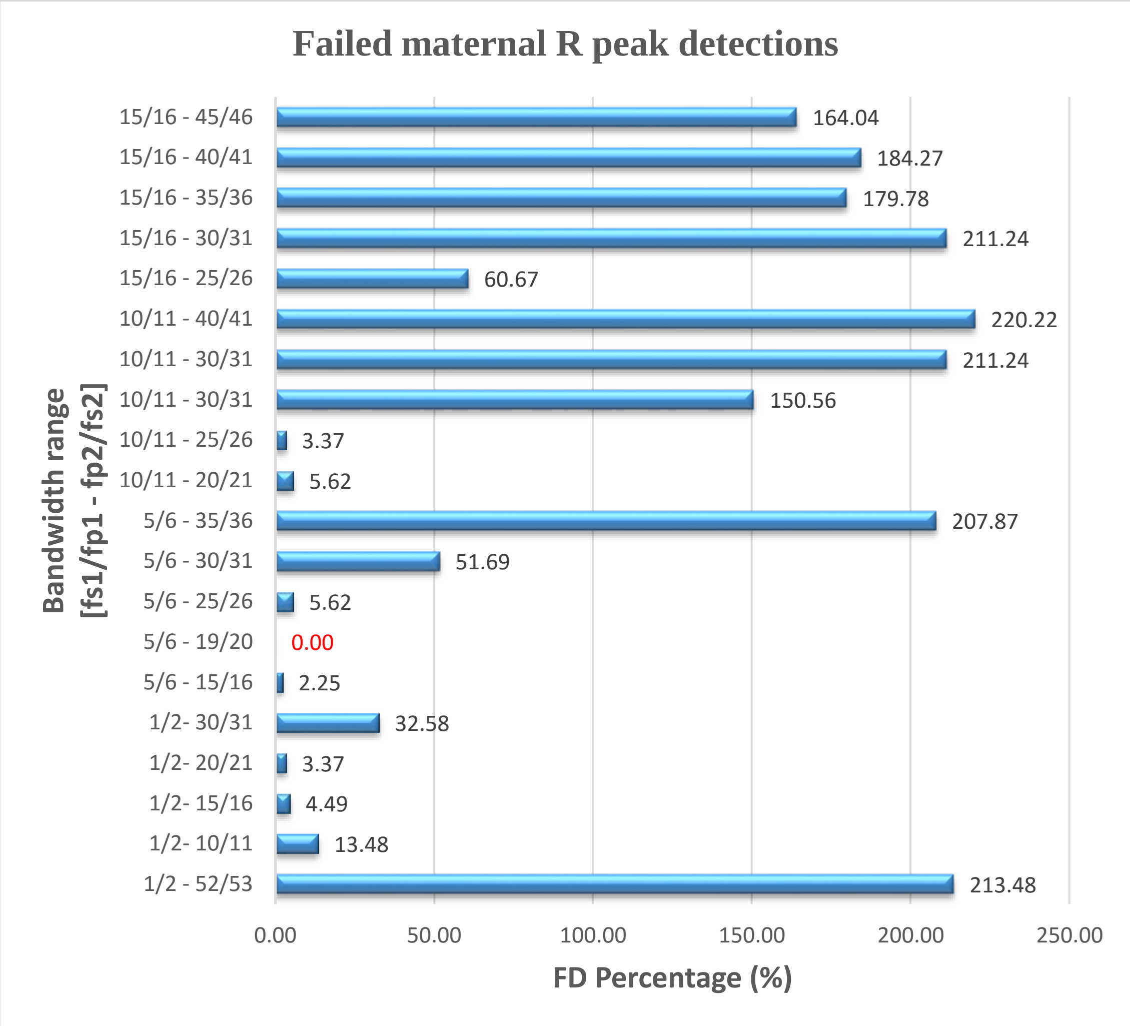

Figure 4.7: Failed maternal R-peak detections for various bandwidth ranges of adfecgdb database for record r01 (channel 4).

4.5 QRS detection using composite LPST FIR BPF Model I

The LPST FIR filters used in tandem were high pass filters followed by the low pass filters. These composite filters formed the pre-processing module in the QRS detector as explained in section 4.2. This is illustrated using the Physionet adfecgdb database (see chapter 2, section 2.7.1). The direct fetal scalp ECG is the true reference FECG signal (channel one) as shown in Figure 4.8a. The raw aECG signals are taken from the record r01 (channel four) as shown in Figure 4.8b.

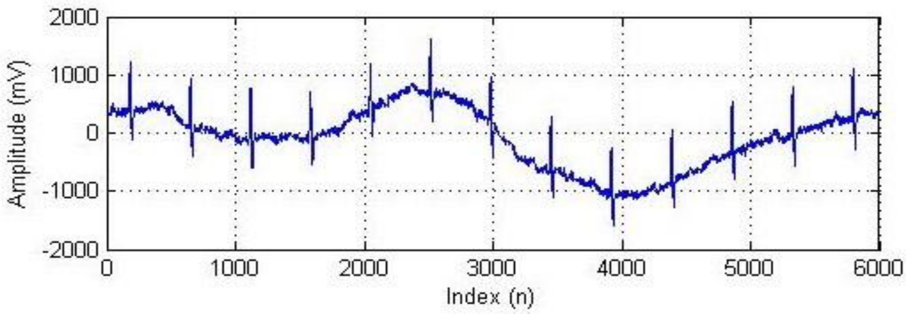

4.8 (a)

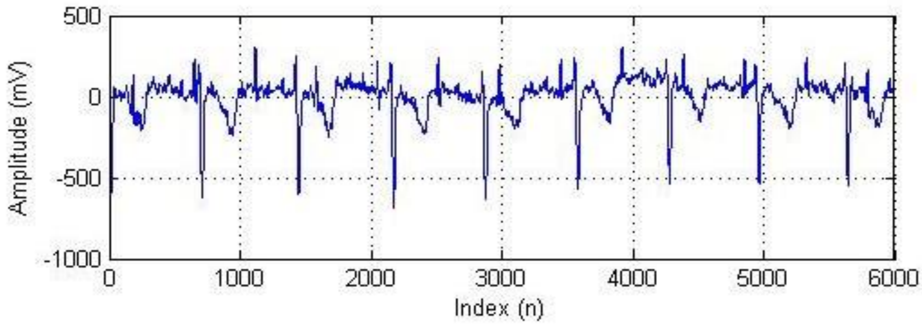

4.8 (b)

Figure 4.8: Physionet adfecgdb database (record r01). (a) Direct fetal scalp ECG signal as true reference FECG (channel one) (b) Raw maternal aECG (channel four).

The composite LPST BPF FIR Model I is designed such that, the cut off frequency of the HPF is 35 Hz and the cut off frequency of the LPF is 49 Hz. When the aECG signal is passed through HPF, it effectively filters the lower frequencies up to 35 Hz. The high pass filtered signal is shown in Figure 4.9a along with the filtered aECG signal in Figure 4.9b. Similarly the frequency spectrum of the aECG signal passed subsequently through LPF indicates the filtering of the frequencies up to the designated frequency of 49Hz as shown in Figure 4.9c. The serial filtering of HP and LP combination effectively gives us the required frequency spectrum of the FECG, which can be seen in the time domain plot in Figure 4.9d.

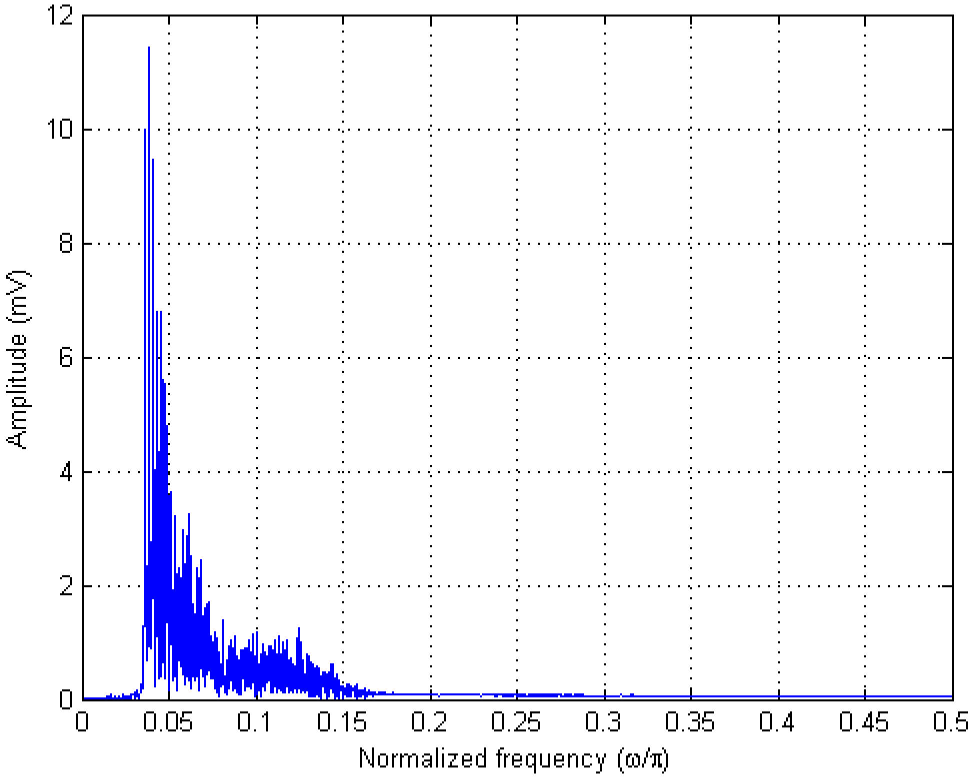

12
10
8
6
4
2
0
Amplitude (mV)
0
0.05
0.1
0.15
0.2
0.25
0.3
0.35
0.4
0.45
0.5
Normalized frequency (ω/π)

4.9 (a)

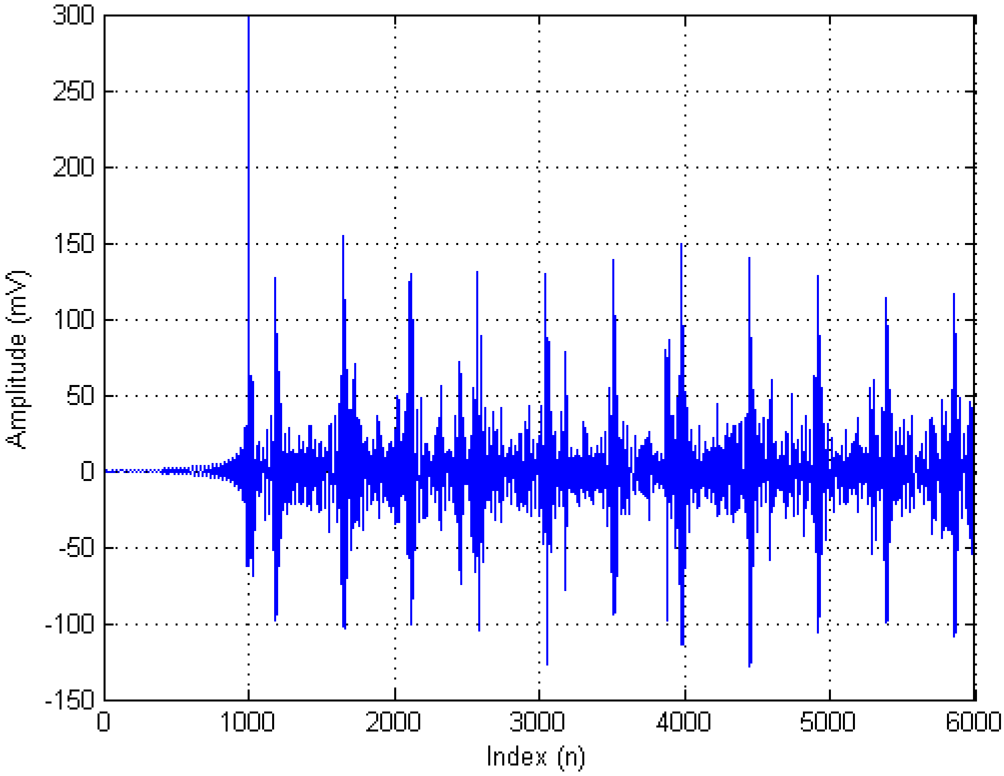

300
250
200
150
100
50
0
-50
-100
-150
Amplitude (mV)
0
1000
2000
3000
4000
5000
6000
Index (n)

4.9 (b)

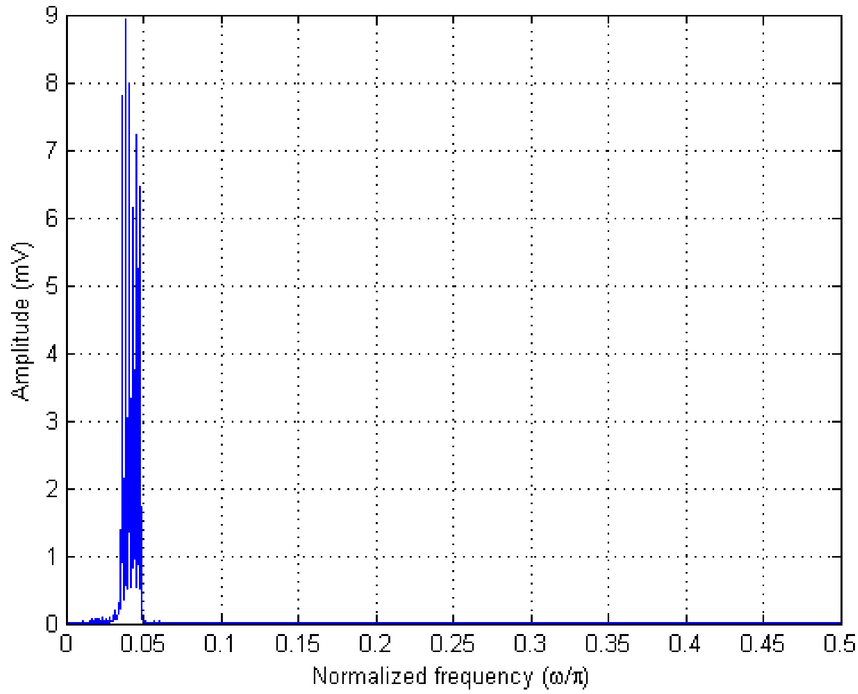

4.9 (c)

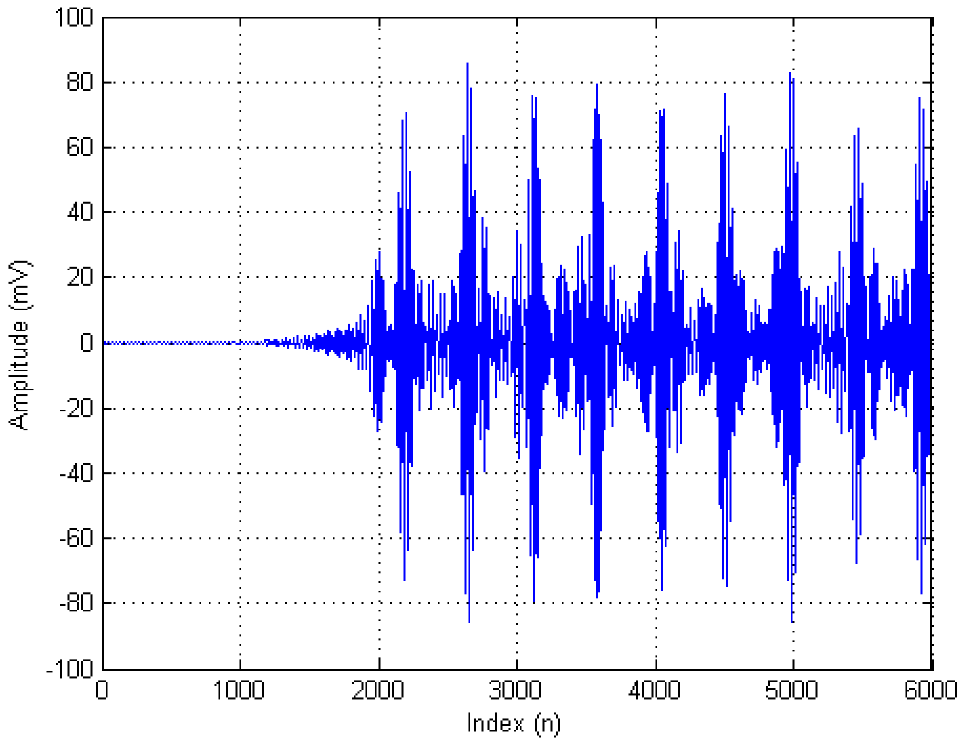

4.9 (d)

Figure 4.9: Filtering of the aECG signal using LPST FIR filter Model I (a) Frequency spectrum of the high pass filtered aECG signal (b) aECG signal after high pass filtering (c) Frequency spectrum of the signal passed through a subsequent low pass filter (d) FQRS signal after low pass filtering.

The filtered FECG signal as shown in Figure 4.9d is further given to the amplitude squaring stage which enables the desired peak signals to be further enlarged and the smaller noise peaks to be reduced as shown in Figure 4.10a. As shown in Figure 4.10b, we used a moving window integration which used a sampling frequency of 1 KHz and a 75 samples wide window. Additionally, a moving average filter smoothened the integrated signal and an adaptive threshold computed fetal R-peaks to display FHRV as seen in Figure 4.10c.

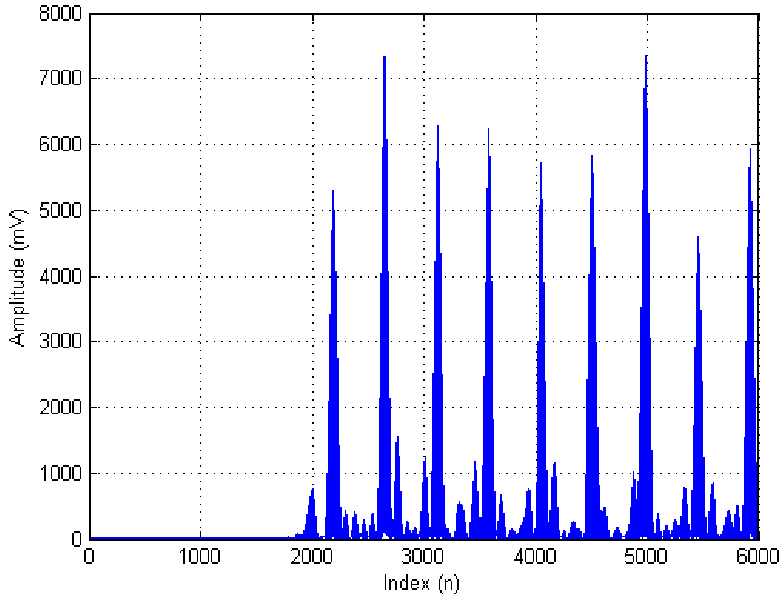

4.10 (a)

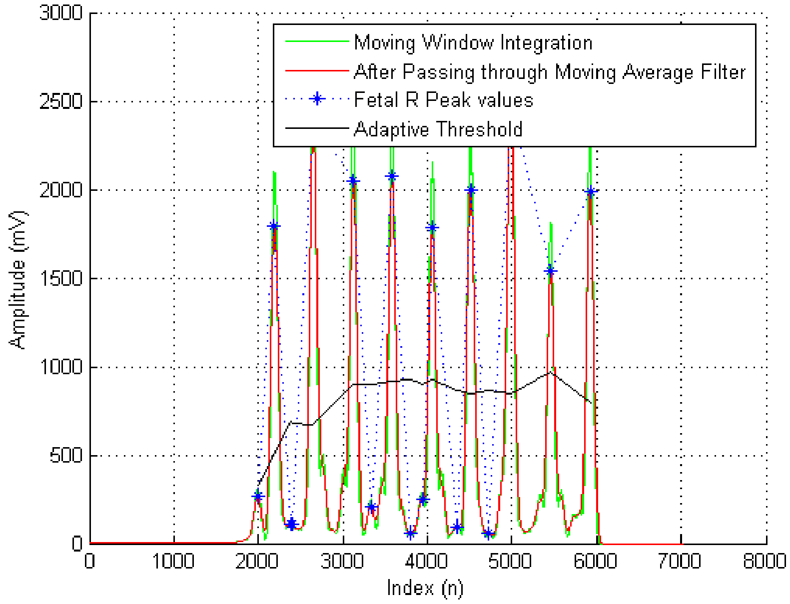

4.10 (b)

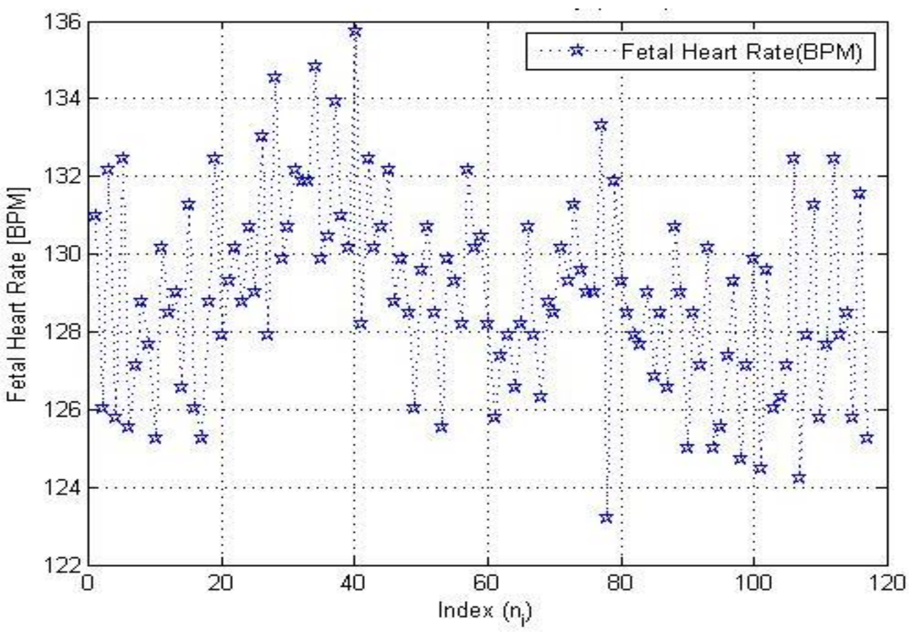

4.10 (c)

Figure 4.10: NIFHR (Non-invasive fetal heart rate) detector (a) Amplitude squaring of fetal R-peaks (b) Moving window integration and adaptive threshold (c) FHRV (n_i is the time index corresponding to the i^{th} computed R-fetal peak at the output of the FQRS detector).

4.5.1 Performance evaluation of the QRS detector to obtain fetal and maternal R-peaks using LPST FIR BPF Model I

The modified QRS detector was used to compute the fetal and maternal R-peaks for the three Physionet databases. Table 4.1 displays the performance evaluation of the FQRS detection using LPST FIR BPF Model I for five adfecgdb records with four channels each. The algorithm fetal R-peaks were compared with the Physionet FQRS annotations. Similarly, the maternal R-peak index values computed from the modified QRS detector are compared with the Physionet lightwave annotation viewer for a) Abdominal and direct fetal ECG database (see Table 4.2) and b) Physionet Challenge 2013 database (set a) for channel four. However nifecgdb database has the MQRS annotations which we used to compare with our extracted maternal R-peaks. The nifecgdb and Physionet Challenge (Phy C) 2013 records displayed in Table 4.3 and Table

4.4 respectively computed FN and FP values. The rest of the other nifecgdb and Phy C records scored 100% accuracy and hence are not displayed in the Tables. (For more details about the databases, see chapter 2, section 2.7). Additionally, the FD are computed for each Phy C record using Eq. 4.9 and are shown in Table 4.4

Figure 4.11 illustrates the true reference FHR bpm plotted with our LPST FIR filter based FHR for the Physionet adfecgdb record r01 (channel four). The dotted lines indicate the ± 10 bpm trace with respect to the true reference FHR trace. It was seen that the difference between the reference FHR and LPST FIR filter FHR was less than the ± 10 bpm.

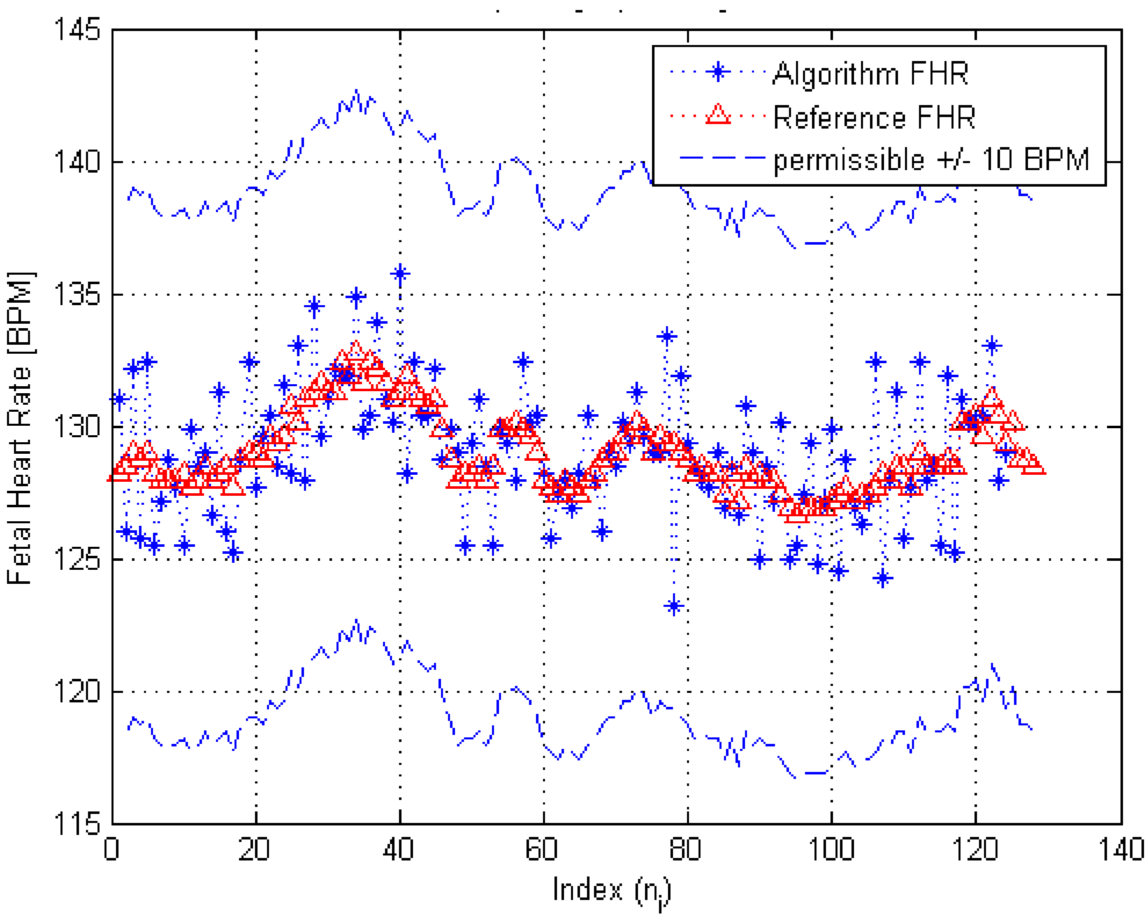

Figure 4.11: Illustration of the true reference FHR (direct scalp ECG) plotted with our algorithm based LPST FIR BPF Model I computed FHR, for record r01 of adfecgdb (channel four) for one minute trace. Blue dotted lines indicate the ±10 bpm limits with respect to the reference FHR trace.

Table 4.1: Performance evaluation of the FQRS detection using LPST FIR BPF Model I for adfecgdb database.

Record [channel]	TP	FN	FP	Se	PPV	F_1
r01 [1]	129	32	7	80.12	94.85	86.87
r01[2]	129	5	0	96.27	100.00	98.10
r01[3]	129	3	0	97.73	100.00	98.85
r01[4]	129	0	0	100.00	100.00	100.00
r04[1]	125	17	5	88.03	96.15	91.91
r04[2]	125	20	2	86.21	98.43	91.91
r04[3]	125	22	6	85.03	95.42	89.93
r04[4]	125	22	7	85.03	94.70	89.61
r07 [1]	132	45	13	74.58	91.03	81.99
r07[2]	132	22	0	85.71	100.00	92.31
r07[3]	132	20	2	86.84	98.51	92.31
r07[4]	132	14	5	90.41	96.35	93.29
r08 [1]	132	28	10	82.50	92.96	87.42
r08[2]	132	4	0	97.06	100.00	98.51
r08[3]	132	2	0	98.51	100.00	99.25
r08[4]	132	0	0	100.00	100.00	100.00
r10 [1]	132	32	9	80.49	93.62	86.56
r10[2]	132	7	2	94.96	98.51	96.70
r10[3]	132	65	4	67.01	97.06	79.28
r10[4]	132	26	5	83.54	96.35	89.49

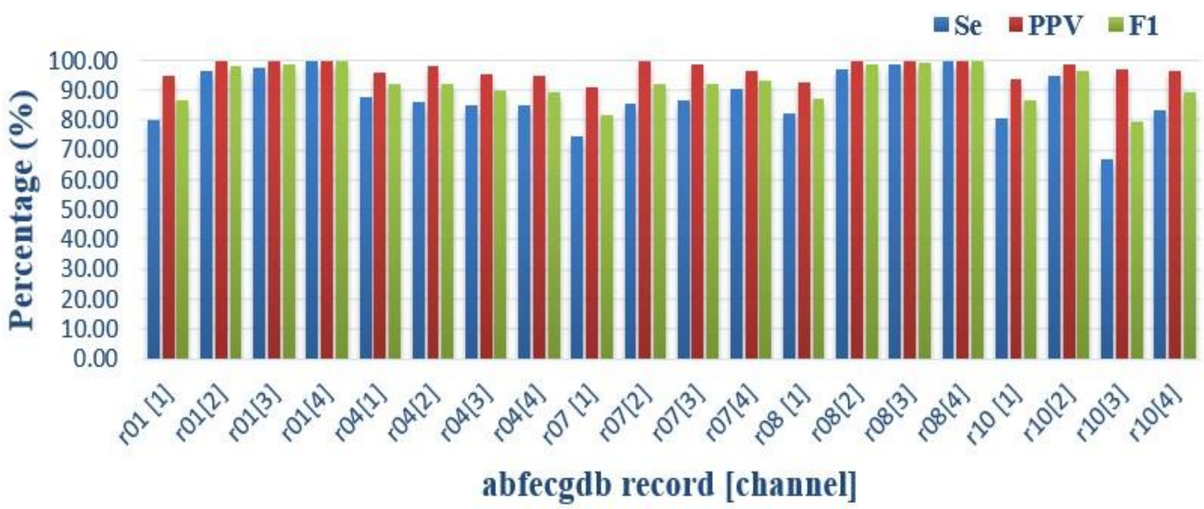

Figure 4.12: Graphical representation of the evaluation of the FQRS detection using LPST FIR BPF Model I for adfecgdb database.

Table 4.2: Performance evaluation of the MQRS detection using LPST FIR BPF Model I for adfecgdb database.

Record [channel]	TP	FN	FP	Se	PPV	F_1
r01 [1]	89	0	2	100.00	97.80	98.89
r01[2]	89	65	11	57.79	89.00	70.08
r01[3]	89	3	1	96.74	98.89	97.80
r01[4]	89	0	1	100.00	98.89	99.44
r04[1]	82	0	0	100.00	100.00	100.00
r04[2]	82	0	1	100.00	98.80	99.39
r04[3]	82	0	0	100.00	100.00	100.00
r04[4]	82	4	2	95.35	97.62	96.47
r07 [1]	77	4	4	95.06	95.06	95.06
r07[2]	77	0	0	100.00	100.00	100.00
r07[3]	77	4	4	95.06	95.06	95.06
r07[4]	77	0	4	100.00	95.06	97.47
r08 [1]	92	0	1	100.00	98.92	99.46
r08[2]	92	0	0	100.00	100.00	100.00
r08[3]	92	2	0	97.87	100.00	98.92
r08[4]	92	0	0	100.00	100.00	100.00
r10 [1]	105	0	0	100.00	100.00	100.00
r10[2]	105	1	1	99.06	99.06	99.06
r10[3]	105	4	1	96.33	99.06	97.67
r10[4]	105	0	0	100.00	100.00	100.00

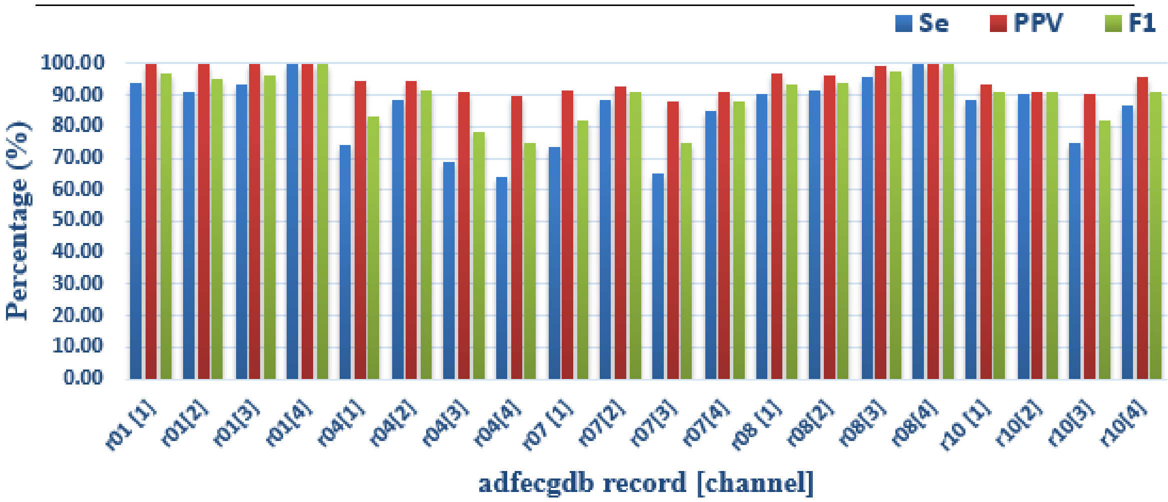

Figure 4.13: Graphical representation of the evaluation of the MQRS detection using LPST FIR BPF Model I for adfecgdb database.

Table 4.3: Performance evaluation of the MQRS detection using LPST FIR BPF Model I for nifecgdb database.

Record [channel]	**TP**	**FN**	**FP**	**Se**	**PPV**	**F_1**
ecgca154[01]	50	0	0	100.00	100.00	100.00
ecgca154[02]	50	1	15	98.04	76.92	86.21
ecgca154[03]	50	0	0	100.00	100.00	100.00
ecgca224[01]	49	0	0	100.00	100.00	100.00
ecgca224[02]	49	0	0	100.00	100.00	100.00
ecgca224[03]	49	0	0	100.00	100.00	100.00
ecgca224[04]	49	1	5	98.00	90.74	94.23
ecgca416[01]	55	0	0	100.00	100.00	100.00
ecgca416[02]	55	4	7	93.22	88.71	90.91
ecgca416[03]	55	0	17	100.00	76.39	86.61
ecgca416[04]	55	0	27	100.00	67.07	80.29
ecgca436[01]	56	0	0	100.00	100.00	100.00
ecgca436[02]	56	0	2	100.00	96.55	98.25
ecgca436[03]	56	0	2	100.00	96.55	98.25
ecgca436[04]	56	0	2	100.00	96.55	98.25
ecgca473[01]	51	0	0	100.00	100.00	100.00
ecgca473[02]	51	0	0	100.00	100.00	100.00
ecgca473[03]	51	0	35	100.00	59.30	74.45
ecgca473[04]	51	0	0	100.00	100.00	100.00
ecgca515[01]	57	0	0	100.00	100.00	100.00
ecgca515[02]	57	0	0	100.00	100.00	100.00
ecgca515[03]	57	0	4	100.00	93.44	96.61
ecgca515[04]	57	0	0	100.00	100.00	100.00
ecgca597[01]	53	0	0	100.00	100.00	100.00
ecgca597[02]	53	0	0	100.00	100.00	100.00
ecgca597[03]	53	2	2	96.36	96.36	96.36
ecgca597[04]	53	2	26	96.36	67.09	79.10
ecgca649[01]	53	0	0	100.00	100.00	100.00
ecgca649[02]	53	2	28	96.36	65.43	77.94
ecgca649[03]	53	0	5	100.00	91.38	95.50
ecgca771[01]	47	0	0	100.00	100.00	100.00
ecgca771[02]	47	0	45	100.00	51.09	67.63
ecgca771[03]	47	0	50	100.00	48.45	65.28
ecgca771[04]	47	0	54	100.00	46.53	63.51
ecgca811[01]	52	0	0	100.00	100.00	100.00
ecgca811[02]	52	0	0	100.00	100.00	100.00

ecgca811[03]	52	7	19	88.14	73.24	80.00
ecgca840[01]	47	0	0	100.00	100.00	100.00
ecgca840[02]	47	0	49	100.00	48.96	65.73
ecgca840[03]	47	0	0	100.00	100.00	100.00
ecgca840[04]	47	0	0	100.00	100.00	100.00
ecgca848[01]	53	0	0	100.00	100.00	100.00
ecgca848[02]	53	0	0	100.00	100.00	100.00
ecgca848[03]	53	3	16	94.64	76.81	84.80
ecgca848[04]	53	2	22	96.36	70.67	81.54
ecgca876[01]	51	0	3	100.00	94.44	97.14
ecgca876[02]	51	0	0	100.00	100.00	100.00
ecgca876[03]	51	0	6	100.00	89.47	94.44
ecgca902[01]	55	0	0	100.00	100.00	100.00
ecgca902[02]	55	0	6	100.00	90.16	94.83
ecgca902[03]	55	0	0	100.00	100.00	100.00
ecgca906[01]	53	1	3	98.15	94.64	96.36
ecgca906[02]	53	0	2	100.00	96.36	98.15
ecgca906[03]	53	1	3	98.15	94.64	96.36
ecgca906[04]	53	4	2	92.98	96.36	94.64
ecgca968[01]	54	0	0	100.00	100.00	100.00
ecgca968[02]	54	2	7	96.43	88.52	92.31
ecgca968[03]	54	0	8	100.00	87.10	93.10
ecgca968[04]	54	20	9	72.97	85.71	78.83

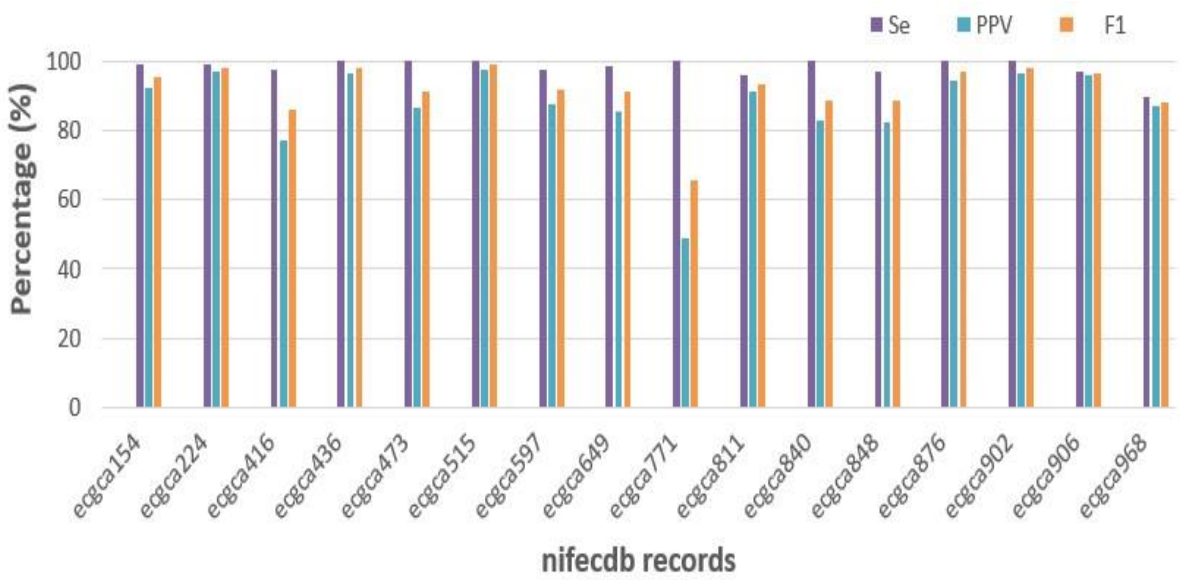

Figure 4.14: Graphical representation of the evaluation of the MQRS detection using LPST FIR BPF Model I for nifecgdb database.

Table 4.4: Performance evaluation of the MQRS detection using LPST FIR BPF Model I for Phy C 2013 database.

Record	TP	FN	FP	FD	Se	PPV	F_1
a02	128	0	3	2.34	100.00	97.71	98.84
a03	140	0	2	1.43	100.00	98.59	99.29
a07	90	0	2	2.22	100.00	97.83	98.90
a16	89	0	7	7.87	100.00	92.71	96.22
a29	62	11	24	56.45	84.93	72.09	77.99
a31	80	0	1	1.25	100.00	98.77	99.38
a33	94	0	15	15.96	100.00	86.24	92.61
a34	76	0	5	6.58	100.00	93.83	96.82
a38	79	19	8	34.18	80.61	90.80	85.41
a41	112	0	4	3.57	100.00	96.55	98.25
a51	86	5	0	5.81	94.51	100.00	97.18
a53	73	1	0	1.37	98.65	100.00	99.32
a56	93	0	3	3.23	100.00	96.88	98.41
a58	108	0	3	2.78	100.00	97.30	98.63
a66	82	0	17	20.73	100.00	82.83	90.61
a73	96	0	4	4.17	100.00	96.00	97.96

*The aECG data was obtained from channel four for all above records.

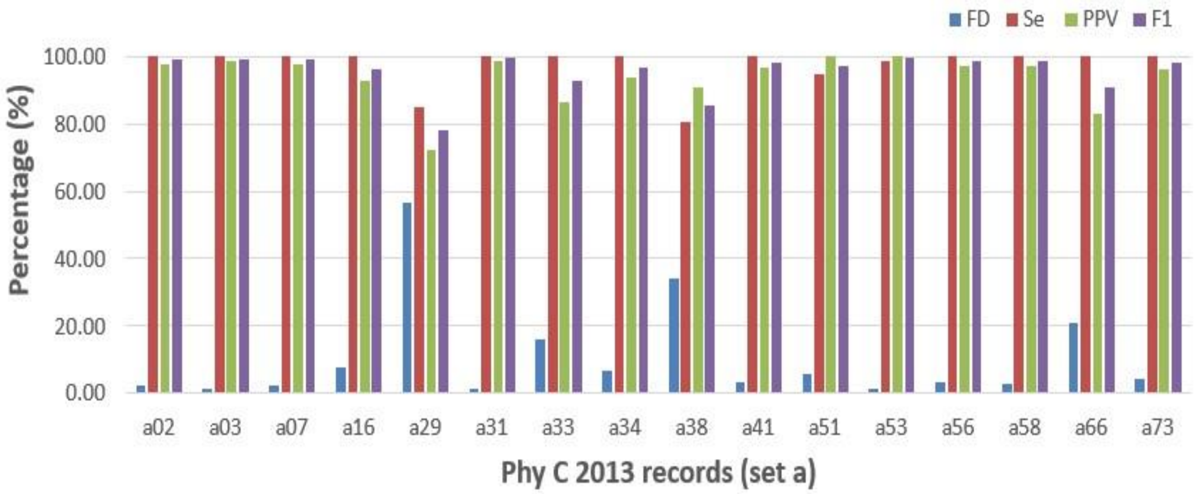

Figure 4.15: Graphical representation of the evaluation of the MQRS detection using LPSR FIR BPF Model I for Physionet challenge 2013 (set a) database.

4.5.2 Discussion of filter synthesis using LPST FIR BPF Model I

When we evaluated our algorithm for the one minute record of r01 (channel 4) and r08 (channel 4) of the adfecgdb database, we found for TP = 129, FN and FP were equal to 0 giving 100% accuracy. Most of the records obtained an average accuracy more than 92%. The worst accuracy of 79.28% was seen for record r10 (channel 3) as seen in Figure 4.12. Using this adfecgdb, it gives relatively better maternal R-peaks for nearly all records and mostly 100% accuracy for channel four as seen in Figure 4.13.The record r01 (channel 2) scored a low 70% accuracy giving large FN and FP values. Out of the 55 nifecgdb records, sixteen records scored FN and FP values in some of its 4 channels. The rest of the 39 records did not miss any R-peaks and gave 100% accuracy. Among the 16 records, three of the four channels of record ecgca771 gave the least accuracy in the range of 63-67% as seen in Figure 4.14. All the seventy-five records from the Phy C database were evaluated using our algorithm as shown in Figure 4.15. Since all channels for each record displayed a similar aECG signal, we referred to channel four for our evaluation. Out of the seventy – five records, fifty-nine records scored 100% for Se, PPV and F_1 as shown in Figure 4.15. Out of the remaining sixteen records only 4 records scored less than 95% accuracy, while record a29 displayed the worst accuracy of 77.99%. Records a29, a33, a38 and a66 displayed poor percentage of FD.

4.6 QRS detection using LPST FIR BPF Model II

4.6.1 Performance evaluation of the QRS detector to obtain fetal and maternal R-peaks using LPST FIR BPF Model II

To illustrate the performance of the FQRS detector we evaluated our LPST algorithm for the adfecgdb database for the one minute record r08 (channel 4) and found the TP = 132; FN = 1 and FP = 0. The sensitivity, PPV and F_1 were obtained to be 99.24 %, 100% and 99.61%, respectively. The average FHR values for the true reference and LPST algorithm FHR were computed to be 132.09 bpm and 132.59 bpm, respectively. The Figure 4.16 illustrates the true reference FHR bpm plotted with our LPST FIR filter algorithm based FHR for record r08. The dotted lines indicate the ± 10 bpm bands with respect to the true reference FHR trace. It was seen that the difference between the reference FHR and algorithm FHR for most peaks was less than ± 8 bpm.

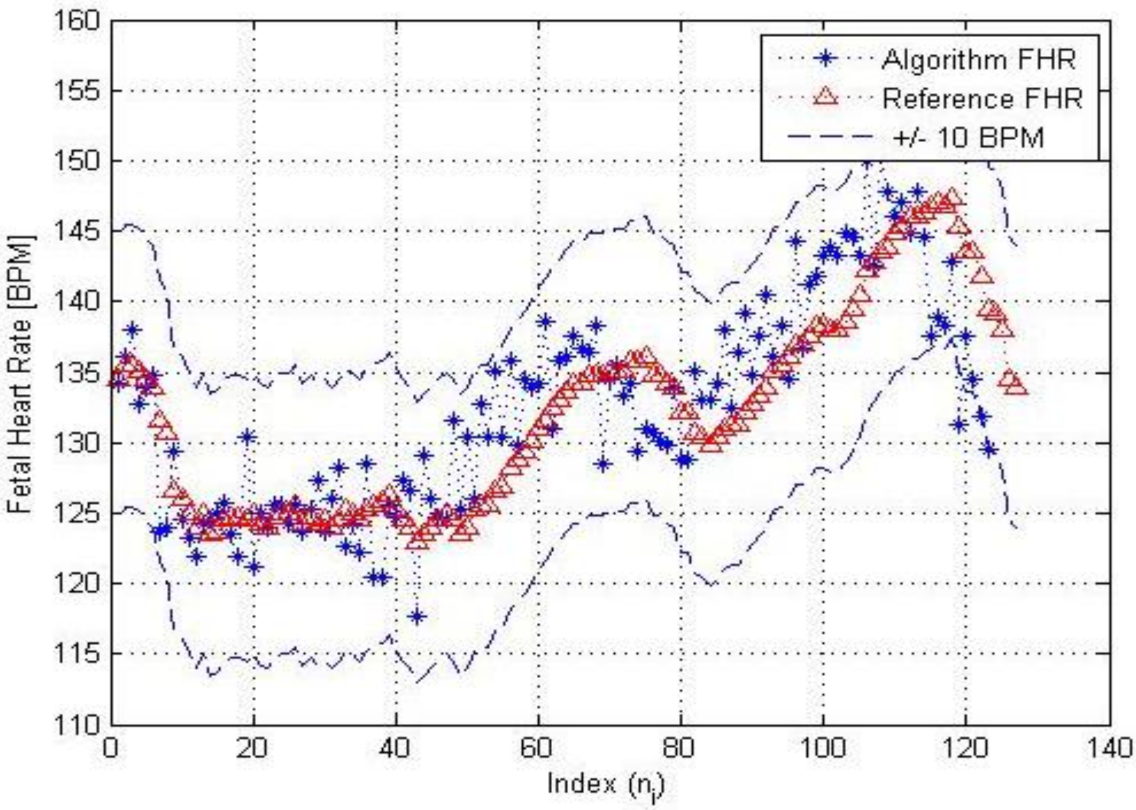

Figure 4.16: Illustration of the true reference FHR (direct scalp ECG) plotted along with the LPST FIR BPF Model II algorithm computed FHR for record r08 of adfecgdb (channel four) for one minute trace with filter order N = 1001. Blue dotted lines indicate the ±10 bpm limits with respect to the reference FHR trace.

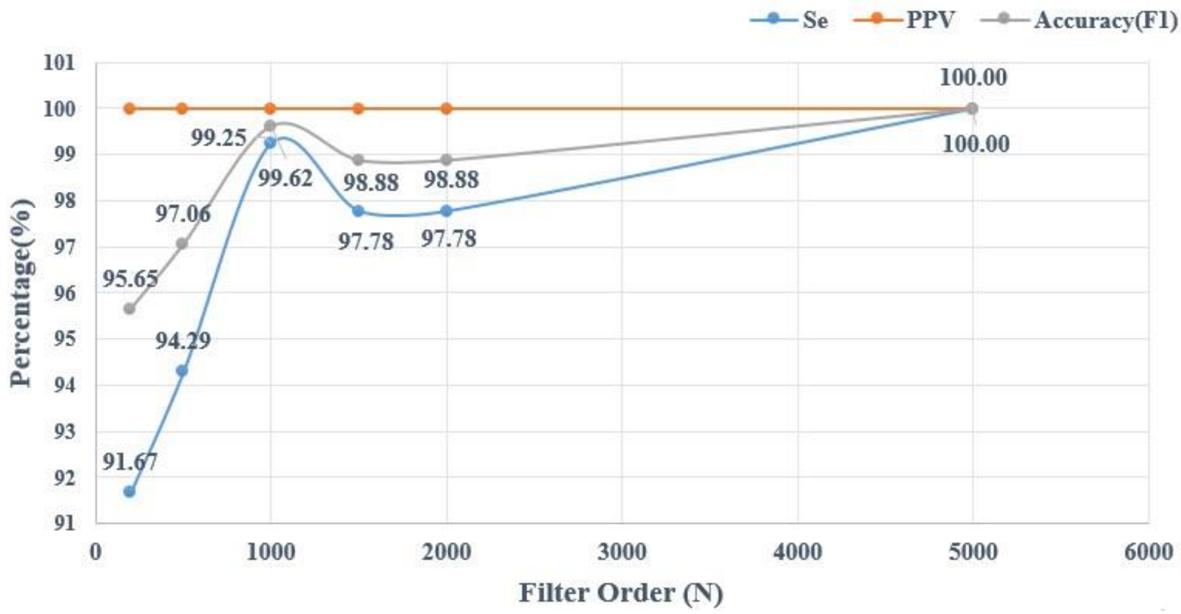

Figure 4.17: Sensitivity (Se), positive predictive value (PPV) and accuracy (F_1) of record r08 (adfecgdb) for various filter order (N).

The performance curve of Se, PPV and F_1 are highly linear in the range of filter orders (N) from 2001 to 5001 as seen in Figure 4.17. This improvement may be due to better filtering at higher order.

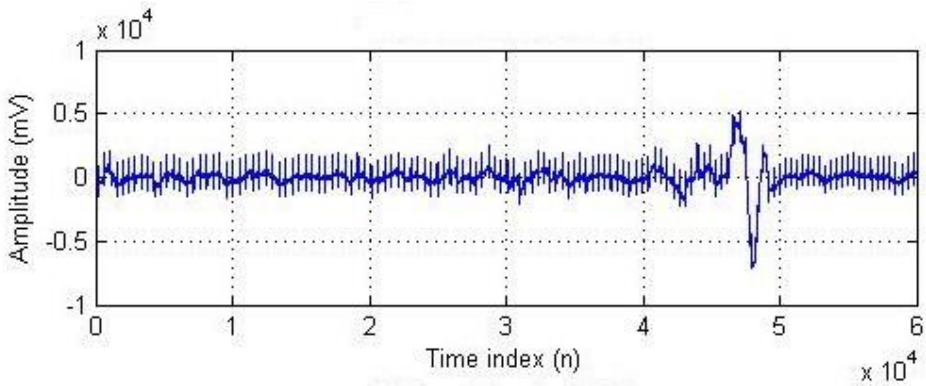

4.18 (a)

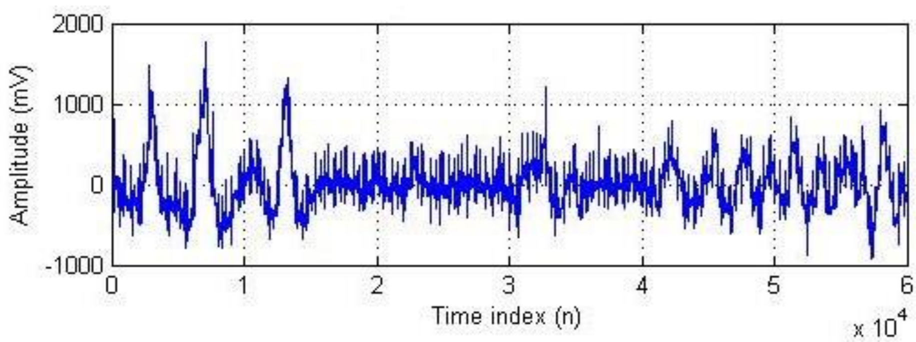

4.18 (b)

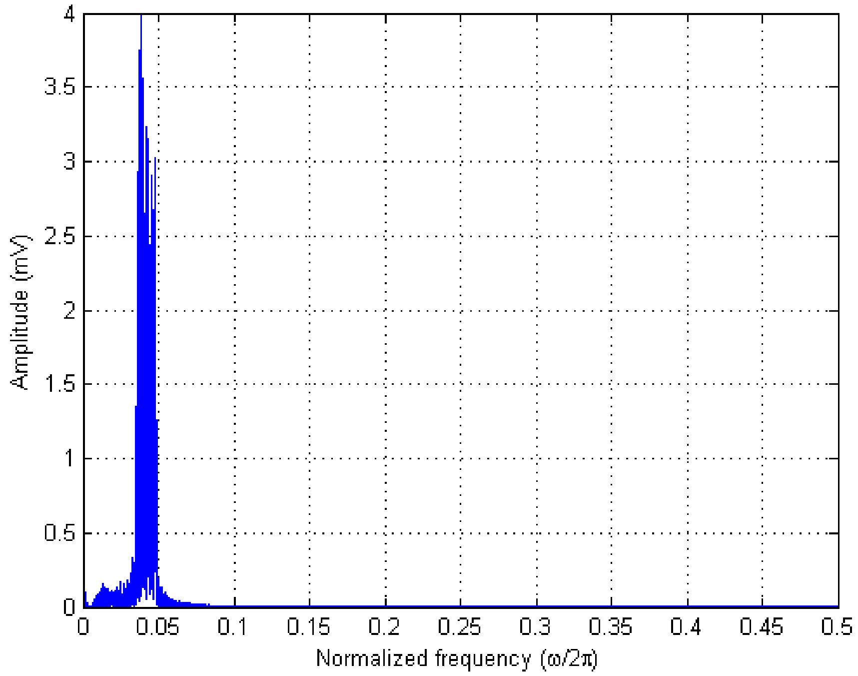

4.18 (c)

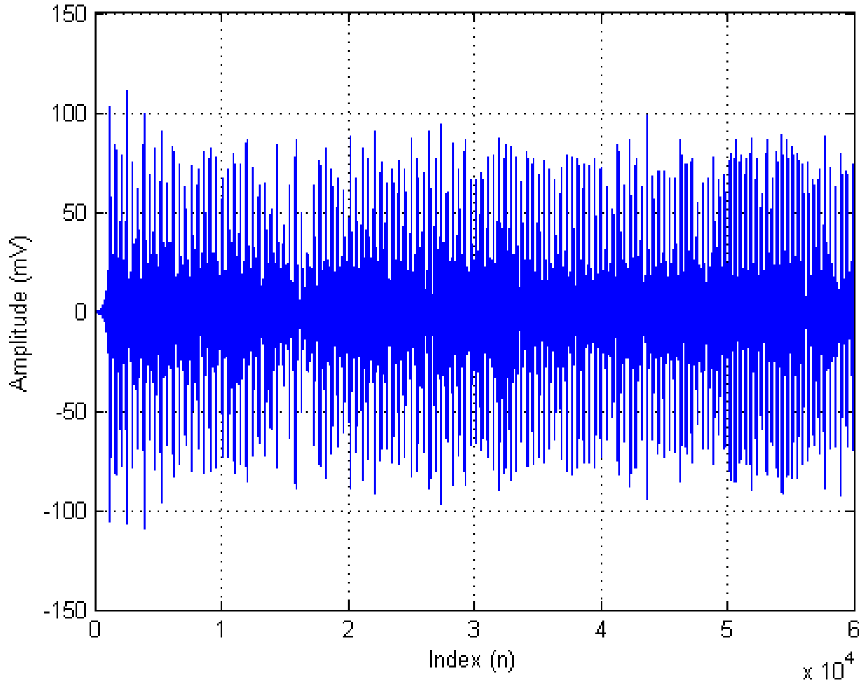

4.18 (d)

Figure 4.18: Physionet adfecgdb database (record r08) (a) Direct fetal scalp ECG signal (channel one) as true reference FECG (b) Raw maternal aECG (channel 4). (c) Frequency spectrum of the narrow sharp transition band pass filtered signal for filter order N = 5001 (d) FQRS signal after band pass filtering.

The direct fetal scalp ECG is the true reference FECG signal (channel one) as shown in Figure 4.18a. The raw maternal aECG signals were taken from record r08 (channel 4) of the adfecgdb database as shown in Figure 4.18b.The frequency spectrum of the signal passed through LPST BPF Model II (the lower frequencies up to 35Hz and higher frequencies higher than 49Hz) is as shown in Figure 4.18c. The band pass filtering effectively gives us the required frequency spectrum of the FECG, which can be seen in the time domain plot in Figure 4.18d.

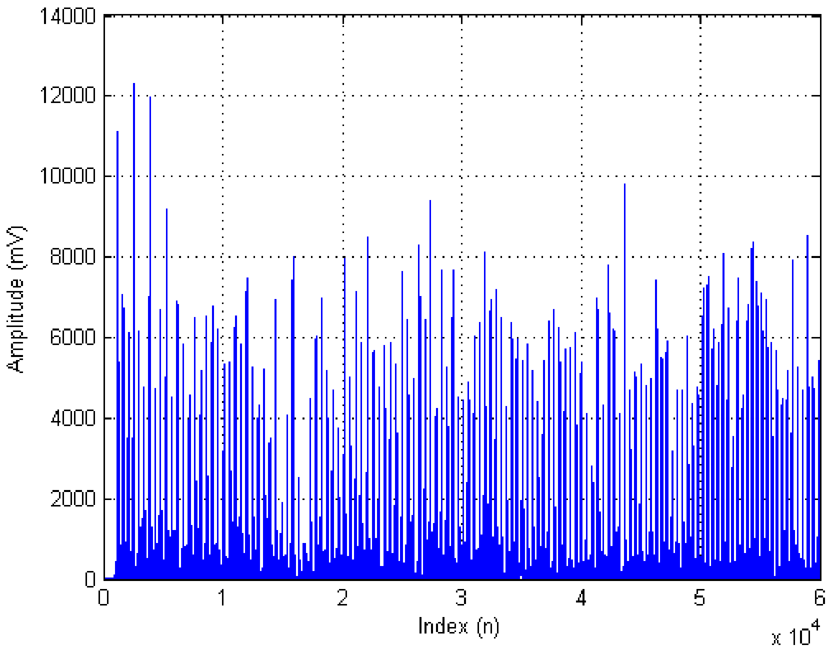

4.19 (a)

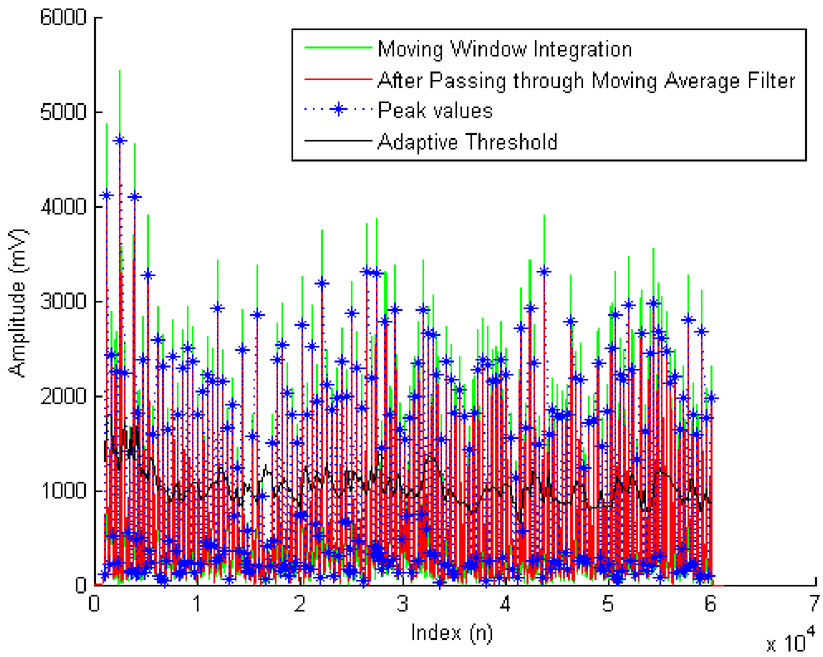

4.19 (b)

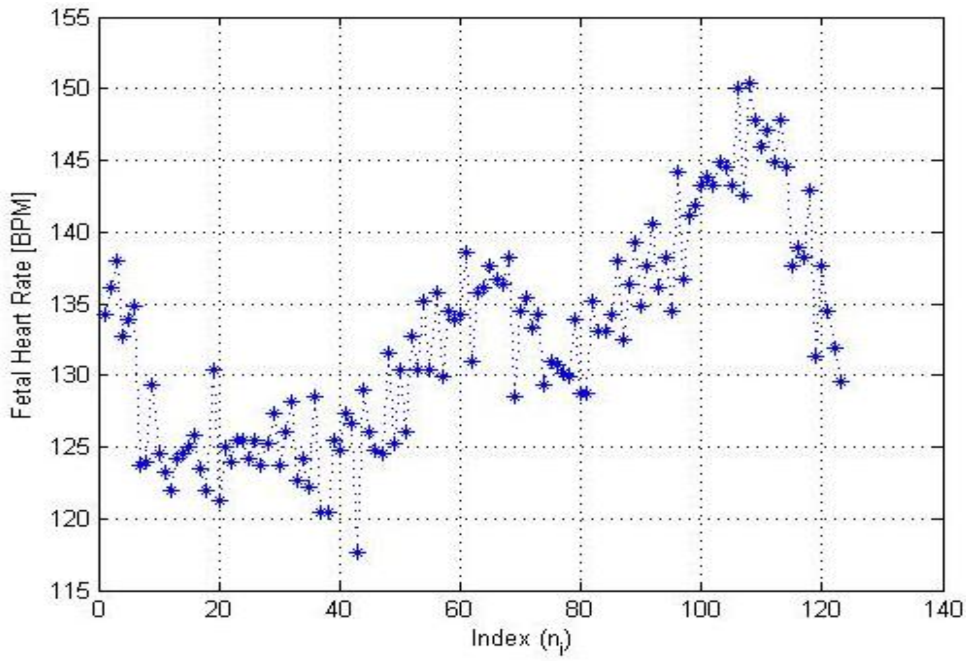

4.19 (c)

Figure 4.19: Non-invasive FHR detector for adfecgdb database (channel 4 - record r08) (a) Amplitude squaring of fetal R-peaks (b) Moving window Integration and adaptive threshold (c) FHRV.

When the FQRS signal is passed through an amplitude squarer, the predefined positive peaks are prominently amplified as shown in Figure 4.19(a). Figure 4.19(b) shows the moving window integrator which integrates this signal with a selected window size effectively picking the correct fetal R-peaks indices. An illustration from Figure 4.19(b) shows the time indices (n) for the first two detected R fetal peaks to be 3155 and 2709 respectively, which are above the adaptive threshold value. As shown in Figure 4.19c, the FHR at these $n_{i=1}$ and $n_{i=2}$ are computed to be 134.52 bpm using the Eq. (4.10).

Among the four cases of fetal frequency fiduciary edges of the BPF, *case 1*: 27Hz – 53Hz will absorb some of the PLI in the ECG record, whereas *case 2*: 27Hz – 48Hz avoids PLI unlike case 1 but has a partial overlap spectrum of maternal ECG. Similarly *case 3*: 35Hz – 53Hz will have PLI problem but has no maternal spectrum overlap. Finally the *case 4*: 35 Hz to 48 Hz can be considered optimum since the maternal spectrum overlap and PLI is absent. In spite of narrowing the spectrum in this case there are no fetal missing beats. The illustration of the true reference FHR plotted with our LPST FIR algorithm computed FHR for the four cases of fetal frequency fiduciary edges of the BPF is seen in the Figure 4.20. The dotted lines indicate the ±10 bpm limit with respect to the reference FHR trace.

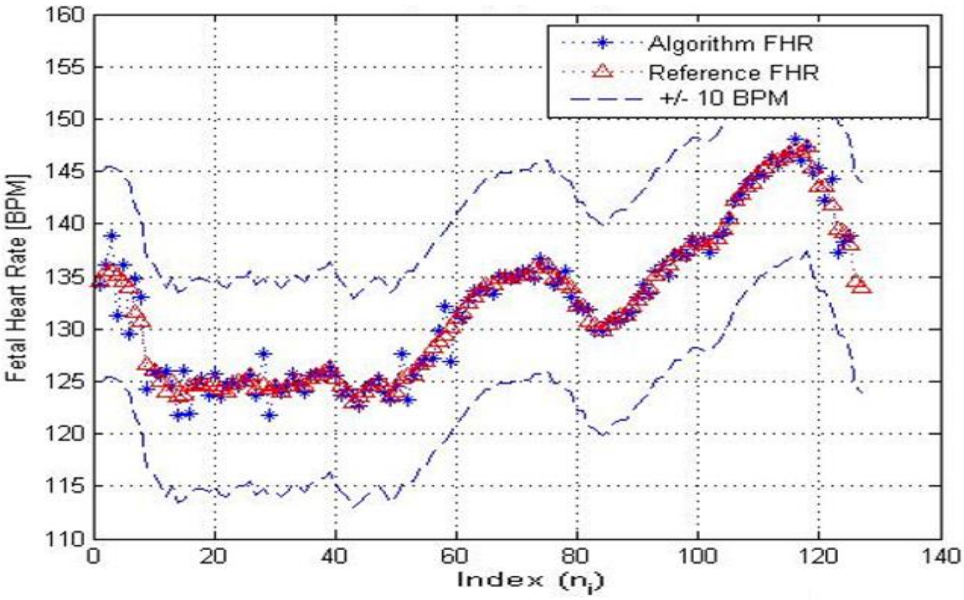

4.20 (a)

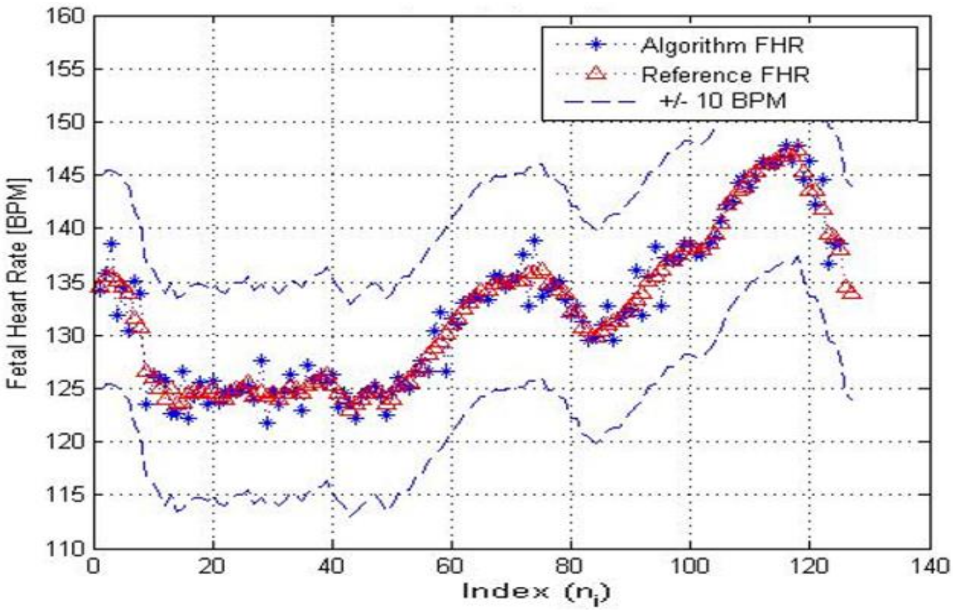

4.20 (b)

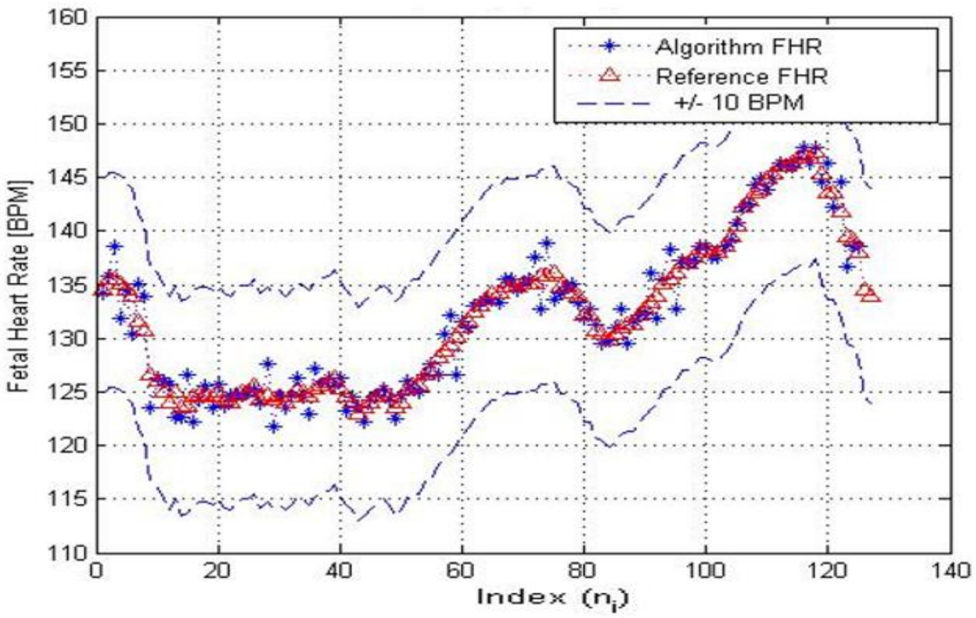

4.20 (c)

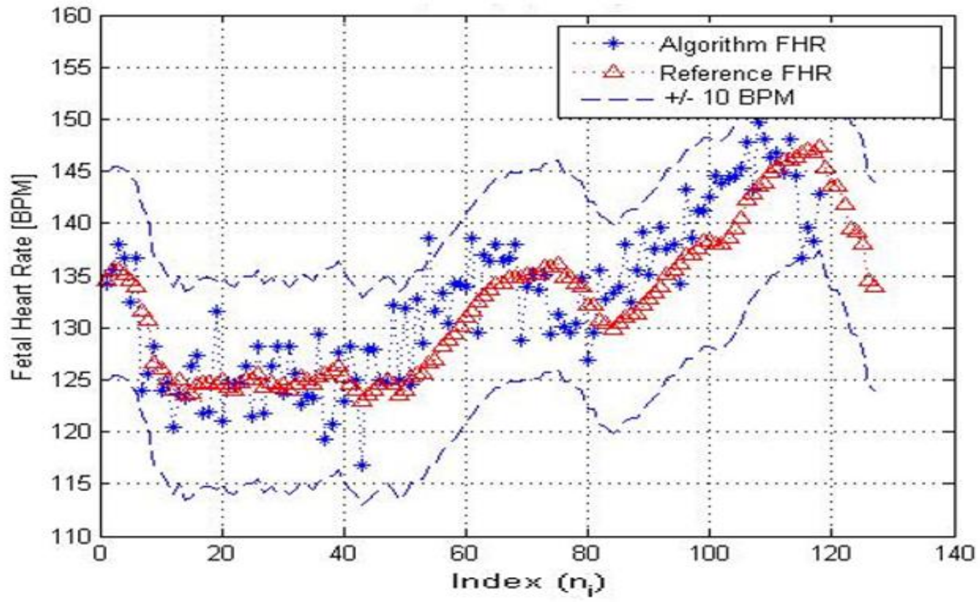

4.20 (d)

Figure 4.20: Illustration of the true reference FHR plotted along with LPST FIR BPF Model II computed FHR for four sets of fetal frequency fiduciary edges of the BPF. The signal used is a one minute trace of record r08, channel 4 of adfecgdb (n_i is the time index corresponding to the i[th] computed fetal R-peak at the output of the FQRS detector). (a) *Case 1*: 27Hz – 53Hz (b) *Case 2*: 27Hz – 48Hz (c) *Case 3*: 35Hz – 53Hz (d) *Case 4*: 35Hz – 48Hz. The dotted lines indicate the ±10 bpm limits with respect to the reference FHR trace.

The modified QRS detector was used to compute the fetal R-peaks for adfecgdb records databases using LPST FIR Model II filter. Table 4.5 displays the performance evaluation of the FQRS detection for the five adfecgdb records. The fetal R-peaks generated by the LPST FIR BPF algorithm were compared with the Physionet FQRS annotations. Graphical representation of the evaluation of the FQRS detection using Model II of adfecgdb database is shown in Figure 4.21.

Table 4.5: Performance evaluation of the FQRS detection using LPST FIR BPF Model II for adfecgdb database.

Record [channel]	TP	FN	FP	Se	PPV	F_1
r01 [1]	129	8	0	94.16	100.00	96.99
r01[2]	129	13	0	90.85	100.00	95.20
r01[3]	129	9	0	93.48	100.00	96.63
r01[4]	129	0	0	100.00	100.00	100.00
r04[1]	125	43	7	74.40	94.70	83.33
r04[2]	125	16	7	88.65	94.70	91.58
r04[3]	125	56	12	69.06	91.24	78.62
r04[4]	125	70	14	64.10	89.93	74.85
r07 [1]	132	47	12	73.74	91.67	81.73
r07[2]	132	17	10	88.59	92.96	90.72
r07[3]	132	70	18	65.35	88.00	75.00
r07[4]	132	23	13	85.16	91.03	88.00
r08 [1]	132	14	4	90.41	97.06	93.62
r08[2]	132	12	5	91.67	96.35	93.95
r08[3]	132	6	1	95.65	99.25	97.42
r08[4]	132	0	0	100.00	100.00	100.00
r10 [1]	132	17	9	88.59	93.62	91.03
r10[2]	132	14	13	90.41	91.03	90.72
r10[3]	132	45	14	74.58	90.41	81.73
r10[4]	132	20	6	86.84	95.65	91.03

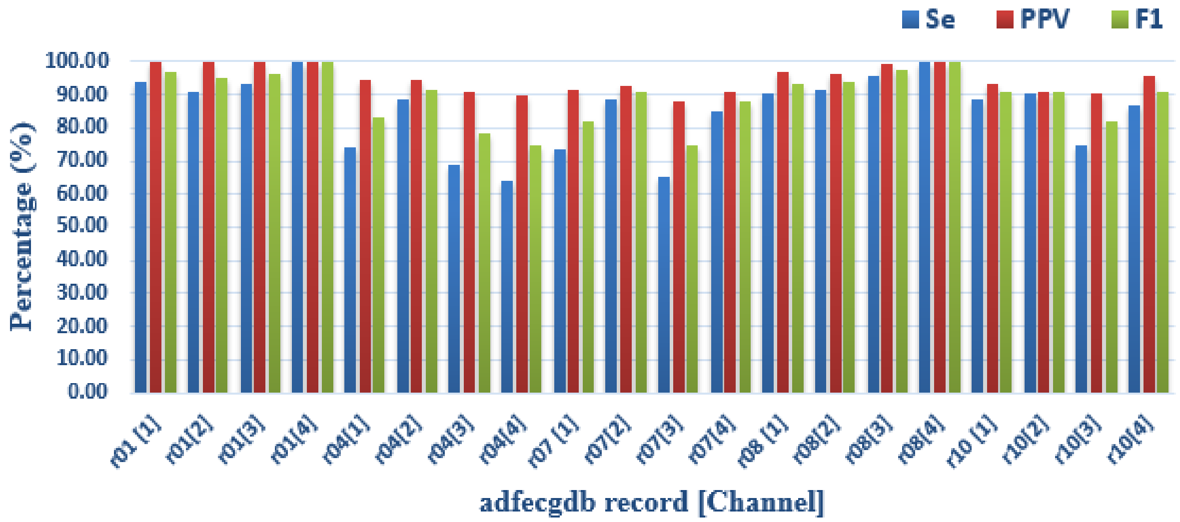

Figure 4.21: Graphical representation of the evaluation of the FQRS detection using LPST FIR BPF Model II of adfecgdb database.

The extension of this technique of non-invasive heart rate detection to maternal heart rate detection is done by merely changing the fiduciary edges of the BPF to $\omega_{s1} = 10\pi$ and $\omega_{s2} = 40\pi$ and is equally effective as in the case of FHR as shown in Figure 4.22(a) to 4.22(d). An illustration of the adfecgdb record r01 (channel 3) detected, TP = 89, FN = 3, FP = 0 to computed Se, PPV and accuracy of 96.74%, 100% and 98.34% respectively as shown in Figure 4.22(e) (see Table 4.6). Similarly the QRS detection algorithm was tested for the MHR using the Physionet nifecgdb database (see chapter section 2.7.2) for all 55 records with variable 3 to 4 channels each.

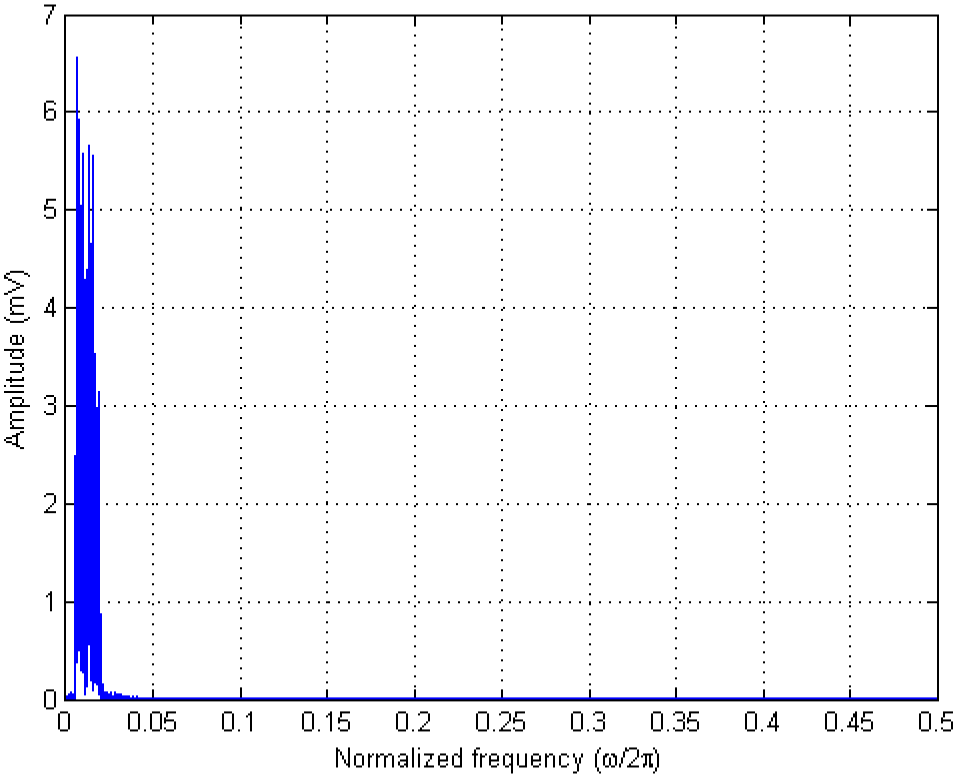

Amplitude (mV)
Normalized frequency (ω/2π)
0
1
2
3
4
5
6
7
0
0.05
0.1
0.15
0.2
0.25
0.3
0.35
0.4
0.45
0.5

4.22 (a)

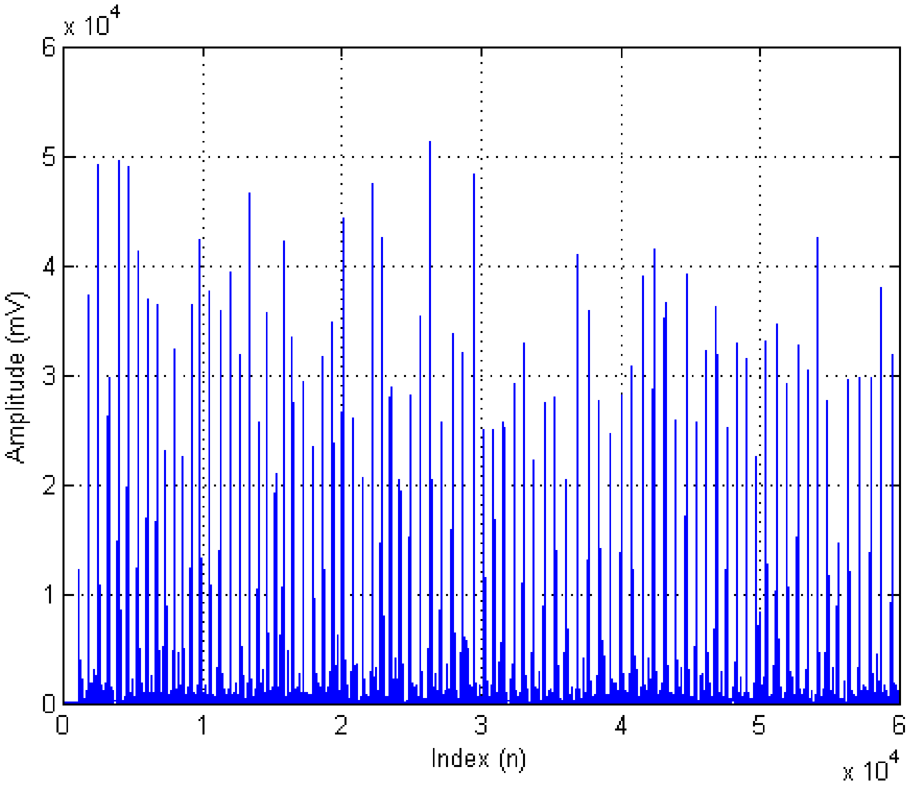

x 10^4
Amplitude (mV)
Index (n)
x 10^4
0
1
2
3
4
5
6

4.22 (b)

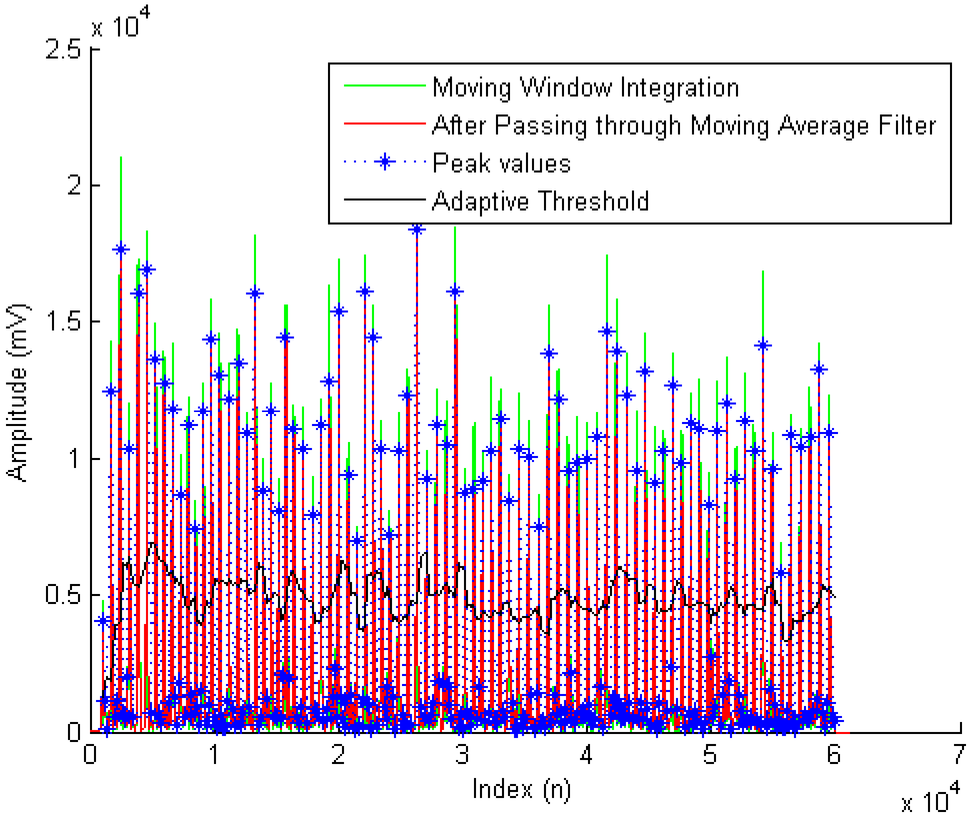
x 10^4
2.5
2
1.5
1
0.5
0
Amplitude (mV)
Moving Window Integration
After Passing through Moving Average Filter
Peak values
Adaptive Threshold
0
1
2
3
4
5
6
7
Index (n)
x 10^4

4.22 (c)

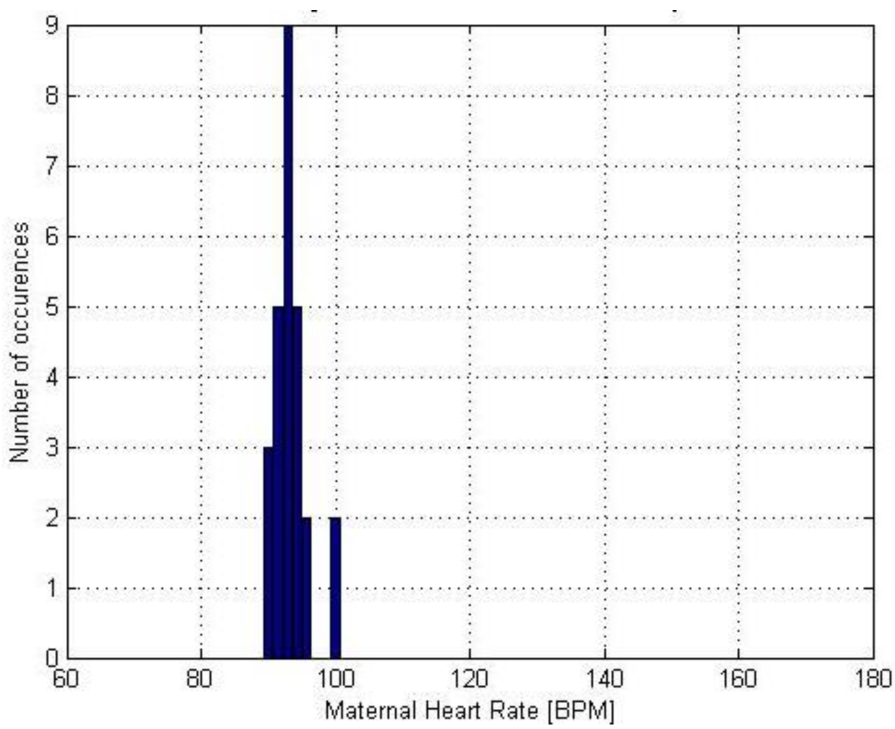
9
8
7
6
5
4
3
2
1
0
Number of occurences
60
80
100
120
140
160
180
Maternal Heart Rate [BPM]

4.22 (d)

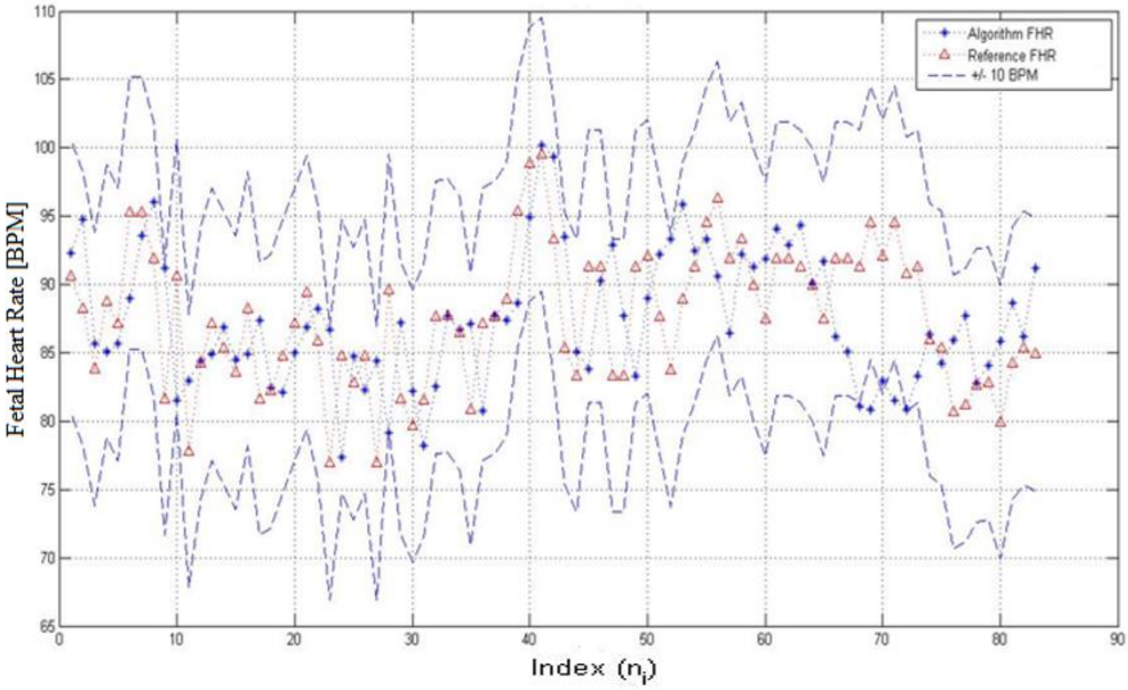

4.22 (e)

Figure 4.22: LPST BPF for MHR detection with fiduciary edges, $\omega_{s1} = 10\pi$ and $\omega_{s2} = 40\pi$ for record r01 (channel 3) of adfecgdb (a) Frequency spectrum of the narrow BPF signal (b) Amplitude squaring of maternal R-peaks (c) Moving window Integration and adaptive threshold (d) Histogram of the MHR (e) The true reference MHR plotted along with the MHR computed with our LPST FIR BPF Model II.

The maternal R wave peak index values computed from the modified QRS detector are compared with the Physionet lightwave annotation viewer for a) Abdominal and direct fetal ECG database (see Table 4.6) and b) Physionet Challenge (Phy C) 2013 database (set a) for channel four, respectively (see Table 4.8). However nifecgdb database has the MQRS annotations which we used to compare with our extracted maternal R-peaks. The nifecgdb and Physionet Challenge (Phy C) 2013 records displayed in Table 4.7 and Table 4.8, respectively computed FN and FP values. The rest of the other nifecgdb and Phy C records scored 100% accuracy and hence are not displayed in the Tables. Additionally, the FD are computed for each Phy C record using Eq. 4.9 and are shown in Table 4.8.

Table 4.6: Performance evaluation of the MQRS detection using LPST FIR BPF Model II for adfecgdb database.

Record [channel]	TP	FN	FP	Se	PPV	F_1
r01 [1]	89	0	2	100.00	97.80	98.89
r01[2]	89	37	5	70.63	94.68	80.91
r01[3]	89	3	0	96.74	100.00	98.34
r01[4]	89	0	0	100.00	100.00	100.00
r04[1]	83	8	0	91.21	100.00	95.40
r04[2]	83	0	0	100.00	100.00	100.00
r04[3]	83	9	2	90.22	97.65	93.79
r04[4]	83	0	2	100.00	97.65	98.81
r07 [1]	77	6	6	92.77	92.77	92.77
r07[2]	77	0	0	100.00	100.00	100.00
r07[3]	77	2	1	97.47	98.72	98.09
r07[4]	77	0	1	100.00	98.72	99.35
r08 [1]	92	0	1	100.00	98.92	99.46
r08[2]	92	42	6	68.66	93.88	79.31
r08[3]	92	2	0	97.87	100.00	98.92
r08[4]	92	1	2	98.92	97.87	98.40
r10 [1]	105	0	6	100.00	94.59	97.22
r10[2]	105	0	3	100.00	97.22	98.59
r10[3]	105	7	6	93.75	94.59	94.17
r10[4]	105	0	0	100.00	100.00	100.00

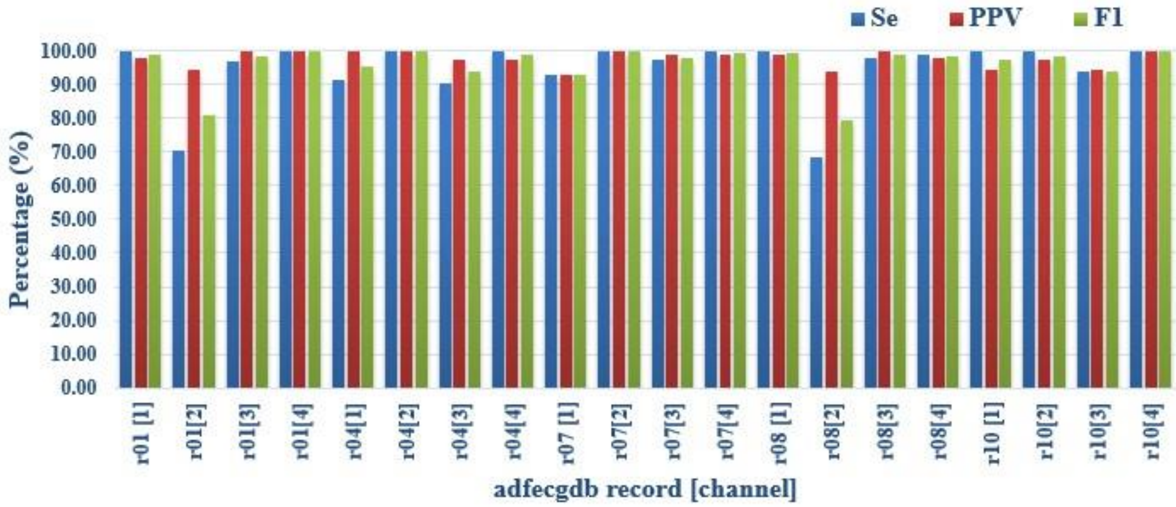

Figure 4.23: Graphical representation of the evaluation of the MQRS detection using LPST FIR BPF Model II for adfecgdb database.

Table 4.7: Performance evaluation of the MQRS detection using LPST FIR BPF Model II for nifecgdb database.

Record [channel]	TP	FN	FP	Se	PPV	F_1
ecgca416[01]	55	0	0	100.00	100.00	100.00
ecgca416[02]	55	3	7	94.83	88.71	91.67
ecgca416[03]	55	0	4	100.00	93.22	96.49
ecgca416[04]	55	0	27	100.00	67.07	80.29
ecgca436[01]	56	0	0	100.00	100.00	100.00
ecgca436[02]	56	0	2	100.00	96.55	98.25
ecgca436[03]	56	0	2	100.00	96.55	98.25
ecgca436[04]	56	0	2	100.00	96.55	98.25
ecgca597[01]	53	0	0	100.00	100.00	100.00
ecgca597[02]	53	0	0	100.00	100.00	100.00
ecgca597[03]	53	0	2	100.00	96.36	98.15
ecgca597[04]	53	0	8	100.00	86.89	92.98
ecgca649[01]	53	0	0	100.00	100.00	100.00
ecgca649[02]	53	2	7	96.36	88.33	92.17
ecgca649[03]	53	0	1	100.00	98.15	99.07
ecgca771[01]	47	0	0	100.00	100.00	100.00
ecgca771[02]	47	1	0	97.92	100.00	98.95
ecgca771[03]	47	0	1	100.00	97.92	98.95
ecgca771[04]	47	0	1	100.00	97.92	98.95
ecgca811[01]	52	0	0	100.00	100.00	100.00
ecgca811[02]	52	0	0	100.00	100.00	100.00
ecgca811[03]	52	0	1	100.00	98.11	99.05
ecgca848[01]	53	0	0	100.00	100.00	100.00
ecgca848[02]	53	0	0	100.00	100.00	100.00
ecgca848[03]	53	3	16	94.64	76.81	84.80
ecgca848[04]	53	2	22	96.36	70.67	81.54
ecgca902[01]	55	0	0	100.00	100.00	100.00
ecgca902[02]	55	0	6	100.00	90.16	94.83
ecgca902[03]	55	0	0	100.00	100.00	100.00
ecgca906[01]	53	0	2	100.00	96.36	98.15
ecgca906[02]	53	0	2	100.00	96.36	98.15
ecgca906[03]	53	1	3	98.15	94.64	96.36
ecgca906[04]	53	0	2	100.00	96.36	98.15
ecgca968[01]	54	0	0	100.00	100.00	100.00
ecgca968[02]	54	1	7	98.18	88.52	93.10
ecgca968[03]	54	0	8	100.00	87.10	93.10
ecgca968[04]	54	20	9	72.97	85.71	78.83

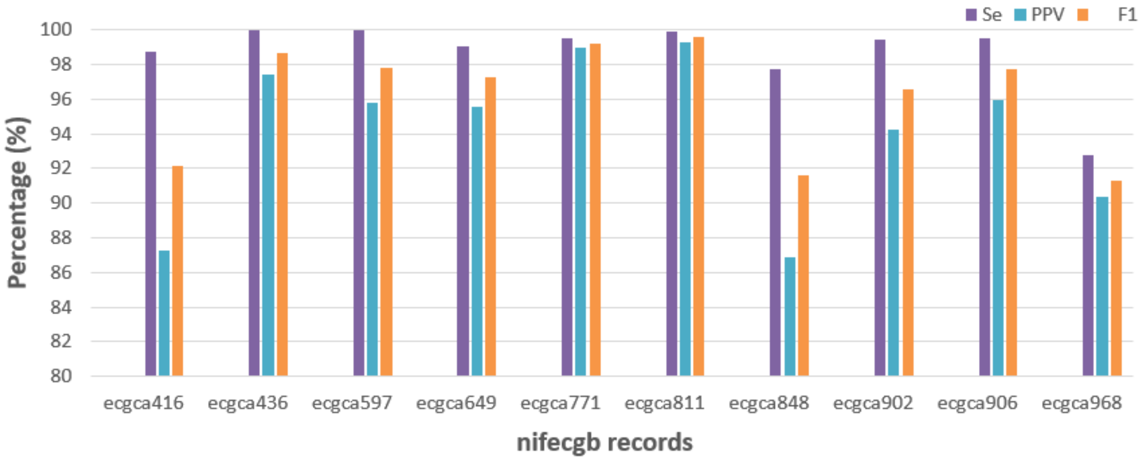

Figure 4.24: Graphical representation of the evaluation of the MQRS detection using LPST FIR BPF Model II for nifecgdb database.

Table 4.8: Performance evaluation of the MQRS detection using LPST FIR BPF Model II for Phy C 2013 database.

Record [channel]	TP	FN	FP	FD	Se	PPV	F_1
a29	62	8	24	51.61	88.57	72.09	79.49
a33	94	0	1	1.06	100.00	98.95	99.47
a34	76	0	14	18.42	100.00	84.44	91.57
a38	79	4	21	31.65	95.18	79.00	86.34
a41	112	0	33	29.46	100.00	77.24	87.16
a53	73	1	34	47.95	98.65	68.22	80.66
a56	93	4	3	7.53	95.88	96.88	96.37
a66	82	65	2	81.71	55.78	97.62	71.00
a73	96	0	5	5.21	100.00	95.05	97.46

*The aECG data was obtained from channel four for all records.

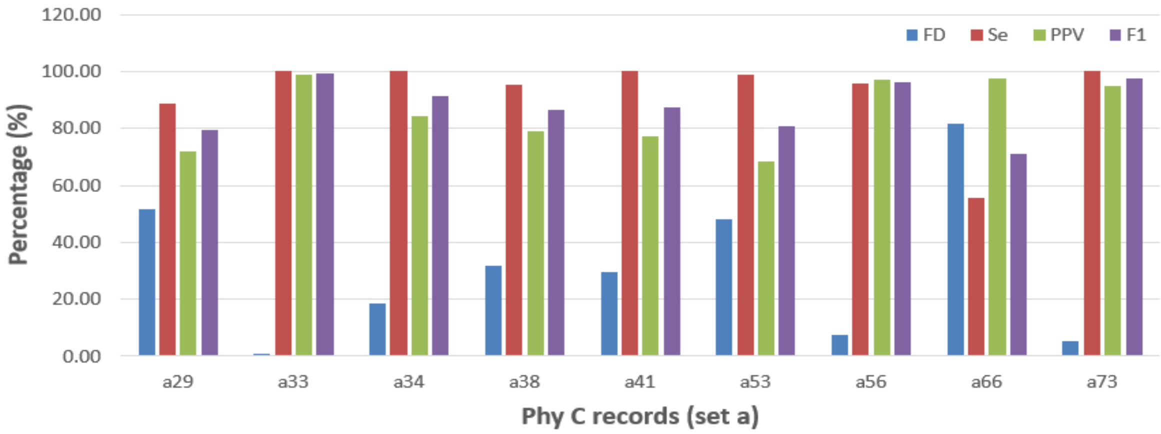

Figure 4.25: Graphical representation of the evaluation of the MQRS detection using LPST FIR BPF Model II for Phy C database.

4.6.2 Discussion of filter synthesis using LPST FIR BPF Model II

The accuracy for detecting fetal R-peaks of adfecgdb was more than 93% for records r01 and r08 for channels 1 to 3 and scored 100% accuracy only for channel 4 as shown in Figure 4.21 and Table 4.5. Poor accuracy of 74.85% was scored by channel 4 of r04. Using the same database, the maternal R-peaks were well detected by using this filter Model giving an accuracy of more than 95% for most records (see Table 4.6). However, the worst scoring for FN was seen for channel 2 for the records r01 and r08 as shown in Figure 4.23. Out of the 55 nifecgdb records, 10 records displayed an accuracy of less than 100% for some of its channels to detect maternal R-peaks (see Table 4.7). It was observed that channel 1 of almost all records gave an accuracy of 100% except record ecgca906 which computed 98.15%. The record ecgca968 (channel 4) scored FN equal to 20 , while record ecgca416 scored a poor 27 for FP value as seen in Table 4.7. The nine records (channel 4) of Phy C database displayed accuracy of less than 100% as shown in Figure 4.25 (see Table 4.8). However, 66 records of the total 75 Phy C records displayed 100% accuracy to detect the maternal R-peaks and hence are not listed in the Table. Records a29, a34, a38, a41, a53 and a66 displayed a considerable percentage of FD (see Table 4.8).

4.7 QRS detection results using LPST FIR BPF Model II with Slope Matching technique (Model III)

4.7.1 Performance evaluation of the QRS detector to obtain fetal and maternal R-peaks using LPST FIR BPF Model III

We evaluated our LPST FIR BPF algorithm to compute the fetal R-peaks for adfecgdb records for all the five Physionet adfecgdb records (all 4 channels) for a duration of one minute each. The raw aECG signals are applied to the proposed LPST BPF_{slope} (Model III) with the specified fiduciary band edges. Each filtered signal is subjected to the FQRS detector. As illustrated in Figure 4.26 (record r01), the direct scalp FHR bpm closely matches the FHR based on our algorithm for filter orders ranging from 101 to 2001.Figure 4.27 shows the accuracy of the fetal R-peak detected and it was computed for all the four channels of the five aECG records. Table 4.9 displays the performance evaluation of the FQRS detection for the five adfecgdb records. The fetal R-peaks generated by the LPST FIR filter algorithm were compared with the Physionet FQRS annotations.

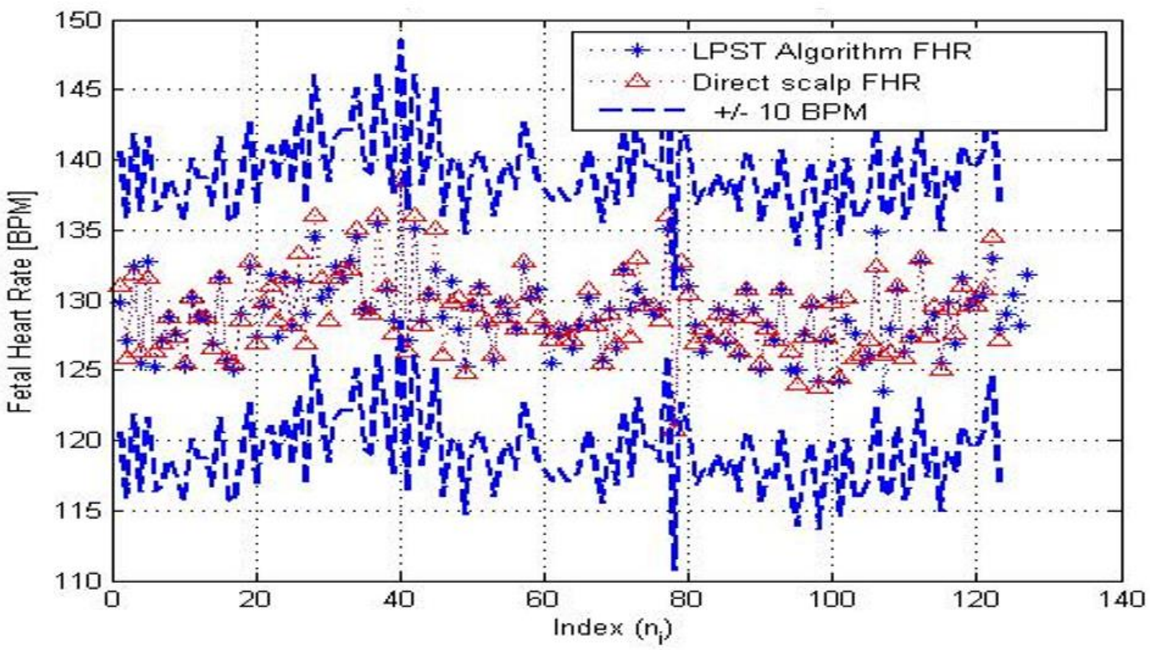

Figure 4.26: Illustration of the true reference FHR (direct scalp ECG) plotted along with the MHR computed with LPST FIR BPF Model III for record r01 of adfecgdb (channel four) for one minute trace. Blue dotted lines indicate the ±10 bpm limits with respect to the reference FHR trace. (n_i is the time index corresponding to the i^{th} computed R-fetal peak at the output of the FQRS detector).

The maternal R-peak index values computed from the modified QRS detector are compared with the Physionet lightwave annotation viewer for a) afecgdb database (see Table 4.10) and b) Physionet Challenge (Phy C) 2013 database (set a) for channel four respectively. However nifecgdb database has the MQRS annotations which we used to compare with our extracted maternal R-peak. The nifecgdb and Physionet Challenge (Phy C) 2013 records displayed in

Table 4.11 and Table 4.12 respectively computed FN and FP values. The rest of the other nifecgdb and Phy C records scored 100% accuracy and hence are not displayed in the Tables. Additionally, the FD are computed for each Phy C record using Eq. 4.9 and are shown in Table 4.12.

Table 4.9: Performance evaluation of the FQRS detection using LPST FIR BPF Model III for adfecgdb database.

Record [channel]	Channel	TP	FN	FP	Se	PPV	F_1
r01 [1]	1	129	4	0	96.99	100.00	98.47
r01[2]	2	129	9	0	93.48	100.00	96.63
r01[3]	3	129	3	0	97.73	100.00	98.85
r01[4]	4	129	0	0	100.00	100.00	100.00
r04[1]	1	125	30	6	80.65	95.42	87.41
r04[2]	2	125	8	1	93.98	99.21	96.53
r04[3]	3	125	34	10	78.62	92.59	85.03
r04[4]	4	125	15	4	89.29	96.90	92.94
r07 [1]	1	132	63	9	67.69	93.62	78.57
r07[2]	2	132	22	2	85.71	98.51	91.67
r07[3]	3	132	22	4	85.71	97.06	91.03
r07[4]	4	132	9	3	93.62	97.78	95.65
r08 [1]	1	132	8	0	94.29	100.00	97.06
r08[2]	2	132	11	0	92.31	100.00	96.00
r08[3]	3	132	6	0	95.65	100.00	97.78
r08[4]	4	132	0	0	100.00	100.00	100.00
r10 [1]	1	132	26	0	83.54	100.00	91.03
r10[2]	2	132	22	4	85.71	97.06	91.03
r10[3]	3	132	43	4	75.43	97.06	84.89
r10[4]	4	132	20	0	86.84	100.00	92.96

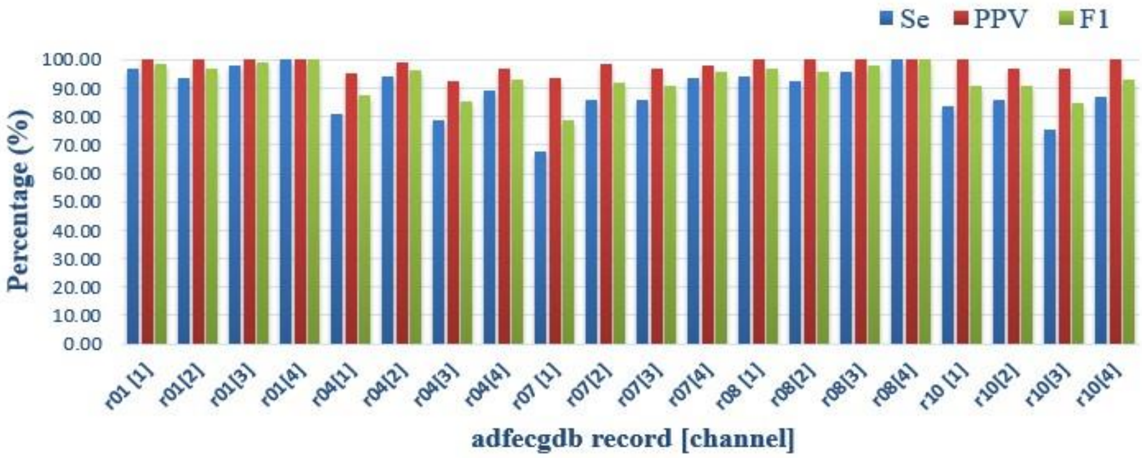

Figure 4.27: Graphical representation of the evaluation of the FQRS detection using LPST FIR BPF Model III for adfecgdb database.

Table 4.10: Performance evaluation of the MQRS detection using LPST FIR BPF Model III for adfecgdb database.

Record [Channel]	TP	FN	FP	Se	PPV	F_1
r01 [1]	89	0	1	100.00	98.89	99.44
r01[2]	89	29	7	75.42	92.71	83.18
r01[3]	89	4	2	95.70	97.80	96.74
r01[4]	89	0	0	100.00	100.00	100.00
r04[1]	83	0	4	100.00	95.40	97.65
r04[2]	83	0	0	100.00	100.00	100.00
r04[3]	83	0	0	100.00	100.00	100.00
r04[4]	83	0	5	100.00	94.32	97.08
r07 [1]	77	0	4	100.00	95.06	97.47
r07[2]	77	18	0	81.05	100.00	89.53
r07[3]	77	0	2	100.00	97.47	98.72
r07[4]	77	0	0	100.00	100.00	100.00
r08 [1]	89	53	7	62.68	92.71	74.79
r08[2]	89	6	10	93.68	89.90	91.75
r08[3]	89	0	4	100.00	95.70	97.80
r08[4]	89	0	3	100.00	96.74	98.34
r10 [1]	105	0	0	100.00	100.00	100.00
r10[2]	105	0	2	100.00	98.13	99.06
r10[3]	105	6	3	94.59	97.22	95.89
r10[4]	105	0	13	100.00	88.98	94.17

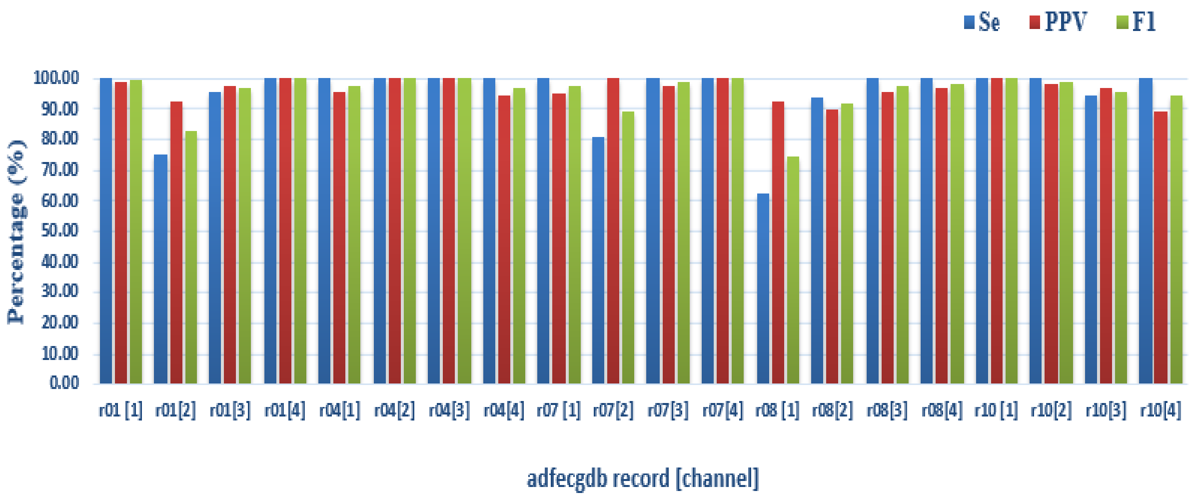

Figure 4.28: Graphical representation of the evaluation of the MQRS detection using LPST FIR BPF Model III for adfecgdb database.

Table 4.11: Performance evaluation of the MQRS detection using LPST FIR BPF filter Model III for nifecgdb database.

Record [channel]	TP	FN	FP	Se	PPV	F_1
ecgca416[01]	55	0	0	100.00	100.00	100.00
ecgca416[02]	55	3	7	94.83	88.71	91.67
ecgca416[03]	55	0	2	100.00	96.49	98.21
ecgca416[04]	55	0	27	100.00	67.07	80.29
ecgca436[01]	56	0	0	100.00	100.00	100.00
ecgca436[02]	56	0	2	100.00	96.55	98.25
ecgca436[03]	56	0	2	100.00	96.55	98.25
ecgca436[04]	56	0	2	100.00	96.55	98.25
ecgca597[01]	53	0	0	100.00	100.00	100.00
ecgca597[02]	53	0	0	100.00	100.00	100.00
ecgca597[03]	53	0	2	100.00	96.36	98.15
ecgca597[04]	53	0	4	100.00	92.98	96.36
ecgca649[01]	53	0	0	100.00	100.00	100.00
ecgca649[02]	53	1	3	98.15	94.64	96.36
ecgca649[03]	53	0	0	100.00	100.00	100.00
ecgca848[01]	53	0	0	100.00	100.00	100.00
ecgca848[02]	53	0	0	100.00	100.00	100.00
ecgca848[03]	53	3	10	94.64	84.13	89.08
ecgca848[04]	53	2	22	96.36	70.67	81.54
ecgca902[01]	55	0	0	100.00	100.00	100.00
ecgca902[02]	55	0	6	100.00	90.16	94.83
ecgca902[03]	55	0	0	100.00	100.00	100.00
ecgca906[01]	53	0	2	100.00	96.36	98.15
ecgca906[02]	53	0	2	100.00	96.36	98.15
ecgca906[03]	53	1	1	98.15	98.15	98.15
ecgca906[04]	53	0	4	100.00	92.98	96.36
ecgca968[01]	54	0	0	100.00	100.00	100.00
ecgca968[02]	54	2	10	96.43	84.38	90.00
ecgca968[03]	54	3	4	94.74	93.10	93.91
ecgca968[04]	54	20	7	72.97	88.52	80.00

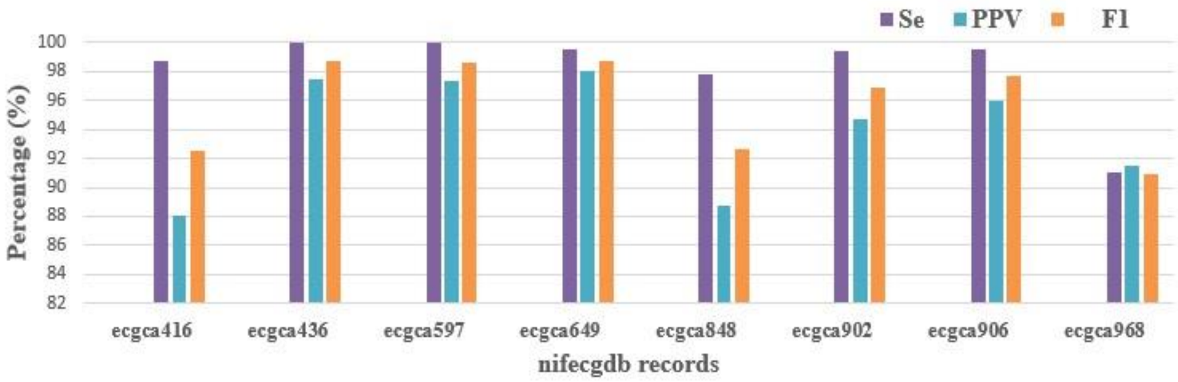

Figure 4.29: Graphical representation of the evaluation of the MQRS detection using LPST FIR BPF Model III for nifecgdb database.

Table 4.12: Performance evaluation of the MQRS detection using LPST FIR BPF Model III for Physionet Challenge 2013 (set a) database.

Record	TP	FN	FP	FD	Se	PPV	F_1
a29	62	11	18	46.77	84.93	77.50	81.05
a33	94	0	5	5.32	100.00	94.95	97.41
a34	76	0	2	2.63	100.00	97.44	98.70
a38	79	8	16	30.38	90.80	83.16	86.81
a41	112	0	0	0.00	100.00	100.00	100.00
a53	73	0	0	0.00	100.00	100.00	100.00
a56	93	0	2	2.15	100.00	97.89	98.94
a66	82	1	0	1.22	98.80	100.00	99.39
a73	96	0	0	0.00	100.00	100.00	100.00

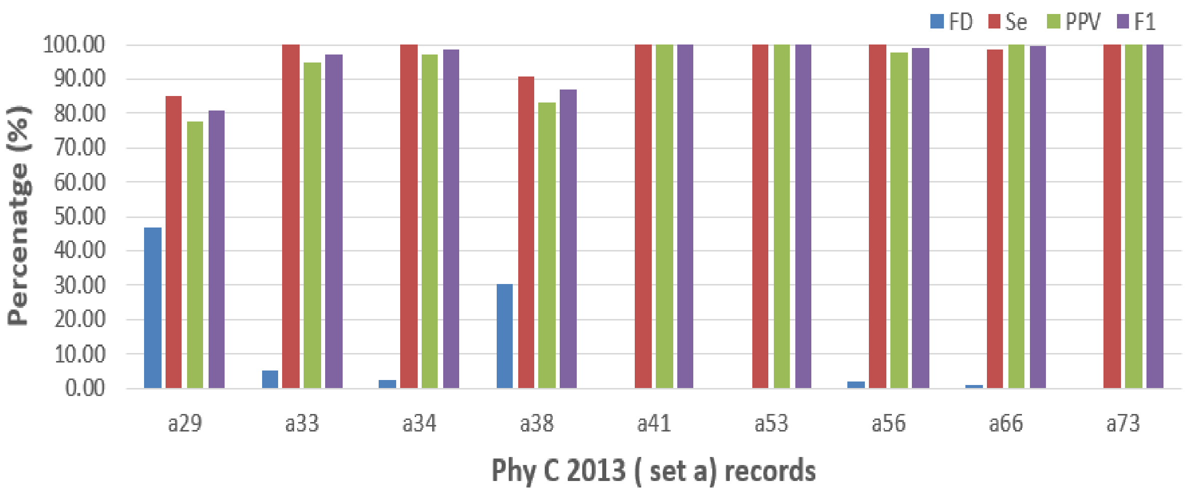

Figure 4.30: Graphical representation of the evaluation of the MQRS detection using LPST FIR BPF Model III of Physionet Challenge 2013 (set a) database.

4.7.2 Discussion of filter synthesis using LPST FIR BPF Model III

It is seen that for most adfecgdb records when compared to the direct fetal scalp recordings, our obtained FHR variability values almost match the reference FHR. Records r04 and r07 showed a few missing fetal peaks, while records r01[4] and r08[4] had fetal beats that were neither falsely identified nor missed, giving 100% accuracy as shown in Figure 4.27. Mostly all channels of the adfecgdb records gave accuracy more than 95% to detect maternal R-peaks except from certain channels of r01 and r08 as shown in Figure 4.28. Eight of the 55 records displayed measure of accuracy between 80 - 100%, record ecg968 (channel 4) having the lowest accuracy of 80% as seen in Figure 4.29. Out of the total 75 Phy C records, only 8% of the records scored an accuracy of less than 100% to detect the maternal R-peaks. The two records a29 and a38, scored FD of 46.77% and 30.38% respectively as shown in Figure 4.30 (see Table 4.12).

4.8 Discussion and conclusion

The accuracy was computed to evaluate the performance of the three LPST FIR filter Models I, II and III for the five adfecgdb records. The average values of accuracy for each record for each of the FIR filter Models are seen in Figure 4.31. It is observed that the accuracy increases from Model I to Model III for some of the records such as r01, r08 and r10.

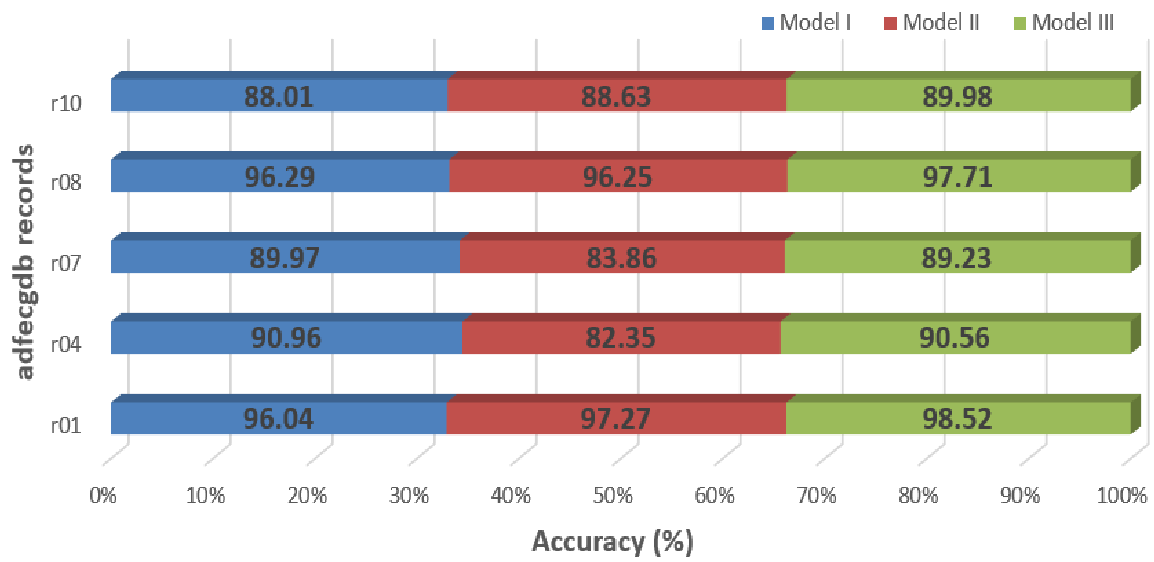

Figure 4.31: Accuracy of FHR detection using LPST FIR BPF Models I, II and IIII for adfecgdb records.

In the abdominal ECG signal, it is observed that the FECG and MECG signals overlap in time domain or exist in very close proximity as shown in Figure 4.32 (a). With our designed LPST FIR filters, it is possible to compute the FHR and MHR with these above constraints. The difference in the FHR and MHR between the LPST FIR filter algorithm HR and reference HR is minimal for the six occurrences of the FQRS-MQRS signals overlap for the adfecgdb record r01, channel four (one minute duration) as shown in Figure 4.33. Similarly, the eleven occurrences where a fetal and maternal QRS exist in close proximity as shown in Figure 4.32 (b) and also have minimal difference in the time index between fetal and maternal R-peaks are shown in Figure 4.34. The use of our LPST FIR filter Models to filter out our designated fetal and maternal fiduciary band edges are not affected by the two above constraints. The same is seen in Figure 4.35 and Figure 4.36, wherein the FHR and MHR for the record r01, channel four gives 100% accuracy and detects all the fetal and maternal R-peaks. It is observed that due to noise corrupted sections in the abdominal ECG (see Figure 4.33(c)) the accuracy for detecting R-peaks is lowered as seen in the record r01 (channel two) of the adfecgdb (see FN value in Table 4.9 and Table 4.10)

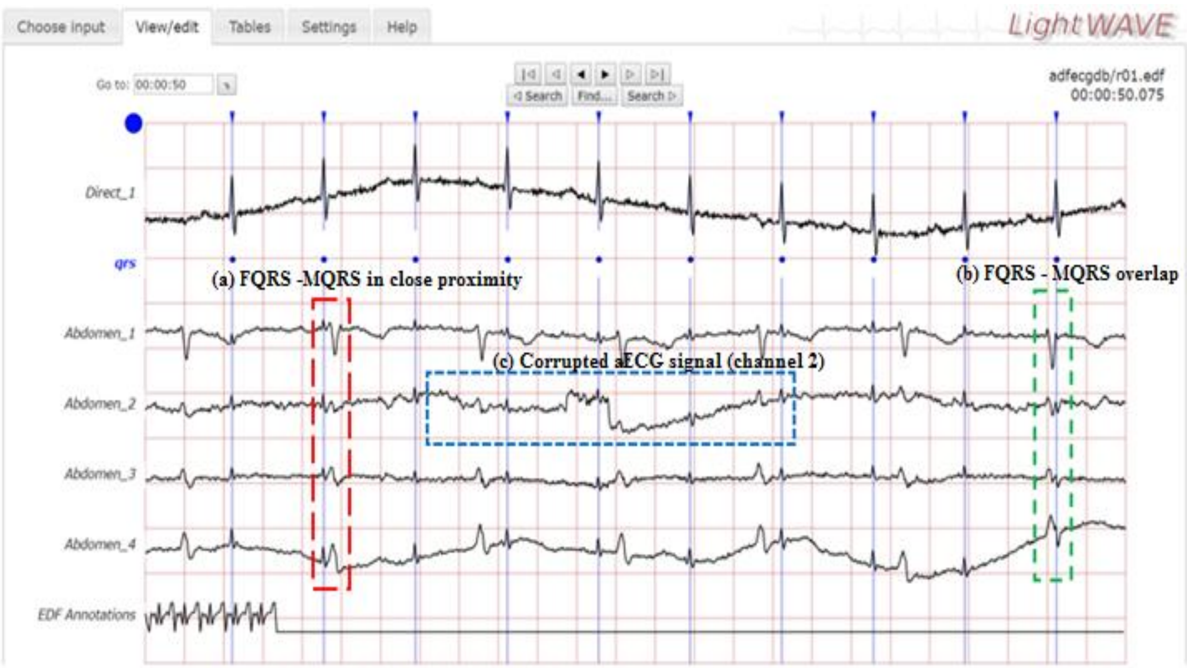

Figure 4.32: FQRS and MQRS signals in time domain (a) Overlap fetal and maternal QRS signals (green dashes) (b) Close proximity of the fetal and maternal QRS signals in time (red dashes). (c) Corrupted abdominal ECG signal (channel 2) scores low measure of accuracy for fetal and maternal QRS detection. Raw abdominal ECG signal record r01 taken from Physionet adfecgdb database.

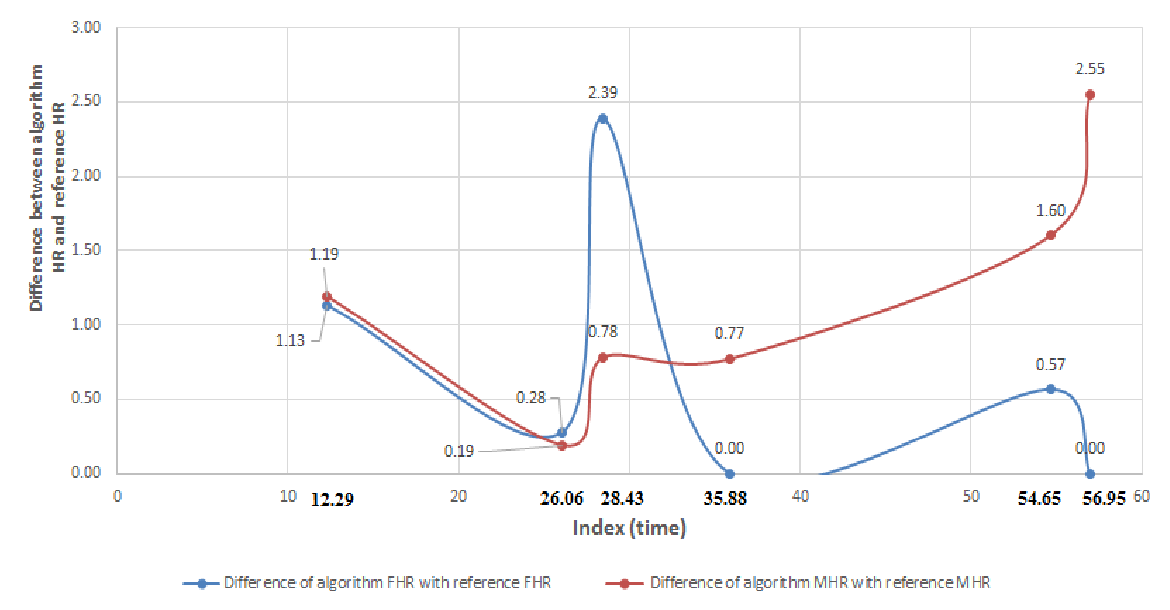

Figure 4.33: Difference in heart rate between fetal and maternal R-peaks when the two signals overlap in time domain.

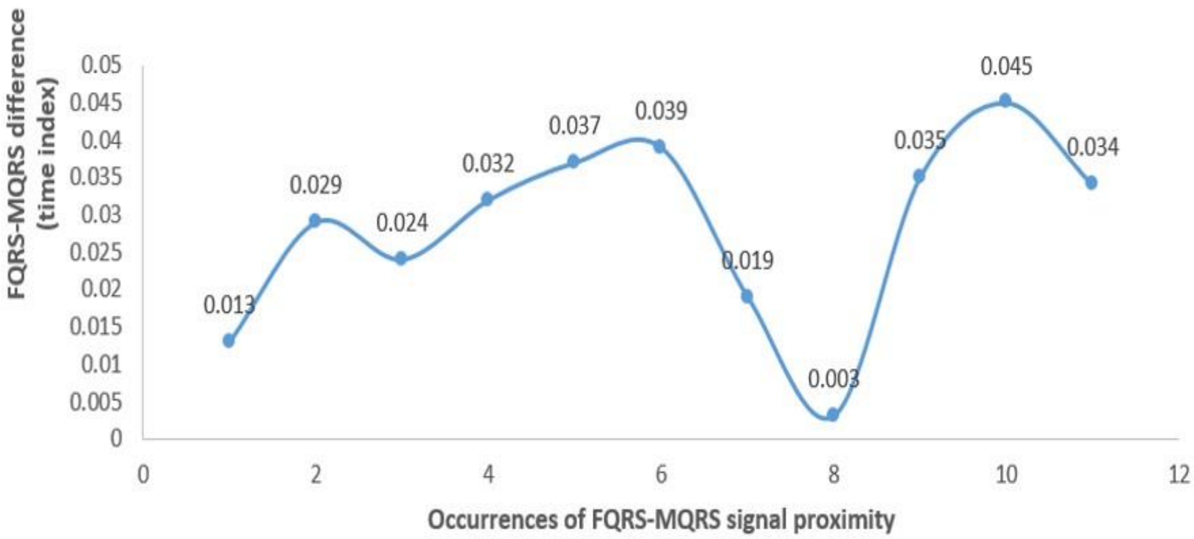

Figure 4.34: Difference in the index between fetal and maternal R-peaks when the two signals are in close proximity in time domain.

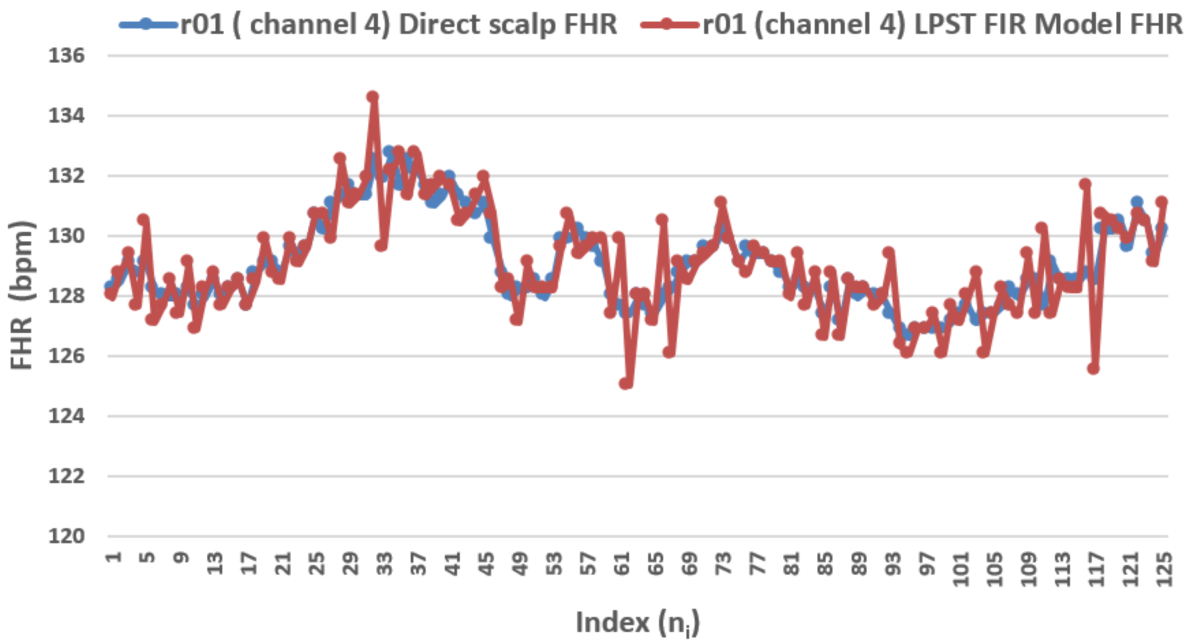

Figure 4.35: Comparison of FHR between direct fetal scalp and LPST FIR band pass filtered signal of adfecgdb database (record r01).

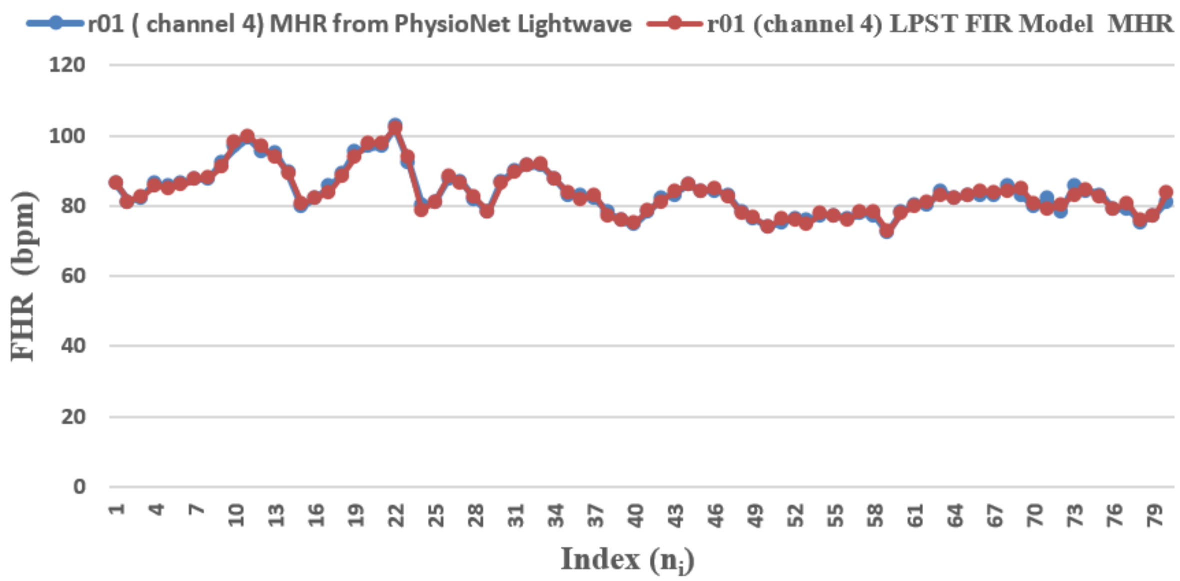

Figure 4.36: Comparison of MHR between Physionet Lightwave and LPST FIR band pass filtered signal of adfecgdb database (record r01).

The LPST FIR filter Models I, II and III for filter order N = 101 exhibit an average accuracy for each channel of adfecgdb to be either higher or equal to the high filter order such as N = 5000 as shown in Figure 4.37. Using this database, we can obtain our objective for detecting FHR using low FIR filter orders.

Figure 4.37: Accuracy of FHR detection using LPST FIR filter Models I, II and III for filter order N = 100 and N = 5000 for adfecgdb (record r01).

The scatter plots shown in Figure 4.38 indicate that the filter Model III for r01 (channel) is more efficient to detect MHR than Model I and II. However from the graph shown in Figure 4.39, the average accuracy is almost similar to the three Models. It is also seen earlier in Table 4.2, that at least one channel of the five records displays 100% accuracy to detect the maternal R-peaks. A similar trend is seen for the maternal QRS detection, filter Models I, II and III for filter order N = 101 also exhibit an average measure of accuracy for each channel of adfecgdb to be either higher or equal to the high filter order such as N = 5000 as shown in Figure 4.40.

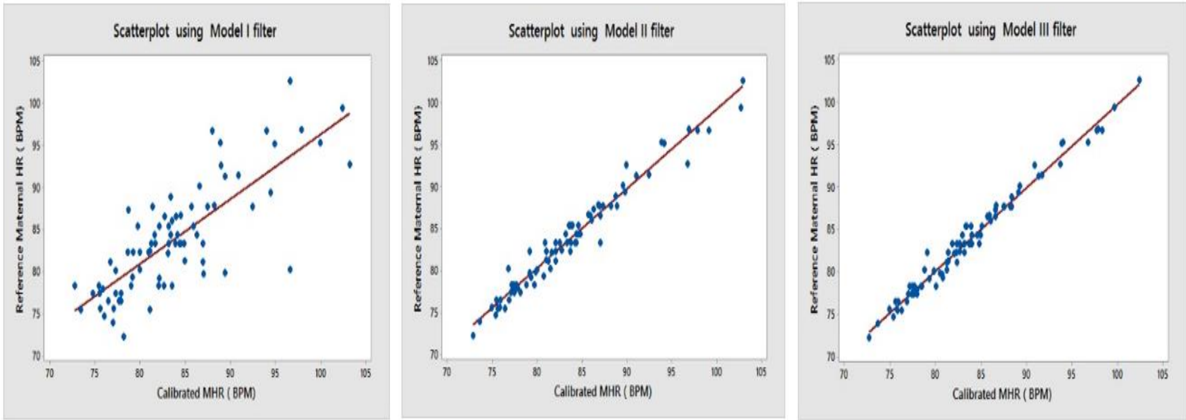

(a) (b) (c)

Figure 4.38: Scatterplots between the references MHR versus calibrated MHR of the r01 record (channel 4) of adfecgdb database. (a) Scatterplot using filter Model I (b) scatterplot using filter Model II (c) scatterplot using filter Model III.

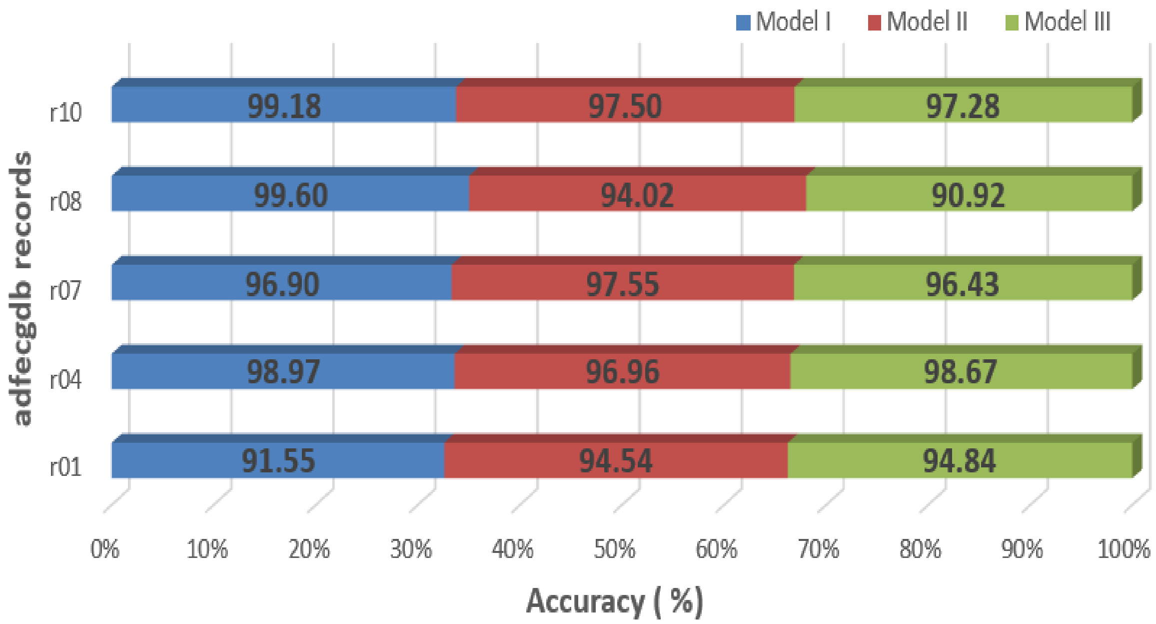

Figure 4.39: Accuracy of MHR detection using LPST FIR BPF Models I, II and III for adfecgdb records.

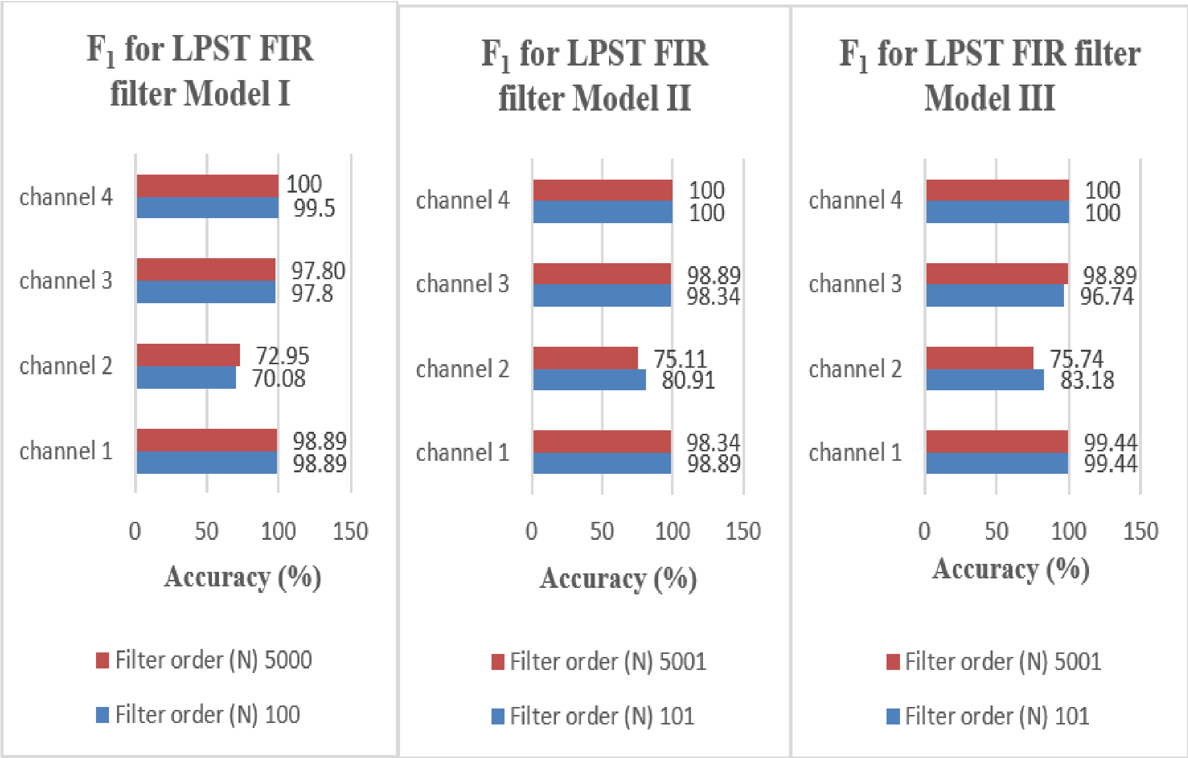

Figure 4.40: Accuracy of MHR detection using LPST FIR BPF Models I, II and III for filter order N = 100 and N = 5000 for adfecgdb (record r01).

The measure of accuracy to detect MHR using our algorithm LPST FIR filter Models I, II and III for nifecgdb is shown with four columns in Figure 4.41 which indicates four stages of filtering. It is observed that the average accuracy for 16 of the 55 records gives less than 100% for filter Model I for N = 100 (refer to column 1 in figure 4.41). After applying these 16 records to filter Model II for N = 101, six records show a 100% mark of accuracy (refer to column 2 in figure 4.41). The remaining 10 records were filtered by the filter Model III for N = 101, out of which two records showed 100% accuracy (refer to column 3 in figure 4.41). In the last phase these 8 records were subjected to the Model III with an increase in the filter order to 5000. Four of the eight records computed 100% accuracy (refer to column 4 in figure 4.41). The remaining four records of ecgca416, ecgca848, and ecgca906 and ecgca968 exhibit FD of 17.73%, 16.98, 3.77% and 20.37% respectively as shown in Figure 4.42. The records shown in Figures 4.43

(a) to (d) show a dip in accuracy from channels 2, 3 and 4. These signals are corrupted by noise in some sections while acquiring the abdominal ECG signal from the mother's abdomen.

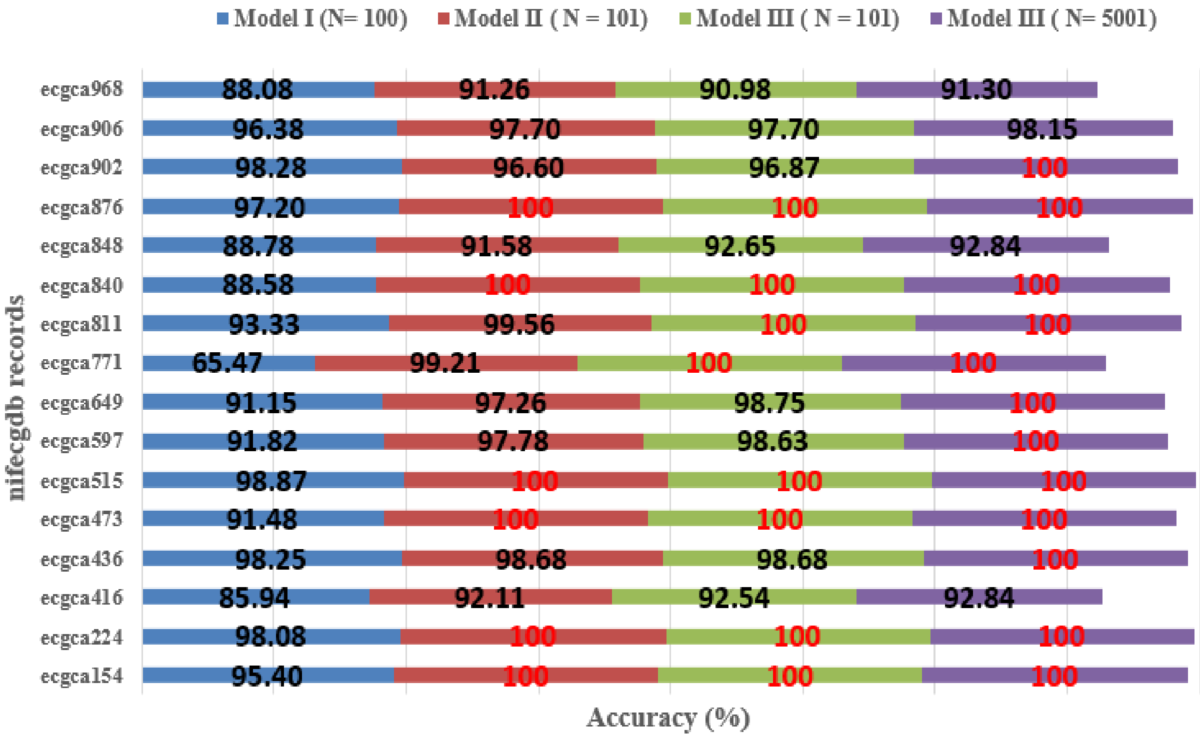

Figure 4.41: Accuracy of MHR detection using LPST FIR BPF Models I, II and III for nifecgdb records.

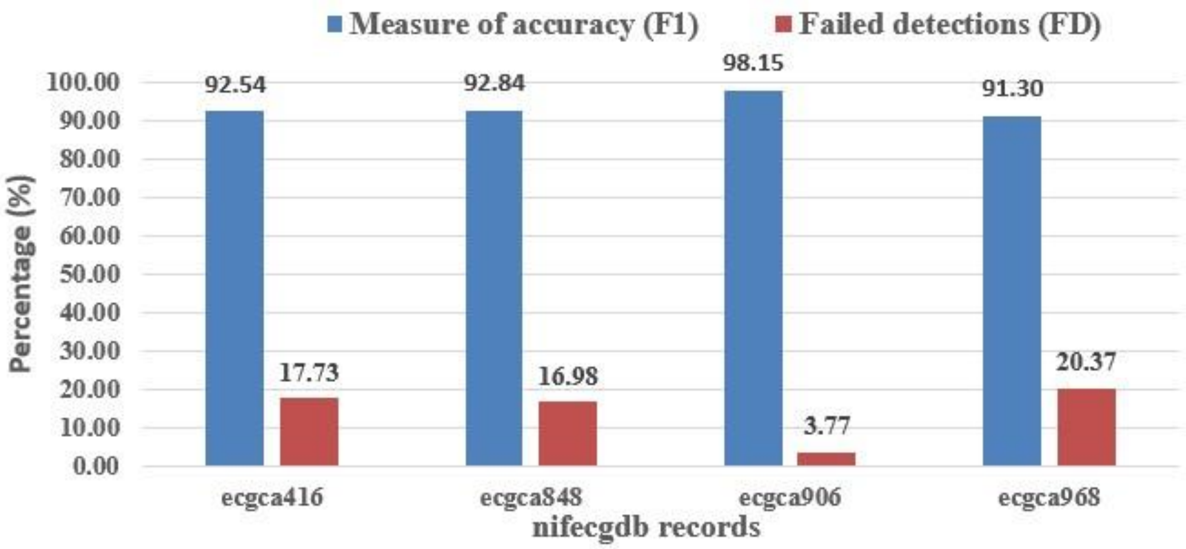

Figure 4.42: Performance evaluation of the MHR detection using LPST FIR BPF Model III of filter order (N = 5001) for four noise corrupted nifecgdb records.

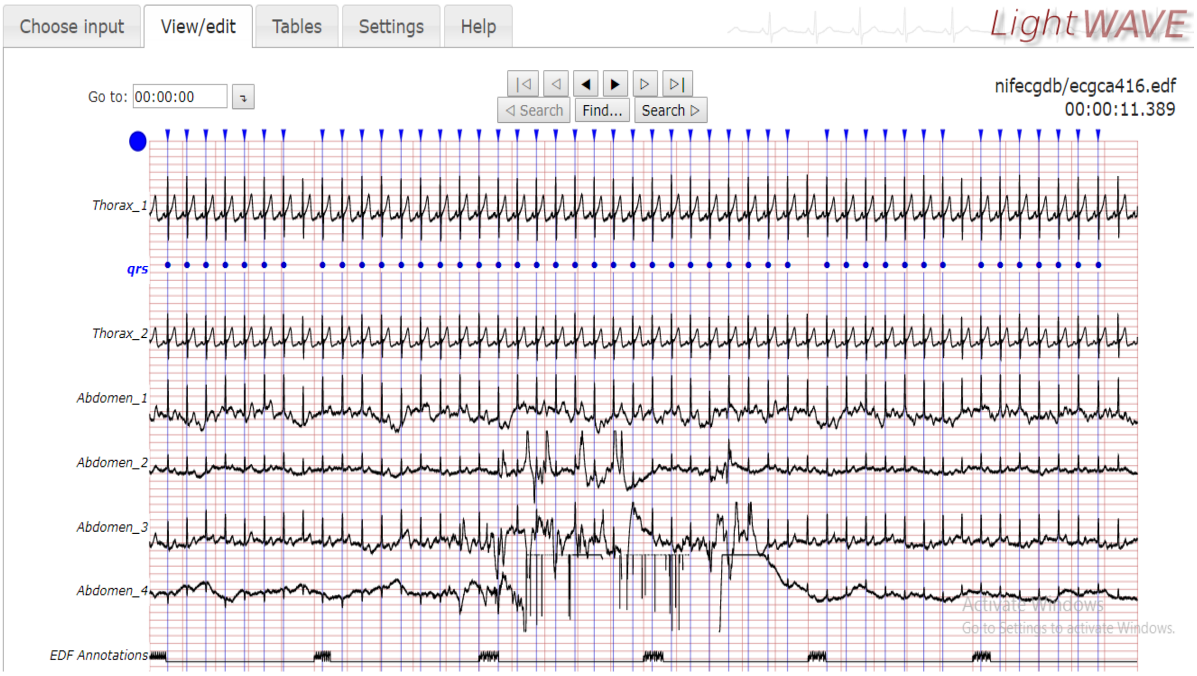
Choose input
View/edit
Tables
Settings
Help
LightWAVE
Go to: 00:00:00
Search
Find...
Search
nifecgdb/ecgca416.edf
00:00:11.389
Thorax_1
qrs
Thorax_2
Abdomen_1
Abdomen_2
Abdomen_3
Abdomen_4
EDF Annotations

4.43 (a)

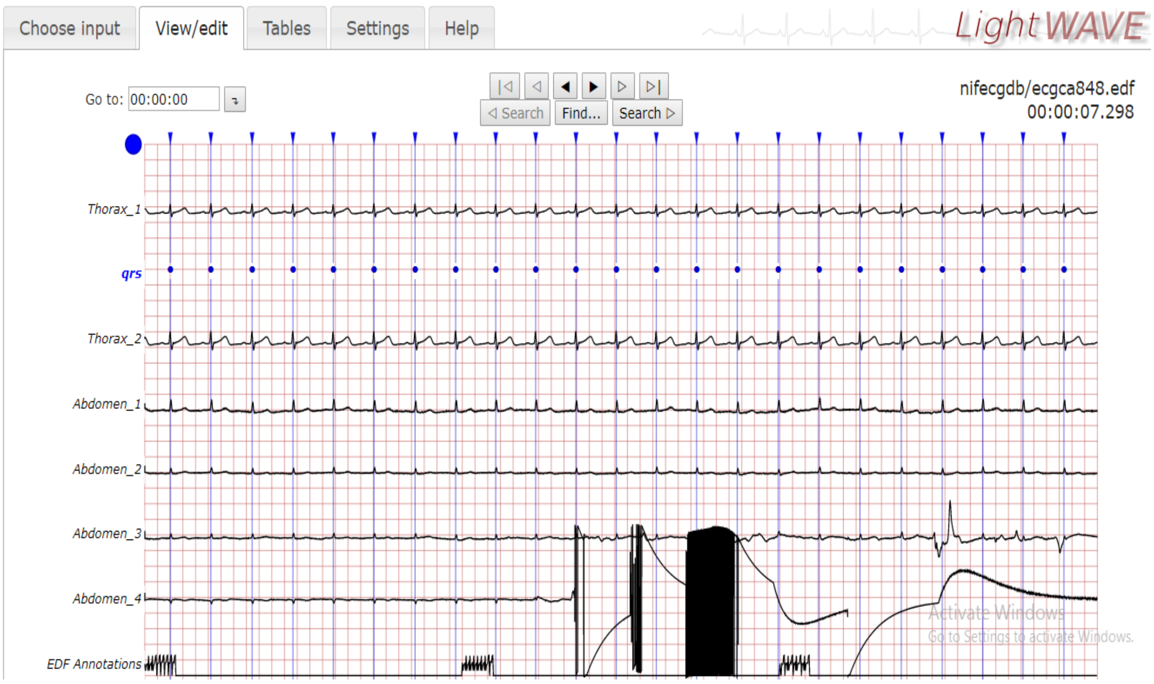
Choose input
View/edit
Tables
Settings
Help
LightWAVE
Go to: 00:00:00
Search
Find...
Search
nifecgdb/ecgca848.edf
00:00:07.298
Thorax_1
qrs
Thorax_2
Abdomen_1
Abdomen_2
Abdomen_3
Abdomen_4
EDF Annotations

4.43 (b)

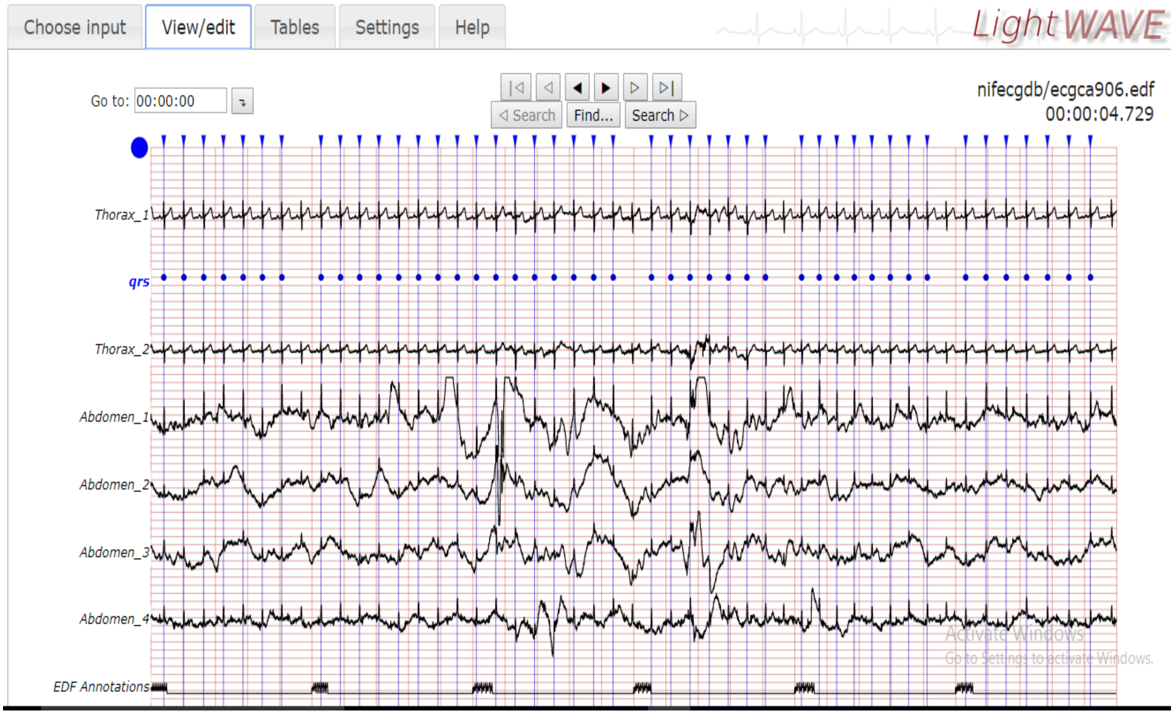

4.43 (c)

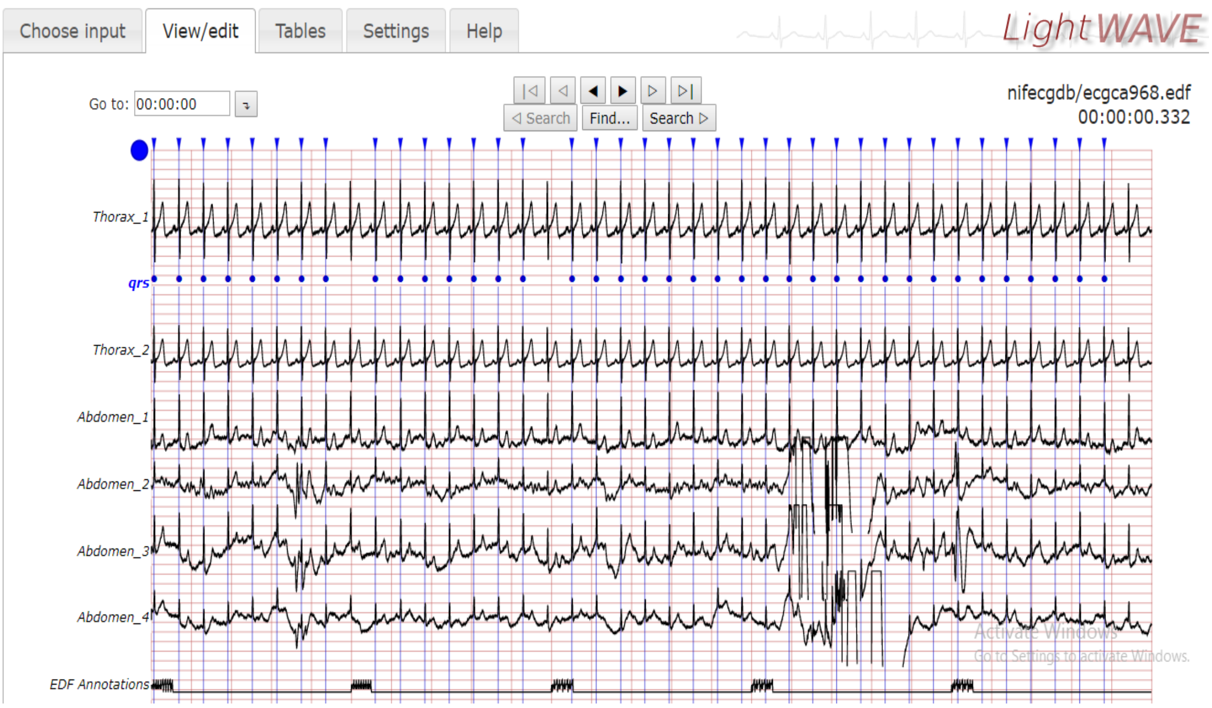

4.43 (d)

Figure 4.43: Noise corrupted aECG records of nifecgdb database (a) ecgca416 (b) ecgca848 (c) ecgca906 (d) ecgca968.

The measure of accuracy to detect MHR was also tested using our LPST FIR filter Models I, II and III for the Physionet Challenge (set a) 75 records. It is observed from Figure 4.44, that the average accuracy for 16 of the 75 records gives less than 100% for Model I for N = 100 (refer to column 1 in figure 4.44). After applying these 16 records to Model II for N = 101, seven records show a 100% mark of accuracy (refer to column 2 in figure 4.44). The remaining nine records were subjected to filter Model III for N = 101, out of which three records showed 100% accuracy (refer to column 3 in figure 4.44). In the last phase, these 6 records having an accuracy of less than 100% were subjected to the filter Model III with an increase in the filter order to 5000. Four of the six records computed 100% accuracy (refer to column 4 in figure 4.44). The remaining two records of a29 and a38 exhibited failed detections of 45.16% and 24.04%, respectively.

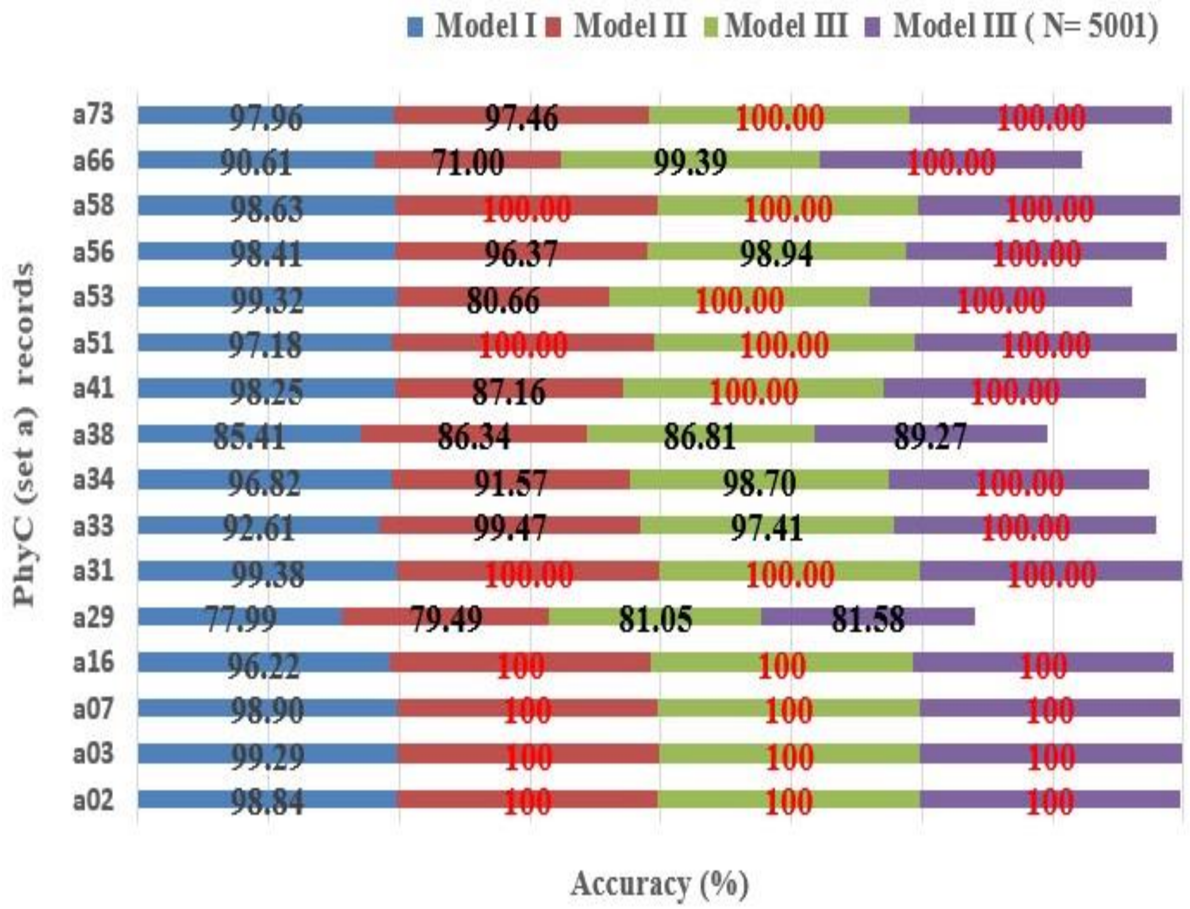

Figure 4.44: Accuracy of MHR detection using LPST FIR BPF Models I, II and III for Phy C (set a) records.

The records shown in Figures 4.45 (a) and (b) shows a dip in accuracy as these two signals are severely corrupted by noise in some sections of its signal. This signal corruption may be due to some electrodes which may have not picked up very good abdominal signals during abdominal electrode placements. In such situations the HR computations become an impossible task.

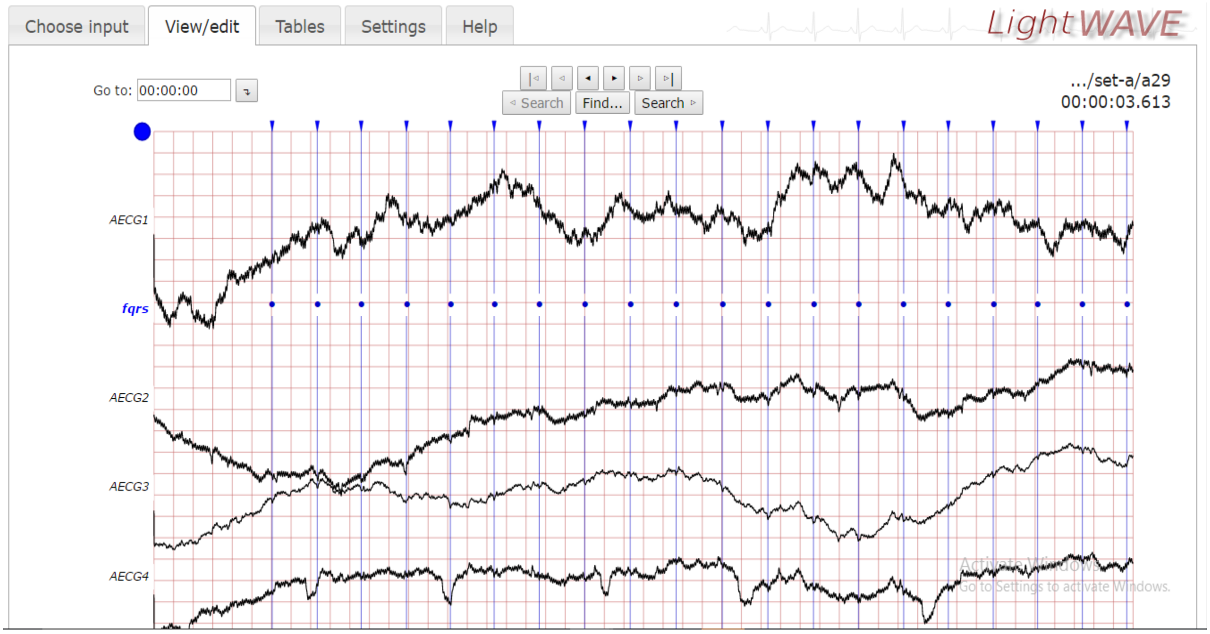

4.45 (a)

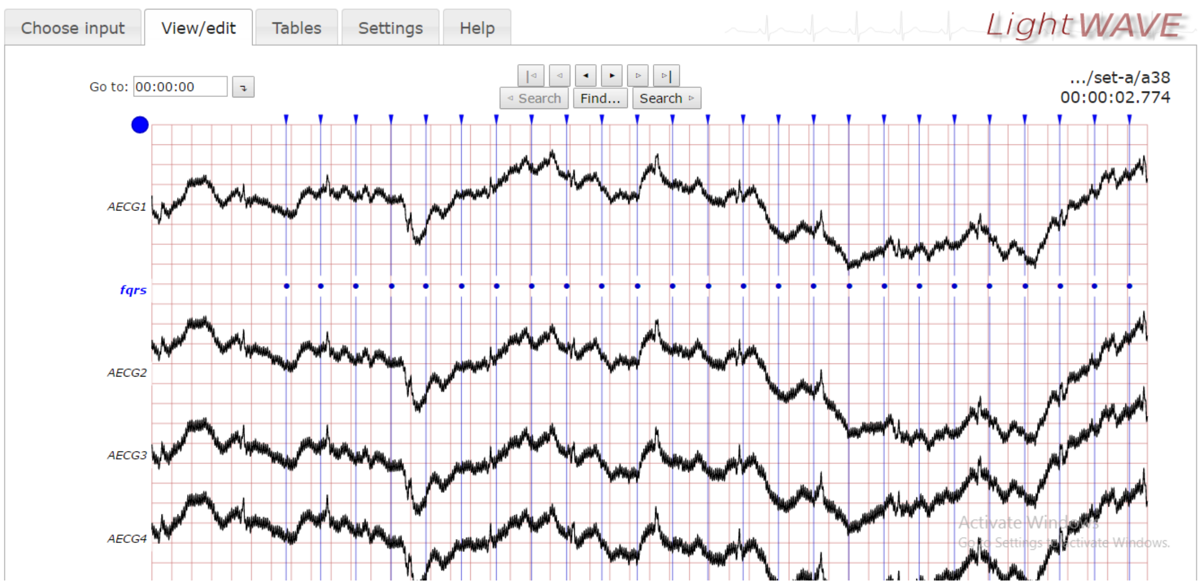

4.45 (b)

Figure 4.45: Noise corrupted aECG records of Phy C 2013 (set a) database (a) a29 (b) a38.

5

Conclusions and Future work

5.1 Conclusions

Three linear phase sharp transition FIR band pass filter models are formulated and their designs are implemented with least passband ripple, good stopband attenuation for any filter order (N). Various regions of the filter response in the frequency domain are approximated using trigonometric functions of frequency, making it convenient to evaluate the impulse response coefficients in closed form. The filter models proposed lay stress on achieving a sharp transition. Sharper the transition, more oscillatory becomes the frequency response near the transition, say at the edge of the passband, a trait described as Gibb's phenomenon. The filter models proposed, achieve a trade-off between the transition bandwidth and Gibb's phenomenon. In addition, emphasis is laid upon a low passband ripple and a large stopband attenuation. Thus a threefold compromise for the satisfactory performance in all the three bands namely passband, transition and stopband is essential in addition to a trade-off between Gibb's phenomenon and sharpness of transition of the filter.

A novel technique is devised to reduce Gibb's phenomenon in the FIR band pass filter. Equations are derived for slopes of the frequency response of the filters at the edges of the transition region and these slopes are matched. The filter design parameters of the model are evaluated by equalizing the slopes of the magnitude response function at both the ends of the transition region. It is found that equalizing the slopes at the edges of the transition region makes the proposed magnitude response of frequency continuous between a pair of adjoining regions that bridge the transition region defined by the model equations. This reduces the effects due to Gibb's phenomenon, thereby reducing ripples at the edges of the transition region of the filter and hence reduces passband ripple and improves stopband attenuation of the filter.

Our research work presented the design of three models of linear phase sharp transition FIR filters which can be used to filter with specified fiduciary band edges in the frequency response and extract maternal and fetal R-peaks from aECG signals, thereby computing the MHR and FHR, respectively. LPST FIR filter Model I employed a BPF containing a tandem of high pass and low pass FIR filters which gave low passband losses and the ripple decreased for a higher filter order. LPST FIR filter Model II described a technique of implementing an integrated LPST BPF. It is found that increasing the filter order (N) to 5001 has improved the average transition bandwidth, passband ripple and stop band attenuation. The FIR BPF Model III used a novel technique to reduce Gibb's phenomenon at the fiduciary band edges of the BPF. The principle underlining this technique is to reduce the amount of discontinuity at the fiduciary edges of the magnitude response of the LPST FIR BPF. It is observed that the stopband attenuation using this method is substantial compared to that obtained without slope matching. Additionally it is seen that, the proposed technique yields a marginal improvement in the transition region width at both the fiduciary edges. This FIR BPF Model III, for lower orders obtained a fairly good magnitude response in all passband, stopband and transition regions with very little computation time and thus is suitable for real time processing of numerous records at a time compared to the Parks-McClellan (PM) algorithm. For lower orders, PM algorithm response is not optimum for both passband and stopband. It was found that the passband loss using our method gave minimum values as compared to the PM algorithm, especially at lower filter orders. However, at filter order 2001, the two algorithms had almost equal values of passband loss and stopband attentuation. Similarly, the PM algorithm displayed low stop band attenuation for all filter orders from N = 101 to 2001. It is observed that Gibb's phenomenon is reduced considerably at the transition edges of the proposed filter and is negligible at higher filter orders. The transition width is reasonably sharp enough for our application to detect precise fetal R-peaks and thus the fetal health condition.

The accuracy and failed detections were computed to evaluate the performance of the three LPST FIR filter Models I, II and III using the three Physionet databases. Using adfecgdb database, it is observed that the accuracy increases from filter Model I to Model III. The filter Model III with slope matching technique shows higher accuracy to detect FHR. In the aECG signal, it is observed that the FQRS and MQRS ECG signals overlap in the time domain or exist in very close proximity. With our designed LPST FIR filters, it is possible to precisely compute the FHR and MHR with these above constraints. Similarly it is seen for the MQRS detection, filter Models I, II and III for filter order N = 101 also exhibits an average accuracy for each channel of adfecgdb to be either higher or equal to the high filter order such as N = 5000. For the database nifecgdb, it is observed that the average channel accuracy for 51 of the 55 records gave 100% for either of the filter Models I, II or III with low filter order such as (N = 100). The remaining four records exhibited large failed detection rates in spite of increasing the filter order. These signals are corrupted by noise in some sections while acquiring the abdominal ECG signal from the mother's abdomen. The accuracy to detect MHR was also tested using our LPST FIR filter Models I, II and III for the Physionet Challenge (set a) database. It is observed that out of the 75 records, only two records scored less than 100% accuracy. These two signals are severely corrupted by noise in some sections of its signal.

A well-researched abdominal ECG electrode placement configuration is desired to obtain the raw aECG signal which is relatively free from artifacts and a fetal ECG signal amplitude which is at least 1/4 of the MECG signal. This will ease the procedure to detect and separate the FECG from the MECG using our method

In the proposed technique, filter transfer function is evolved both in frequency and time domain. The approach is simple, versatile and analytical without extensive computations. Our LPST FIR filter results show that the proposed filters have sharp transition, good stopband attenuation and less passband ripple with least filter order. This approach is better than the conventional FIR design methods of window and frequency sampling techniques. The peak passband in conventional FIR designs is about 18% which is reduced to around 1.5 % with the use of trigonometric functions in the proposed filter model combined with slope equalization technique.

5.2 Suggestions for future Work

Proposed FIR filters can be used as initial filters to obtain better filter performance with reduced filter order. For a suitable filter structure, the hardware details like number of multipliers and delays etc. required to realize the filter can be carried out. The proposed filters can be implemented on a FPGA / ASIC and DSP processor and the performance can be studied. Using the proposed approach, filter models with any desired magnitude response can be developed for any specific signal processing application. In this current research work, the proposed LPST FIR filters precisely computed FHR for a single fetus. After a study of twin pregnancies and the associated frequency spectrum of the two fetuses, our proposed filters could be tested for real time aECG signals. A noise free aECG signal with good resolution fetal and maternal signals are desired for signal processing and future fetal morphological analysis. From a real time extracted FECG, we can detect for any fetal tachycardia or bradycardia among other congential diseases.

Extraction of real time ECG signals from the maternal abdomen can be acquired with more research work done on the different configurations and schemes using the standard 12 lead surface ECG electrodes. A large and complete database can be generated so that any existing and novel non-invasive fetal extraction algorithms can be evaluated on it. The aECG database must have at least one reference maternal thoracic ECG recording along with at least 6-8 abdominal ECG signals. The duration of the recordings have to be large enough, of at least 30 minutes at delivery to capture the mild contractions that occur. Recordings can be done at various gestation ages ranging from the 28th week to full term for a mother's age group of 20-41 years. Clinical Information such as maternal history, outcome of delivery should be recorded to assess whether the non-invasive FECG obtained is predictive of the delivery outcomes. Fetal and maternal heart rate computation can be implemented in real time on a fetal and maternal HR monitor having higher resolution. This low power smart phone based monitor can then transmit the fetal and maternal HRV to the mother and the doctor wirelessly, thus providing a complete and regular health status of the fetus and mother to the clinicians. This health service can be very useful in rural clinics and in areas where high powered systems such as ultrasound machines may not be able to be used. The proposed LPST FIR filters could be also used in various other biomedical applications such as speech or image processing,etc.

References

[1] Winkler, Carey L., John C. Hauth, J. Martin Tucker, John Owen, and Cynthia G. Brumfield. "Neonatal complications at term as related to the degree of umbilical artery acidemia." American journal of obstetrics and gynecology, vol. 164(2), pp. 637-641 (1991).

[2] WHO Media Center 2012. [Online]. Available: http://www.searo.who.int/thailand/news/wbdd2015/en/

[3] Open Government data platform India. [Online]. Available: https://data.gov.in/catalog/major-socio-economic-indicators-states-india.

[4] Population Reference Bureau. [Online]. Available: http://www.prb.org/pdf15/2015-world-population-data-sheet_eng.pdf

[5] Marchon, Niyan, Gourish Naik, and Radhakrishna Pai. "Linear Phase FIR Filter to Compute Fetal Heart Rate Variability." International Journal of Engineering & Technology. Vol 7 No 4.5 (2018): Special Issue 5. https://doi.org/10.14419/ijet.v7i4.5.21141 (2018).

[6] Behar, Joachim, Fernando Andreotti, Sebastian Zaunseder, Julien Oster, and Gari D. Clifford. "A practical guide to non-invasive foetal electrocardiogram extraction and analysis." Physiological measurement, vol. 37(5), pp. R1-R35 (2016).

[7] Tunçalp, Özge, Juan Pablo Pena-Rosas, Theresa Lawrie, Maurice Bucagu, Olufemi T. Oladapo, Anayda Portela, and A. Metin Gülmezoglu. "WHO recommendations on antenatal care for a positive pregnancy experience-going beyond survival." BJOG: An International Journal of Obstetrics & Gynaecology, vol. 124(6), pp. 860-862 (2017).

[8] Hasan, Muhammad Asfarul, M. B. I. Reaz, M. I. Ibrahimy, M. S. Hussain, and J. Uddin. "Detection and processing techniques of FECG signal for fetal monitoring." Biological procedures online, vol. 11(1), pp. 263-295 (2009).

[9] Hasan, M. A., M. I. Ibrahimy, and M. B. I. Reaz. "Techniques of FECG signal analysis: detection and processing for fetal monitoring." WIT Transactions on Biomedicine and Health, vol. 12, pp. 295-305 (2007).

[10] Ananth, Cande V., Suneet P. Chauhan, Han-Yang Chen, Mary E. D'Alton, and Anthony M. Vintzileos. "Electronic fetal monitoring in the United States: temporal trends and adverse perinatal outcomes." Obstetrics & Gynecology, vol. 121(5), pp. 927-933 (2013).

[11] Sameni, Reza, and Gari D. Clifford. "A review of fetal ECG signal processing; issues and promising directions." The open pacing, electrophysiology & therapy journal, vol. 3, pp. 4-20 (2010).

[12] Corton, Marlene M., et al. Williams Obstetrics 24/E. McGraw Hill Professional, 2014.

[13] Clifford, Gari D., Ikaro Silva, Joachim Behar, and George B. Moody. "Non-invasive fetal ECG analysis." Physiological measurement, vol. 35(8), pp. 1521-1536 (2014).

[14] Cohen, Wayne R., et al. "Accuracy and reliability of fetal heart rate monitoring using maternal abdominal surface electrodes." Acta obstetricia et gynecologica Scandinavica, vol. 91(11), pp. 1306-1313 (2012).

[15] Peters, Maria, John Crowe, Jean-Francois Piéri, Hendrik Quartero, Barrie Hayes-Gill, David James, Jeroen Stinstra, and Simon Shakespeare. "Monitoring the fetal heart non-invasively: a review of methods." Journal of perinatal medicine, vol. 29(5), pp. 408-416 (2001).

[16] Goli, Srinivas, Anu Rammohan, and Jalandhar Pradhan. "High spending on maternity care in India: What are the factors explaining it?" PloS one, vol. 11(6), pp.1-17 (2016).

[17] Jagannath, D. J., and A. Immanuel Selvakumar. "Issues and research on foetal electrocardiogram signal elicitation." Biomedical signal processing and control, vol. 10, pp. 224-244 (2014).

[18] Andreotti, Fernando, Maik Riedl, Tilo Himmelsbach, Daniel Wedekind, Sebastian Zaunseder, Niels Wessel, and Hagen Malberg. "Maternal signal estimation by Kalman filtering and template adaptation for fetal heart rate extraction." In Computing in Cardiology Conference (CinC) IEEE, pp. 193-196 (2013).

[19] Swarnalatha, R., and D. V. Prasad. "A novel technique for extraction of FECG using multi stage adaptive filtering." Journal of Applied Sciences, vol. 10(4), pp. 319-324 (2010).

[20] Reaz, Mamun Bin Ibne, and Lee Sze Wei. "Adaptive linear neural network filter for fetal ECG extraction." In Intelligent Sensing and Information Processing, 2004. Proceedings of International Conference on IEEE, pp. 321-324 (2004).

[21] Kezi Selva Vijiila, C. and Kanagasabapathy, P., "Intelligent technique of canceling maternal ECG in FECG extraction". Iranian Journal of Fuzzy Systems, 5(1), pp.27-45 (2008).

[22] Ye, Yalan, Zhi-Lin Zhang, Jiazhi Zeng, and Lei Peng. "A fast and adaptive ICA algorithm with its application to fetal electrocardiogram extraction." Applied Mathematics and Computation, vol. 205(2), pp. 799-806 (2010).

[23] Kanjilal, Partha Pratim, Sarbani Palit, and Goutam Saha. "Fetal ECG extraction from single-channel maternal ECG using singular value decomposition." IEEE Transactions on Biomedical Engineering, vol. 44(1), pp. 51-59 (1997).

[24] Van Bemmel, J. H. "Detection of weak foetal electrocardiograms by autocorrelation and crosscorrelation of envelopes." IEEE Transactions on Biomedical Engineering, vol.1, pp. 17-23 (1968).

[25] Bergveld, Piet, and Wietze JH Meijer. "A new technique for the suppression of the MECG." IEEE Transactions on Biomedical Engineering vol. 4, pp. 348-354 (1981).

[26] Hon, E. H., and S. T. Lee. "Averaging techniques in fetal electrocardiography." Medical electronics and biological engineering, vol. 2(1), pp. 71-76 (1964).

[27] Kam, Amit, and Arnon Cohen. "Detection of fetal ECG with IIR adaptive filtering and genetic algorithms." In Acoustics, Speech, and Signal Processing. Proceedings of IEEE International Conference, vol. 4, pp. 2335-2338 (1999).

[28] Datian, Ye, and Ouyang Xuemei. "Application of wavelet analysis in detection of fetal ECG." In Engineering in Medicine and Biology Society, 1996. Bridging Disciplines for Biomedicine. Proceedings of the 18th Annual International Conference of the IEEE, vol. 3, pp. 1043-1044 (1996).

[29] A.C. Guyton and J.E. Hall, Textbook of 'Medical Physiology', W.B. Saunders company, Philadelphia, USA, tenth edition (2000).

[30] Anatomy and Physiology [Online]. Available:https://opentextbc.ca/anatomyandphysiology/

[31] Thakor, Nitish V., and Y-S. Zhu. "Applications of adaptive filtering to ECG analysis: noise cancellation and arrhythmia detection." IEEE transactions on biomedical engineering, vol 38(8), pp. 785-794 (1991).

[32] M. J. Sexton and L. A. Latson, Fetal blood flow, Healthwise, Inc., October 2005. [Online]. Available: http://www.memorialhermann.org/

[33] M. Artman, L. Mahony, and D.F. Teitel, 'Neonatal cardiology', McGraw-Hill companies, USA (2002).

[34] DePasquale, Nicholas P., and George E. Burgh. "The electrocardiogram, ventricular gradient and spatial vectorcardiogram during the first week of life." The American journal of cardiology, vol. 12(4), pp. 482-493 (1963).

[35] Hornberger, Lisa K., and David J. Sahn. "Rhythm abnormalities of the fetus." Heart, vol. 93 (10), pp. 1294-1300 (2007).

[36] Van Leeuwen, Peter, Silke Lange, Henrik Bettermann, Dietrich Grönemeyer, and Wolfgang Hatzmann. "Fetal heart rate variability and complexity in the course of pregnancy." Early human development, vol. 54(3), pp. 259-269 (1999).

[37] Van Leeuwen, Peter, Silke Lange, Anita Klein, Daniel Geue, and Dietrich HW Grönemeyer. "Dependency of magnetocardiographically determined fetal cardiac time intervals on gestational age, gender and postnatal biometrics in healthy pregnancies." BMC pregnancy and childbirth, vol. 4(1), pp. 6-16 (2004).

[38] Marchon, Niyan and Gourish Naik."Assessment of the fetal health using NI-aECG." Advanced Computational and Communication Paradigms, Lecture Notes in Electrical Engineering, 475, Springer Nature Singapore Pte Ltd. 2018. (ICACCP), SMIT, Sikkim, https://doi.org/10.1007/978-981-10-8240-5_40 (2017).

[39] Karvounis, Evaggelos C., Markos G. Tsipouras, Dimitrios I. Fotiadis, and Katerina K. Naka. "An automated methodology for fetal heart rate extraction from the abdominal electrocardiogram." IEEE Transactions on Information technology in Biomedicine, vol. 11(6), pp. 628-638 (2007).

[40] Renou, Peter, Warwick Newman, and Carl Wood. "Autonomic control of fetal heart rate." American journal of Obstetrics and Gynecology, vol. 105(6), pp. 949-953 (1969).

[41] Thakor, Avnesh S., and Dino A. Giussani. "Effects of acute acidemia on the fetal cardiovascular defense to acute hypoxemia." American Journal of Physiology-Regulatory, Integrative and Comparative Physiology, vol. 296(1), pp. R90-R99 (2009).

[42] Freeman, Roger K., Thomas J. Garite, Michael P. Nageotte, and Lisa A. Miller. Fetal heart rate monitoring. Lippincott Williams & Wilkins, 2012.

[43] Jaeggi, Edgar T., and Mark K. Friedberg. "Diagnosis and management of fetal bradyarrhythmias." Pacing and clinical electrophysiology, vol. 31(s1), pp. S50-S53 (2008).

[44] Gilstrap 3rd, L. C., John C. Hauth, G. D. Hankins, and Amy W. Beck. "Second-stage fetal heart rate abnormalities and type of neonatal acidemia." Obstetrics and gynecology, vol. 70(2), pp. 191-195 (1987).

[45] Van Geijn, Herman P., Henk W. Jongsma, Jelte de Haan, and Tom KAB Eskes. "Analysis of heart rate and beat-to-beat variability: Interval difference index." American journal of obstetrics and gynecology, vol. 138(3), pp. 246-252 (1980).

[46] Pillai, Mary, and David James. "The development of fetal heart rate patterns during normal pregnancy." Obstetrics & Gynecology, vol. 76(5), pp. 812-816 (1990).

[47] Paul, Richard H., Aida Khazin Suidan, Sze-Ya Yeh, Barry S. Schifrin, and Edward H. Hon. "Clinical fetal monitoring: VII. The evaluation and significance of intrapartum baseline FHR variability." American journal of obstetrics and gynecology, vol. 123(2), pp. 206-210 (1975).

[48] Devoe, Lawrence D., Michael Ross, Clayton Wilde, Maureen Beal, Andrej Lysikewicz, Jeffrey Maier, Victor Vines et al. "United States multicenter clinical usage study of the STAN 21 electronic fetal monitoring system." American journal of obstetrics and gynecology, vol. 195(3), pp. 729-734 (2006).

[49] Agostinelli, Angela, Marla Grillo, Alessandra Biagini, Corrado Giuliani, Luca Burattini, Sandro Fioretti, Francesco Di Nardo, Stefano R. Giannubilo, Andrea Ciavattini, and Laura Burattini. "Noninvasive fetal electrocardiography: an overview of the signal

electrophysiological meaning, recording procedures, and processing techniques." Annals of Noninvasive Electrocardiology, vol. 20(4), pp. 303-313 (2015).

[50] Hutter, Damian, and Edgar Jaeggi. "Causes and mechanisms of intrauterine hypoxia and its impact on the fetal cardiovascular system: a review." International journal of paediatrics, vol. 10, pp. 1-9 (2010).

[51] Amer-Wåhlin, I. and Maršál, K., “ST analysis of fetal electrocardiography in labor.” Semin. Fetal Neonatal Med., vol. 16(1), pp. 29–35 (2011).

[52] Ayres-de Campos, D. and Arulkumaran, S. FIGO. “Consensus guidelines on intrapartum fetal monitoring: Physiology of fetal oxygenation and the main goals of intrapartum fetal monitoring”. Int. J. Gynaecol. Obs., vol. 131(1), pp. 5–8 (2015).

[53] Murabayashi, Taizo, Barry Fetics, David Kass, Erez Nevo, Boris Gramatikov, and Ronald D. Berger. "Beat-to-beat QT interval variability associated with acute myocardial ischemia." Journal of electrocardiology, vol. 35(1), pp. 19-25 (2002).

[54] Piccirillo, Gianfranco, Damiano Magrì, Sabrina Matera, Marzia Magnanti, Alessia Torrini, Eleonora Pasquazzi, Erika Schifano et al. "QT variability strongly predicts sudden cardiac death in asymptomatic subjects with mild or moderate left ventricular systolic dysfunction: a prospective study." European heart journal, vol. 28(11), pp. 1344-1350 (2006).

[55] Barry S. Schifrin. “Fetal heart rate monitoring during labor”. The American College of Obstetricians and Gynecologists, vol. 222 (2) (1972).

[56] Bassil, Hany E., and James H. Dripps. "Real time processing and analysis of fetal phonocardiographic signals." Clinical Physics and Physiological Measurement, vol. 10(4B), pp. 67-77 (1989).

[57] Crowe, J. A., J. M. Herbert, X. B. Huang, N. Reed, M. S. Woolfson, D. Rassi, Y. E. Zhuravlev, and S. J. Emery. "Sequential recording of the abdominal fetal electrocardiogram and magnetocardiogram." Physiological measurement, vol. 16(1), pp. 43-52 (1995).

[58] Sundström, Anna-Karin, David Rosén, and K. G. Rosén. "Fetal surveillance." Gothenburg: Neoventa Medical AB (2000).

[59] Marchon, Niyan, Gourish Naik, and Radhakrishna Pai. "ECG Electrode Configuration to Extract Real Time FECG Signals." Procedia Computer Science, vol. 125, pp. 501-508 (2018).

[60] Ungureanu, M., Bergmans, J.W. M., Mischi, M., et al. “Improved method for fetal heart rate monitoring.” 27th Annual International conference of the engineering in medicine and biology society, IEEE-EMBS, Shanghai, China, pp. 5916–5919 (2015).

[61] Lawson, G. W., R. Belcher, G. S. Dawes, and C. W. G. Redman. "A comparison of ultrasound (with autocorrelation) and direct electrocardiogram fetal heart rate detector systems." American journal of obstetrics and gynecology vol. 147(6), pp. 721-722 (1983).

[62] Oostendorp, T. F., A. Van Oosterom, and H. W. Jongsma. "Electrical properties of tissues involved in the conduction of foetal ECG." Medical and Biological Engineering and Computing vol. 27(3), pp. 322-324 (1989).

[63] Martinek, Radek, Radana Kahankova, Homer Nazeran, Jaromir Konecny, Janusz Jezewski, Petr Janku, Petr Bilik, Jan Zidek, Jan Nedoma, and Marcel Fajkus. "Non-Invasive Fetal Monitoring: A Maternal Surface ECG Electrode Placement-Based Novel Approach for Optimization of Adaptive Filter Control Parameters Using the LMS and RLS Algorithms." Sensors vol. 17(5), pp. 1154-1185 (2017).

[64] Zarzoso, V., A. K. Nandi, and E. Bacharakis. "Maternal and foetal ECG separation using blind source separation methods." Mathematical Medicine and Biology vol. 14(3), pp. 207-225 (1997).

[65] Goldberger, Ary L., Luis AN Amaral, Leon Glass, Jeffrey M. Hausdorff, Plamen Ch Ivanov, Roger G. Mark, Joseph E. Mietus, George B. Moody, Chung-Kang Peng, and H. Eugene Stanley. "Physiobank, physiotoolkit, and physionet." Circulation vol. 101(23), pp. e215-e220 (2000).

[66] Abdominal and Direct Fetal Electrocardiogram Database (adfecgdb). Available from: URL: https://www.Physionet.org/physiobank/database/adfecgdb.

[67] Non-Invasive Fetal Electrocardiogram Database (nifecgdb). Available from: URL: https://Physionet.org/physiobank/database/nifecgdb.

[68] Vullings, Rik. "Non-invasive fetal electrocardiogram: analysis and interpretation." PhD diss., Doctoral Dissertation, 2010.

[69] Oostendorp, T. F., A. Van Oosterom, and H. W. Jongsma. "The effect of changes in the conductive medium on the fetal ECG throughout gestation." Clinical Physics and Physiological Measurement, vol. 10(4B), pp. 11-20 (1989).

[70] Oostendorp, T. F., A. Van Oosterom, and Henk W. Jongsma. "The fetal ECG throughout the second half of gestation." Clinical physics and physiological measurement, vol. 10(2), pp. 147-160 (1989).

[71] Oldenburg, John T., and Martin Macklin. "Changes in the conduction of the fetal electrocardiogram to the maternal abdominal surface during gestation." American journal of obstetrics and gynecology, vol. 129(4), pp. 425-433 (1977).

[72] Marchon, Niyan, and Gourish Naik. "Detection of fetal heart rate using ANFIS displayed on a smartphone." In Region 10 IEEE Conference (TENCON), Singapore, pp. 1519-1523 (2016).

[73] Nasiri, Maryam, Karim Faez, and Ali Motie Nasrabadi. "A new method for extraction of fetal electrocardiogram signal based on Adaptive Nero-Fuzzy Inference System." In Signal and Image Processing Applications (ICSIPA), 2011 IEEE International Conference, pp. 456-461 (2011).

[74] Ye, Yalan, Zhi-Lin Zhang, Jiazhi Zeng, and Lei Peng. "A fast and adaptive ICA algorithm with its application to fetal electrocardiogram extraction." Applied Mathematics and Computation vol. 205(2), pp. 799-806 (2008).

[75] Rooijakkers, Michael Johannes, Shuang Song, Chiara Rabotti, S. Guid Oei, Jan WM Bergmans, Eugenio Cantatore, and Massimo Mischi. "Influence of electrode placement on signal quality for ambulatory pregnancy monitoring." Computational and mathematical methods in medicine 2014 (2014).

[76] Marchon, Niyan, and Gourish Naik. "Electrode positioning for monitoring Fetal ECG: A review." IEEE International Conference on Information Processing (ICIP), Pune, pp. 5-10 (2015).

[77] Monica Healthcare Ltd AN24. Available from: URL: http://www.monicahealthcare.com.

[78] Rooijakkers, Michael J., Chiara Rabotti, S. Guid Oei, and Massimo Mischi. "Low-complexity R-peak detection for ambulatory fetal monitoring." Physiological measurement, vol. 33(7), pp. 1135-1142 (2012).

[79] Jie-Min, Zhang, Guan Qun, Tang Li-Ming, Liu Tie-Bing, Liu Hong-Xing, Huang Xiao-Lin, and Si Jun-Feng. "Position difference regularity of corresponding R-wave peaks for maternal ECG components from different abdominal points." Chinese Physics B, vol. 23(1), pp. 018701(1-7) (2013).

[80] Andreotti, Fernando, Maik Riedl, Tilo Himmelsbach, Daniel Wedekind, Niels Wessel, Holger Stepan, Claudia Schmieder, Alexander Jank, Hagen Malberg, and Sebastian

Zaunseder. "Robust fetal ECG extraction and detection from abdominal leads." Physiological measurement, vol 35(8), pp. 1551- 1567 (2014).

[81] MindChild Meridian fetal monitoring System. Available from: URL: http://www.mindchild.com/meridian-monitor.html.

[82] Clifford, Gari, Reza Sameni, Jay Ward, Julian Robinson, and Adam J. Wolfberg. "Clinically accurate fetal ECG parameters acquired from maternal abdominal sensors." American journal of obstetrics and gynecology, vol. 205(1), pp. 47-e1 – 47-e5 (2011).

[83] Sameni, Reza, Frédéric Vrins, F. Parmentier, Christophe Herail, Vincent Vigneron, Michel Verleysen, Christian Jutten, and M. B. Shamsollahi. "Electrode selection for noninvasive fetal electrocardiogram extraction using mutual information criteria." In AIP Conference Proceedings, vol. 872(1), pp. 97-104 (2006).

[84] Jie-Min, Zhang, Huang Xiao-Lin, Guan Qun, Liu Tie-Bing, Li Ping, Zhao Ying, and Liu Hong-Xing. "Some regularity on how to locate electrodes for higher fECG SNRs." Chinese Physics B, vol. 24(3), pp. 038702(1-5) (2015).

[85] Kallows Engineering, Goa India. Available from: URL: http://www.kallows.com.

[86] IEC 60601-2-51 standard. Available from: URL: http://standards.globalspec.com/std/276494/iec-60601-2-51

[87] Callaerts, Dirk, Joos Vandewalle, Willy Sansen, J. Janssens, and Gaston Vantrappen. "Acquisition and processing of the antepartum FECG." A critical appraisal of fetal surveillance, Elsevier Science BV, chapter 43, pp. 371-380 (1994).

[88] Taylor, Myles JO, Mark J. Smith, Matthew Thomas, Andrew R. Green, Floria Cheng, Salome Oseku-Afful, Ling Y. Wee, Nicholas M. Fisk, and Helena M. Gardiner. "Non-invasive fetal electrocardiography in singleton and multiple pregnancies." BJOG: An International Journal of Obstetrics & Gynaecology, vol. 110(7), pp. 668-678 (2003).

[89] Peddaneni, Hemanth. Comparison of algorithms for fetal ECG extraction. PhD dissertation University of Florida, 2004.

[90] Chia, Ee Ling, Ting Fei Ho, Mary Rauff, and William CL Yip. "Cardiac time intervals of normal fetuses using noninvasive fetal electrocardiography." Prenatal diagnosis, vol. 25(7), pp. 546-552 (2005).

[91] Vullings, Rik, Chris Peters, Massimo Mischi, Guid Oei, and Jan Bergmans. "Maternal ECG removal from non-invasive fetal ECG recordings." In Engineering in Medicine and Biology Society, 2006. EMBS'06. 28th Annual International Conference of the IEEE, pp. 1394-1397 (2006).

[92] Martens, Suzanna MM, Chiara Rabotti, Massimo Mischi, and Rob J. Sluijter. "A robust fetal ECG detection method for abdominal recordings." Physiological measurement, vol. 28(4), pp. 373-380 (2007).

[93] Graatsma, E. M., B. C. Jacod, L. A. J. Van Egmond, E. J. H. Mulder, and G. H. A. Visser. "Fetal electrocardiography: feasibility of long-term fetal heart rate recordings." BJOG: An International Journal of Obstetrics & Gynaecology, vol. 116(2), pp. 334-338 (2009).

[94] Vullings, R., C. H. L. Peters, R. J. Sluijter, M. Mischi, S. G. Oei, and J. W. M. Bergmans. "Dynamic segmentation and linear prediction for maternal ECG removal in antenatal abdominal recordings." Physiological measurement, vol. 30(3), pp. 291-298 (2009).

[95] Ravindrakumar, S., and K. Bommanna Raja. "Fetal ECG extraction and enhancement in prenatal monitoring—Review and implementation issues." In Trendz in Information Sciences & Computing (TISC) IEEE, pp. 16-20 (2010).

[96] Algunaidi, MM Sheikh, MA Mohd Ali, and Md Fokhrul Islam. "Evaluation of an improved algorithm for fetal QRS detection." International Journal of Physical Sciences, vol. 6(2), pp. 213-220 (2011).

[97] Physionet/Computing in Cardiology Challenge 2013 Database. Available from: URL: http://www.Physionet.org/challenge/2013/.

[98] Swarnalatha, R., and D. V. Prasad. "A novel technique for extraction of FECG using multi stage adaptive filtering." Journal of Applied Sciences, vol. 10(4), pp. 319-324 (2010).

[99] Widrow B, Stearns S, Adaptive signal processing. Prentice-Hall, Upper Saddle River (1985).

[100] Widrow, Bernard, John R. Glover, John M. McCool, John Kaunitz, Charles S. Williams, Robert H. Hearn, James R. Zeidler, JR Eugene Dong, and Robert C. Goodlin. "Adaptive noise cancelling: Principles and applications." Proceedings of the IEEE, vol. 63(12), pp. 1692-1716 (1975).

[101] Widrow, Bernard, John M. McCool, Michael G. Larimore, and C. Richard Johnson. "Stationary and nonstationary learning characteristics of the LMS adaptive filter." Proceedings of the IEEE, vol. 64(8), pp. 1151-1162 (1976).

[102] Martens, S. M. M., J. W. M. Bergmans, and S. G. Oei. "A simple adaptive interference cancellation method for power line reduction in electrocardiography." In Proceedings of the 25th Symposium on Information Theory in the Benelux, pp. 49-56 (2004).

[103] Martens, Suzanna MM, Massimo Mischi, S. Guid Oei, and Jan WM Bergmans. "An improved adaptive power line interference canceller for electrocardiography." IEEE transactions on Biomedical Engineering, vol. 53(11), pp. 2220-2231 (2006).

[104] Ungureanu, Mihaela, Johannes WM Bergmans, Swan Guid Oei, and Rodica Strungaru. "Fetal ECG extraction during labor using an adaptive maternal beat subtraction technique." Biomedizinische Technik, vol. 52(1), pp. 56-60 (2007).

[105] Rahman, Muhammad Zia Ur, Rafi Ahamed Shaik, and DV Rama Koti Reddy. "Efficient sign based normalized adaptive filtering techniques for cancelation of artifacts in ECG signals: Application to wireless biotelemetry." Signal processing, vol. 91(2), pp. 225-239 (2011).

[106] De Sa, JP Marques, L. Paul Reis, J. Nuno Lau, and J. Bernardes. "Estimation and classification of fetal heart rate baselines using artificial neural networks." In Computers in Cardiology, IEEE, pp. 541-544 (1994).

[107] Selvan, S., and R. Srinivasan. "A novel adaptive filtering technique for the processing of abdominal fetal electrocardiogram using neural network." In Adaptive Systems for Signal Processing, Communications, and Control Symposium 2000. AS-SPCC IEEE, pp. 289-292 (2000).

[108] Reaz, Mamun Bin Ibne, and Lee Sze Wei. "Adaptive linear neural network filter for fetal ECG extraction." In Intelligent Sensing and Information Processing, 2004. Proceedings of International IEEE Conference, pp. 321-324 (2004).

[109] Amin, M. S., Md Mamun, Fazida Hanim Hashim, and Hafizah Husain. "Separation of fetal electrocardiography (ECG) from composite ECG using adaptive linear neural network for fetal monitoring." International Journal of Physical Sciences, vol. 6(24), pp. 5871-5876 (2011).

[110] Magenes, Giovanni, Maria G. Signorini, and Domenico Arduini. "Detection of normal and pathological fetal states by means of neural and fuzzy classifiers applied to CTG parameters." In Engineering in Medicine and Biology, 1999. 21st Annual Conference and the 1999 Annual Fall Meetring of the Biomedical Engineering Society] BMES/EMBS, IEEE Conference Proceedings of the First Joint, vol. 2, pp. 936-942 (1999).

[111] Azad, Khandaker Abul Kalam. "Fetal QRS complex detection from abdominal ECG: a fuzzy approach." In Proceedings of IEEE nordic signal processing symposium. Kolmarden, Sweden, pp. 275-278 (2000).

[112] Camps, G., M. Martinez, and E. Soria. "Fetal ECG extraction using an FIR neural network." In Computers in Cardiology, IEEE, pp. 249-252 (2001).

[113] Warrick, Philip, Emily Hamilton, and Maciej Macieszczak. "Neural network based detection of fetal heart rate patterns." In Neural Networks, 2005. IJCNN'05. Proceedings. 2005 IEEE International Joint Conference, vol. 4, pp. 2400-2405 (2005).

[114] Assaleh, Khaled. "Extraction of fetal electrocardiogram using adaptive neuro-fuzzy inference systems." IEEE Transactions on Biomedical Engineering, vol. 54(1), pp. 59-68 (2007).

[115] Nasiri, Maryam, and Karim Faez. "Extracting fetal electrocardiogram signal using ANFIS trained by genetic algorithm." In Biomedical Engineering (ICoBE), IEEE International Conference, pp. 197-202 (2012).

[116] Ali, Mahmoud Ahmed Suliman, and XiaoPing Zeng. "A novel technique for extraction foetal electrocardiogram using adaptive filtering and simple genetic algorithm." American Journal of Biostatistics, vol. 1(2), pp. 75-82 (2010).

[117] Nazmy, T. M., H. El-Messiry, and B. Al-Bokhity. "Adaptive neuro-fuzzy inference system for classification of ECG signals." In Informatics and Systems (INFOS), 7th IEEE International Conference, pp. 1-6 (2010).

[118] Sargolzaei, A., K. Faez, and S. Sargolzaei. "A new method for Foetal Electrocardiogram extraction using Adaptive Nero-Fuzzy Interference System trained with PSO algorithm." In Electro/Information Technology (EIT), IEEE International Conference, pp. 1-5 (2011).

[119] Vullings, Rik, Bert De Vries, and Jan WM Bergmans. "An adaptive Kalman filter for ECG signal enhancement." IEEE transactions on biomedical engineering, vol. 58(4), pp. 1094-1103 (2011).

[120] Sameni, Reza. "Extraction of fetal cardiac signals from an array of maternal abdominal recordings." PhD diss., Institut National Polytechnique de Grenoble-INPG; Sharif University of Technology (2008).

[121] Oikonomou, V. P., and D. I. Fotiadis. "A Bayesian PCA approach for fetal ecg extraction." In IFMBE Proc, vol. 11(1), pp. 1727-1983 (2005).

[122] Yin, Ying, Mao Ye, Dongxiao Ren, Yuanxiang Zhu, and Chenxue Yang. "FECG extraction using bayesian inference and neural networks approximation." Journal of Computational Information Systems, vol. 6(6), pp. 1769-1778 (2010).

[123] Z. Shi, C. Zhang, Semi-blind source extraction for fetal electrocardiogram extraction by combining non-Gaussianity and time-correlation, Neurocomputing, 70(7-9), pp. 1574–1581 (2007).

[124] Levkov, Chavdar, Georgy Mihov, Ratcho Ivanov, Ivan Daskalov, Ivaylo Christov, and Ivan Dotsinsky. "Removal of power-line interference from the ECG: a review of the subtraction procedure." BioMedical Engineering OnLine, vol. 4(1), pp. 50-58 (2005).

[125] Tompkins, Willis J. ‘Biomedical digital signal processing.’ Editorial Prentice Hall (1993).

[126] Alcaraz, R., and J. J. Rieta. "Adaptive singular value QRST cancellation for the analysis of short single lead atrial fibrillation electrocardiograms." In Computers in Cardiology, IEEE, pp. 513-516 (2007).

[127] Chmelka, L., and J. Kozumplik. "Wavelet-based wiener filter for electrocardiogram signal denoising." In Computers in Cardiology, IEEE, pp. 771-774 (2005).

[128] Nikolay Nikolaev, Atanas Gotchev. “ECG signal denoising using wavelet domain Wiener filtering”.In: Proc. Of the European Signal Processing Conference in EUSIPCO-2000, Tampere, Finland, pp. 51–54 (2000).

[129] Papadimitriou, S., D. Gatzounas, V. Papadopoulos, V. Tzigounis, and A. Bezerianos. "Fetal heart rate signal denoising by processing the wavelet transform modulus maxima." In Engineering in Medicine and Biology Society, 1996. Bridging Disciplines for Biomedicine. Proceedings of the 18th Annual International Conference of the IEEE, vol. 3, pp. 1029-1030 (1996).

[130] Echeverria, Juan C., N. Ramirez, A. B. Pimentel, R. Rodriguez, R. Gonzalez, and V. Medina. "Fetal QRS extraction based on wavelet analysis and pattern matching." In Engineering in Medicine and Biology Society, 1996. Bridging Disciplines for Biomedicine. Proceedings of the 18th Annual International Conference of the IEEE, vol. 4, pp. 1656-1657 (1996).

[131] Echeverria, J. C., R. Ortiz, N. Ramirez, V. Medina, and R. Gonzalez. "A reliable method for abdominal ECG signal processing." In Computers in Cardiology IEEE, pp. 529-532 (1998).

[132] Mochimaru, F., Y. Fujimoto, and Y. Ishikawa. "Detecting the fetal electrocardiogram by wavelet theory-based methods." Progress in Biomedical Research vol.7, pp. 185-193 (2007).

[133] Karvounis, E. C., C. Papaloukas, D. I. Fotiadis, and L. K. Michalis. "Fetal heart rate extraction from composite maternal ECG using complex continuous wavelet transform." In Computers in Cardiology, IEEE, pp. 737-740 (2004).

[134] Karvounis, E. C., Markos G. Tsipouras, Dimitrios I. Fotiadis, and K. K. Naka. "A method for fetal heart rate extraction based on time-frequency analysis." In Computer-Based Medical Systems, 2006. CBMS 2006. 19th IEEE International Symposium, pp. 347-347(2006).

[135] Azzerboni, Bruno, Fabio La Foresta, Nadia Mammone, and Francesco Carlo Morabito. "A new approach based on wavelet-ICA algorithms for fetal electrocardiogram extraction." In ESANN, pp. 193-198 (2005).

[136] Almagro, S., M. M. Elena, M. J. Bastiaans, and J. M. Quero. "A new mother wavelet for fetal electrocardiography, to achieve optimal denoising and compressing results." In Computers in Cardiology, IEEE, pp. 157-160 (2006).

[137] Kadambe, Shubha, Robin Murray, and G. Faye Boudreaux-Bartels. "Wavelet transform-based QRS complex detector." IEEE Transactions on biomedical Engineering vol. 46(7), pp. 838-848 (1999).

[138] Desai, K. D., and Manoj S. Sankhe. "A real-time fetal ECG feature extraction using multiscale discrete wavelet transform." In Biomedical Engineering and Informatics (BMEI), 2012 5th IEEE International Conference, pp. 407-412 (2012).

[139] Anisha, M., S. S. Kumar, and M. Benisha. "Methodological survey on fetal ECG extraction." Journal of Health & Medical Informatics, vol. 5(4), pp. 1-8 (2014).

[140] Khamene, Ali, and Shahriar Negahdaripour. "A new method for the extraction of fetal ECG from the composite abdominal signal." IEEE Transactions on Biomedical Engineering, vol. 47(4), pp. 507-516 (2000).

[141] Chareonsak, Charayaphan, Farook Sana, Yu Wei, and Xiong Bing. "Design of FPGA hardware for a real-time blind source separation of fetal ECG signals." In Biomedical Circuits and Systems, 2004 IEEE International Workshop, pp. S2-4 (2004).

[142] Jafari, Maria G., and Jonathon A. Chambers. "Fetal electrocardiogram extraction by sequential source separation in the wavelet domain." IEEE Transactions on Biomedical Engineering, vol. 52(3), pp. 390-400 (2005).

[143] Li, Yunxia, and Zhang Yi. "An algorithm for extracting fetal electrocardiogram." Neurocomputing, vol. 71(7), pp. 1538-1542 (2008).

[144] Karvounis, E. C., M. G. Tsipouras, C. Papaloukas, D. G. Tsalikakis, K. K. Naka, and D. I. Fotiadis. "A non-invasive methodology for fetal monitoring during pregnancy." Methods of information in medicine, vol. 49(3), pp. 238-246 (2010).

[145] De Lathauwer, Lieven, Bart De Moor, and Joos Vandewalle. "Fetal electrocardiogram extraction by blind source subspace separation." IEEE transactions on biomedical engineering, vol. 47(5), pp. 567-572 (2000).

[146] Marossero, Dorothee E., Deniz Erdogmus, Neil Euliano, Jose C. Principe, and K. E. Hild. "Independent components analysis for fetal electrocardiogram extraction: a case for the data efficient mermaid algorithm." In Neural Networks for Signal Processing, 2003. NNSP'03. 2003 IEEE 13th Workshop, pp. 399-408 (2003).

[147] De Araujo, Draulio, Allan Kardec Barros, Oswaldo Baffa, Ronald Wakai, Hui Zhao, and Noboru Ohnishi. "Fetal magnetocardiographic source separation using the poles of the autocorrelation function." In Proceedings of the 4th international symposium on independent component analysis and blind signal separation, Nara, Japan, pp. 1-4 (2003).

[148] Najafabadi, Farshid Soheili, Edmond Zahedi, and Mohd Alauddin Mohd Ali. "A novel model for abdominal electrocardiography of a pregnant woman." In Sensors and the International Conference on new Techniques in Pharmaceutical and Biomedical Research, 2005 Asian IEEE Conference, pp. 64-68 (2005).

[149] Luo, Dongfang. "Research and application of fetal electrocardiogram blind signal separation technology." Res. J. Appl. Sci. Eng. Technol, vol. 4(14), pp. 2231-2235 (2012).

[150] Martin-Clemente, Ruben, Jose Luis Camargo-Olivares, Susana Hornillo-Mellado, Mar Elena, and Isabel Roman. "Fast technique for noninvasive fetal ECG extraction." IEEE Transactions on Biomedical Engineering, vol. 58(2), pp. 227-230 (2011).

[151] Camargo-Olivares, José Luis, Rubén Martín-Clemente, Susana Hornillo-Mellado, M. M. Elena, and Isabel Román. "The maternal abdominal ECG as input to MICA in the fetal ECG extraction problem." IEEE Signal Processing Letters, vol. 18(3), pp. 161-164 (2011).

[152] Ungureanu, G. Mihaela, Ana Maria Ilincai, Werner Wolf, Ilinca Gussi, Dragos D. Taralunga, and Rodica Strungaru. "Improved fetal ECG extraction by applying adaptive filtering." In Advanced Topics in Electrical Engineering (ATEE), 2011 7th IEEE International Symposium, pp. 1-6 (2011).

[153] Vigneron, Vincent, Anisoara Paraschiv-Ionescu, Annabelle Azancot, Olivier Sibony, and Christian Jutten. "Fetal electrocardiogram extraction based on non-stationary ICA and wavelet denoising." In Signal Processing and Its Applications, 2003. Proceedings. Seventh IEEE International Symposium, vol. 2, pp. 69-72 (2003).

[154] Hyvarinen, Aapo. "Fast and robust fixed-point algorithms for independent component analysis." IEEE transactions on Neural Networks, vol. 10(3), pp. 626-634 (1999).

[155] Romero, Inaki. "PCA-based noise reduction in ambulatory ECGs." In Computing in Cardiology, IEEE, pp. 677-680 (2010).

[156] Gao, Ping, Ee-Chien Chang, and Lonce Wyse. "Blind separation of fetal ECG from single mixture using SVD and ICA." In Information, Communications and Signal Processing, 2003 and Fourth Pacific Rim Conference on Multimedia. Proceedings of the 2003 Joint Conference of the Fourth IEEE International Conference, vol. 3, pp. 1418-1422 (2003).

[157] Barros, Allan Kardec, and Andrzej Cichocki. "Extraction of specific signals with temporal structure." Neural computation, vol. 13(9), pp. 1995-2003 (2001).

[158] De Lathauwer, Lieven, Bart De Moor, and Joos Vandewalle. "SVD-based methodologies for fetal electrocardiogram extraction." In Acoustics, Speech, and Signal Processing. ICASSP'00. Proceedings. IEEE International Conference, vol. 6, pp. 3771-3774 (2000).

[159] Mooney, Donna M., Lynn J. Grooome, Lynn S. Bentz, and J. Doug Wilson. "Computer algorithm for adaptive extraction of fetal cardiac electrical signal." In Proceedings of the ACM symposium on applied computing, pp. 113-117 (1995).

[160] Pieri, J. F., J. A. Crowe, B. R. Hayes-Gill, C. J. Spencer, K. Bhogal, and D. K. James. "Compact long-term recorder for the transabdominal foetal and maternal electrocardiogram." Medical and Biological Engineering and Computing, vol. 39(1), pp. 118-125 (2001).

[161] Ibrahimy, Muhammad I., et al. "Real-time signal processing for fetal heart rate monitoring." IEEE transactions on biomedical engineering, vol. 50(2), pp. 258-261 (2003).

[162] Swarnalatha, R., and D. V. Prasad. "Interference Cancellation in FECG Using Wavelet-Adaptive Filtering Technique." Journal of Engineering and Applied Sciences, vol. 4(5-6), pp. 353-357 (2009).

[163] Swarnalatha, R., and D. V. Prasad. "Maternal ECG cancellation in abdominal signal using ANFIS and wavelets." Applied Science, vol. 10, pp. 868-77 (2010).

[164] Varanini, M., G. Tartarisco, L. Billeci, A. Macerata, G. Pioggia, and R. Balocchi. "An efficient unsupervised fetal QRS complex detection from abdominal maternal ECG." Physiological measurement, vol. 35(8), pp. 1607-1614 (2014).

[165] MATLAB Mobile [Online]. Available : http://in.mathworks.com/products/matlab-mobile/features.html

[166] Lamesgin, Gizeaddis, Yonas Kassaw, and Dawit Assefa. "Extraction of fetal ecg from abdominal ecg and heart rate variability analysis." In Afro-European Conference for Industrial Advancement, Springer, Cham, pp. 65-76 (2015).

[167] E.C. Ifeachor and B.W. Jervis, ‘Digital signal processing: a practical approach.’ Pearson Education, pp. 367-379 (2002).

[168] Proakis, John G., and Dimitris G. Manolakis. ‘Digital signal processing-principles, algorithms and applications.’ (1992).

[169] Paley, Raymond Edward Alan Christopher, Norbert Wiener, and Norbert Wiener. ‘Fourier transforms in the complex domain.’ Vol. 19. New York: American Mathematical Society, 1934.

[170] A J. Gibbs, ‘The Design of Digital Filters,’ in Australian Telecommunication, Research Journal, vol 4, pp. 29-34 (1970).

[171] Johnson, Johnny R. ‘Introduction to digital signal processing.’ Introduction to digital signal processing, by JR Johnson. Englewood Cliffs, NJ, Prentice Hall, pp. 426-440 (1989).

[172] Charalambous, Christakis, and Hana Khreishi. "A computer program for designing optimum 2-D FIR linear phase digital filters." In Acoustics, Speech, and Signal Processing, IEEE International Conference on ICASSP'86, vol. 11, pp. 549-552 (1986).

[173] Pei, Soo-Chang, and Peng-Hua Wang. "Design of equiripple FIR filters with constraint using a multiple exchange algorithm." IEEE Transactions on Circuits and Systems I: Fundamental Theory and Applications, vol. 49(1), pp. 113-116 (2002).

[174] Lim, Yong. "Frequency-response masking approach for the synthesis of sharp linear phase digital filters." IEEE transactions on circuits and systems, vol. 33(4), pp. 357-364 (1986).

[175] Jing, Zhongqi, and Adly Fam. "A new structure for narrow transition band, lowpass digital filter design." IEEE transactions on acoustics, speech, and signal processing, vol. 32(2), pp. 362-370 (1984).

[176] Principe, Jose C., and Jack R. Smith. "Design and implementation of linear phase FIR filters for biological signal processing." IEEE transactions on biomedical engineering, vol. 6, pp. 550-559 (1986).

[177] Rabiner, Lh, and R. Crochiere. "A novel implementation for narrow-band FIR digital filters." IEEE Transactions on Acoustics, Speech, and Signal Processing, vol. 23(5), pp. 457-464 (1975).

[178] Rabiner, Lawrence R., James H. McClellan, and Thomas W. Parks. "FIR digital filter design techniques using weighted Chebyshev approximation." Proceedings of the IEEE, vol. 63(4) 595-610 (1975).

[179] Lim, Yong Ching, and Yong Lian. "The optimum design of one-and two-dimensional FIR filters using the frequency response masking technique." IEEE Transactions on Circuits and Systems II: Analog and Digital Signal Processing, vol. 40(2), pp. 88-95 (1993).

[180] Saramaki, Tapio, and Yong Ching Lim. "Use of the Remez algorithm for designing FIR filters utilizing the frequency-response masking approach." In Circuits and Systems, 1999. ISCAS'99. Proceedings of the 1999 IEEE International Symposium, vol. 3, pp. 449-455 (1999).

[181] Saramäki, Tapio, and Yong Ching Lim. "Use of the Remez Algorithm for Designing FRM Based FIR Filters." Circuits, systems, and signal processing, vol. 22(2), pp. 77-97 (2003).

[182] Zhang, Lei, Yong Lian, and C. C. Ko. "A new approach for design sharp FIR filters using frequency-response masking technique." In Proc. 9th IEEE DSP Workshop and 1st IEEE Signal Processing Education Workshop, pp. 1-5 (2000).

[183] Neuvo, Yrjo, Ganesh Rajan, and Sanjit K. Mitra. "Design of narrow-band FIR bandpass digital filters with reduced arithmetic complexity." IEEE transactions on circuits and systems, vol. 34(4), pp. 409-419 (1987).

[184] Rodrigues, Joseph X., and K. R. Pai. "Modified linear phase frequency response masking FIR filter." In Image and Signal Processing and Analysis, 2005. ISPA 2005. Proceedings of the 4th IEEE International Symposium, pp. 434-439 (2005).

[185] Rodrigues, Joseph, and K. R. Pai. "New approach to the synthesis of sharp transition FIR digital filter." In Industrial Electronics, 2005. ISIE 2005. Proceedings of the IEEE International Symposium, vol. 3, pp. 1171-1173 (2005).

[186] Mintzer, Fred, and Bede Liu. "Practical design rules for optimum FIR bandpass digital filters." IEEE Transactions on Acoustics, Speech, and Signal Processing, 27(2), pp. 204-206 (1979).

[187] Rajan, G., Y. Neuvo, and S. K. Mitra. "On the design of sharp cutoff wide-band FIR filters with reduced arithmetic complexity." IEEE transactions on circuits and systems, vol. 35(11), pp. 1447-1454 (1988).

[188] Saramaki, Tapio, T. Neuvo, and Sanjit K. Mitra. "Design of computationally efficient interpolated FIR filters." IEEE Transactions on Circuits and Systems, vol. 35(1), pp. 70-88 (1988).

[189] Vaidyanathan, P. "Optimal design of linear phase FIR digital filters with very flat passbands and equiripple stopbands." IEEE transactions on circuits and systems, vol. 32(9), pp. 904-917 (1985).

[190] Sheikh, Zaka Ullah, and Oscar Gustafsson. "Design of narrow-band and wide-band frequency-response masking filters using sparse non-periodic sub-filters." In Signal Processing, 18th European IEEE Conference, pp. 1704-1707 (2010).

[191] Alam, Syed Asad, and Oscar Gustafsson. "Implementation of narrow-band frequency-response masking for efficient narrow transition band FIR filters on FPGAs." In NORCHIP IEEE, pp. 1-4 (2011).

[192] Yang, Ronghuan, Bede Liu, and Yong Ching Lim. "A new structure of sharp transition FIR filters using frequency-response masking." IEEE transactions on circuits and systems, vol. 35(8), pp. 955-966 (1988).

[193] Henzel, Norbert, and Jacek M. Leski. "Generalized constraint design of linear-phase FIR digital filters." In Proceedings of the 8th International Conference on Computer Recognition Systems CORES 2013, Springer, Heidelberg, pp. 53-62 (2013).

[194] Alkhairy, Ashraf, Kevin Christian, and J. Lim. "Design of FIR filters by complex Chebyshev approximation." In Acoustics, Speech, and Signal Processing, ICASSP-91, IEEE International Conference, pp. 1985-1988 (1991).

[195] Pan, Jiapu, and Willis J. Tompkins. "A real-time QRS detection algorithm." IEEE transactions on biomedical engineering, vol. 3, 230-236 (1985).

[196] Marchon, Niyan, and Gourish Naik. "QRS detector for maternal abdominal ECG." In Signal and Information Processing (IConSIP), IEEE International Conference, pp. 1-5 (2016).

[197] Symonds, Edwin Malcolm, Allan Chang, and Daljit Sahota. ‘Fetal electrocardiography’. World Scientific (2001).

[198] Von Steinburg, Stephanie Pildner, Anne-Laure Boulesteix, Christian Lederer, Stefani Grunow, Sven Schiermeier, Wolfgang Hatzmann, Karl-Theodor M. Schneider, and Martin Daumer. "What is the “normal” fetal heart rate?" PeerJ 1, pp. e82 – e89 (2013).

[199] Donn, Steven M., M. Blennow, K. Marsal, K. Boggess, P. C. Ng, F. A. Chervenak, D. Peebles et al. "Seminars in Fetal & Neonatal Medicine.", vol. 19(1), pp. 1-6 (2014).

[200] Karin, J., M. Hirsch, O. Segal, and S. Akselrod. "Non invasive fetal ECG monitoring." In Computers in Cardiology, IEEE, pp. 365-368 (1994).

[201] Matonia, Adam, Janusz Jezewski, Tomasz Kupka, Krzysztof Horoba, Janusz Wrobel, and Adam Gacek. "The influence of coincidence of fetal and maternal QRS complexes on fetal heart rate reliability." Medical and Biological Engineering and Computing, vol. 44(5), pp. 393-403 (2006).

[202] Kohler, B-U., Carsten Hennig, and Reinhold Orglmeister. "The principles of software QRS detection." IEEE Engineering in Medicine and Biology Magazine, vol. 21(1), pp. 42-57 (2002).

[203] Elgendi, Mohamed, Mirjam Jonkman, and Friso DeBoer. "Frequency bands effects on QRS detection." Pan 5(15), pp. 1-5 (2010).

[204] Azevedo, Stephen, and Richard L. Longini. "Abdominal-lead fetal electrocardiographic R-wave enhancement for heart rate determination." IEEE Transactions on Biomedical Engineering, vol. 5, pp. 255-260 (1980).

[205] Kligfield, Paul, Leonard S. Gettes, James J. Bailey, Rory Childers, Barbara J. Deal, E. William Hancock, Gerard van Herpen et al. "Recommendations for the Standardization and Interpretation of the Electrocardiogram." Circulation, vol. 115(10), pp. 1306-1324 (2007).

[206] Fukushima, Teiichiro, Carlos A. Flores, Edward H. Hon, and Ezra C. Davidson. "Limitations of autocorrelation in fetal heart rate monitoring." American journal of obstetrics and gynecology, vol. 153(6), pp. 685-692 (1985).

[207] ANSI/AAMI/ISO EC57 1998/(R) 2008 Testing and reporting performance results of cardiac rhythm and ST-segment measurement algorithms.

[208] Jyh-Shing Roger Jang, "ANFIS: adaptive-network-based fuzzy inference system." IEEE Transactions on Systems, Man, and Cybernetics, vol. 23(3), pp. 665-685 (1993).

List of Publications

A] Research articles in Journals

1. Marchon, Niyan, Gourish Naik, and Radhakrishna Pai. "*Monitoring of Fetal Heart Rate using Sharp Transition FIR Filter*". Biomedical Signal Processing and Control 44 (2018) pp: 191-199. https://doi.org/10.1016/j.bspc.2018.04.017.

2. Marchon, Niyan, Gourish Naik, and Radhakrishna Pai, *"Linear Phase Sharp Transition BPF to detect Noninvasive Maternal and Fetal Heart Rate"*. Journal of Healthcare Engineering, *Hindawi*, vol. 2018 (2018). Article ID 5485728. https://doi.org/10.1155/2018/5485728.

3. Marchon, Niyan, Gourish Naik, and Radhakrishna Pai. "Linear Phase FIR Filter to Compute Fetal Heart Rate Variability." International Journal of Engineering & Technology. Vol 7 No 4.5, (2018) pp. 492-496 https://doi.org/10.14419/ijet.v7i4.5.21141.

4. Marchon, Niyan and Gourish Naik. "*Detecting Heart Rates of Expectant Mothers in their 3rd Trimester*" International Journal of Recent Development in Engineering and Technology, ISSN: 2347-6435, vol. 2, no. 5 (2014).

5. Marchon, Niyan and Gourish Naik. "*Design and Implementation of wireless heart monitor for expectant mothers in their 3rd trimester*", IJMER, ISSN: 2249–6645, vol. 4, no. 3, pp: 33-37 (2014).

6. Marchon, Niyan and Gourish Naik. "*Denoising of Abdominal Maternal ECG signals"*, International J. of Engg. Research & Indu. Appls. IJERIA, ISSN: 0974-1518, vol.7, no. 1, pp: 59-69 (2014).

B] Research Papers presented: (Conference Proceedings)

International Conferences

7. Marchon, Niyan, Gourish Naik, and Radhakrishna Pai. "*ECG Electrode Configuration to Extract Real Time FECG Signals*." Procedia Computer Science vol. 125, pp: 501-508. International Conference on Smart Computing & Communications (ICSCC), NIT, Kurukshetra, (2017). https://doi.org/10.1016/j.procs.2017.12.065 (2018).

8. Marchon, Niyan and Gourish Naik."*Assessment of the fetal health using NI-aECG*." Advanced Computational and Communication Paradigms, Lecture Notes in Electrical Engineering 475, Springer Nature Singapore Pte Ltd. 2018. Advanced Computational and Communication Paradigms (ICACCP), SMIT, Sikkim, (2017). https://doi.org/10.1007/978-981-10-8240-5_40.

9. Marchon, Niyan and Gourish Naik." *FIR Filter Design Technique to Mitigate Gibb's Phenomenon.*" XV Control Instrumentation System Conference, Lecture Notes in Electrical Engineering, Springer Nature Singapore Pte Ltd. XV Control Instrumentation System Conference (CISCON), MIT, Manipal , October 2018 [In press].

IEEE International Conferences

10. Marchon, N. and Naik, G., December. "*Electrode positioning for monitoring Fetal ECG: A review*". IEEE International Conference on Information Processing (ICIP) Pune, 2015 (pp: 5-10), (2015). https://doi.org/10.1109/INFOP.2015.7489341.

11. Marchon, N. and Naik, G.,"*QRS detector for maternal abdominal ECG*". IEEE International Conference on Signal and Information Processing (IConSIP) Nanded, pp: 1-5, (2016). https://doi.org/10.1109/ICONSIP.2016.7857463.

12. Marchon, N. and Naik, G., "*Detection of fetal heart rate using ANFIS displayed on a smartphone*". In Region 10, IEEE International Conference (TENCON) Singapore, pp: 1519-1523, (2016). https://doi.org/10.1109/TENCON.2016.7848269.

13. Marchon, Niyan and Gourish Naik "*A Novel Linear Phase FIR High Pass Filter For Biomedical Signals*". 2018 IEEE Distributed Computing, VLSI, Electrical Circuits and Robotics (DISCOVER) August 2018. [In Press]

National Conferences / Symposiums

14. Marchon, Niyan and Gourish Naik. "*To detect real time non-invasive FECG using an appropriate methodology: a review*" at the 8th Annual National Symposium on VLSI and Embedded systems at Padre Conceicao College of Engineering, Goa, India,(2014).

15. Marchon, Niyan and Gourish Naik. "*Detection of Fetal Distress using Non-invasive FECG: a review*" at the 9th Annual National Symposium on VLSI and Embedded systems at Carmel College, Goa, India, (2015).

16. Marchon, Niyan and Gourish Naik. "*Monitoring of Fetal heart beat in Labor*" at the 11th Annual National Symposium on VLSI AND EMBEDDED SYSTEM, 22-23 March. 2018 Goa University India, pp: 72-76. ISSN: 978-93-5300-578-8 (2018).

17. Marchon, Niyan and Gourish Naik. "*Sharp filters to extract absence seizures EEG signals*" at the National Conference (NCETCE) and International Journal of Scientific Research in Computer Science, Engineering and Information Technology at Don Bosco College of Engineering (DBCE), Goa ,November 2018. Volume 1, Issue 1,ISSN : 2456-3307.[In press]

C] Funding of Minor research project:

Our minor research project entitled "*To extract real time FECG (non-invasively) using DSP Embedded Technology*" by Department of Science and Technology, Goa centre with Reference: No.8-319-2016/STE-DIR/606 is under review.

D] Awards:

- Niyan Marchon was awarded the '**Travel Bursary Award'** at the IEEE International Conference on Signal and Information Processing (IConSIP) Nanded, in October 2016 for the research paper titled "*QRS detector for maternal abdominal ECG*".
- Niyan Marchon was awarded the '**Best Paper Award'** at the National Conference in Computers and Electronics Engineering (NCETCE) at DBCE, Goa in November 2018 for the research paper titled "*Sharp filters to extract absence seizures EEG signals*".

Appendix A

Proposed electrode configurations to acquire FECG

We proposed three schemes for the electrode placements using the standard 12-lead ECG machine, made by Kallows Engineering, Goa India [85]. This configuration is based on the lead configuration for a commercial 5 lead fetal ECG as per the IEC 60601-2-51 standard [86] wherein the right leg lead (black) is placed on the right thigh and the other four leads are arrayed around the fetus. With proper consent from the subject, it was reported that the young mother was 24 years old with the gestational age of 34 weeks, 5 days and as per the clinical impression: a live fetus in cephalic presentation. At the clinic, the nurses cleaned the abdominal skin with alcohol to avoid dry skin around the area where the surface electrodes would be placed. The removal of grease would further enhance the conductivity of the electrodes. We placed the limb leads around the fetus to get good strength differential leads (I, II and III) as well as placing four of the precordial leads whose voltages will be with respect to the spot we have labelled as Wilson’s Central Terminal (WCT). Finally, we placed V5 and V6 on the mother's upper arms to get some strong maternal ECG references as seen in Figure A.1 for scheme 1. We inverted this configuration for the scheme 2 (so that RA, LA are shifted down and LL is at the top) for the difference in fetus orientation (head up vs. head down).The scheme 3 is similar to scheme 2 except that the V5 and V6 are placed at the maternal thoracic area to compare the MECG signals from both the schemes. An eighteen minute recording was done for each of the electrode positions.

Measurements were performed on a single pregnant woman with single fetus, with a gestation period of 34 weeks. The experiment was conducted in three modes by using the standard 12 lead resting ECG recorder called Mobmon. The device had the capability to send live ECG streams to the remote doctor’s phone. Initially we tested the scheme 1 thoroughly for few minutes before we could set to record each scheme for 18 minutes each (as shown in Figure A.2a). The largest fetal ECG amplitudes are recorded during the 2nd scheme giving an average FHR value as 132 bpm which was similar to the CTG recordings taken an hour before. The maternal signals were stronger than the FECG for the other two schemes which displayed the mother’s heart rate values only. The recordings of the three schemes are displayed in Figure A.2, while the CTG reading of the subject is seen in Figure A.3.

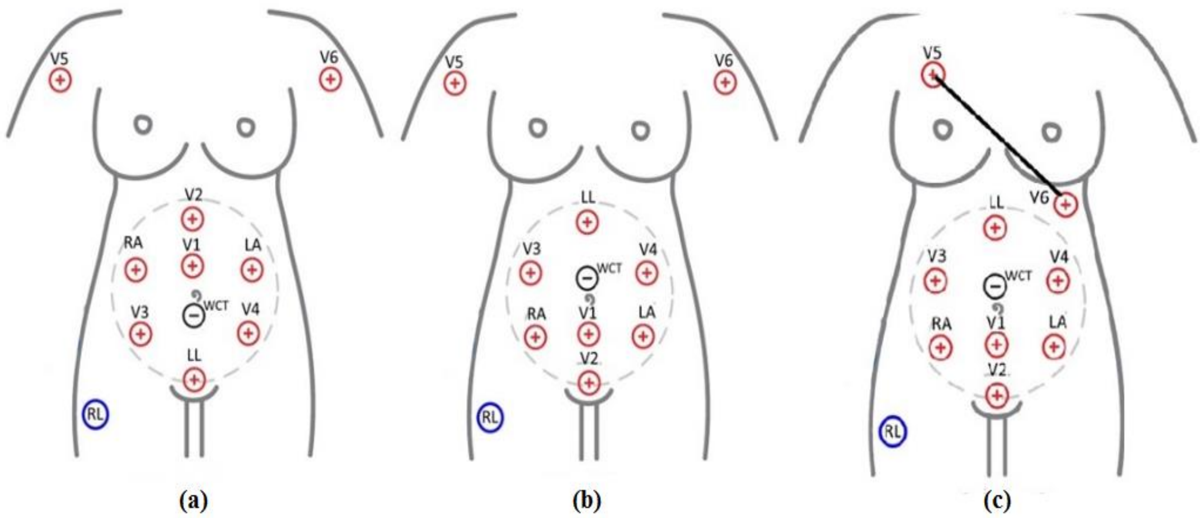

Figure A.1: Proposed electrode placement schemes based on the schemes refered in Fig 2.11 (a) scheme 1 (b) scheme 2 (c) scheme 3. The schemes are based on the positions of the pre cordial active electrodes (V1 –V6) and the four limb electrodes (RA, LA, LL. RL is placed on the right thigh as a reference electrode. WCT is the virtual reference point for the V1-V6 leads.

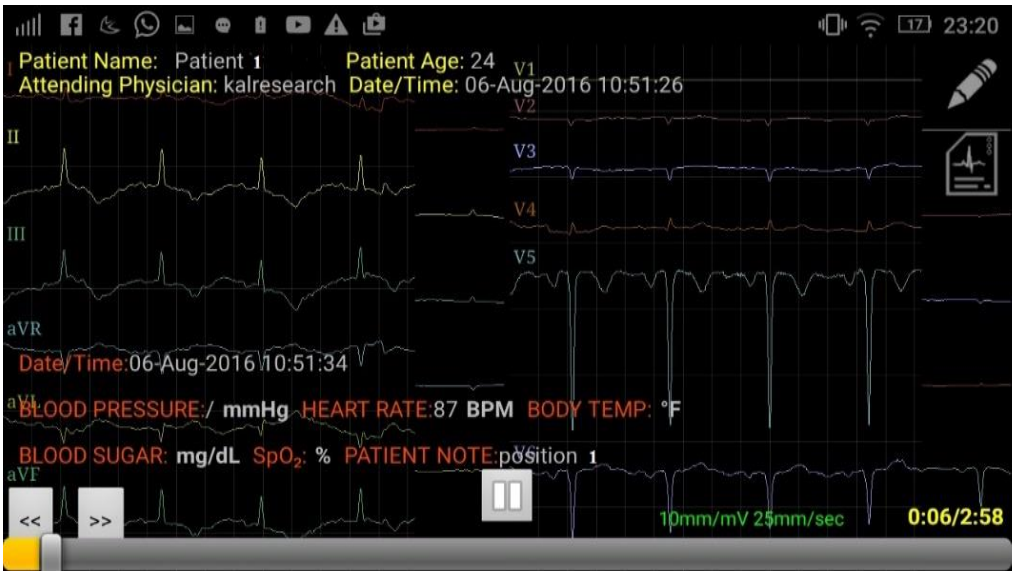

(a)

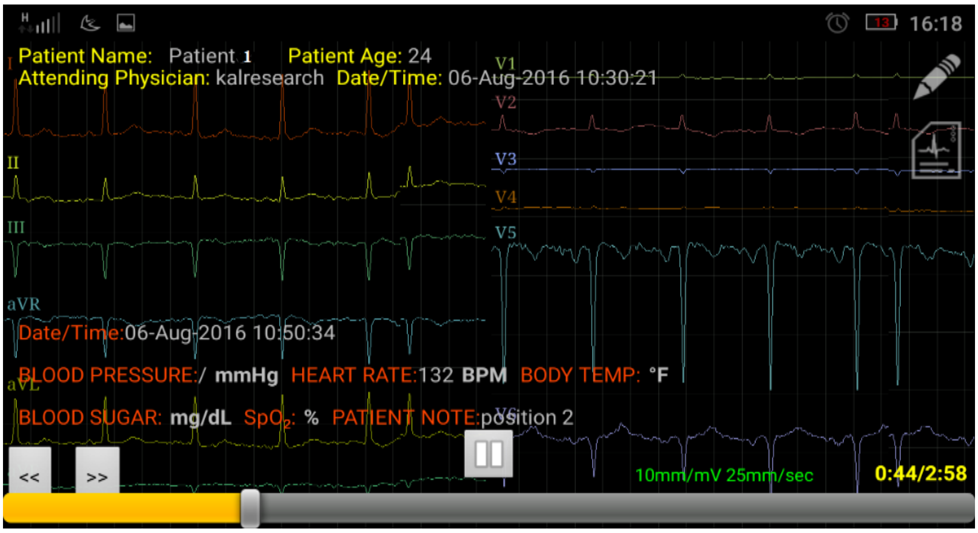

(b)

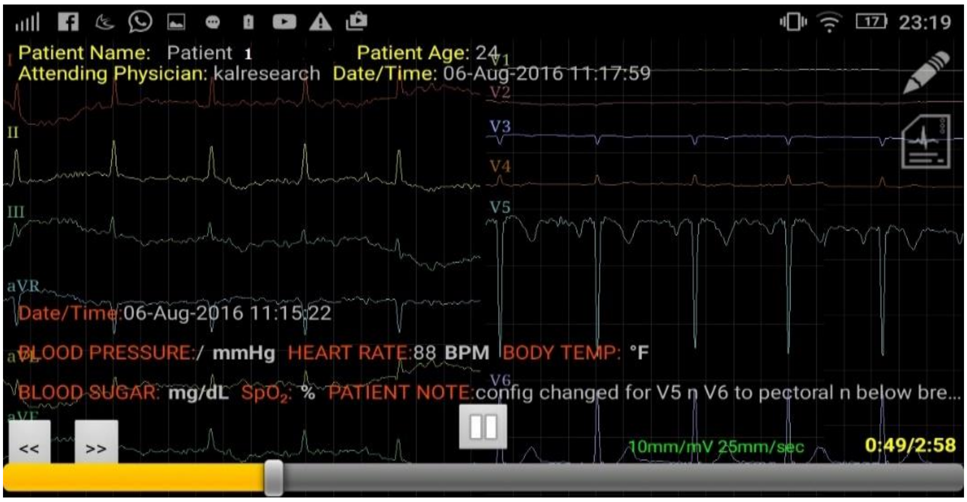

(c)

Figure A.2: Recordings of the three schemes using the Mobmon 12 lead resting ECG recorder (a) Scheme 1 (b) Scheme 2 and (c) Scheme 3.

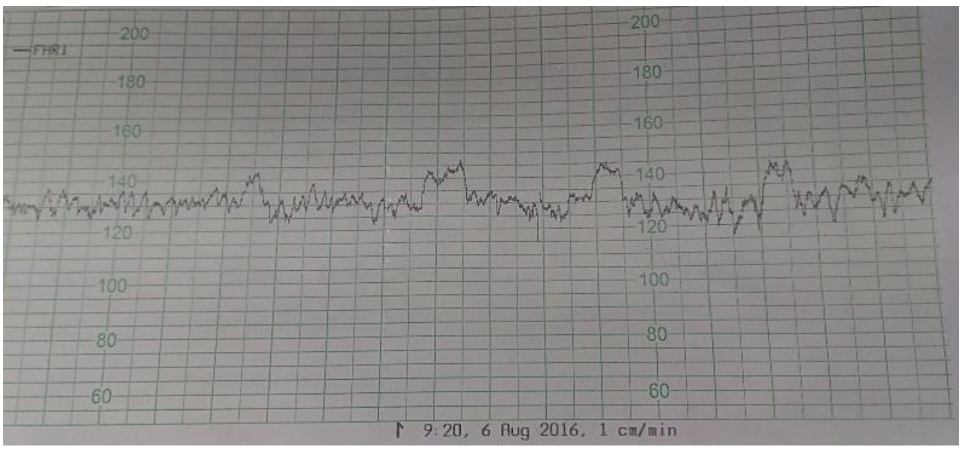

Figure A.3: CTG recording of the subject taken earlier to the aECG recording

Appendix B

Implementation of FECG extraction Techniques

B.1 Proposed Synthesized QRS Template

In this method we propose a two-step approach for maternal and fetal QRS extraction described as follows: a) Pre-processing from the raw abdominal ECG signal b) Generation of the synthesized QRS template (maternal and fetal) to be convoluted with of one of the filtered abdominal channels.

a. Pre-processing (baseline wandering removal)

The baseline signal was computed applying a low pass first order Butterworth filter in forward and backward direction to avoid phase distortion with a frequency cut off of 3.17 Hz [6]. Figure 3.3 shows the channel 4 abdominal ECG after pre-processing.

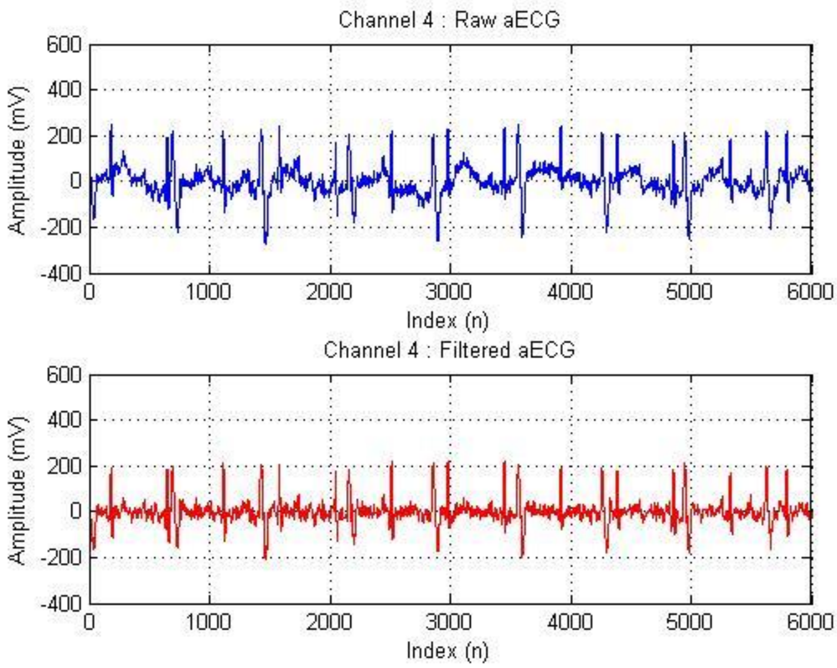

Figure B.1: Pre-processing stage for syntheszised QRS template method (adfecgdb aECG record r01).

b. Proposed Synthesized QRS template

The synthesized QRS template waveforms for both maternal and fetal ECG signals were computed for the three online Physionet database. The following six slopes for the QRS waveform were generated: zero-Q, Q-zero, zero-R, R-zero, zero-S and S-zero as shown in Figure B.2.

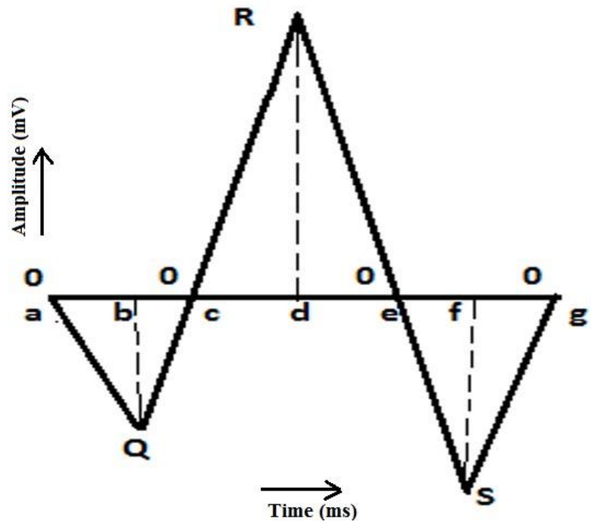

Figure B.2: Proposed synthesized QRS template for MQRS and FQRS.

A typical synthesized MQRS waveform can be computed for the following parameters: QRS (amplitude) = 211 µv; QRS (width) = 115ms and from Figure 3.4, the amplitudes at Q = -37 µv, R = 211 µv and S = -163 µv. (assume $n_o = 1$)

MQRS	$= -1.21(n - n_o)$	$no < n < n_o+33$	(point a)
	$= -37 + 5.28 (n - n_o - 33)$	$n_o+33 < n < n_o+40$	(point b)
	$= 11.72 (n - n_o - 40)$	$n_o+40 < n < n_o+58$	(point c)
	$= 211 - (11.72) (n - n_o - 58)$	$n_o+58 < n < n_o+76$	(point d)
	$= -9.58 (n - n_o - 76)$	$n_o+76 < n < n_o+93$	(point e)
	$= -163+ 7.76 (n - n_o - 93)$	$n_o+93 < n < n_o+114$	(point f)

Similarly using the above method, the synthesized FQRS can also be computed for the same database with QRS (amplitude) = 192 µv and QRS (width) = 58ms. The Q-R-S amplitudes will vary for each record.

In order to extract the MQRS and FQRS, we have taken the abdominal and direct fetal electrocardiogram database signals. To determine the correlations and convolutions between the original maternal and synthesized MQRS, the following two operations were simulated using Matlab 2013a for the entire database.

i) A train of synthesized MQRS signal x_1 (n) (with average beats per minute assumed to be equal to 88) is cross-correlated with the filtered aECG signal x_2 (n + j) as per Eq. (B.1) and shown in Figure B.3.

$$r_{12}(j) = \frac{1}{N}\sum_{n=0}^{N-1} x_1(n)\, x_2(n+j) \tag{B.1}$$

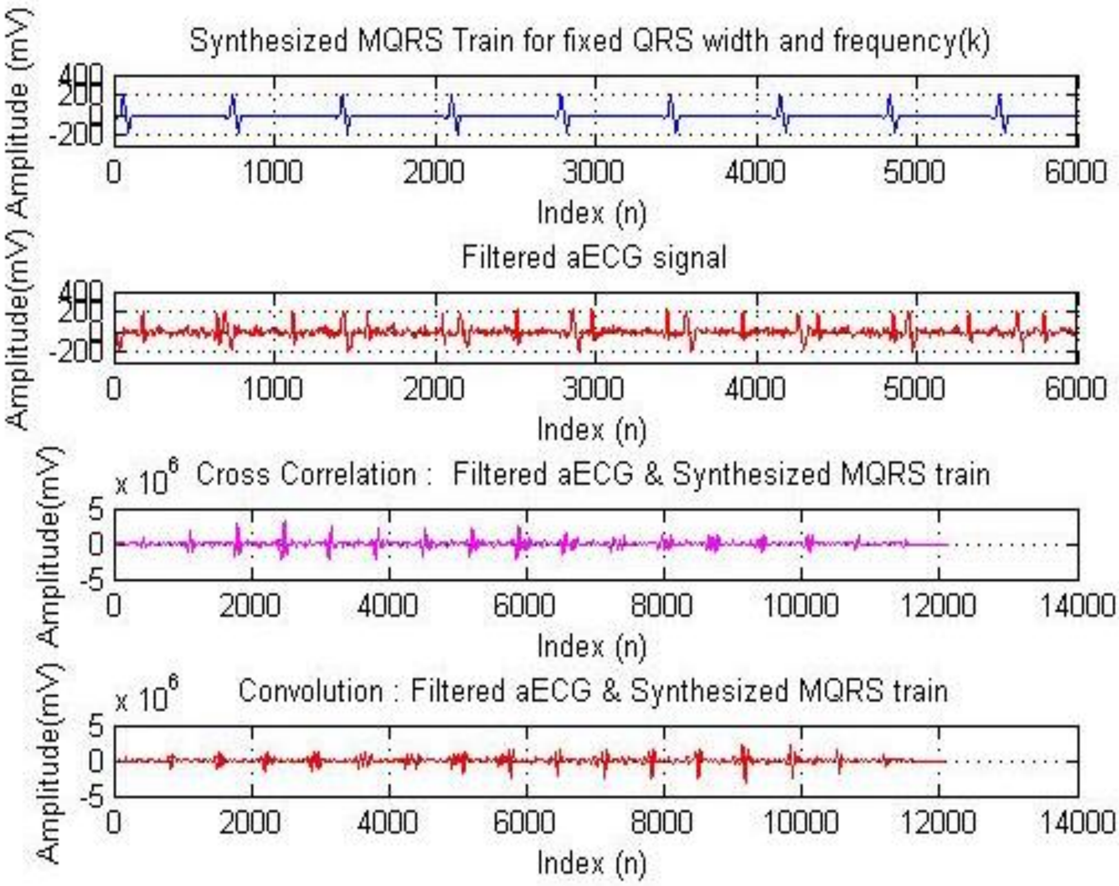

Figure B.3: Cross correlation and convolution of synthesized MQRS with filtered aECG.

ii) A multiplication of the pulse train of synthesized signals $x_1(k)$ with the filtered aECG signal $x_2(n - k)$ as per Eq. (B.2) is shown in Figure B.4.

$$y(n) = \frac{1}{N}\sum_{n=0}^{N-1} x_1(k)\, x_2(n-k) \tag{B.2}$$

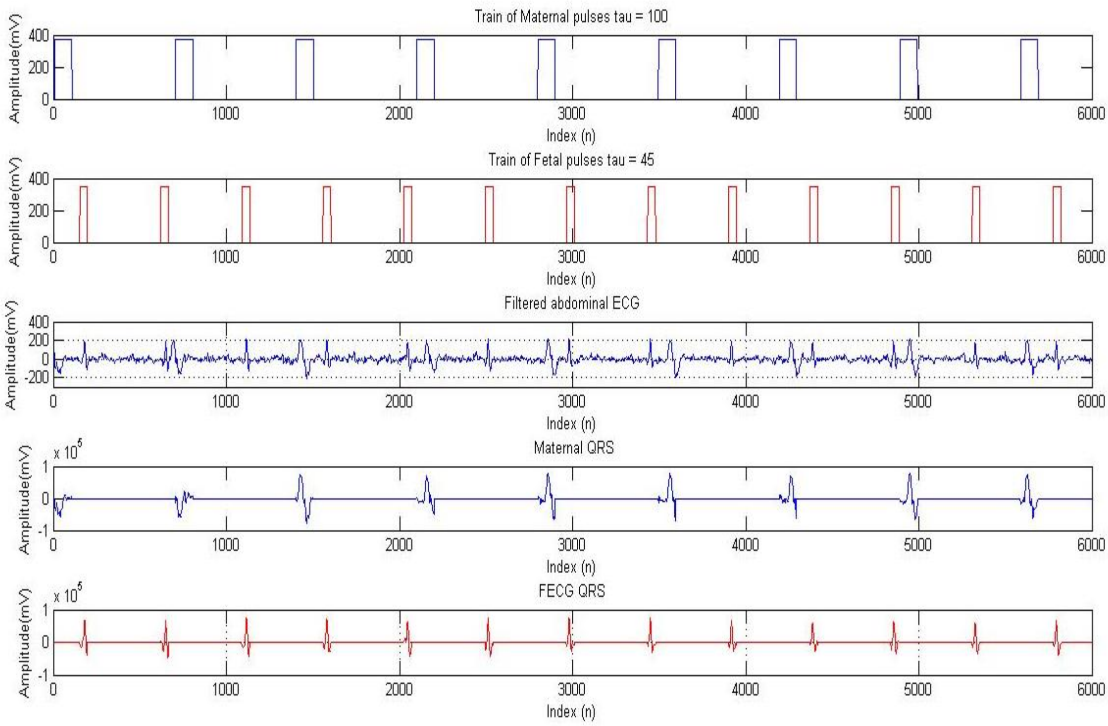

Figure B.4: Multiplication of synthesized pulses with filtered aECG to obtain MQRS and FQRS signals.

B.2 Proposed ICA method

In this section, we present an approach for detection of FQRS signals and FHR from non-invasive abdominal multi-channel signal using a three stage ICA method. The technique is based on two steps: a) Pre-processing of the channels and b) two stage ICA for fetal and maternal separations.

a) Pre-processing stage of all channels

The pre-filtering step is crucial for this method using ICA. The baseline wander is caused by the patient's breathing or movements during recording. The frequency of the baseline wander due to breathing is in the range of 1 Hz [8], hence the recorded signals were filtered by an FIR high pass filter with frequencies f_s = 1 Hz and f_c = 3 Hz. This is followed by a low pass filter with f_c = 25 Hz and f_s = 40 Hz which will eliminate EMG noise (artifacts of muscular contractions) characterized by relatively high frequency noise and the power line interference at 50Hz. The pre-processed abdominal channels are shown in Figure B.5.

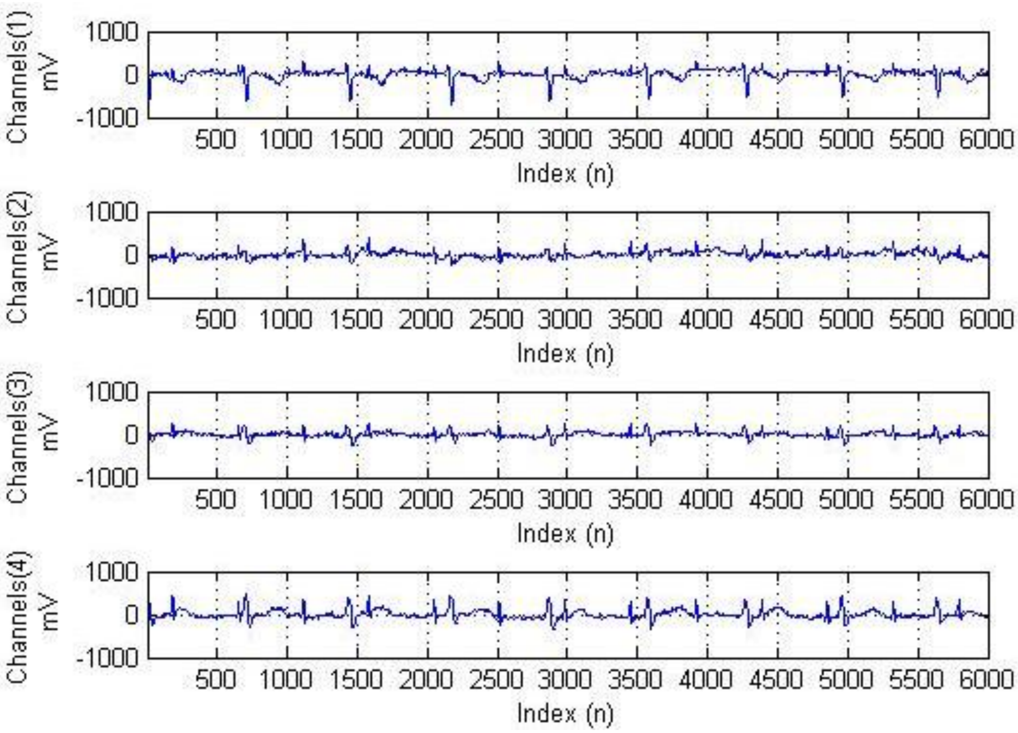

Figure B.5: Pre-processing the four adfecgdb abdominal channels for ICA method.

b) Two stage ICA for fetal and maternal separations.

After the filtering sequence, the ICA was applied to the four abdominal channels to separate maternal ECG from the other components. After the first stage application of ICA, channel 1 contains a strong MECG, channel 2 displays a mixture of FECG and MECG signals while, channel 3 and 4 contains the noise components shown by Figure B.6.

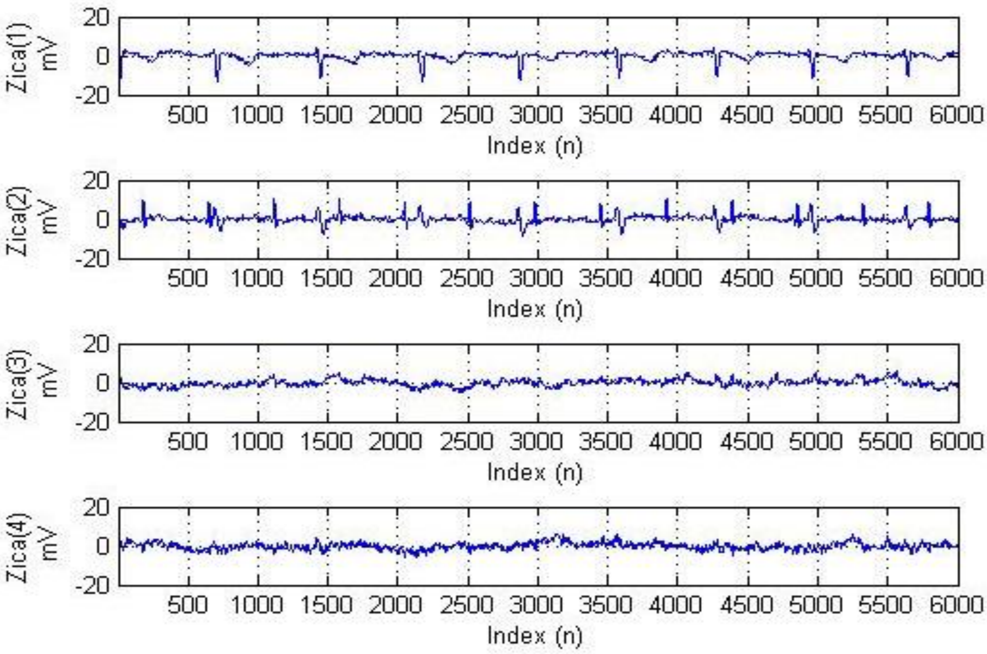

Figure B.6: Application of ICA to the 4 pre-processed abdominal channels (stage I).

After zeroing the noisy channels 3 and 4, four new channels are generated from the two valid channels 1 and 2 as shown in Figure B.7. The 2nd stage ICA is applied to these four generated channels, thus obtaining stronger MECG on channel 1, a prominent fetal signal on channel 2 with smaller amplitude traces of maternal ECG while channel 3 and 4 contain no noise signals as shown in Figure B.7. EEGLAB, an interactive Matlab toolbox was used for processing continuous and event-related EEG, and other electrophysiological data incorporating ICA.

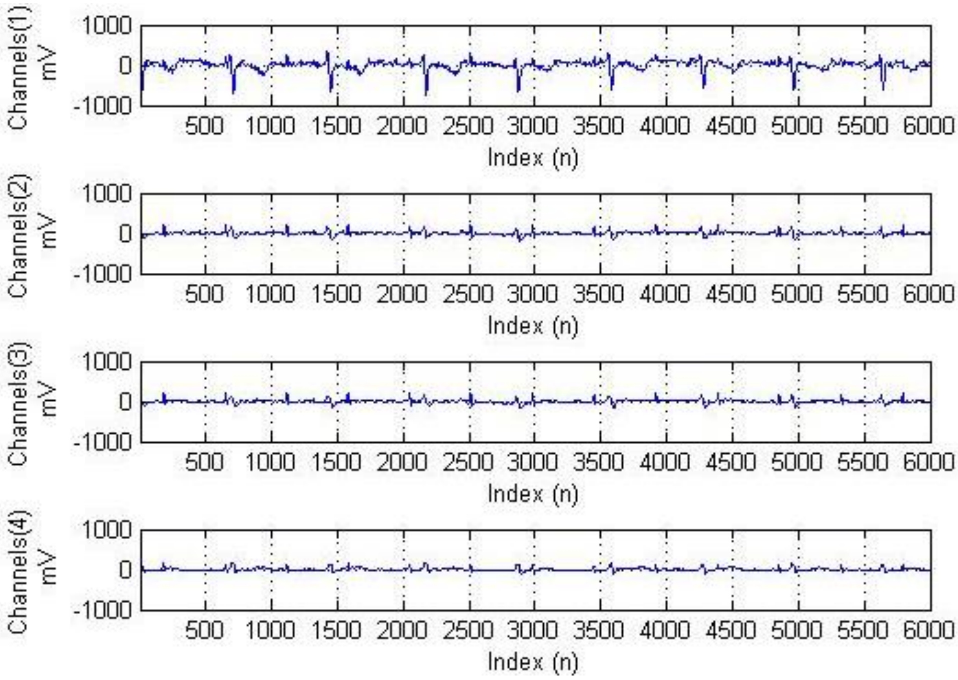

Figure B.7: Generation of four new abdominal channels from stage I.

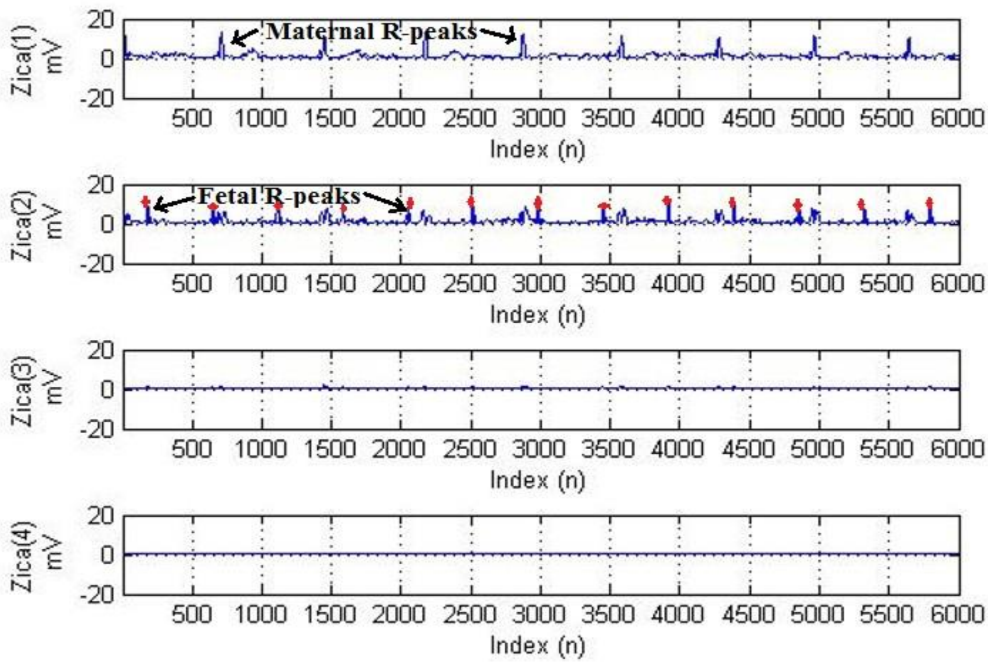

Figure B.8: Application of ICA to the four pre-processed abdominal channels (stage II). (The R –peaks with red dots indicate the fetal R-peaks).

The channel 2 from the ICA stage 2 is processed for reliable detection of fetal R-peaks which is the important task in computing the fetal heart rates. In the presence of noise, the performance of the QRS detector is greatly degraded.

B.3 Adaptive Neuro-Fuzzy Inference System (ANFIS)

In this section, we propose a technique to cancel the maternal ECG from the aECG using adaptive neuro-fuzzy inference system (ANFIS) based on Takagi–Sugeno fuzzy inference system [208].

In our case, MECG is the main noise source which needs to be eliminated from the abdominal composite signal. Since ANFIS is an adaptive noise cancellation system, it adjusts itself to filter the maternal ECG giving the estimated fetal ECG signal. Figure B.9, shows the proposed fetal extraction method which extracts fetal R peaks using a fetal QRS detector to obtain FHRs.

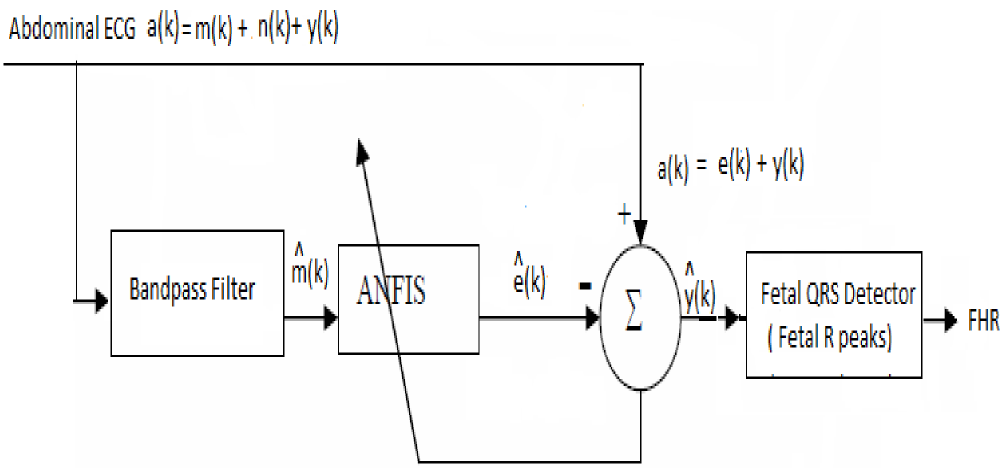

Figure B.9: Schematic diagram of ANFIS with QRS detector for extracting fetal R-peaks.

In this technique, the abdominal ECG signal is represented by a(k) while, the signal y(k) represents the fetal ECG information, which needs to be obtained from the abdominal signal a(k). The signal m(k) is the MECG signal and n(k) is the composite of all other noise signals. The aim is to extract y(k) from the composite maternal abdominal signal a(k) which contains the desired FECG signal y(k) plus e(k), where e(k) is m(k) + n(k). To estimate the m(k) and n(k) signals, we need to first obtain a filtered MECG m (k) estimate signal as a reference signal. This is done by a band pass filter with 3Hz and 15Hz as the cut-off frequencies as shown in Figure B.9. Our method is useful to compute the ê(k). When the two signals e(k) and the estimated ê(k) are identical, the signals cancel each other and we get the estimated fetal ECG output signal ŷ(k) which is identical to the fetal scalp ECG signal.

The estimated maternal ECG m(k) is fed to the ANFIS as a reference signal along with the MECG signal a(k) shown in Figure B.10 (a). The ANFIS tries to estimate the MECG present in the composite abdominal signal. When the desired epoch is obtained, ANFIS will stop training and output the new estimated MECG ê(k).Once the estimated ê(k) is computed using the Matlab command "evalfis", the estimated FECG is easily obtained by subtracting the estimated MECG ê(k) from the composite MECG a(k). The estimated FECG signal shown in Figure B.10 (d), is approximately the same as the direct fetal scalp ECG as show in Figure B.10 (b). The five records from the abfecgdb were evaluated for the fetal R-peaks and FHR.

The basic ANFIS algorithm used to compute the estimated output FECG signal ŷ (k) using Matlab is given below:

```
% Generating the initial FIS
  Set the number of membership functions (mf) to 2
  Set the number of step size (ss) to 0.2

 % Band pass filtered Abdominal ECG
  d = m (k) estimate

  % Abdominal ECG (aecg) = MECG + FECG + (Noise)
  delayed_d = [0; d (1: length (d)-1)]
  train_data = [delayed_d d aecg]

  % Generate the initial fuzzy network
  in_fismat = genfis1 (train_data, mf, mftype)

  % Using ANFIS for fine tuning the FIS for 20 epochs
  out_fismat = anfis (train_data, in_fismat, [20 nan ss])

  % Testing the tuned model with training data
  Ê (k) = evalfis (train_data (: , 1:2), out_fismat)
   Estimated FECG [ŷ (k)] = aECG - estimate [ê (k)]
```

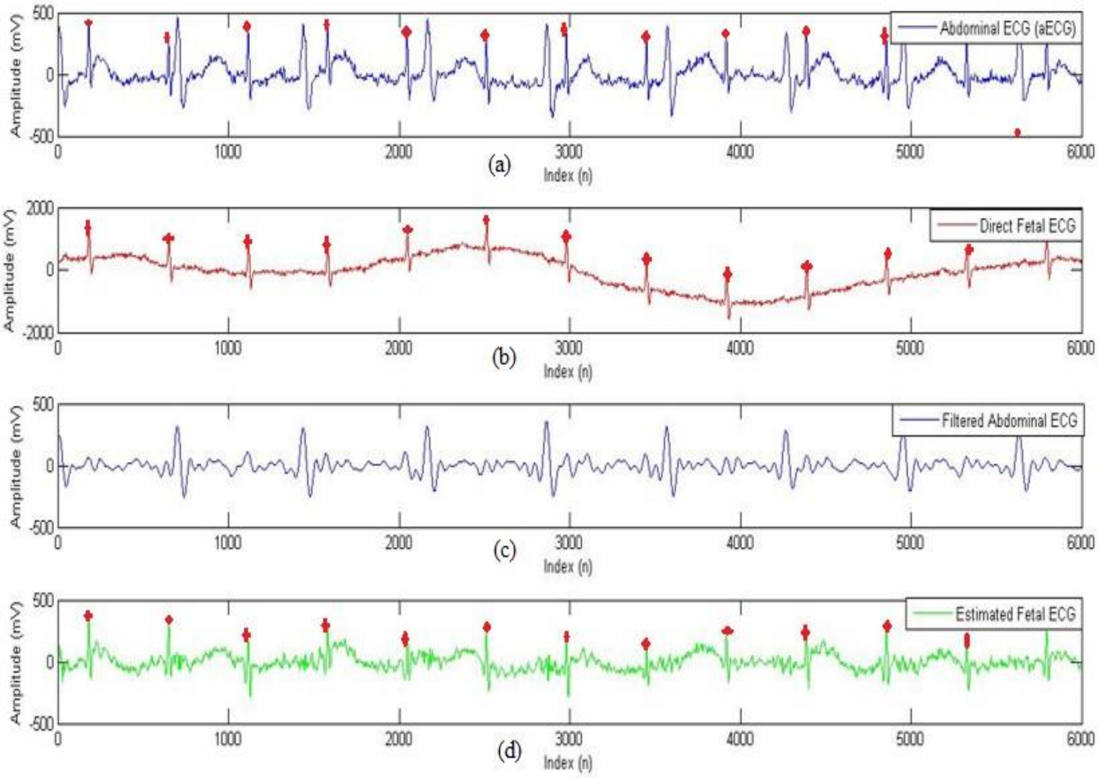

Figure B.10: ANFIS computations for fetal R-peaks (a) aECG a(k). (b) Direct scalp FECG. (c) Filtered aECG and (d) Estimated FQRS ŷ (k) shown by red dots are the fetal R-peaks.

Appendix C

Connecting to a smart phone using MATLAB Mobile

MATLAB Mobile is an application on your smartphone device which connects to a MATLAB session that is running on your laptop or desktop [165]. On the smartphone we can create a username and configure the IP address, while at the desktop or laptop we can use the command “connector on” to directly connect to the smartphone. This allows remote access to your scripts and also allows you to view the simulation plots, figures and results. Connecting to a Matlab session on your computer requires that you have the Matlab Connector running on that session. Additionally, the mobile device requires network access to the computer you are connecting it to. We connected our Android smartphone to Matlab via the Matlab Mobile as shown in Figure C.1 to view the Matlab files of the QRS detector. ANFIS extracted FECG and the fetal heart rate. Figure C.2 (a) and (b) show the Matlab mobile screenshots of the FHR variability and the average FHR value respectively.

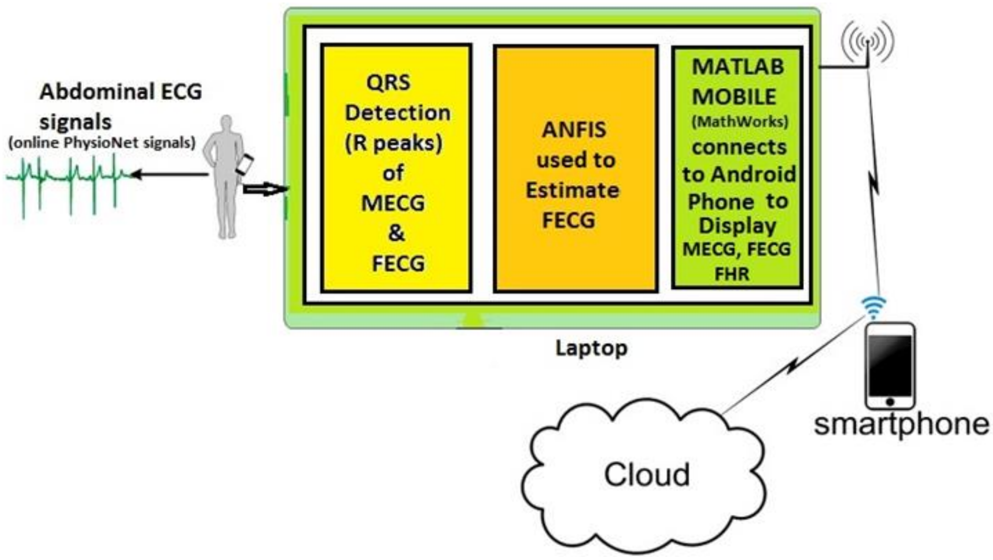

Figure C.1: Matlab Mobile set up to display FHR on smart phones.

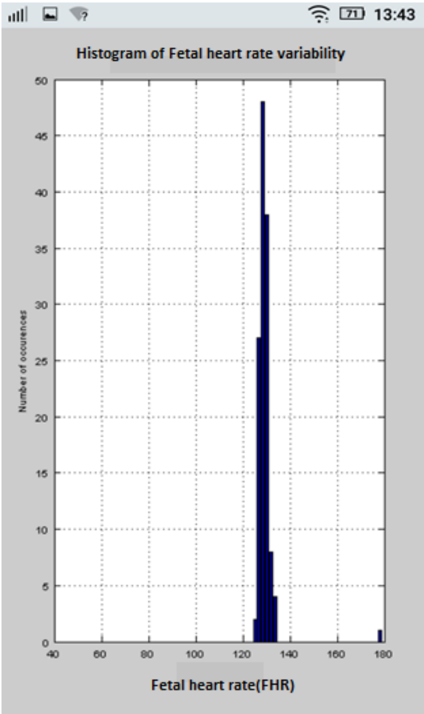

C.2 (a)

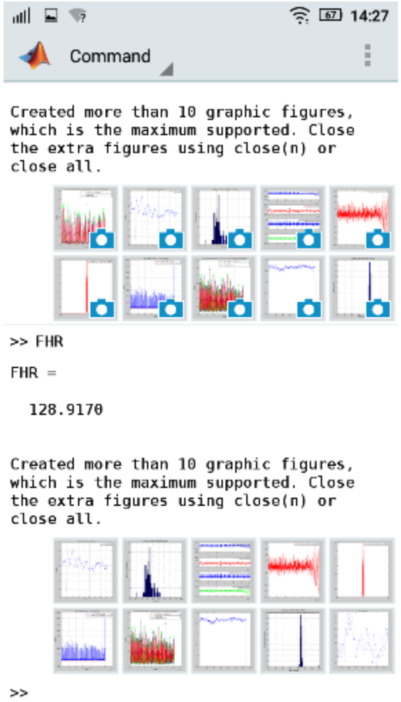

C.2 (b)

Figure C.2: Display of FHR on a smart phone using Matlab Mobile (a) Histogram of the FHR variability. (b) Matlab command prompt showing the FHR value for the record r01 of adfecgdb database (channel 4).

Appendix D

Linear phase sharp transition FIR filter designs

D1. Model I (a): LPST high pass FIR filter model and design

In this section, the design of the high pass with a LPST FIR filter is presented. For the proposed high pass filter model, the three regions of the filter response H (ω) are modelled using trigonometric functions of frequency as shown in Figure 3.4 of Chapter 3. The filter design parameters k_{sh}, k_{th} and k_{ph} for the three regions of the high pass filter are evaluated below:

(i) In the stopband region, for $0 \le \omega \le \omega_{sh}$,the frequency response

$$H(\omega) = \delta_s (1 - \cos(k_{sh}\,\omega)), \tag{D1.1}$$

$$\text{At } \omega = 0; \qquad H(0) = \delta_s - \delta_s \cos(k_{sh}(0)) = 0$$

$$\text{At } \omega = \omega_{sh} \qquad H(\omega_{sh}) = \delta_s - \delta_s \cos(k_{sh}\,\omega_{sh}) = \delta_s$$

$$\therefore \cos(k_{sh}\,\omega_{sh}) = 0$$

$$k_{sh}\,\omega_{sh} = \frac{\pi}{2}$$

$$\therefore k_{sh} = \frac{\pi}{2\omega_{sh}} \tag{D1.2}$$

In Eq. (D1.1), ω is the frequency variable, H (ω) is the magnitude of the filter response, δ_s is the stopband attenuation, k_{sh} is the stopband filter design parameter and ω_{sh} is the stopband edge frequency.

ii) In the sharp transition region for $\omega_{sh} \le \omega \le \omega_{ch}$, the frequency response is

$$H(\omega) = \delta_s + (1 - \delta_p - \delta_s) \sin(k_{th}(\omega - \omega_{sh})) \tag{D1.3}$$

$$\text{At } \omega = \omega_{sh}; \qquad H(\omega_{sh}) = \delta_s + (1 - \delta_p - \delta_s) \sin(k_{th}(0)) = \delta_s$$

$$\text{At } \omega = \omega_{ch}; \qquad H(\omega_{ch}) = \delta_s + (1 - \delta_p - \delta_s) \sin(k_{th}(\omega_{ch} - \omega_{sh})) = 1 - \delta_p$$

$$H(\omega_{ch}) = \delta_s + (1 - \delta_p - \delta_s)(1)$$

$$\therefore \sin(k_{th}(\omega_{ch} - \omega_{sh})) = 1$$

$$(k_{th}(\omega_{ch} - \omega_{sh})) = \frac{\pi}{2}$$

$$\therefore k_{th} = \frac{\pi}{2(\omega_{ch} - \omega_{sh})} \tag{D1.4}$$

where, δ_p is the passband ripple, k_{th} is the transition filter design parameter and ω_{ch} is the cut off frequency in the passband.

iii) In the passband region for $\omega_{ch} \leq \omega \leq \pi$, the frequency response is

$$H(\omega) = (1-\delta_p) + \delta_p \sin(k_{ph}(\omega-\omega_{ch})) \quad \text{(D1.5)}$$

$$At\ \omega = \omega_{ch}; \qquad H(\omega_{ch}) = (1-\delta_p) + \delta_p \sin(k_{ph}(0)) = (1-\delta_p)$$

$$At\ \omega = \pi; \qquad H(\pi) = (1-\delta_p) + \delta_p \sin(k_{ph}(\pi-\omega_{ch})) = 1$$

$$H(\pi) = (1-\delta_p) + \delta_p = 1$$

$$\therefore \sin(k_{ph}(\pi-\omega_{ch})) = 1$$

$$k_{ph}(\pi-\omega_{ch}) = \frac{\pi}{2}$$

$$\therefore k_{ph} = \frac{\pi}{2(\pi-\omega_{ch})} \quad \text{(D1.6)}$$

where, k_{ph} is the passband filter design parameter.

D1.1 Expressions for Impulse Response Coefficients for the high pass FIR Filter.

The impulse response coefficients h (n) for the high pass FIR filter are obtained by computing the integral limits of the three regions as shown in the filter model magnitude response in Figure 3.4.

$$h(n) = \frac{1}{\pi}\left[\int_0^{\pi} H(\omega)\ \sin(k\omega)\ d\omega\right] \quad \text{(D1.7)}$$

$$h(n) = \frac{1}{\pi}\left\{\int_0^{\omega_{sh}} H(\omega)\ \sin(k\omega)\ \partial\omega + \int_{\omega_{sh}}^{\omega_{ch}} H(\omega)\ \sin(k\omega)\ \partial\omega + \int_{\omega_{ch}}^{\pi} H(\omega)\ \sin(k\omega)\ \partial\omega\right\} \quad \text{(D1.8)}$$

Substituting Eq.s (D1.1) to (D1.6) in Eq. (D1.8) we get,

$$h(n) = \frac{1}{\pi}\left\{\int_0^{\omega_{sh}} \delta_s\ (1 - \cos(k_{sh}\ \omega))\ \sin(k\omega)\ \partial\omega + \int_{\omega_{sh}}^{\omega_{ch}} (\delta_s + (1 - \delta_p - \delta_s)\ \sin(k_{th}(\omega-\omega_{sh})))\ \sin(k\omega)\ \partial\omega\right.$$

$$\left. + \int_{\omega_{ch}}^{\pi} ((1-\delta_p) + \delta_p \sin(k_{ph}(\omega-\omega_{ch})))\ \sin(k\omega)\ \partial\omega\right\} \quad \text{(D1.9)}$$

Solving the 1st term from Eq. (D1.9) we get,

$$1st\ term = h_{1h}(n) = \frac{1}{\pi}\int_0^{\omega_{sh}} H(\omega)\ \sin(k\omega)\ \partial\omega$$

$$h_{1h}(n) = \frac{1}{\pi}\int_0^{\omega_{sh}} \delta_s\ (1 - \cos(k_{sh}\ \omega))\ \sin(k\omega)\ \partial\omega$$

$$h_{1h}(n) = \frac{\delta_s}{\pi}\left[\left.\frac{-\cos k\omega}{k}\right|_0^{\omega_{sh}} - \int_0^{\omega_{sh}} \cos(k_{sh}\omega)\ \sin(k\omega)\ \partial\omega\right]$$

$$h_{1h}(n) = \frac{\delta_s}{k\pi}\left[-\cos(k\omega_{sh})+1\right]-\frac{\delta_s}{2\pi}\int_0^{\omega_{sh}}\left\{\sin(k\omega+k_{sh}\omega)+\sin\left[(k-k_{sh})\omega\right]\right\}\partial\omega$$

$$h_{1h}(n) = \frac{\delta_s}{k\pi}\left[1-\cos(k\omega_{sh})\right]-\frac{\delta_s}{2\pi}\left[\frac{-\cos(k+k_{sh})\omega}{(k+k_{sh})}-\frac{\cos(k-k_{sh})\omega}{(k-k_{sh})}\right]\Bigg|_0^{\omega sh}$$

$$h_{1h}(n) = \frac{\delta_s}{k\pi}\left[1-\cos(k\omega_{sh})\right]+\frac{\delta_s}{2\pi}\left[\frac{\cos\left[(k+k_{sh})\omega_{sh}\right]-\cos(0)}{(k+k_{sh})}+\frac{\cos\left[(k-k_{sh})\omega_{sh}\right]-1}{(k-k_{sh})}\right]$$

$$h_{1h}(n) = \frac{\delta_s}{k\pi}\left[1-\cos(k\omega_{sh})\right]+\frac{\delta_s}{2\pi}\left[\frac{\cos\left[(k+k_{sh})\omega_{sh}\right]-1}{(k+k_{sh})}+\frac{\cos\left[(k-k_{sh})\omega_{sh}\right]-1}{(k-k_{sh})}\right] \tag{D1.10}$$

Solving the 2nd term from Eq. (D1.9) we get,

$$2nd\ term = h_{2h}(n) = \frac{1}{\pi}\int_{\omega_{sh}}^{\omega_{ch}} H(\omega)\ \sin(k\omega)\ \partial\omega$$

$$h_{2h}(n) = \frac{1}{\pi}\int_{\omega_{sh}}^{\omega_{ch}} (\delta_s+(1-\delta_p-\delta_s)\ \sin\ (k_{th}\ (\omega-\omega_{sh})))\ \sin(k\omega)\ \partial\omega$$

$$h_{2h}(n) = \frac{\delta_s}{\pi}\left[\frac{-\cos k\omega}{k}\Bigg|_{\omega sh}^{\omega ch}\right]+\frac{(1-\delta_p-\delta_s)}{\pi}\int_{\omega_{sh}}^{\omega_{ch}}\sin\left[k_{th}(\omega-\omega_{sh})\right]\sin(k\omega)\ \partial\omega$$

$$h_{2h}(n)= \frac{\delta_s\left[\cos(k\omega_{sh})-\cos(k\omega_{ch})\right]}{k\pi}+\frac{(1-\delta_p-\delta_s)}{\pi}.\frac{1}{2}\int_{\omega_{sh}}^{\omega_{ch}}\left\{\cos\ [(k_{th}-k)\omega-k_{th}\ \omega_{sh}]-\cos\ [(k_{th}+k)\omega-k_{th}\ \omega_{sh}]\right\}\partial\omega$$

$$h_{2h}(n)= \frac{\delta_s\left[\cos(k\omega_{sh})-\cos(k\omega_{ch})\right]}{k\pi}+\frac{(1-\delta_p-\delta_s)}{2\pi}\left[\frac{\sin\ [(k_{th}-k)\omega-k_{th}\ \omega_{sh}}{k_{th}-k}-\frac{\sin\ [(k_{th}+k)\omega-k_{th}\ \omega_{sh}]}{k_{th}+k}\right]_{\omega sh}^{\omega ch}$$

$$h_{2h}(n) = \frac{\delta_s}{k\pi}\left[\cos k\omega_{sh}-\cos k\omega_{ch}\right]+\frac{(1-\delta_p-\delta_s)}{2\pi}\left[\begin{array}{l}\dfrac{\sin\ [(k_{th}-k)\omega_{ch}-k_{th}\ \omega_{sh}]+\sin k\omega_{sh}}{k_{th}-k}\\ +\dfrac{-\sin\ [(k_{th}+k)\omega_{ch}-k_{th}\ \omega_{sh}]+\sin(k\omega_{sh})}{k_{th}+k}\end{array}\right]$$

$$h_{2h}(n) = \frac{\delta_s}{k\pi}\left[\cos k\omega_{sh}-\cos k\omega_{ch}\right]+\frac{(1-\delta_p-\delta_s)}{2\pi}\left[\begin{array}{l}\dfrac{\sin\ [(k_{th}-k)\omega_{ch}-k_{th}\ \omega_{sh}]+\sin k\omega_{sh}}{k_{th}-k}\\ +\dfrac{\sin(k\omega_{sh})-\sin\ [(k_{th}+k)\omega_{ch}-k_{th}\ \omega_{sh}]}{k_{th}+k}\end{array}\right] \tag{D1.11}$$

Solving the 3rd term from Eq. (D1.9) we get,

$$3rd\ term = h_{3h}(n) = \frac{1}{\pi}\int_{\omega_{ch}}^{\pi} H(\omega)\ \sin(k\omega)\ \partial\omega$$

$$h_{3h}(n) = \frac{1}{\pi}\int_{\omega_{ch}}^{\pi}\left[(1-\delta_p)+\delta_p\ \sin\ (k_{ph}\ (\omega-\omega_{ch}))\right]\ \sin\ (k\omega)\ \partial\omega$$

$$h_{3h}(n)=\frac{1-\delta_p}{\pi}\left[\frac{-\cos k\omega}{k}\Bigg|_{\omega_{ch}}^{\pi}\right]+\frac{\delta_p}{\pi}.\frac{1}{2}\int_{\omega_{ch}}^{\pi}\left\{\cos\left[(k_{ph}-k)\omega-k_{ph}\,\omega_{ch}\right]-\cos\left[(k_{ph}+k)\omega-k_{ph}\,\omega_{ch}\right]\right\}\partial\omega$$

$$h_{3h}(n)=\frac{(1-\delta_p)\left[\cos(k\omega_{ch})-\cos(k\pi)\right]}{k\pi}+\frac{\delta_p}{2\pi}\left[\frac{\sin\left[(k_{ph}-k)\omega-k_{ph}\,\omega_{ch}\right]}{k_{ph}-k}-\frac{\sin\left[(k_{ph}+k)\omega-k_{ph}\,\omega_{ch}\right]}{k_{ph}+k}\right]_{\omega_{ch}}^{\pi}$$

$$h_{3h}(n)=\frac{(1-\delta_p)\left[\cos(k\omega_{ch})-\cos(k\pi)\right]}{k\pi}+\frac{\delta_p}{2\pi}\left[\begin{array}{c}\dfrac{\sin\left[(k_{ph}-k)\pi-k_{ph}\,\omega_{ch}\right]+\sin(k\omega_{ch})}{k_{ph}-k}\\ +\dfrac{\sin(k\omega_{ch})-\sin\left[(k_{ph}+k)\pi-k_{ph}\,\omega_{ch}\right]}{k_{ph}+k}\end{array}\right] \qquad \text{(D1.12)}$$

The Eq. (D1.10) to (D1.12) are evaluated to obtain the expression for the high pass filter model impulse response h (n).

$$\begin{aligned}h(n) = &\left\{\left(\frac{\delta_s}{k\pi}\right)\left[1-\cos(k\omega_{sh})\right]+\left(\frac{\delta_s}{2\pi}\right)\left[\frac{\cos\left[(k+k_{sh})\omega_{sh}\right]-1}{(k+k_{sh})}+\frac{\cos\left[(k-k_{sh})\omega_{sh}\right]-1}{(k-k_{sh})}\right]\right\}\\ &+\left\{\left(\frac{\delta_s}{k\pi}\right)\left[\cos(k\omega_{sh})-\cos(k\omega_{ch})\right]+\left(\frac{1-\delta_p-\delta_s}{2\pi}\right)\left[\begin{array}{c}\dfrac{\sin\left[(k_{th}-k)\omega_{ch}-k_{th}\omega_{sh}\right]+\sin(k\omega_{sh})}{(k_{th}-k_{sh})}\\ +\dfrac{\sin(k\omega_{sh})-\sin\left[(k_{th}+k)\omega_{ch}-k_{th}\omega_{sh}\right]}{(k_{th}+k_{sh})}\end{array}\right]\right\}\\ &+\left\{\left(\frac{1-\delta_s}{k\pi}\right)\left[\cos(k\omega_{ch})-\cos(k\pi)\right]+\left(\frac{\delta_p}{2\pi}\right)\left[\begin{array}{c}\dfrac{\sin\left[(k_{ph}-k)\pi-k_{ph}\omega_{ch}\right]+\sin(k\omega_{ch})}{(k_{ph}-k)}\\ +\dfrac{\sin(k\omega_{ch})-\sin\left[(k_{ph}+k)\pi-k_{ph}\omega_{ch}\right]}{(k_{ph}+k)}\end{array}\right]\right\}\end{aligned} \qquad \text{(D1.13)}$$

The Eq. (D1.13) is the expression for the high pass filter model impulse response h (n).

D2. Model I (b): LPST low pass FIR filter model and design

In this section, the design of the LPST low pass FIR filter is presented. For the proposed low pass filter model, the three regions of the filter response are modelled using trigonometric functions of frequency. As in high pass filter design, ω is the frequency variable, H (ω) is the magnitude of the filter response, δ_s is the stopband attenuation and δ_p is the passband ripple. k_{pl}, k_{tl} and k_{sl} are the passband, transition and stopband filter design parameters respectively. The filter model magnitude response H (ω) is shown in Figure 3.5 in chapter 3. The filter design parameters k_{pl}, k_{tl} and k_{sl} for the three regions of the low pass filter are evaluated below:

In the passband region of $0 \le \omega \le \omega_{cl}$, the frequency response is

$$H(\omega) = (1-\delta_p) + \delta_p \cos(k_{pl}\,\omega) \qquad \text{(D2.1)}$$

$$At\ \omega = 0; \quad H(0) = (1-\delta_p) + \delta_p = 1$$

$$At\ \omega = \omega_{cl}; \quad H(\omega_{cl}) = (1-\delta_p) + \delta_p \cos(k_{pl}\,\omega_{cl}) = 1-\delta_p$$

$$\therefore \cos(k_{pl}\,\omega_{cl}) = 0$$

$$k_{pl}\,\omega_{cl} = \frac{\pi}{2}$$

$$\therefore k_{pl} = \frac{\pi}{2\omega_{cl}} \qquad \text{(D2.2)}$$

(i) In the sharp transition region for $\omega_{cl} \le \omega \le \omega_{sl}$, the frequency response is,

$$H(\omega) = \delta_s + (1-\delta_p-\delta_s)\cos k_{tl}(\omega-\omega_{cl}) \qquad \text{(D2.3)}$$

$$At\ \omega = \omega_{cl}; \quad H(\omega_{cl}) = \delta_s + (1-\delta_p-\delta_s) = 1-\delta_p$$

$$At\ \omega = \omega_{sl}; \quad H(\omega_{sl}) = \delta_s + (1-\delta_p-\delta_s)\cos k_{tl}(\omega_{sl}-\omega_{cl}) = \delta_s$$

$$\therefore \cos k_{tl}(\omega_{sl}-\omega_{cl}) = 0$$

$$k_{tl}(\omega_{sl}-\omega_{cl}) = \frac{\pi}{2}$$

$$\therefore k_{tl} = \frac{\pi}{2(\omega_{sl}-\omega_{cl})} \qquad \text{(D2.4)}$$

(ii) In the stop band region for $\omega_{sl} \le \omega \le \pi$, the frequency response is,

$$H(\omega) = \delta_s - \delta_s \sin(k_{sl}(\omega-\omega_{sl})) \qquad \text{(D2.5)}$$

$$At\ \omega = \omega_{sl}; \quad H(\omega_{sl}) = \delta_s - \delta_s \sin k_{sl}(\omega-\omega_{sl}) = \delta_s$$

$$At\ \omega = \pi; \quad H(\pi) = \delta_s - \delta_s \sin k_{sl}(\pi-\omega_{sl}) = 0$$

$$\therefore \sin k_{sl}(\pi-\omega_{sl}) = 1$$

$$k_{sl}(\pi-\omega_{sl}) = \frac{\pi}{2}$$

$$\therefore k_{sl} = \frac{\pi}{2(\pi-\omega_{sl})} \qquad \text{(D2.6)}$$

D2.1 Expressions for Impulse Response Coefficients for the low pass FIR Filter.

The impulse response coefficients h (n) for the low pass FIR filter are obtained by computing the weighted integral of the magnitude response over three regions shown in the filter model magnitude response in Figure 3.5.

$$h(n) = \frac{1}{\pi}\left[\int_0^{\pi} H(\omega)\ \cos k\omega\ \mathrm{d}\omega\right] \tag{D2.7}$$

$$h(n) = \frac{1}{\pi}\left\{\int_0^{\omega_{cl}} H(\omega)\ \cos k\omega\ \partial\omega\ +\int_{\omega_{cl}}^{\omega_{sl}} H(\omega)\ \cos k\omega\ \partial\omega\ +\int_{\omega_{sl}}^{\pi} H(\omega)\ \cos k\omega\ \partial\omega\right\} \tag{D2.8}$$

Solving the 1st term from Eq. (D2.8)

$$1st\ \text{term} = h_{1l}(n) = \frac{1}{\pi}\int_0^{\omega_{cl}} [(1-\delta_p)\ +\ \delta_p\ \cos\ k_{pl}\ \omega]\ \cos k\omega\ \partial\omega$$

$$= \frac{1}{\pi}\left[\frac{(1-\delta_p)\sin k\omega}{k}\Bigg|_0^{\omega cl} + \frac{\delta_p}{2}\int_0^{\omega_{cl}} [\cos\ (k_{pl}+k)\omega + \cos\ (k_{pl}-k)\omega]\ \partial\omega\right]$$

$$= \frac{1}{\pi}\left[\frac{(1-\delta_p)\ \sin k\omega_{cl}}{k} + \frac{\delta_p}{2}\left[\frac{\sin\ (k_{pl}+k)\omega}{(k_{pl}+k)} + \frac{\sin\ (k_{pl}-k)\omega}{(k_{pl}-k)}\right]\Bigg|_0^{\omega cl}\right]$$

$$= \frac{(1-\delta_p)\ \sin k\omega_{cl}}{k\pi} + \frac{\delta_p}{2\pi}\left[\frac{\sin\ (k_{pl}+k)\omega_{cl}}{(k_{pl}+k)} + \frac{\sin\ (k_{pl}-k)\omega_{cl}}{(k_{pl}-k)}\right]$$

$$= \frac{(1-\delta_p)\ \sin k\omega_{cl}}{k\pi} + \frac{\delta_p}{2\pi(k_{pl}^2-k^2)}\ \left\{(k_{pl}-k)\left[\sin\ (k_{pl}+k)\omega_{cl}\right] + (k_{pl}+k)\left[\sin\ (k_{pl}-k)\omega_{cl}\right]\ \right\}$$

$$= \frac{(1-\delta_p)\ \sin k\omega_{cl}}{k\pi} + \frac{\delta_p}{2\pi(k_{pl}^2-k^2)}\begin{bmatrix} k_{pl}\ \left\{\left[\sin(k_{pl}+k)\omega_{cl}\right] + \left[\sin\ (k_{pl}-k)\omega_{cl}\right]\right\} \\ +k\left\{\left[\sin(k_{pl}-k)\omega_{cl}\right] - \left[\sin(k_{pl}+k)\omega_{cl}\right]\right\}\end{bmatrix}$$

$$= \frac{(1-\delta_p)\ \sin k\omega_{cl}}{k\pi} + \frac{\delta_p}{2\pi(k_{pl}^2-k^2)}\left[2k_{pl}\ \sin(k_{pl}\omega_{cl})\cos(k\omega_{cl}) - 2k\cos(k_{pl}\omega_{cl})\sin(k\omega_{cl})\right]$$

$$= \frac{(1-\delta_p)\ \sin k\omega_{cl}}{k\pi} + \frac{\delta_p}{\pi(k_{pl}^2-k^2)}\left[k_{pl}\ \sin(k_{pl}\omega_{cl})\cos(k\omega_{cl}) - k\cos(k_{pl}\omega_{cl})\sin(k\omega_{cl})\ \right] \tag{D2.9}$$

Solving the 2nd term from Eq. (D2.8)

$$2nd\ \text{term} = h_{21}(n) = \frac{1}{\pi}\int_{\omega_{cl}}^{\omega_{sl}} [\delta_s + (1-\delta_p-\delta_s)\ \cos\ k_{tl}\ (\omega-\omega_{cl})\ ]\ \cos k\omega\ \partial\omega$$

$$= \left[\frac{\delta_s \sin k\omega}{k\pi}\Bigg|_{\omega cl}^{\omega sl} + \frac{(1-\delta_p-\delta_s)}{2\pi}\int_{\omega_{cl}}^{\omega_{sl}}\left\{\cos\ [(k_{tl}+k)\omega - k_{tl}\ \omega_{cl}] + \cos\ [(k_{tl}-k)\omega - k_{tl}\ \omega_{cl}]\right\}\partial\omega\right]$$

$$= \frac{\delta_s}{k\pi}\left[\sin k\omega_{sl} - \sin k\omega_{cl}\right] + \frac{(1-\delta_p-\delta_s)}{2\pi}\left[\frac{\sin\ \left[(k_{tl}+k)\omega - k_{tl}\ \omega_{cl}\right]}{k_{tl}+k} + \frac{\sin\ [(k_{tl}-k)\omega - k_{tl}\ \omega_{cl}]}{k_{tl}-k}\right]_{\omega cl}^{\omega sl}$$

$$= \frac{\delta_s}{k\pi}\left[\sin k\omega_{sl} - \sin k\omega_{cl}\right] + \frac{(1-\delta_p-\delta_s)}{2\pi}\begin{bmatrix}\dfrac{\sin\ [(k_{tl}+k)\omega_{sl} - k_{tl}\ \omega_{cl}] - \sin k\omega_{cl}}{k_{tl}+k} \\ +\dfrac{\sin\ [(k_{tl}-k)\omega_{sl} - k_{tl}\ \omega_{cl}] - \sin(-k\omega_{cl})}{k_{tl}-k}\end{bmatrix}$$

$$= \frac{\delta_s}{k\pi}\left[\sin k\omega_{sl} - \sin k\omega_{cl}\right] + \frac{(1-\delta_p-\delta_s)}{2\pi(k_{tl}^2-k^2)}\begin{bmatrix}(k_{tl}-k)\left\{\sin\ [(k_{tl}+k)\omega_{sl} - k_{tl}\ \omega_{cl}] - \sin k\omega_{cl}\right\} + \\ (k_{tl}+k)\left\{\sin\ [(k_{tl}-k)\omega_{sl} - k_{tl}\ \omega_{cl}] + \sin(k\omega_{cl})\right\}\end{bmatrix}$$

$$= \frac{\delta_s}{k\pi}\left[\sin k\omega_{sl} - \sin k\omega_{cl}\right] + \frac{(1-\delta_p-\delta_s)}{2\pi(k_{tl}^2 - k^2)}\begin{bmatrix} k_{tl}\left\{\sin\ [(k_{tl}+k)\omega_{sl} - k_{tl}\ \omega_{cl}] + \sin\ [(k_{tl}-k)\omega_{sl} - k_{tl}\ \omega_{cl}]\right\} \\ +k\left\{\sin\ [(k_{tl}-k)\omega_{sl} - k_{tl}\ \omega_{cl}] - \sin\ [(k_{tl}+k)\omega_{sl} - k_{tl}\ \omega_{cl}]\right\} \\ +\ \sin k\omega_{cl}\left[k_{tl}+k-(k_{tl}-k)\right] \end{bmatrix}$$

$$= \frac{\delta_s}{k\pi}\left[\sin k\omega_{sl} - \sin k\omega_{cl}\right] + \frac{(1-\delta_p-\delta_s)}{2\pi(k_{tl}^2 - k^2)}\begin{bmatrix} 2k_{tl}\sin k_{tl}(\omega_{sl}-\omega_{cl})\cos(k\omega_{sl}) - 2k\cos k_{tl}(\omega_{sl}-\omega_{cl})\sin(k\omega_{sl}) \\ +2k\sin(k\omega_{cl}) \end{bmatrix}$$

$$= \frac{\delta_s}{k\pi}\left[\sin k\omega_{sl} - \sin k\omega_{cl}\right] + \frac{(1-\delta_p-\delta_s)}{\pi(k_{tl}^2 - k^2)}\begin{bmatrix} k_{tl}\sin k_{tl}(\omega_{sl}-\omega_{cl})\cos(k\omega_{sl}) - k\cos k_{tl}(\omega_{sl}-\omega_{cl})\sin(k\omega_{sl}) \\ +k\sin(k\omega_{cl}) \end{bmatrix} \qquad \text{(D2.10)}$$

Solving the 3rd term from Eq. (D2.8)

$$3rd\ \text{term} = h_{31}(n) = \frac{1}{\pi}\int_{\omega_{sl}}^{\pi} [\delta_s - \delta_s \sin\ (k_{sl}\ (\omega-\omega_{sl}))\ ]\ \cos k\omega\ \partial\omega$$

$$= \left.\frac{\delta_s \sin k\omega}{k\pi}\right|_{\omega_{sl}}^{\pi} - \frac{\delta_s}{2\pi}\int_{\omega_{sl}}^{\pi} [\sin\ (k_{sl}\ (\omega-\omega_{sl})+k\omega) + \sin\ (k_{sl}\ (\omega-\omega_{sl})-k\omega)]\partial\omega$$

$$= \frac{\delta_s}{k\pi}\left[\sin k\pi - \sin k\omega_{sl}\right] - \frac{\delta_s}{2\pi}\left[\frac{-\cos\ [(k_{sl}+k)\omega - k_{sl}\ \omega_{sl}}{k_{sl}+k} - \frac{\cos\ [(k_{sl}-k)\omega - k_{sl}\ \omega_{sl}]}{k_{sl}-k}\right]_{\omega_{sl}}^{\pi}$$

$$= \frac{\delta_s}{k\pi}\left[\sin k\pi - \sin k\omega_{sl}\right] + \frac{\delta_s}{2\pi}\left[\frac{\cos\ [(k_{sl}+k)\pi - k_{sl}\ \omega_{sl}] - \cos k\omega_{sl}}{k_{sl}+k} + \frac{\cos\ [(k_{sl}-k)\pi - k_{sl}\ \omega_{sl}] - \cos\ (-k\omega_{sl})}{k_{sl}-k}\right]$$

$$= \frac{\delta_s}{k\pi}\left[\sin k\pi - \sin k\omega_{sl}\right] + \frac{\delta_s}{2\pi(k_{sl}^2 - k^2)}\begin{bmatrix} (k_{sl}-k)\left\{\cos\ [(k_{sl}+k)\pi - k_{sl}\ \omega_{sl}] - \cos k\omega_{sl}\right\} \\ +(k_{sl}+k)\left\{\cos\ [(k_{sl}-k)\pi - k_{sl}\ \omega_{sl}] - \cos\ (k\omega_{sl})\right\} \end{bmatrix}$$

$$= \frac{\delta_s}{k\pi}\left[\sin k\pi - \sin k\omega_{sl}\right] + \frac{\delta_s}{2\pi(k_{sl}^2 - k^2)}\begin{bmatrix} k_{sl}\left\{\cos[(k_{sl}+k)\pi - k_{sl}\omega_{sl}] + \cos[(k_{sl}-k)\pi - k_{sl}\ \omega_{sl}]\right\} \\ +k\left\{\cos[(k_{sl}-k)\pi - k_{sl}\ \omega_{sl}] - \cos[(k_{sl}+k)\pi - k_{sl}\ \omega_{sl}]\right\} \\ -\ \cos k\omega_{sl}\left[(k_{sl}-k)+k_{sl}+k\right] \end{bmatrix}$$

$$= \frac{\delta_s}{k\pi}\left[\sin k\pi - \sin k\omega_{sl}\right] + \frac{\delta_s}{2\pi(k_{sl}^2 - k^2)}\begin{bmatrix} 2k_{sl}\ \cos[(k_{sl}(\pi - \omega_{sl})\cos k\pi + 2k\sin[(k_{sl}(\pi - \omega_{sl})\sin k\pi \\ -\ 2k_{sl}\ \cos(k\omega_{sl}) \end{bmatrix}$$

$$= \frac{\delta_s}{k\pi}\left[\sin k\pi - \sin k\omega_{sl}\right] + \frac{\delta_s}{\pi(k_{sl}^2 - k^2)}\begin{bmatrix} k_{sl}\ \cos[(k_{sl}(\pi - \omega_{sl})\cos k\pi + k\sin[(k_{sl}(\pi - \omega_{sl})\sin k\pi \\ -\ k_{sl}\ \cos(k\omega_{sl}) \end{bmatrix} \qquad \text{(D2.11)}$$

By substituting Eq.s (D2.9) to (D2.11) in Eq. (D2.8) we obtain the expression for the low pass filter impulse response h (n). Where $k \neq k_{tl}$, k_{pl} *and* k_{sl}.

Thus,

$$h(n) = h_{11}(n) + h_{21}(n) + h_{31}(n) \qquad \text{(D2.13)}$$

$$h(n) = \left\{\left(\frac{\delta_s}{k\pi}\right)\left[\sin\ (k\omega_{sl}) - \sin\ (k\omega_{cl}) + \sin\ (k\pi) - \sin\ (k\omega_{sl})\right] + \frac{(1-\delta_p)\ \sin(k\omega_{cl})}{k\pi}\right\}$$
$$+ \left\{\left(\frac{\delta_p}{\pi(k_{pl}^2 - k^2)}\right)\left[k_{pl}\sin(k_{pl}\omega_{cl})\cos(k\omega_{cl}) - k\cos(k_{pl}\omega_{cl})\sin(k\omega_{cl})\right]\right\}$$
$$+ \left\{\left(\frac{(1-\delta_p-\delta_s)}{\pi(k_{tl}^2 - k^2)}\right)\left[k\sin(k\omega_{cl}) + k_{tl}\sin(k_{tl}(\omega_{sl}-\omega_{cl}))\cos(k\omega_{sl}) - k\cos(k_{tl}(\omega_{sl}-\omega_{cl}))\sin(k\omega_{sl})\right]\right\}$$
$$+ \left\{\left(\frac{\delta_s}{\pi(k_{sl}^2 - k^2)}\right)\left[k_{sl}\cos(k_{sl}(\pi-\omega_{sl}))\cos(k\pi) + k\sin(k_{sl}(\pi-\omega_{sl}))\sin(k\pi) - k_{sl}\cos(k\omega_{sl})\right]\right\} \qquad \text{(D2.14)}$$

Eq. (D2.14) is further simplified to obtain Eq. (D2.15)

$$h(n) = \left\{\left(\frac{1}{k\pi}\right)\left[(1-\delta_p-\delta_s)\ \sin(\mathrm{k}\,\omega_{cl})+\delta_s\ \sin(\mathrm{k}\,\pi)\right]\right\}$$

$$+\left\{\left(\frac{\delta_p}{\pi(k_{pl}{}^2-\ k^2)}\right)\left[k_{pl}\sin(k_{pl}\omega_{cl})\cos(k\omega_{cl})-k\cos(k_{pl}\omega_{cl})\sin(k\omega_{cl})\right]\right\}$$

$$+\left\{\left(\frac{(1-\delta_p-\delta_s)}{\pi(k_{tl}{}^2-\ k^2)}\right)\left[k\sin(k\omega_{cl})+k_{tl}\sin(k_{tl}(\omega_{sl}-\omega_{cl}))\cos(k\omega_{sl})-k\cos(k_{tl}(\omega_{sl}-\omega_{cl}))\sin(k\omega_{sl})\right]\right\}$$

$$+\left\{\left(\frac{\delta_s}{\pi(k_{sl}{}^2-\ k^2)}\right)\left[k_{sl}\cos(k_{sl}(\pi-\omega_{sl}))\cos(k\pi)+k\sin(k_{sl}(\pi-\omega_{sl}))\sin(k\pi)-k_{sl}\cos(k\omega_{sl})\right]\right\} \quad \text{(D2.15)}$$

Where $k \neq k_{tl}$, k_{pl} *and* k_{sl}.

The Eq. (D2.15) is the simplified expression for the low pass filter model impulse response h (n).

D3. Model II: LPST BPF Model and Design

In this section, the design of the integrated LPST band pass FIR filter is presented. For the proposed filter model, the five regions of the filter response are modelled using trigonometric functions of frequency. The filter model magnitude response H(ω) is shown in Figure 3.8. The filter design parameters k_1, k_2, k_3, k_4 and k_5 for the five regions of the band pass filter are evaluated below:

(i) In the region 1 (stopband), for $0 \le \omega \le \omega_{s1}$, the frequency response

$$H\ (\omega)\ =\ -\frac{\delta_s}{2}\ \cos\ (k_1\ \omega)\ , \quad \text{(D3.1)}$$

$$At\ \omega\ =\ 0\ ; \qquad H\ (0)\ =\ -\frac{\delta_s}{2}$$

$$At\ \omega\ =\ \omega_{s1} \qquad H\ (\omega_{s1})\ =\ 0$$

$$\therefore\ -\frac{\delta_s}{2}\ \cos\ (k_1\ \omega_{s1})\ =\ 0$$

$$k_1\ \omega_{s1} = \left(\mathrm{m}_1+\frac{1}{4}\right)2\pi$$

$$\therefore\ k_1\ =\ \frac{2\pi\mathrm{m}_1+\dfrac{\pi}{2}}{\omega_{s1}} \qquad \textit{where}\ \mathrm{m}_1\ \text{is an integer.} \quad \text{(D3.2)}$$

In Eq. (D3.1), ω is the frequency variable, H (ω) is the magnitude of the filter response, δ_s is the stopband attenuation, k_1 is the stopband filter design parameter , m_1 is an integer , ω_{s1} is the stopband edge frequency.

ii) In the region 2 (sharp transition) for $\omega_{s1} \le \omega \le \omega_{p1}$, the frequency response is

$$H(\omega) = \mathrm{k}_2\ (\omega-\omega_{s1}) \quad \text{(D3.3)}$$

$$At\ \omega\ =\ \omega_{s1}\ ; \qquad H(\omega_{s1})\ =\ 0$$

$$At\ \omega\ =\ \omega_{p1}\ ; \qquad H(\omega_{p1})\ =\ \mathrm{k}_2\ (\omega_{p1}-\omega_{s1})\ = 1.0$$

$$\therefore\ k_2\ =\ \frac{1}{(\omega_{p1}\ -\ \omega_{s1})}\ , \quad \text{(D3.4)}$$

where, k_2 is the transition filter design parameter and ω_{p1} is the cut off frequency in the passband.

iii) In the region 3 (passband) for $\omega_{p1} \le \omega \le \omega_{p2}$, the frequency response is

$$H(\omega) = 1 + \frac{\delta_p}{2} \sin (k_3 (\omega - \omega_{p1})) \tag{D3.5}$$

$$At\ \omega = \omega_{p1}; \qquad H(\omega_{p1}) = 1.0$$

$$At\ \omega = \omega_{p2}; \qquad H(\omega_{p2}) = 1 + \frac{\delta_p}{2} \sin (k_3 (\omega_{p2} - \omega_{p1})) = 1$$

$\therefore$ Either $k_3 (\omega_{p2} - \omega_{p1})) = 0$ or

with reference to Figure 3.8, $k_3 (\omega_{p2} - \omega_{p1}) = (2 m_3 + 1)\pi$

$$\therefore k_3 = \frac{(2 m_3 + 1)\pi}{(\omega_{p2} - \omega_{p1})}, \tag{D3.6}$$

where, k_3 is the passband filter design parameter, δ_p is the passband ripple and m_3 is an integer.

iv) In the region 4 (sharp transition) for $\omega_{p2} \leq \omega \leq \omega s_2$, the frequency response is

$$H(\omega) = 1 - k_4 (\omega - \omega_{p2}) \tag{D3.7}$$

$$At\ \omega = \omega_{p2}; \qquad H(\omega_{p2}) = 1$$

$$At\ \omega = \omega_{s2}; \qquad H(\omega_{s2}) = 1 - k_4 (\omega_{s2} - \omega_{p2}) = 0$$

$$k_4 (\omega_{s2} - \omega_{p2}) = 1$$

$$\therefore k_4 = \frac{1}{(\omega_{s2} - \omega_{p2})}, \tag{D3.8}$$

where, k_4 is the transition region filter design parameter.

v) In the region 5 (stopband) for $\omega_{s2} \leq \omega \leq \pi$, the frequency response is

$$H(\omega) = -\frac{\delta_s}{2} \sin (k_5 (\omega - \omega_{s2})) \tag{D3.9}$$

$$At\ \omega = \omega_{s2}; \qquad H(\omega_{s2}) = 0$$

$$At\ \omega = \pi \qquad H(\pi) = -\frac{\delta_s}{2} \sin (k_5 (\pi - \omega_{s2})) = -\frac{\delta_s}{2}, \text{ as shown in Figure 3.8}$$

$$\therefore \quad k_5 (\pi - \omega_{s2}) = \left(\mathrm{m}_5 + \frac{1}{4} \right) 2\pi$$

$$\therefore k_5 = \frac{2\pi \mathrm{m}_5 + \frac{\pi}{2}}{(\pi - \omega_{s2})}, \tag{D3.10}$$

where, k_5 is the stopband region filter design parameter and m_5 is an integer.

D3.1 Expressions for Impulse Response Coefficients of the LPST BPF FIR.

The impulse response coefficients $h_{bp}(n)$ for the integrated band pass FIR filter are obtained from,

$$h_{bp}(n) = \frac{1}{\pi}\left[\int_0^{\pi} H(\omega) \sin(k\omega) \ d\omega \right] \tag{D3.11}$$

$$h_{bp}(n) = \frac{1}{\pi} \left\{ \int_0^{\omega_{s1}} H(\omega) \sin(k\omega)\, \partial\omega + \int_{\omega_{s1}}^{\omega_{p1}} H(\omega) \sin(k\omega)\, \partial\omega + \int_{\omega_{p1}}^{\omega_{p2}} H(\omega) \sin(k\omega)\, \partial\omega \right.$$

$$\left. + \int_{\omega_{p2}}^{\omega_{s2}} H(\omega) \sin(k\omega)\, \partial\omega + \int_{\omega_{s2}}^{\pi} H(\omega) \sin(k\omega)\, \partial\omega \right\} \tag{D3.12}$$

Substituting Eq.s (D3.1) to (D3.10) in Eq. (D3.12) we get,

$$h_{bp}(n) = \frac{1}{\pi}\left\{\int_{0}^{\omega_{s1}} -\frac{\delta_s}{2}\cos(k_1\omega)\sin(k\omega)\,\partial\omega + \int_{\omega_{s1}}^{\omega_{p1}} \mathrm{k}_2(\omega-\omega_{s1})\sin(k\omega)\,\partial\omega\right.$$

$$+\int_{\omega_{p1}}^{\omega_{p2}}\left(1+\frac{\delta_p}{2}\sin\left(k_3(\omega-\omega_{p1})\right)\right)\sin(k\omega)\,\partial\omega + \int_{\omega_{p2}}^{\omega_{s2}}\left(1-k_4(\omega-\omega_{p2})\right)\sin(k\omega)\,\partial\omega$$

$$\left.+\int_{\omega_{s2}}^{\pi}\left(-\frac{\delta_s}{2}\sin\left(k_5(\omega-\omega_{s2})\right)\right)\sin(k\omega)\,\partial\omega\right\} \tag{D3.13}$$

Solving the 1st term from Eq. (D3.13)

$$1st\ \text{term} = h_{1bp}(n) = \frac{1}{\pi}\int_{0}^{\omega_{s1}} -\frac{\delta_s}{2}\cos(k_1\omega)\sin(k\omega)\,\partial\omega$$

$$h_{1bp}(n) = -\frac{\delta_s}{2\pi}\int_{0}^{\omega_{s1}} -\frac{1}{2}\left[\sin(k+k_1)\omega+\sin(k-k_1)\omega\right]\partial\omega$$

$$h_{1bp}(n) = -\frac{\delta_s}{4\pi}\left[\frac{-\cos(k+k_1)\omega}{(k+k_1)} - \frac{\cos(k-k_1)\omega}{(k-k_1)}\right]_{0}^{\omega s1}$$

$$h_{1bp}(n) = -\frac{\delta_s}{4\pi}\left[-\left[\frac{\cos(k+k_1)\omega_{s1}-1}{(k+k_1)} + \frac{\cos(k-k_1)\omega_{s1}-1}{(k-k_1)}\right]\right]$$

$$h_{1bp}(n) = \frac{\delta_s}{4\pi}\left[\frac{-1+\cos(k+k_1)\omega_{s1}}{(k+k_1)} + \frac{-1+\cos(k-k_1)\omega_{s1}}{(k-k_1)}\right] \tag{D3.14}$$

Solving the 2nd term from Eq. (D3.13)

$$2nd\ \text{term} = h_{2bp}(n) = \frac{1}{\pi}\int_{\omega_{s1}}^{\omega_{p1}} \mathrm{k}_2(\omega-\omega_{s1})\sin(k\omega)\,\partial\omega$$

$$h_{2bp}(n) = \frac{1}{\pi}\int_{\omega_{s1}}^{\omega_{p1}} \mathrm{k}_2\omega\,.\sin(k\omega)\,\partial\omega + \frac{1}{\pi}\int_{\omega_{s1}}^{\omega_{p1}} -\mathrm{k}_2\omega_{s1}\,.\sin(k\omega)\,\partial\omega$$

$$h_{2bp}(n) = \frac{\mathrm{k}_2}{\pi}\int_{\omega_{s1}}^{\omega_{p1}} \omega\,.\frac{d(-\cos k\omega)}{k} + \frac{\mathrm{k}_2\omega_{s1}}{\pi}\left[\frac{\cos k\omega}{k}\right]_{\omega s1}^{\omega p1}$$

$$h_{2bp}(n) = \frac{\mathrm{k}_2}{k\pi}\left[\left[\omega\left(-\cos k\omega\right)\Big|_{\omega s1}^{\omega p1}\right] - \int_{\omega_{s1}}^{\omega_{p1}}(-\cos k\omega)\left(\frac{d\omega}{d\omega}\right)d\omega\,.\right] + \frac{\mathrm{k}_2\omega_{s1}}{k\pi}\left[\cos k\omega_{p1}-\cos k\omega_{s1}\right]$$

$$h_{2bp}(n) = \frac{\mathrm{k}_2}{k\pi}\left[\left[-\omega_{p1}(\cos k\omega p1)+\omega_{s1}(\cos k\omega s1)\right] + \int_{\omega_{s1}}^{\omega_{p1}}\cos k\omega\, d\omega\,.\right] + \frac{\mathrm{k}_2\omega_{s1}}{k\pi}\left[\cos k\omega_{p1}-\cos k\omega_{s1}\right]$$

$$h_{2bp}(n) = \frac{\mathrm{k}_2}{k\pi}\left[\left[\omega_{s1}(\cos k\omega s1)-\omega_{p1}(\cos k\omega p1)\right] + \frac{\mathrm{k}_2}{k\pi}\left[\frac{\sin k\omega}{k}\right]_{\omega s1}^{\omega p1}\right] + \frac{\mathrm{k}_2\omega_{s1}}{k\pi}\left[\cos k\omega_{p1}-\cos k\omega_{s1}\right]$$

$$h_{2bp}(n)=\frac{\mathrm{k}_2}{k\pi}\left[\left[\omega_{s1}(\cos k\omega s1)-\omega_{p1}(\cos k\omega p1)\right]+\frac{\mathrm{k}_2}{k^2\pi}\left[\sin k\omega_{p1}-\sin k\omega_{s1}\right]\right]$$
$$+\ \frac{\mathrm{k}_2\omega_{s1}}{k\pi}\left[\cos k\omega_{p1}-\cos k\omega_{s1}\right] \qquad \text{(D3.15)}$$

Solving the 3rd term from Eq. (D3.13)

$$3rd\ \text{term} = h_{3bp}(n) = \ \frac{1}{\pi}\int_{\omega_{p1}}^{\omega_{p2}}\left(1+\frac{\delta_p}{2}\ \sin k_3(\omega-\omega_{p1})\right)\ \sin(k\omega)\ \partial\omega$$

$$h_{3bp}(n)=\ \frac{1}{\pi}\int_{\omega_{p1}}^{\omega_{p2}}\sin(k\omega)\ \partial\omega+\frac{1}{\pi}\int_{\omega_{p1}}^{\omega_{p2}}\ \frac{\delta_p}{2}.\frac{1}{2}\left\{\cos\left[(k-k_3)\omega+k_3\omega_{p1}\right]-\cos\left[(k+k_3)\omega-k_3\omega_{p1}\right]\right\}\partial\omega$$

$$h_{3bp}(n)=\ \frac{1}{\pi}\ \left[\frac{-\cos k\omega}{k}\right]_{\omega p1}^{\omega p2}+\frac{\delta_p}{4\pi}\left[\frac{\sin\left[(k-k_3)\omega+k_3\omega_{p1}\right]}{(k-k_3)}-\frac{\sin\left[(k+k_3)\omega-k_3\omega_{p1}\right]}{(k+k_3)}\right]_{\omega p1}^{\omega p2}$$

$$h_{3bp}(n)=-\frac{1}{k\pi}\left[\cos k\omega_{p2}-\cos k\omega_{p1}\right]+\frac{\delta_p}{4\pi(k-k_3)}\left\{\sin\left[(k-k_3)\omega_{p2}+k_3\omega_{p1}\right]-\sin\left[(k-k_3)\omega_{p1}+k_3\omega_{p1}\right]\right\}$$
$$-\ \ \frac{\delta_p}{4\pi(k+k_3)}\left\{\sin\left[(k+k_3)\omega_{p2}-k_3\omega_{p1}\right]-\sin\left[(k+k_3)\omega_{p1}-k_3\omega_{p1}\right]\right\}$$

$$h_{3bp}(n)=-\frac{1}{\pi}\left(\frac{\cos k\omega_{p2}-\cos k\omega_{p1}}{k}\right)+\frac{\delta_p}{4\pi(k-k_3)}\left\{\sin\left[(k-k_3)\omega_{p2}+k_3\omega_{p1}\right]-\sin k\omega_{p1}\right\}$$
$$-\ \ \frac{\delta_p}{4\pi(k+k_3)}\left\{\sin\left[(k+k_3)\omega_{p2}-k_3\omega_{p1}\right]-\sin k\omega_{p1}\right\} \qquad \text{(D3.16)}$$

Solving the 4th term from Eq. (D3.13)

$$4th\ \text{term} = h_{4bp}(n) = \ \frac{1}{\pi}\int_{\omega_{p2}}^{\omega_{s2}}\left[1-k_4\ (\omega-\omega_{p2})\right]\sin(k\omega)\ \partial\omega$$

$$h_{4bp}(n)=\ \frac{1}{\pi}\int_{\omega_{p2}}^{\omega_{s2}}\sin(k\omega)\ \partial\omega-\frac{k_4}{\pi}\int_{\omega_{p2}}^{\omega_{s2}}\omega.\sin(k\omega)\ \partial\omega\ +\frac{k_4}{\pi}\ \omega_{p2}\int_{\omega_{p2}}^{\omega_{s2}}\ \sin(k\omega)\ \partial\omega$$

$$h_{4bp}(n)=\ \left[\frac{-\cos k\omega}{\pi k}\right]_{\omega p2}^{\omega s2}-\frac{k_4}{\pi}\int_{\omega_{p2}}^{\omega_{s2}}\omega\frac{d(-\cos k\omega)}{k}+\frac{k_4}{\pi}\ \omega_{p2}\left[\frac{-\cos k\omega}{k}\right]_{\omega p2}^{\omega s2}$$

$$h_{4bp}(n)=\ \frac{1}{\pi k}\left[-\cos k\omega_{s2}+\ \cos k\omega_{p2}\right]-\frac{k_4}{\pi k}\left[-\omega.\cos k\omega\right]_{\omega p2}^{\omega s2}-\frac{k_4}{\pi}\int_{\omega_{p2}}^{\omega_{s2}}\ \frac{(-\cos k\omega)}{k}\partial\omega$$
$$+\ \frac{k_4\ \omega_{p2}}{\pi k}\left[-\cos k\omega_{s2}+\ \cos k\omega_{p2}\right]$$

$$h_{4bp}(n)=\ \frac{1}{\pi k}\left[-\cos k\omega_{s2}+\ \cos k\omega_{p2}\right]+\frac{k_4}{\pi k}\left[\omega_{s2}\cos k\omega_{s2}-\ \omega_{p2}\cos k\omega_{p2}\right]-\frac{k_4}{k\pi}\left[\frac{-\sin k\omega}{k}\right]_{\omega p2}^{\omega s2}$$
$$+\frac{k_4\ \omega_{p2}}{\pi k}\left[-\cos k\omega_{s2}+\ \cos k\omega_{p2}\right]$$

$$h_{4bp}(n)=\frac{1}{k\pi}\left[-\cos k\omega_{s2}+\cos k\omega_{p2}\right]+\frac{k_4}{k\pi}\left[\omega_{s2}\cos k\omega_{s2}-\omega_{p2}\cos k\omega_{p2}\right]+\frac{k_4}{k^2\pi}\left[\sin k\omega_{s2}-\sin k\omega_{p2}\right]$$
$$+\frac{k_4\,\omega_{p2}}{k\pi}\left[-\cos k\omega_{s2}+\cos k\omega_{p2}\right] \qquad \text{(D3.17)}$$

Solving the 5th term from Eq. (D3.13)

$$5th\ \text{term} = h_{5bp}(n)=\frac{1}{\pi}\int_{\omega_{s2}}^{\pi}\left(-\frac{\delta_s}{2}\ \sin\left[k_5\ (\omega-\omega_{s2})\right]\right)\sin(k\omega)\ \partial\omega$$

$$h_{5bp}(n)=-\frac{1}{\pi}\ \frac{\delta_s}{2}\int_{\omega_{s2}}^{\pi}\frac{1}{2}\ .\left[\cos\left[(k_5-k)\omega-k_5\omega s_2\right]-\cos\left[(k_5+k)\omega-k_5\omega s_2\right]\right]\partial\omega$$

$$h_{5bp}(n)=-\frac{\delta_s}{4\pi}\left[\frac{\sin\left[(k_5-k)\omega-k_5\omega_{s2}\right]}{(k_5-k)}-\frac{\sin\left[(k_5+k)\omega-k_5\omega_{s2}\right]}{(k_5+k)}\right]\Bigg|_{\omega s2}^{\pi}$$

$$h_{5bp}(n)=-\frac{\delta_s}{4\pi}\left[\begin{array}{l}\dfrac{\sin\left[(k_5-k)\pi-k_5\omega_{s2}\right]-\sin\left[(k_5-k)\omega_{s2}-k_5\omega_{s2}\right]}{(k_5-k)}\\ -\dfrac{\sin\left[(k_5+k)\pi-k_5\omega_{s2}\right]-\sin\left[(k_5+k)\omega_{s2}-k_5\omega_{s2}\right]}{(k_5+k)}\end{array}\right]$$

$$h_{5bp}(n)=-\frac{\delta_s}{4\pi}\left[\frac{\sin\left[(k_5-k)\pi-k_5\omega_{s2}\right]+\sin k\omega_{s2}}{(k_5-k)}-\frac{\sin\left[(k_5+k)\pi-k_5\omega_{s2}\right]-\sin k\omega_{s2}}{(k_5+k)}\right] \qquad \text{(D3.18)}$$

The Eq. (D3.12) is evaluated to obtain the expression for the band pass filter model impulse response h (n), using equations (D3.13 to D3.18)

$$h(\text{n})=\left\{\left(\frac{\delta_s}{4\pi}\right)\left[\frac{\cos\ ((k+k_1)\ \omega_{s1})\ -1}{(k+k_1)}+\frac{\cos\ ((k-k_1)\ \omega_{s1})\ -1}{(k-k_1)}\right]\right\}$$
$$+\left\{\begin{array}{l}\left(\dfrac{k_2}{k\pi}\right)\left[(-\omega_{p1})\cos(k\omega_{p1})+(\omega_{s1})\cos(k\omega_{s1})\right]\ -\\ \left(\dfrac{k_2}{k^2\pi}\right)\left[\sin(k\omega_{p1})-\sin(k\omega_{s1})\right]+\left(\dfrac{k_2\omega_{s1}}{k\pi}\right)\left[\cos(k\omega_{p1})-\cos(k\omega_{s1})\right]\end{array}\right\}$$
$$+\left\{\begin{array}{l}\left(-\dfrac{1}{\pi}\right)\left[\dfrac{\cos(k\omega_{p2})-\cos(k\omega_{p1})}{k}\right]+\left(\dfrac{\delta_p}{4\pi\ (k-k_3)}\right)\left[\sin\left[(k-k_3)\ \omega_{p2}+k_3\,\omega_{p1}\right]-\sin(k\omega_{p1})\right]\\ +\left(\dfrac{-\delta_p}{4\pi\ (k+k_3)}\right)\left[\sin\left[(k+k_3)\ \omega_{p2}-k_3\,\omega_{p1}\right]-\sin(k\omega_{p1})\right]\end{array}\right\}$$
$$+\left\{\begin{array}{l}\left(\dfrac{1}{k\pi}\right)\left[-\cos(k\omega_{s2})+\cos(k\omega_{p2})\right]+\left(\dfrac{k_4}{k\pi}\right)\left[(\omega_{s2})\cos(k\omega_{s2})-(\omega_{p2})\cos(k\omega_{p2})\right]\\ +\left(\dfrac{k_4}{k^2\pi}\right)\left[\sin(k\omega_{s2})-\sin(k\omega_{p2})\right]+\left(\dfrac{k_4\omega_{p2}}{k\pi}\right)\left[-\cos(k\omega_{s2})+\cos(k\omega_{p2})\right]\end{array}\right\}$$
$$+\left\{\left(\frac{-\delta_s}{4\pi}\right)\left[\left(\frac{\sin((k_5-k)\ \pi-k_5\omega_{s2})+\sin(k\omega_{s2})}{(k_5-k)}\right)-\left(\frac{\sin((k_5+k)\ \pi-k_5\omega_{s2})-\sin(k\omega_{s2})}{(k_5+k)}\right)\right]\right\} \qquad \text{(D3.19)}$$

where , $k=\left[\left(\frac{N-1}{2}\right)-n\right]$.

The Eq. (D3.19) is the expression for the band pass filter model impulse response h (n). We can choose the effective pass band width ($\omega_{p2} \sim \omega_{p1}$) such that ($\omega_{s1} \sim \omega_{p1}$) = ($\omega_{s2} \sim \omega_{p2}$), as small as possible for sharp transition of passband edge. Once ω_{p1}, ω_{p2}, ω_{s1} and ω_{s2} are chosen k_1, k_2, k_3, k_4 and k_5 are determined.